A Spin- and Angle-Resolved Photoemission Study of the Rashba-Bychkov Effect in Lead Quantum Well States

Dissertation
zur Erlangung der naturwissenschaftlichen Doktorwürde
(Dr. sc. nat.)
vorgelegt der
Mathematisch-naturwissenschaftlichen Fakultät
der
Universität zu Zürich

von

Bartosz Slomski
aus Polen

Promotionskomitee
Prof. Dr. Jürg Osterwalder (Vorsitz und Leitung der Dissertation)
Dr. J. Hugo Dil
Dr. Gian Salis

Zürich 2013

Die vorliegende Arbeit wurde von der Mathematisch-Naturwissenschaftlichen Fakultät der Universität Zürich im Früjahrssemester 2013 als Dissertation angenommen.

Promotionskomitee:
Vorsitzender und Leiter der Dissertation: Prof. Dr. Jürg Osterwalder
Betreuer: .... Dr. J. Hugo Dil
Gutachter: .... Dr. Gian Salis
Tag der mündlichen Prüfung: .... 14. März 2013

To Tine & Jakub

Abstract

In the rapidly developing field of spintronics whose central issue is the utilization of the spin instead of the charge of the electron, the active control of spin-polarized carriers (electrons or holes) utilizing electric rather than magnetic fields has highest priority. Researchers world wide are searching for a realization of a spin-based field-effect transistor (spin-FET) that has the potential to revolutionize electronic devices and carries new prospects of data manipulation.

The present thesis deals with the investigation of the Rashba-Bychkov effect as a possible candidate for a spin-FET formed by an ultra-thin Pb film on a silicon substrate, using spin- and angle-resolved photoemission spectroscopy. The reduced dimensionality of such an epitaxially grown metallic film results in a two-dimensional (2D) electron gas associated with quantum well states (QWS). These states are free to move within the sample plane, while they are confined perpendicularly by the energy gap of the Si substrate on one side and by the repulsive image potential toward the vacuum on the other side, reminiscent of the particle-in-the-box model. Due to the broken inversion symmetry along the confinement direction and the high nuclear charge of Pb the QWS show a Rashba-type spin splitting which builds up throughout the whole metal layer along the growth direction as a result of competing effects between the metal-substrate and metal-vacuum interfaces.

In this thesis the focus lies on altering the interface region between the film and the substrate to provide more insight into the origin of the Rashba effect and other phenomena such as the effective mass of the bands and Schottky barrier formation.

In the first approach we have varied the chemistry of the interface by studying various interfactants such as Pb, Bi and Ag, which form highly regular structures of $(\sqrt{3} \times \sqrt{3})$R30° symmetry on Si. It is found that the size of the Rashba effect changes dramatically among these interfaces: replacing the Pb interface by a Bi layer reduced the Rashba parameter by 60%, whereas QWS in Pb films grown on a Ag reconstructed Si substrate showed no measurable spin splitting. Interestingly, the Schottky barrier of these systems, and the effective mass of the states varies in the same manner. For future device application it is necessary to control the Rashba parameter by external means. The results of our second approach, the study of the influence of the substrate doping concentration on the Rashba effect in Pb QWS, revealed a very promising pathway: by increasing the donor concentration by a factor of 20, we could tune the Rashba parameter by a factor of two. A simulation of the relevant parameter indeed showed that a gate voltage of only 12 V is enough to switch a 1 nm lateral spin-FET from the insulating to the conducting state. These findings are discussed in the framework of the interface dipole model and a doping dependent Schottky barrier.

In order to gain more insight into the interplay of band dispersion, orbital character, and spin, we have focused on a wave vector region in Pb QWS where avoided crossing hybridization induced by spin-orbit coupling alters the band structure significantly. A breakdown of the Rashba effect is found which manifests itself in a spin splitting that is no longer proportional to the in-plane momentum of the electrons. Furthermore it is found that these hybridization effects can cause a reversal of the sign of the momentum splitting which is well explained by an interband spin-orbit coupling between states of anti-parallel spin directions.

From a fundamental scientific view-point, the body of this thesis illustrates the subtle interplay of the electronic, spin and structural properties of the overlayer and their sensitivity to the boundary conditions and specifically the metal-substrate interface.

Keywords: Spin- and angle-resolved photoemission spectroscopy
Quantum well states
Rashba-Bychkov effect
Spintronics
Schottky barrier
Interface dipole model
Interband spin-orbit coupling

Zusammenfassung

Das Hauptaugenmerk auf dem schnell expandierenden Gebiet der Spintronik liegt auf der Verwendung des Spins statt der elektrischen Ladung des Elektrons. Idealerweise sollte eine aktive Kontrolle von spin-polarisierten Ladungsträgern mittels elektrischen statt magnetischen Feldern erzielt werden. Weltweit versuchen Forscher den sog. Spin-Feld-Effekt-Transistor (Spin-FET) zu realisieren, weil sich damit unter anderem neue Möglichkeiten in der Datenmanipulation ergeben.

Die vorliegende Dissertation untersucht mittels der Methode der spin- und winkelaufgelösten Photoemissions-Spektroskopie den Rashba-Bychkov-Effekt in Nanostrukturen bestehend aus dünnen Bleischichten auf dem Halbleitersubstrat Silizium. Das Besondere an solchen epitaktisch gewachsenen Dünnschichten ist, dass sich spezielle elektronische Zustände ausbilden, sogenannte Quantentopfzustände (*engl. quantum well states*), die als stehende Elektronenwellen aufgefasst werden können. Diese entstehen, da in Richtung des Halbleitersubstrates dessen Bandlücke, und in Richtung des Vakuums, das abstossende Bildladungspotential als Potentialbarrieren für die Elektronen wirken. Lateral erfahren die Elektronen keine Einschränkung, weshalb sie sich mehr oder weniger frei bewegen können.

Die hohe Kernladung der Bleiatome führt zu einer starken Spin-Bahn-Kopplung, welche zusammen mit der entlang der Wachstumsrichtung gebrochenen Inversionssymmetrie der Dünnschicht in den Quantentopfzustände eine Rashba-artige Spinaufspaltung hervorrufen. Hierbei ist zu beachten, dass jede Bleilage entlang der Wachstumsrichtung einen Beitrag zur Spinaufspaltung liefert aufgrund der unterschiedlichen Barrieren an der Metal-Halbleiter- und Metal-Vakuum-Grenzregion.

Das Ziel dieser Dissertation ist es, zu erkunden, welchen Einfluss die Metal-Halbleiter-Grenzregion auf den Rashba-Bychkov-Effekt, auf die effektive Masse der Elektronen, sowie auf die Ausbildung der Schottky Barriere ausübt.

Um dies herauszufinden variierten wir in einer ersten Studie die chemische Zusammensetzung der Grenzschicht, indem wir Bleifilme auf unterschiedlichen Oberflächenrekonstruktionen untersuchten, bestehend aus Blei, Bismut oder Silber. Diese Rekonstruktionen haben gemeinsam, dass sie wohldefinierte Strukturen mit einer sogenannten $(\sqrt{3}\times\sqrt{3})\mathrm{R}30^\circ$ Symmetrie auf dem Silizium-Substrat bilden. Wir konnten zeigen, dass der Rashba-Parameter sehr stark von der Grenzschicht abhängt, da er um ca. 60% abnimmt, wenn eine Oberflächenrekonstruktion aus Blei mit einer aus Bismut ersetzt wird. Quantentopfzustände in Bleifilmen auf einer Silbergrenzschicht weisen dagegen eine Spinaufspaltung auf, die kleiner als das Auflösungsvermögen der Messapparatur ist. Interessanterweise zeigen die Schottky-Barriere der Nanostrukturen und die effektive Masse der Elektronen ein ähnliches Verhalten.

Für etwaige Spin-FET Anwendungen in der Zukunft ist es notwendig, den Rashba-Effekt mittels externer Parameter zu kontrollieren. Zu diesem Zweck haben wir in einer zweiten Studie den Einfluss der Dotierungsdichte des Siliziums auf den Rashba-Effekt in Bleifilmen untersucht. Auch hier haben wir eine starke Abhängigkeit gefunden, welche sich dadurch äussert, dass eine Erhöhung der Dotierdichte z.B. um den Faktor 20 den Rashba-Parameter um den Faktor zwei vergrössert. Eine Simulation des relevanten Parameters zeigt sogar, dass eine Spannung von etwa 12 V aus-

reicht, um einen Spin-FET mit einer lateralen Ausdehnung von nur einem Nanometer aus dem Sperr- in den Leitungszustand zu schalten. Diese Resultate werden auf der Basis des sogenannten Grenzschicht-Dipol-Modells (engl. *interface dipole model*) und einer dotierabhängigen Schottky-Barriere diskutiert.
Abschliessend haben wir das Zusammenspiel zwischen Banddispersion, dem orbitalen Charakter und dem Spin der Zustände untersucht. Hierbei haben wir unser Augenmerk auf eine Wellenvektorregion gerichtet, die durch eine von der Spin-Bahn-Kopplung induzierten Hybridisierung (engl. *SOI-induced avoided crossing hybridization*) beachtlich modifiziert wird. Gleichzeitig führt die Hybridisierung zu einem Zusammenbruch des Rashba-Effekts, der dadurch gekennzeichnet ist, dass die Spinaufspaltung nicht mehr linear mit dem Wellenvektor zunimmt. Ferner induziert der Effekt eine Vorzeichenänderung in der Wellenvektor-Aufspaltung. Unsere Resultate lassen sich sehr gut mit dem Modell der sogenannten Interband-Spin-Bahn-Kopplung (engl. *interband spin-orbit coupling*) erklären, das eine Mischung von Zuständen mit antiparallelen Spins annimmt.

Vom wissenschaftlichen Standpunkt aus betrachtet veranschaulicht diese Dissertation das Zusammenspiel zwischen elektronischen Eigenschaften, der Spintextur und dem strukturellen Aufbau der Dünnschicht und ihre Sensitivität auf Randbedingungen, vor allem auf die Metal-Halbleiter-Grenzregion.

Schlüsselbegriffe: Spin- und winkelaufgelöste Photoemissions-Spektroskopie
Quantentopfzustände
Rashba-Bychkov-Effekt
Spintronik
Schottky-Barriere
Grenzschicht-Dipol-Modell
Interband-Spin-Bahn-Kopplung

List of acronyms

Spin-FET	spin field-effect transistor
1D/ 2D/ 3D	one-/ two-/ three-dimensional
QWS	quantum well state
GMR	giant magnetoresistance
FM	ferromagnetic
SOI	spin-orbit interaction
ARPES	angle-resolved photoemission spectroscopy
SARPES	spin- and angle-resolved photoemission spectroscopy
XPS	X-ray photoemission spectroscopy
LEED	low energy electron diffraction
DFT	density functional theory
COPHEE	(the) complete photoemission experiment
PAM	phase accumulation model
QWR	quantum well resonance
DOS	density of states
SBZ	surface Brillouin zone
QSE	quantum size effect
SB	Schottky barrier
IDM	interface dipole model
VB	valence band
CLS	core-level shift
MDC	momentum distribution curve
EDC	energy distribution curve
STM(S)	scanning tunneling microscopy (spectroscopy)

Contents

1 Introduction

Otto Stern and Walther Gerlach discovered in their pioneering experiment in 1922, that electrons possess beside a mass and a negative charge an intrinsic angular momentum - the spin [1]. This fundamental property of fermions, quantized in its nature, has stimulated the physicists both in theory and experiment. Later, the progress in energy resolution of spectroscopic experiments have indeed identified that spectral lines of atomic levels show additional energy splittings, which were explained as due to the interaction of the spin with the orbital angular momentum (fine structure) and the interaction of the spin with magnetic moments generated by the nucleus (hyperfine structure) [2].

In condensed matter physics the spin of an electron is not only at the heart of magnetic phenomena, which deal e.g. with the ordering of spin structures in real space, but is also becoming increasingly important in the multidisciplinary field of *spintronics* whose central issue is the active manipulation of spin degrees of freedom.

To illustrate the technological relevance of this field let us recall the principle of an already commercially implemented device utilizing the giant magnetoresistance (GMR), discovered by the group of Peter Grünberg [3] and by Albert Fert [4] in 1988. Both scientists were jointly awarded with the Nobel Prize in physics in 2007.

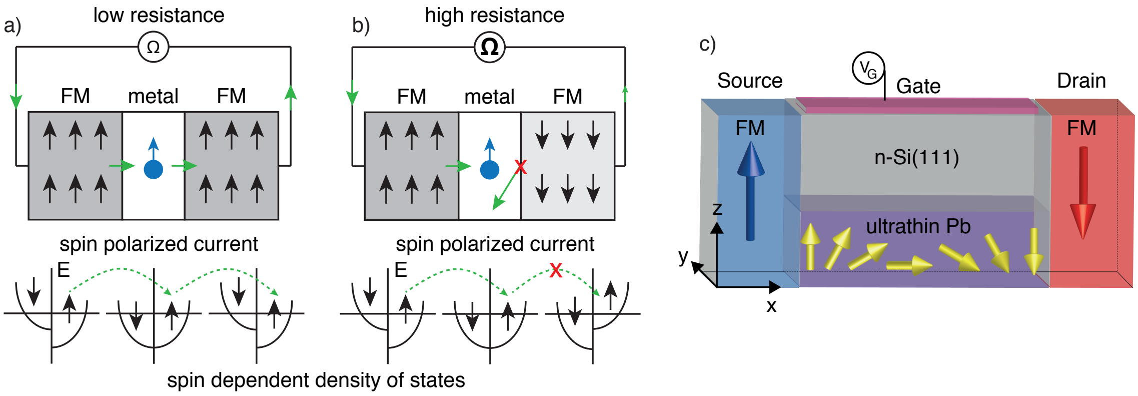

Figure 1: *Schematic drawing of a device utilizing the GMR effect with (a) parallel and (b) anti-parallel configuration of the magnetization directions (upper panel) and spin dependent density of states (lower panel) [adapted from Ref. [5]]. (c) Scheme of the Datta-Das spin-FET. The ferromagnetic source and drain serve as a spin injector and spin detector, respectively. Due to the spin-orbit interaction in the channel (e.g. ultra-thin Pb film) the injected spin of the spin-polarized electrons precesses in the x-z plane. High conductance is achieved when the magnetic moment of electrons is aligned parallel with the magnetization direction of the drain. The advantage of such a device is that, unlike in GMR, the high and low resistance states can be controlled by a gate voltage alone leaving the magnetization of the two ferromagnetic layers unchanged.*

Consider a non-magnetic layer acting as a spacer sandwiched between two magnetic layers of different coercive fields, as shown in Figs. 1 (a-b). To avoid confusion in the following discussion we focus on the magnetic moment of an electron ($\vec{\mu}_s$) instead of its spin ($\vec{s}$), because both are related to each other via

$$\vec{\mu}_s = -g\mu_B \frac{\vec{s}}{\hbar} \tag{1}$$

where g = 2,002319 is the g-factor and μ_B is the Bohr magneton. A small voltage applied to the system induces a current flowing perpendicular to the multi layers. The initially randomly oriented magnetic moments of the electrons acquire a common magnetic moment direction when passing through the first ferromagnetic (FM) layer, i.e. the current gets spin-polarized with a magnetic moment direction corresponding to that of the first FM layer. Depending on the magnetic moment direction of the second ferromagnetic layer, the spin-polarized current can either easily continue or gets suppressed. A high current passes through the device (low resistance) when both the direction of the magnetic moments of the spin current and the direction of the magnetic moments in the second FM layer are aligned parallel. This is understood by the fact, that the spin-polarized current can scatter into a high density of free electronic states with the same magnetic moment direction [6], as schematically shown in the lower panel of Fig. 1 (a). A reversal of the magnetization direction of the second FM layer leads thus to a low current, because the spin-polarized electrons find less available states to scatter into, see Fig. 1 (b). The key success of magnetoresistance-based applications is due to the fact that the resistance of a device can be controlled via the active manipulation of the relative orientations of the magnetization directions in the ferromagnetic layers.

To date, the majority of electronic devices, such as transistors in integrated circuits, are based on semiconductor technology. The question of whether a similar effect can be achieved in devices made of semiconductors have been answered by Datta and Das in the 1990's by proposing the spin field-effect transistor [7], which is schematically displayed in Fig. 1 (c). The operating principle of such a device is as follows. A metallic and non-magnetic layer, grown on a semiconducting substrate, forms a two-dimensional (2D) narrow channel between FM source and drain electrodes acting as the injector and detector of the electron spin. The source injects electrons with a certain magnetic moment (spin) direction into the narrow channel. In analogy to the GMR based device, depending on whether the magnetic moments of electrons are aligned parallel or antiparallel with the magnetization direction of the drain after propagating along the channel, a high or low current passes through the device. The role of the gate electrode is to control the spin precession of electrons in the narrow channel by means of applying an electric field rather than a magnetic field. It is the spin-orbit interaction in the non-magnetic channel which allows for such an active control of the resulting magnetic moment (spin) orientation of electrons at the interface to the drain.

Spin-orbit interaction in low-dimensional systems is a fascinating property that locks the spin of an electron to its momentum. Depending on the crystal symmetries of the material and structural properties, the spin-orbit interaction can take different functional forms resulting in effective Hamiltonians that are either modeled by the Rashba-Bychkov [8] or the Dresselhaus effect [9]. The focus of this thesis is to explore possible mechanisms leading to a modification of the spin-orbit interaction in a Rashba system, where the structural inversion symmetry parallel to the plane of a 2D electron gas is broken by the presence of a surface or interface. In the simplest case this generates a spin texture in the Fermi surface consisting of a pair of circles centered around the time-reversal invariant momentum $\overline{\Gamma}$ point with tangentially aligned spins of opposite directions, forming spin vortices of different radii. The difference of the radii, i.e. the momentum splitting of the Rashba pairs depends on the size of SOI and is one of the key-functionalities for the design of a spin-FET.

As a playground for studying the Rashba effect in low-dimensional systems we chose Pb on Si(111) for various reasons. The most important ones are as follows:

- **Well-organized growth and non-dilute interfaces**
  Pb atoms form highly ordered two-dimensional atomic arrays on Si(111) that grow in a layer-by-layer fashion allowing for the control of the system on the atomic scale. The interface between Si and Pb is non-dilute and abrupt, even when an additional layer of foreign atoms is sandwiched between the Pb film and the Si substrate. This property is highly desirable for the study of interface induced effects.

- **Quantum size effects**
  The most dramatic change in material properties takes place in quantum size structures when valance electrons are confined to dimensions of the order of the de Broglie wavelength. That way, quantum mechanical properties become important resulting in the formation of e.g. standing electron waves, known as quantum well states - the central interest of this thesis.

- **Rashba-type spin-orbit interaction**
  The high nuclear charge of the Pb cores together with the symmetry-broken environment at both, the metal-vacuum and metal-substrate interface have lead to the observation of the Rashba effect in this system.

As a method of choice we use a combination of angle-resolved photoemission spectroscopy (ARPES) with spin resolution (SARPES) to map electronic and spin properties of the systems. Since our approach is to use as many surface analysis techniques as possible, we employ also low energy electron diffraction (LEED) and core-level spectroscopy (XPS). All these techniques are briefly introduced in Chapter 2. Chapter 3 is dedicated to a general introduction into the concept of quantum well states with particular emphasis on Pb/Si(111). In Chapter 4 we introduce the different Si terminations used to explore how structural and electronic properties of the interfacial region influences the SOI in the Pb film.

The second part of this thesis starts with Chapter 5, where we briefly introduce the theoretical background of spin-orbit interaction with a detailed description of the Rashba-Bychkov effect.

In addition we review the present understanding of SOI in low-dimensional systems with a special treatment of the Rashba effect due to SOI in the ultra-thin Pb film. In Chapter 6 we investigate the spin properties of the Pb films as a function of interface. Our approach in this study is to maintain the Pb film and the substrate while changing the intra-layer to isolate interface-induced effects.

For future device applications in the field of spintronics it is desirable to control the Rashba effect by external means, ideally by a gate voltage. Since applying a back-gate voltage to a Rashba system while performing spin-resolved ARPES experiments at the same time needs a re-design of the present experimental setup, we first focus on the influence of the substrate charge density on the Rashba-type spin splitting - the topic of the second part of Chapter 6.

Chapter 7 of this thesis is dedicated to a rather common effect in condensed matter physics, the so-called avoided crossing hybridization due to SOI. Here we investigate by means of SARPES a particular momentum region of Pb QWS, where the avoided crossing effect between states alters the dispersions significantly.

2 Experimental and theoretical methods

The aim of this chapter is to briefly introduce the reader into the techniques which were used in this thesis. The investigation of the electronic structure was done with angle-resolved photoemission spectroscopy (ARPES) with spin resolution (SARPES). The analysis of the surface quality and symmetry has been performed using low energy electron diffraction (LEED), while theoretical band structures where calculated employing the *WIEN2K* code based on density functional theory (DFT).

2.1 Angle-resolved photoemission spectroscopy

Angle-resolved photoemission spectroscopy is nowadays a widely established tool to investigate the electronic structure of solids and surfaces in a most direct way. It relies on the photoelectric effect, by which electrons are emitted from an illuminated sample. It was first discovered by H. Hertz in 1887 [10] and later explained by A. Einstein in 1905 [11] as a quantum phenomenon. In the following we restrict our introduction to the basics of ARPES using the single particle picture. A more sophisticated description can be found e.g. in [12–15]. The basic principles of a photoemission experiment are as follows. A collimated beam of monochromatized light, with energy $h\nu$, generated either by a gas-discharge lamp, laser or by a synchrotron radiation source, impinges on a sample. As a result of the photoelectric effect, photoelectrons escape from the solid and are emitted in all directions into the vacuum. These photoelectrons are then collected with an electrostatic analyzer of finite acceptance angle as a function of their kinetic energy (E_{kin}) and emission angles (ϑ_S, φ_S) with respect to the sample surface (Fig. 2 (b)). From the knowledge of the emission angles, the wave vector of the photoelectron outside the solid, i.e. $\mathbf{K} = \mathbf{p}/\hbar$, is completely determined via

$$\begin{aligned} K_x &= \frac{1}{\hbar}\sqrt{2m_e E_{\text{kin}}} \cdot \sin\vartheta_S \cdot \cos\varphi_S \\ K_y &= \frac{1}{\hbar}\sqrt{2m_e E_{\text{kin}}} \cdot \sin\vartheta_S \cdot \sin\varphi_S \\ K_z &= \frac{1}{\hbar}\sqrt{2m_e E_{\text{kin}}} \cdot \cos\vartheta_S \end{aligned} \tag{2}$$

where $\hbar$ is the reduced Planck constant and m_e the electron mass. By taking advantage of energy and momentum conservation laws and considering that the photon momentum can be neglected at VUV photon energies typically used in ARPES experiments, it is straightforward to relate the measured kinetic energy of the photoelectron to its binding energy (E_b) before excitation:

$$E_{kin} = h\nu - \Phi_s - |E_b| \tag{3}$$

where Φ_s is the work function of the sample. Figure 2 (a) illustrates the energetics in the photoemission process by the example of a metallic sample, in which electronic states are occupied up to the Fermi level (E_F). The absorption of light lifts electrons above the vacuum level (E_{vac}) of the solid, where they get measured by the detector. The energetic distribution of the photoelectrons in

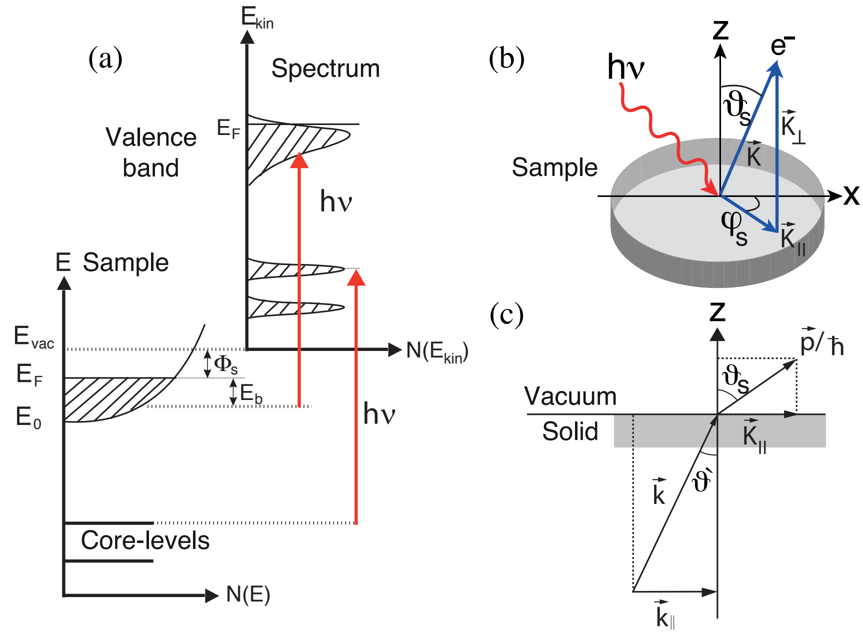

Figure 2: *(a) Energetics of the photoemission process: the occupied density of states is mapped above the vacuum level upon absorption of incoming photons, where it is measured by an electrostatic analyzer. The electron energy distribution inside the solid is expressed in terms of the binding energy (E_b), which is referenced to the Fermi energy (E_F). The photoelectron energy distribution is referenced to the vacuum level (E_{vac}) (adapted from [12]). (b) Geometry of an ARPES experiment. The sample is placed onto a goniometer (not shown) which allows for precise setting of the emission angles ϑ_S and φ_S. (c) Illustration of the conversation of the parallel momentum component of the photoelectron upon crossing the solid-vacuum interface (adapted from [12])*

the spectrum is such that electronic states inside the solid close to E_F appear in the spectrum with the highest kinetic energy, while states with higher binding energies appear with the lowest E_{kin}. To access deep lying core-levels it is necessary to use high photon energies, typically $h\nu > 100$ eV. This technique, known as X-ray photoemission spectroscopy (XPS), has been also applied in this work to study the chemical composition and bonding properties of interfaces.

Furthermore, in the photoemission process the parallel component of the photoelectron momentum is conserved during the transmission through the surface, as depicted in Fig. 2 (c). This way, the parallel momentum of the photoelectron in the vacuum, i.e. $\mathbf{K}_{\|} = (K_x, K_y, 0)$, can be directly linked to the parallel component of the electron crystal momentum $\mathbf{k}_{\|} = (k_x, k_y, 0)$ via

$$|\mathbf{k}_{\|}| = |\mathbf{K}_{\|}| = \frac{1}{\hbar}\sqrt{2m_e E_{\text{kin}}} \cdot \sin\vartheta_S \tag{4}$$

Notice that the perpendicular momentum component $\hbar\mathbf{k}_{\perp}$ is not conserved in the photoemission process because the outgoing photoelectron has to penetrate the surface potential barrier of the solid. However, for two-dimensional electronic states, i.e. quantum well states and surface states, this restriction has no influence because only $\mathbf{k}_{\|}$ is the relevant quantum number.

2.2 Spin- and angle-resolved photoemission spectroscopy

Spin- and angle-resolved photoemission spectroscopy combines the technique of ARPES with a spin-sensitive detector. The goal of SARPES is to measure the spin polarization of the photocurrent, defined as a vector of expectation values of the three spin operators (S_x, S_y, S_z) of a given ensemble of states [16]

$$\mathbf{P} = \begin{pmatrix} P_x \\ P_y \\ P_z \end{pmatrix} = \frac{2}{\hbar} \begin{pmatrix} \langle S_x \rangle \\ \langle S_y \rangle \\ \langle S_z \rangle \end{pmatrix} , \tag{5}$$

where the constant $2/\hbar$ makes sure that the absolute value is $|\mathbf{P}| \leq 1$. Whether SARPES is capable of measuring the spin properties of the initial states is still under debate [17,18]. In the case of linear polarized light[1], as used in this thesis, e.g. the *Fano effect* can be excluded, which generates spin polarization in the photocurrent from non-polarized initial states through optical alignment [19]. Further to assign the measured polarization of photoelectrons (i.e. after excitation) to the initial states (i.e. before excitation), important requirements have to be met. First, the measured polarization has to be independent on the photon energy. Second, the polarization has to reflect the symmetry properties of the crystal lattice and third, for Rashba systems the spin splitting has to be proportional to the wave vector. As will be demonstrated in this thesis all of these points are exactly fulfilled, strongly suggesting that the spin of spin-polarized initial states is conserved in the photoemission process.

Nowadays several techniques are used to measure the polarization of an electron beam, such as spin-polarized low energy electron diffraction [20], which is based on electron diffraction from a W(110) surface or Mott scattering [21], which relies on the spin-dependent back-scattering potential introduced by the heavy nuclear charge target. For reviews see [22,23]. The experimental setup used in this thesis, named COPHEE, is shown in Fig. 3 (a) and is situated at the Surface And Interface Spectroscopy (SIS) beamline of the Swiss Light Source (SLS). COPHEE is an acronym for COmplete PHotoEmission Experiment, because it is capable to measure all relevant quantum numbers of photoelectrons, i.e. binding energy (E_b), parallel ($k_{||}$) and perpendicular ($k_{\perp}$) momentum and the three-dimensional (3D) spin polarization [24–27].

The principle is as follows: after energy and momentum selection through a hemispherical analyzer the photoelectrons are distributed into two orthogonally mounted polarimeters by an electrostatic deflector operated at 1 Hz. Note that the electrostatic transport of the electrons preserves the spin. The electrons are then accelerated in a high-voltage field (typically 40 kV) to high energies in order to induce the relativistic Mott back-scattering off the high-Z element Au ($Z = 79$). The interaction of the electrons with the Coulomb field of the Au nuclei results in a spin-dependent back-scattering due to the spin-orbit interaction [16]. Figure 3 (b) illustrates the underlying mechanism for the polarimeter I: electrons with an unknown spin polarization are directed onto the Au foil (thickness ≈ 800 Å) and backscattered. Each scattering geometry allows to measure two polarization components, i.e. $P_{\tilde{z}}$ and $P_{\tilde{y}}$, transverse to the incoming beam. There is a higher

---

[1] The selection rule for optical transition reduces to $\Delta l = \pm 1$ and $\Delta m = 0$.

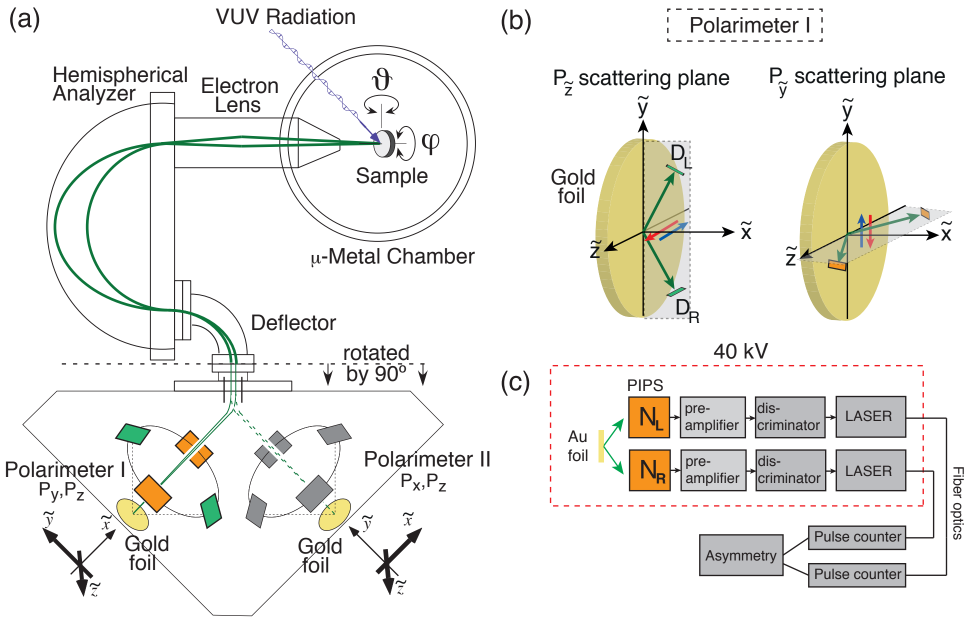

Figure 3: *(a) Experimental setup of the COPHEE spectrometer (adapted from [24]). (b) Mott scattering geometry of polarimeter I. (c) Schematic drawing of the electron counting electronics for one asymmetry direction. Note, the decoupling of the high-voltage is performed with optical fibers.*

probability that electrons with spin direction along the positive $\tilde{z}$-direction (indicated by the red arrow) perpendicular to the scattering plane are scattered toward the left (D_L) than toward the right (D_R) detector. The polarization component, here $P_{\tilde{z}}$, is then determined from the scattering asymmetry $A_{\tilde{z}}$ divided by the Sherman function S:

$$P_{\tilde{z}} = \frac{A_{\tilde{z}}}{S} = \frac{1}{S}\frac{N_L - N_R}{N_L + N_R} \tag{6}$$

where $N_{L,R}$ is the number of the backscattered electrons into the left and right detector. The Sherman function is the asymmetry that would be measured in the case of a fully polarized electron beam. The function is detector specific and depends on several parameters such as the atomic number of the target, the acceleration voltage and the measurement geometry[2]. The electron counting electronics (see Fig. 3 (c)) consist of passivated implanted planar silicon barrier detectors (PIPS), preamplifiers and discriminators which separate the elastically from the inelastically scattered electrons. Finally a fiber-optical system brings the high-voltage counting signal down to ground potential.

Another important parameter characterizing the overall efficiency of a spin detector is the figure of merit calculated as,

$$\epsilon = \left(\frac{N}{N_0}\right) S^2 \tag{7}$$

---

[2] Throughout this thesis a Sherman function of $S = -0.068$ has been used.

and is typically in the range of 10^{-3} to 10^{-4} for Mott-based polarimeters. The reason for the small value lies in the small cross-section of Mott scattering, i.e. only few percent of the total number of impinging electrons (N_0) are backscattered (N) while the others ($N_0 - N$) go simply through the target and are not detected. This is the main reason why a spin-resolved ARPES experiment is typically operated with an increased synchrotron spot size ($\approx 800\ \mu m \times 200\ \mu m$) and entrance slit of the analyzer (∅ 6 mm) to maximize the number of electrons at the expense of angular and energy resolution. However a good compromise has been found, where the angular and energy resolution are set to ± 0.75° and 80 meV, respectively.
The absolute statistical error of the polarization due to electron counting is calculated from:

$$\Delta P_i = \frac{\Delta A_i}{S} = \frac{1}{S\sqrt{N_L + N_R}} \tag{8}$$

To achieve a satisfying error bar of typically $\Delta P = \pm 0.01$ at each data point, long counting times are necessary, typically 4 minutes per data point. A typical spin-resolved energy distribution curve with an energy range of 1 eV and an energy step size of 20 meV takes approximately three hours. Such time consuming measurements, which depend on small differences in the backscattered intensities can only be performed at a stable beamline, e.g. with a constant photon flux, to provide a maximal signal-to-background ratio.
The COPHEE spectrometer is unique, because it consists of two Mott polarimeters which are mounted orthogonal to each other. Polarimeter I measures the spin polarization components $P_{\tilde{y},\tilde{z}}$ and polarimeter II $P_{\tilde{x},\tilde{z}}$ in the coordinate system $(\tilde{x}, \tilde{y}, \tilde{z})$ spanned by the two polarimeters. **P** in the sample coordinate system is obtained by applying a rotation matrix (R) containing the emission angle ϑ_S[3]:

$$\begin{pmatrix} P_x \\ P_y \\ P_z \end{pmatrix} = R \begin{pmatrix} P_{\tilde{x}} \\ P_{\tilde{y}} \\ P_{\tilde{z}} \end{pmatrix} = \frac{1}{\sqrt{2}} \begin{pmatrix} \cos\vartheta_S & -\cos\vartheta_S & \sqrt{2}\sin\vartheta_S \\ 1 & 1 & 0 \\ -\sin\vartheta_S & \sin\vartheta_S & \sqrt{2}\cos\vartheta_S \end{pmatrix} \begin{pmatrix} P_{\tilde{x}} \\ P_{\tilde{y}} \\ P_{\tilde{z}} \end{pmatrix} \tag{9}$$

The capability for measuring all components of the spin polarization for every point in reciprocal space makes this spectrometer excellent for studying spin-orbit interaction in low-dimensional systems, where the quantization axis for the spin can point in principle in any direction. In the next sections we will show (i) how polarization data are obtained from the scattering intensities recorded by the Mott polarimeters and (ii) how a quantitative analysis is performed using a vectorial spin analysis within the framework of the two-step fitting routine.

2.3 From raw data to spin polarization curves

The following example demonstrates how spin polarization data are obtained from the scattering spectra. Figure 4 (a) displays a band dispersion of a quantum well state in a 10 monolayer Pb film on the Bi reconstructed Si(111) measured with ARPES (see Sec. 2.1). This system is

---

[3] The sample is usually rotated about the z-axis to access photoelectrons with different $k_\parallel$ while the in-plane angle φ_S is set to zero.

explained in detail in Chap. 4. The relatively weak band dispersion of the QWS requires a spin-resolved measurement in the so-called spin-resolved energy distribution curve (SR-EDC) mode. For a fixed polar angle ϑ_S (i.e. $k_\parallel$ according to Eq. 4) scattering spectra $I^{L,R}_{\tilde{x},\tilde{y},\tilde{z}}$ for each spin polarization component are recorded as a function of the binding energy, see Fig. 4 (c). This way, one obtains eight spectra from which the scattering asymmetries are calculated and displayed in Fig. 4 (d). The scattering spectra are recorded with Si diodes (PIPS) which differ slightly in their detection efficiency. This is seen in Fig. 4 (c) in the high binding energy tail of the peaks. Away from the peak maximum, at around 0.6 eV, one can fairly assume the asymmetry to be zero, because the measured intensity arise mainly from the non spin-polarized background. However the left Si-diode e.g. of the $\tilde{y}$-direction counts $3.1 \cdot 10^5$, while the right diode counts $2.5 \cdot 10^5$ electrons. This gives an asymmetry of 0.114 and hence a polarization of 167%, which is not physical. This instrumental asymmetry can be removed by applying so-called sensitivity factors η_i in order calculate the corrected asymmetries [24]:

$$A_{\tilde{y}} = \frac{I^L_{\tilde{y}} - \eta_{\tilde{y}} I^R_{\tilde{y}}}{I^L_{\tilde{y}} + \eta_{\tilde{y}} I^R_{\tilde{y}}}, \qquad A_{\tilde{x}} = \frac{I^L_{\tilde{x}} - \eta_{\tilde{x}} I^R_{\tilde{x}}}{I^L_{\tilde{x}} + \eta_{\tilde{x}} I^R_{\tilde{x}}}, \qquad A_{\tilde{z}} = \frac{I^L_{\tilde{z}} - \eta_{\tilde{z}} I^R_{\tilde{z}}}{I^L_{\tilde{z}} + \eta_{\tilde{z}} I^R_{\tilde{z}}} \tag{10}$$

The corrected asymmetries are shown in Fig. 4 (e) and were calculated using the following sensitivity factors:

$$\eta_{\tilde{y}} = 1.25646, \qquad \eta_{\tilde{x}} = 0.93933, \qquad \eta_{\tilde{z}} = 0.807187$$

The last step consists of normalizing the asymmetry by the Sherman function to obtain the polarization and transformation of the polarization data into the sample coordinate system. The data in Fig. 4 (f) are the result of applying the mentioned steps and are ready for further analysis.

2.3.1 Quantitative analysis of spin polarization data

The main goal of a quantitative analysis of spin polarization data is to determine the polarization vector of the individual bands and the energetic separation between peaks, from which important parameters such as the Rashba parameter (see Sec. 5.1.2) can be deduced. For this purpose a powerful tool, the so-called two-step fitting routine, has been developed in our group which will be briefly described here. A detailed description of the routine can be found in [28, 29]. A spin-resolved measurement delivers intensity data from which the polarization data are calculated, as described in the previous section. In the first step of the fitting routine the total measured intensity which is the sum over all Mott detector channels is fitted assuming a proper number of peaks and a background:

$$I^{FIT}_{tot}(E_b) = \sum_{i=1}^{n} I_i(E_b) + B(E_b) \tag{11}$$

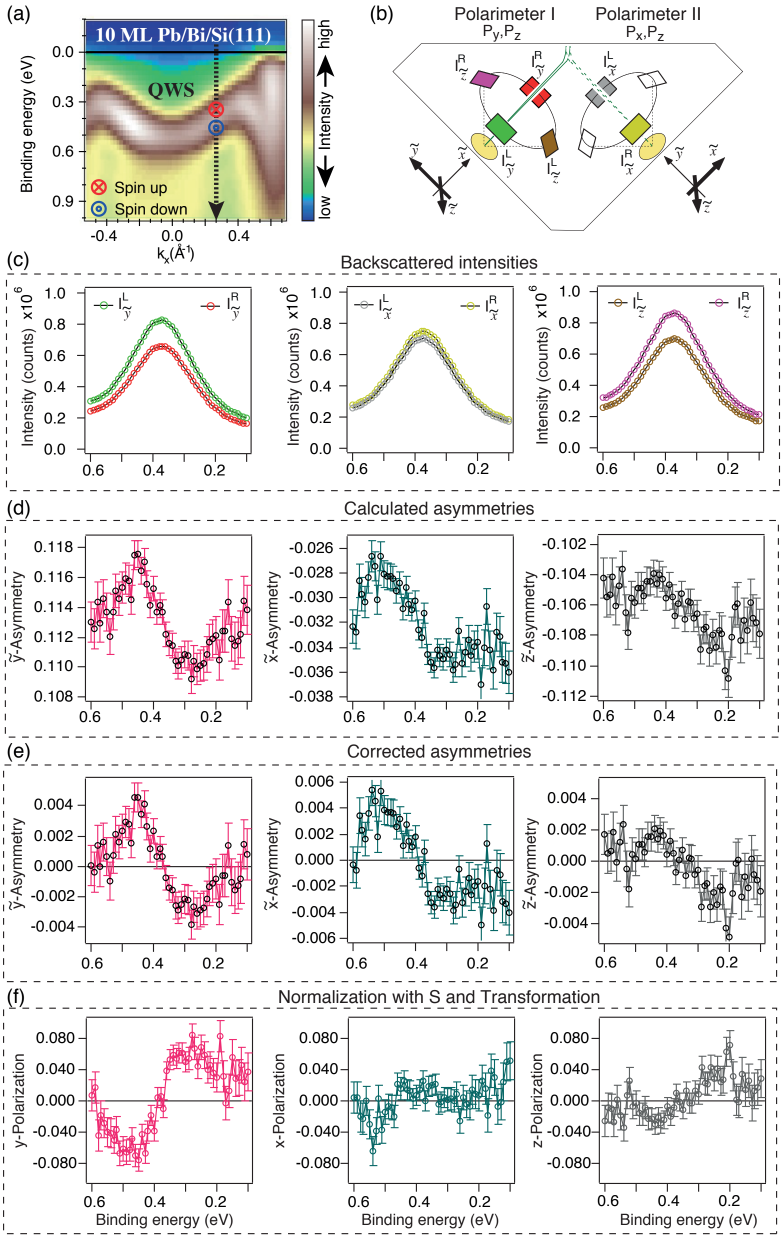

Figure 4: *(a) Exemplary band dispersion of Pb QWS. The scan position of the spin-resolved EDC is indicated by the dashed arrow. (b) Schematic drawing of the two Mott polarimeters mounted in orthogonal geometry. (c) Backscattering intensities as a function of binding energy for the three Mott coordinates* $(\tilde{x}, \tilde{y}, \tilde{z})$*. (d) Calculated asymmetries* $A_{\tilde{x}}, A_{\tilde{y}}, A_{\tilde{z}}$*. (e) Corrected asymmetries according to Eq. 10. (f) Polarization data obtained from (e) after applying the rotation matrix and division by the Sherman function.*

In the case of data obtained from Pb quantum well states with Rashba-type spin splitting it is sufficient to assume two Voigt profiles[4] and an unpolarized background which is increasing linearly towards higher binding energy. In the second step an initial polarization vector is assigned to each peak I_i and defined in spherical coordinate system as:

$$\mathbf{P_i} = \begin{pmatrix} P_{x,i} \\ P_{y,i} \\ P_{z,i} \end{pmatrix} = c_i \begin{pmatrix} \sin\theta_i \cos\varphi_i \\ \sin\theta_i \sin\varphi_i \\ \sin\theta_i \end{pmatrix} \tag{12}$$

From the initial orientation of $\mathbf{P_i}$ together with I_i obtained from the first step one calculates the spin-resolved intensities projected on the three directions (x, y, z) and the corresponding polarization curves (P_x, P_y, P_z) via

$$I^{\uparrow,\downarrow}_{x,y,z}(E_b) = \frac{B(E_b)}{2} + \sum_{i=1}^{n} \frac{I_i(E_b)}{2} \left(1 \pm P^i_{x,y,z}\right) \tag{13}$$

$$P_{x,y,z}(E_b) = \frac{I^{\uparrow}_{x,y,z}(E_b) - I^{\downarrow}_{x,y,z}(E_b)}{I^{\uparrow}_{x,y,z}(E_b) + I^{\downarrow}_{x,y,z}(E_b)} \tag{14}$$

A self-consistent fitting is then performed by varying the parameters of both, the polarization vectors, i.e. the angles θ_i and φ_i, and the peak parameters, i.e. peak position, intensity and width. The length of each polarization vector describes the degree of the polarization of the photocurrent and can in principle range between $0 < c \leq 1$. The analysis of Rashba-type spin-split states considered in this thesis gave excellent results with c set to 1. This serves as a further indication that properties of the initial states are determined with SARPES. In this example polarization data as a function of the binding energy were chosen, because most of the presented data were recorded in this mode. However, the same analysis applies for polarization data recorded as a function of the in-plane momentum.

2.4 Low energy electron diffraction

Low energy electron diffraction is a process highly suitable for studying structural properties of crystalline surfaces such as its symmetry, and quality of the surface layers. The surface sensitivity of this method is due to the low energies of the incident electrons, which range between 10 and 300 eV, allowing to investigate only 2-3 atomic layers. At these energies the de Broglie wavelength of electrons is between 4 and 0.7 Å and matches therefore typical interatomic dimensions at surfaces. The condition for constructive interference between an incident electron wave with wave vector $\mathbf{k}_{\text{in}}$ and an outgoing wave with wave vector $\mathbf{k}_{\text{out}}$ is given by the Laue condition [30],

$$\mathbf{g}_{||} = \Delta\mathbf{k} = \mathbf{k}_{\text{out}} - \mathbf{k}_{\text{in}} \tag{15}$$

and states that the momentum transfer $\Delta\mathbf{k}$ has to equal a reciprocal substrate lattice vector $\mathbf{g}_{||}$. Figure 5 (a) shows a schematic setup of a LEED experiment. An electron gun at a negative

---

[4] A Voigt profile results from a convolution of a Lorentzian profile, that describes the broadening of a spectral line due to the lifetime of the photohole and a Gaussian profile, that describes the broadening of a spectrum due to the finite resolution of the experiment.

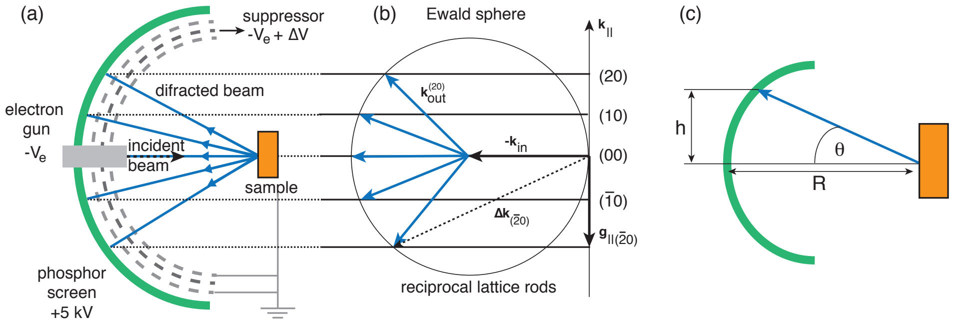

Figure 5: *(a) Schematic setup of a LEED experiment. (b) Illustration of the Laue condition for a 2D crystal. (c) Geometry of LEED: the in-plane lattice constant $a_{||}$ is inversely proportional to h/2 for fixed R and beam energy (adapted from [30]).*

potential ($-V_e$) produces a monochromatic beam with energy E that impinges on the sample at normal incidence. The diffracted beam is then imaged on a phosphor screen and the luminescent pattern is recorded with a standard CCD camera. To separate the inelastically from the elastically scattered electrons a grid (suppressor) is placed with an potential just below the acceleration voltage ($-V_e + \Delta V$). The inner and outer grids at ground potential shield the sample and the suppressor from the high voltage of the phosphor screen. Figure 5 (b) shows the condition for constructive interference in the case of an ideal 2D crystal. The reciprocal lattice consists of lattice rods (black lines) instead of points as in the case of a 3D crystal, which are separated by the reciprocal lattice vector $g_{||} = 2\pi/a_{||}$. Here $a_{||}$ is the in-plane lattice vector in real space. For each intersection of the Ewald sphere with radius k_{in} with a reciprocal lattice rod the condition of Eq. 15 is met and the diffracted wave with $\mathbf{k}_{\text{out}}$ produces spots labeled as (00), (01), ..., on the screen. The position of the interference pattern is easily calculated using $h = R\sin(\theta)$, $k_{\text{in}} = k_{\text{out}}$ and $\sin(\theta) = \hbar g_{||}/\sqrt{2mE}$. For constant R (typically unknown) and beam energy E relative changes in $g_{||}$ and $a_{||}$ can therefore be traced. This method has been successfully applied to measure the in-plane lattice constant as a function of Pb film thickness, as will be demonstrated in Chap. 4.

2.5 Density functional theory

The understanding of experimental data often requires comparison to theoretical calculations. In condensed matter physics so-called *first principles* calculations provide the necessary ground. In this work the well-established *density functional theory* (DFT) implemented in the WIEN2k[5] code has been used to simulate band structures of free-standing Pb films .

The general Eigenvalue problem (EWP) of a many-body system containing N electrons and M nuclei is written as [31]:

$$\hat{H}\Psi = E\Psi \tag{16}$$

---

[5] www.wien2k.at

with the ab initio Hamiltonian

$$\hat{H} = \hat{T}_M + \hat{T}_N + \hat{V}_{M,N} + \hat{V}_{N,N} + \hat{V}_{M,M} \tag{17}$$

$$\hat{H} = -\frac{\hbar^2}{2}\sum_i^M \frac{\nabla^2_{\mathbf{R_i}}}{M_{\text{ion}}} - \frac{\hbar^2}{2}\sum_i^N \frac{\nabla^2_{\mathbf{r_i}}}{m_e} \tag{18}$$

$$- \frac{1}{4\pi\epsilon_0}\sum_{i,j}^N \frac{e^2 Z_i}{|\mathbf{R_i} - \mathbf{r_j}|} + \frac{1}{8\pi\epsilon_0}\sum_{i\neq j}^N \frac{e^2}{|\mathbf{r_i} - \mathbf{r_j}|} + \frac{1}{8\pi\epsilon_0}\sum_{i\neq j}^N \frac{e^2 Z_i Z_j}{|\mathbf{R_i} - \mathbf{R_j}|} \tag{19}$$

and the many-body wave function

$$\Psi(\mathbf{R_1}, \mathbf{r_1}, ..., \mathbf{R_M}, \mathbf{r_N})$$

Here $\hat{T}_{M,N}$ is the sum of all kinetic energies of the nuclei and of the electrons, respectively. $\hat{V}_{M,N}$ is the sum of all Coulomb interactions between the i-th nuclei and j-th electron. $\hat{V}_{N,N}$ ($\hat{V}_{M,M}$) is the sum of all Coulomb repulsions between the i-th and j-th electron (nuclei). Even within the Born-Oppenheimer approximation, that freezes the coordinates of the nuclei and therefore reduces the many-body wave function from 3(N+M) down to 3N dimensions, the EWP is still difficult to solve[6]. To circumvante this problem Hohenberg and Kohn postulated that the ground-state energy from Schrödinger's equation is a unique functional of the electron density ρ and the electron density that minimizes the energy of the overall functional is the true electron density corresponding to the full solution of the many-body Schrödinger equation [32]:

$$E[\rho] = \langle\Psi|\hat{H}|\Psi\rangle = \langle\Psi|\hat{T} + \hat{V}|\Psi\rangle + \langle\Psi|\hat{V_{ext}}|\Psi\rangle \tag{20}$$

$$= \underbrace{F_{HK}[\rho]}_{HK functional} + V_{ext}[\rho] \tag{21}$$

Here $\hat{T}$ denotes the kinetic energy of the interacting electron gas, $\hat{V}$ is the potential energy due to electron-electron interaction and $\hat{V}_{ext}$ is the energy of electrons in the potential of the nuclei. The Hohenberg-Kohn functional is further decomposed into a kinetic term of a non-interacting electron gas, a Hartree term and a term describing exchange and correlation effects:

$$F_{HK}[\rho] = T_0[\rho] + V_H[\rho] + V_{xc}[\rho] \tag{22}$$

One major challenge in the research field of DFT is to find the exact exchange-correlation functional. However very good match between experiment and theory is often achieved using local density approximation (LDA) or generalized gradient approximation (GGA) [33]. A very useful recipe to construct the electron density has been given by Kohn and Sham which states that the exact ground-state density of a N-electron system is calculated from single-particle wave functions of the Kohn-Sham Eigenvalue problem [34]:

$$\rho(\mathbf{r}) = \sum_i^N \phi_i^\star(\mathbf{r})\phi_i(\mathbf{r}) \tag{23}$$

$$\hat{H}_{KS}\phi_i = E\phi_i \tag{24}$$

---

[6] For example the CO_2 molecule has 22 electrons, i.e. the wave function has then 66 dimensions.

The problem thus reduces from 3N to 3, because to find the ground-state density, one needs to solve the Schrödinger-like non-interacting single particle equations. This has to be done iteratively, because the Hartree, the exchange-correlation potential and the wave functions depend on ρ. Most of the available programs, such as WIEN2K or FLEUR[7], use the so-called full-potential linearized augmented plane wave method to solve the Kohn-Sham equations. In this method the unit cell is divided into a region of non-overlapping atomic spheres and an interstitial region. Within the muffin tin approximation the wave functions are assumed to be spherically symmetric at the atomic sites, while outside the so-called muffin tin sphere they are of plane-wave character [31]. We would like to emphasize that part of the theoretical work presented in this thesis was performed with the WIEN2K code, such as simulations of band structures of free-standing Pb films. Calculations on free-standing films are in general easy to perform and do not require sophisticated computational infrastructure. In contrast, the fully relativistic calculations of Pb films on Si(111) to model the Rashba effect (see Chap. 6) were performed by Gustav Bihlmayer[8].

---

[7] www.flapw.de

[8] G.Bihlmayer@fz-juelich.de

3 Quantum well states

The following chapter introduces some fundamental aspects prerequisite for the formation of confined electronic states in metallic overlayers. Later, we will focus in more detail on the system Pb as an adsorbate on Si(111) and introduce the reader into the concept of Schottky barrier formation at a metal-semiconductor junction using the interface dipole model.

3.1 General description

3.1.1 Phase accumulation model

When the thickness of a metallic layer is reduced to the nanoscale, electron confinement by the band gap of the substrate and the repulsive image potential in front of the metallic surface leads to the formation of standing electron waves associated with quantum well states (QWS). These electrons, while bouncing back and forth between the metal-substrate and metal-vacuum interface, are free to move within the sample plane and can be therefore regarded as a quasi two-dimensional electron gas (2DEG). In a first approximation the confinement of the conduction electrons within the metal can be treated similarly to the well-known one-dimensional particle-in-a-box model. In this model the confinement of a particle by infinite potential barriers leads to discrete energy levels with standing wave solutions having nodes exactly at the boundaries of the box of width d [2]:

$$k_n = \frac{n\pi}{d} \;,\; \Psi_n = \frac{1}{\sqrt{d}} \sin\left(\frac{n\pi}{d} z\right) \;,\; E_n = \frac{\hbar^2}{2m_e}\left(\frac{n\pi}{d}\right)^2 \tag{25}$$

where k_n is the quantized wave vector, Ψ_n is the wave function, E_n is the eigenenergy, and n is a positive integer. A more realistic treatment of the confinement is to approximate the boundaries of the box by barriers of finite height. In this case the wave function describing the particle will have a certain penetration depth into the barrier specified by a phase shift. The main difference between the two approximations is that, in the case of finite barrier, the penetration of the wave function will lead to a larger effective width d of the confinement box and therefore to a lower eigenenergy of the particle since $E_n \propto d^{-2}$.

The description of QWS as standing waves allows application of the so-called phase-accumulation model (PAM) introduced by Pendry and Echenique in 1978 [35] and illustrated in Figure 6.

A standing wave may form when the total accumulated phase Φ_T is an integer number n of 2π. Here the total phase of the wave can be split into a contribution from the propagation through the overlayer $2dk_z$, when the electron travels back and forth through the medium, and a phase shift upon reflection at the metal-vacuum interface Φ_V and the metal-substrate interface Φ_S:

$$\Phi_T = \Phi_V + \Phi_S + 2d_0 N k_z = 2\pi n \tag{26}$$

where d_0 is the interlayer spacing (Pb; d_0 = 2.85 Å) and N denotes the number of monolayers. Because the thickness of the overlayer is an integer number of d_0, i.e. is discrete, a change in the thickness by one atomic layer leads to discontinuous shifts of the energies of quantum well

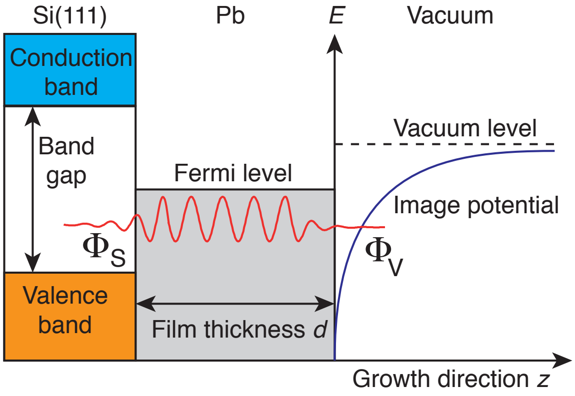

Figure 6: *Schematic illustration of electron confinement in an ultra-thin metallic film on a crystal with a band gap. The finite confinement potentials towards the vacuum and the substrate allows the wave function to tunnel into a region which is classically forbidden (adapted from [35]).*

states. These discrete changes allow for a determination of the absolute film thickness through the measurement of the binding energies as a function of deposition time.

The repulsive image potential is due to the charge spilling into the vacuum and the induced energy-dependent phase shift upon reflection is calculated in the Wentzel-Kramers-Brillouin (WKB) approximation [36]:

$$\Phi_V = \pi\left(\sqrt{\frac{3.4\ \mathrm{eV}}{E_{\mathrm{Vac}} - E}} - 1\right) \tag{27}$$

where E_{Vac} denotes the vacuum energy level in eV. It should be noted that all ultra-thin Pb films investigated in this thesis produce the same metal-vacuum phase shift.

For constructive interference an electron traveling towards the substrate must be reflected by the metal-substrate interface. In the case of a semiconducting material such as Si the reflection is due to the lack of bulk states within the absolute energy gap to which the electrons can couple. In addition, confinement of electrons in the overlaying material can be also realized in systems, where the substrate has a directional band gap such as the case for noble metals Ag, Au and Cu in the [111] direction [37–39]. The energy-dependent phase-shift at the metal-substrate interface is given by [40]:

$$\Phi_S = A + B\sqrt{E - E_0}\Theta(E - E_0) \tag{28}$$

Here A is in general unknown and serves as a fit parameter, E_0 is the energy of the valence band maximum, Θ the Heaviside function, and B a constant related to the electronic structure of the substrate. One of the main advantages of the *PAM* is that the exact nature of the complex potentials at the interfaces need not necessarily to be known. The influence of the potential variations at the interfaces is modeled by phase shifts.

3.1.2 Probability density distribution

Having established the general description of QWS we will now show how the phase shifts across the interfaces influence the probability density $|\psi(z)|^2$ of the confined electron waves. Figure 7

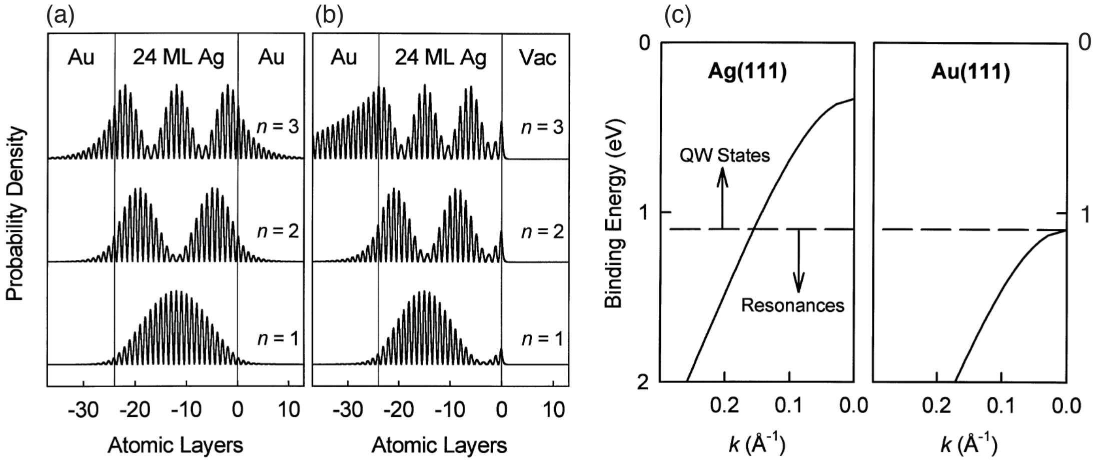

Figure 7: *Calculated probability density of QWS with quantum numbers $n = 1-3$ confined in (a) a symmetrically and (b) an asymmetrically terminated Ag film, where one termination is vacuum. (c) Illustration of the confinement threshold: states with energies above the sp valence band edge of Au(111) (marked as a dashed line) are QWS, while states below the edge are quantum well resonances (adapted from [37]).*

displays a calculation of $|\psi(z)|^2$ for (a) a symmetric film composed of a 24 ML thick Ag film sandwiched between two semi-infinite Au(111) crystals and (b) an asymmetric film between Au(111) and vacuum, both for quantum numbers $n = 1, 2$, and 3 [37]. The probability density actually consists of a rapid oscillation accounting for the inter-atomic periodicity normal to the surface, known as the Bloch factor, which is modulated by a longer wave component from the standing wave solutions as defined in Eq. 26. Thus the quantum number n counts the number of anti-nodes in the quantized envelope function. For the case of a symmetric confinement the probability density extends to the same amount at both sides of the well, while for the asymmetric confinement $|\psi(z)|^2$ is shifted towards the Au substrate irrespective of n. The fast decay of the states towards the vacuum is due to the large energy difference between the energetic position of the QWS and the vacuum level.

According to Fig. 7 (c) confinement of electrons in Ag is mediated by the k-dependent energy gap of Au(111) of 1.1 eV width measured from the top of the *sp* valence band (marked as a dashed line) to the Fermi level. Only within this energy window QWS can be confined, while outside the gap so-called quantum well resonances (QWR) form because of the available density of states in the substrate. The state labeled with $n = 3$ is slightly above the confinement threshold, giving raise to a long tail into the substrate. For a slightly thinner Ag film, this state would eventually drop below the confinement threshold resulting in a QWR.

As will be shown in Chap. 4, in a photoemission experiment one can clearly distinguish between QWS and QWR based on their linewidth, and therefore accurately determine the confinement threshold.

3.1.3 Bandstructure quantization

As can be seen from Eq. 26 the reduction of the dimensionality leads to the quantization of the momentum perpendicular to the confinement direction z. The allowed normal wave vectors in the film are calculated from Eq. 26 via

$$k_{z,n} = \frac{\pi n}{d_0 N} - \frac{1}{N}\left(\frac{\Phi_S + \Phi_B}{2d_0}\right) \tag{29}$$

As a consequence the bulk band structure in the $\overline{\Gamma}$-$\overline{\mathrm{L}}$ direction of the material gets quantized in equal parts separated by $1/N$ corresponding to the number of monolayers N. Thus the energy levels are not defined by Eq. 25, but through the k_z-quantization. This situation is visualized in Fig. 8 (a) for a freestanding Pb film of 11 ML thickness, i.e. $N = 11$. Pb has an electronic configuration of [Xe]4f^{15}5d^{10}6s^{2}6p^2 with 4 valence electrons and can be regarded as simple metal with quasi free-electron-like sp-bands that cross the Fermi level. It should be noted that QWS with momenta $k_{z,n}$ cutting the band dispersion between the Fermi level and the sp band gap of Pb are derived from p-orbitals, while states originating from the quantization of the band below the gap are $6sp_z$ derived. However, in the present case of Pb on Si(111), the valence band edge of Si provides the confinement threshold which allows for the observation of QWS only in the energy window of size 0.6 eV, measured from E_F. Consequently, all investigated states in this thesis are derived from p-orbitals.

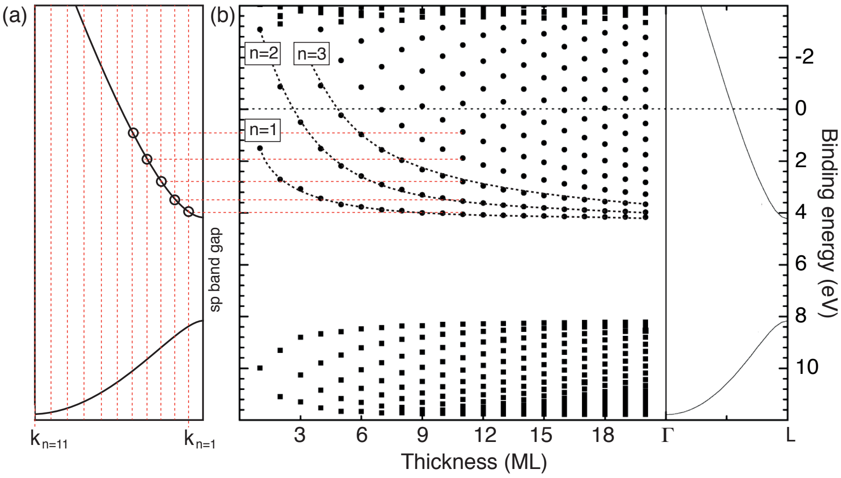

Figure 8: *(a) Quantization of bulk band structure of Pb along the [111] direction for a film thickness of 11 ML. Notice that due to the back-folding of the p-like band from the second Brioullin zone the numbering n of the states starts at the L-point. (b) Energy levels as a function of film thickness. For constant n and increasing thickness the levels move down in energy. Approximately every 2 ML a new state crosses the Fermi level and becomes occupied (adapted from [41]).*

A direct consequence of the bandstructure quantization is that the energy spacings between QWS are sensitive to the dispersion of the band from which they are derived. Therefore a detailed study of QWS energies as a function of thickness allows the determination of the bulk band structure of the film material which is usually not a trivial task [42, 43]. The advantage of this method is also that such an experiment can be performed with a single photon energy, in contrast to other techniques. However this method is restricted, of course, to materials which form crystalline structures on a supporting substrate.

Figure 8 (b) displays the evolution of the QWS binding energy with thickness at normal emission. As the film thickness increases a new state crosses the Fermi level with a periodicity of ≈ 2 ML and becomes occupied. Consequently the density of states (DOS) at E_F oscillates as a function of film thickness. Since many physical properties depend on the DOS at E_F they will oscillate as well. This is the driving force for the so-called *quantum size effects* (QSEs) which are of electronic origin because the periodicity of Fermi level crossings depends on the Fermi wave vector k_F of the material and the inter-plane distance d_0. For Pb with $d_0 = 2.86$ Å and $k_F = 0.49$ Å^{-1} the number of monolayers that are needed to add one extra QWS to the upper branch is:

$$\Delta N = \frac{\lambda_F}{2d_0} = \frac{\pi}{k_F d_0} = 2.24 \text{ ML} \tag{30}$$

Note, the p-like band dispersing through the Fermi level is back-folded from the second Brillouin zone with the band bottom at the L-point and k_F should thus be determined relative to this point [41, 44].

3.2 Quantum size effects

QSEs have been observed for many physical properties in Pb/Si(111), such as oscillations in the Hall coefficient [45], in the 2D conductivity [46], in the surface chemical reactivity [47], in the reflection high energy electron diffraction (RHEED) specular beam intensity during the growth of Pb films on Si(111) [48], and in the superconducting transition temperature [49].

Another intriguing property due to QSEs in Pb/Si(111) is the formation of the so-called *magic height islands* which is related to self-organized growth [50–53]. Figure 9 (a) shows the thickness-dependent oscillations of the surface energy of a free-standing slab calculated with DFT. A stable thickness, i.e. with a low surface energy, has an occupied QWS far away from the Fermi level. Comparing with Fig. 8 this is the case for even thicknesses ($N = 2, 4, 6, 8$), while unstable islands are of odd thickness ($N = 3, 5, 7, 9$). Figure 9 (b) shows a topography image of Pb islands grown on a $(\sqrt{3} \times \sqrt{3})$R30°-Pb/Si(111) reconstruction which was measured using a scanning tunneling microscope (STM) [50]. In this experiment Pb has been stepwise deposited; first 1.6 ML followed by 1.3 ML on top of the already formed islands. The numbers label the island height measured from the Si(111) substrate. Although a total amount of 2.9 ML has been deposited the majority of islands are of 6 ML height, which agrees well with the aforementioned stable thickness. Most strikingly is however the observed growth morphology which depends on whether the island is stable or not. While the unstable islands complete their top by growing from the perimeter towards the center, the growth mechanism on top of a stable island is favored by the nucleation of small compact islands at the island center. The authors explain this behavior in terms of QSEs

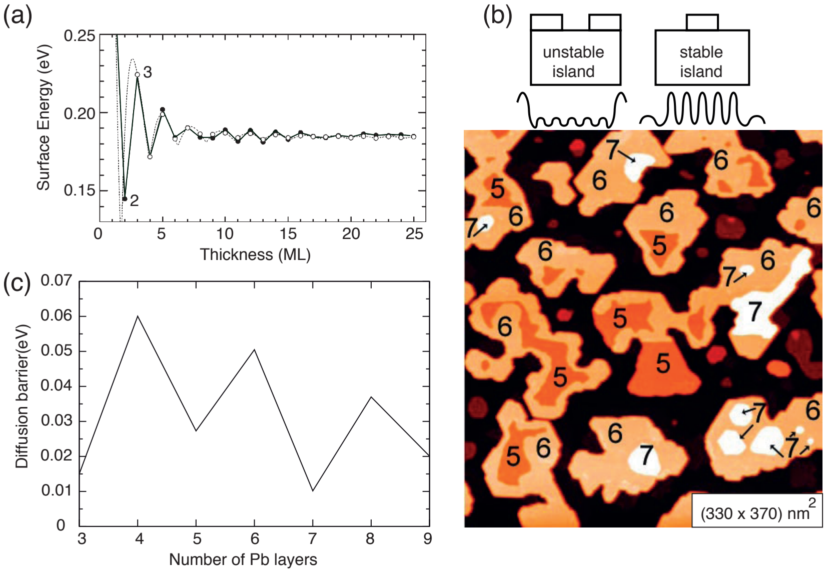

Figure 9: *Examples of QSE: (a) Oscillation of the surface energy as a function of film thickness (adapted from [41]). The surface energy is minimal for a thickness of 2 ML, i.e. when a QWS is far away from* E_F *and maximal for a thickness of 3 ML, i.e. when a state is close to* E_F*, compare with Fig. 8 (b). (b) STM topography image of stable and unstable Pb islands. Notice the different growth mechanism for unstable and stable islands. (c) Oscillation of the diffusion barrier as a function thickness. Stable islands (even thickness) have a high diffusion barrier and vice versa (both Figs. adapted from [50]).*

and the associated oscillation in the diffusion barrier as shown in Fig. 9 (c). The diffusion barrier is the energy barrier that an atom has to overcome in order to diffuse on top of the Pb film. It is maximal for stable heights, where the surface energy is low and vice versa.

These few examples already demonstrate that many interesting phenomena can be studied in Pb/Si(111). Prerequisite for theses studies is that QWS are trapped in well-defined films on top of Si. In this thesis we will also show that crystalline films of high quality can be also fabricated on differently reconstructed Si substrates.

3.3 The bandstructure of Pb QWS

In the previous section the quantization of the band structure along the growth direction has been introduced as the major consequence of size reduction. Within the sample plane the electrons form a quasi 2DEG that is expected to behave nearly free-electron-like since no confinement along the in-plane directions exist.

A prototypical example illustrating the quasi free-electron-like dispersion within the sample plane is Pb grown on graphitized SiC [51], as shown in Fig. 10. The cut through the two-dimensional hexagonal surface Brillouin zone (SBZ) along the crystallographic direction $\overline{\Gamma}$-$\overline{\text{M}}$ resolves several

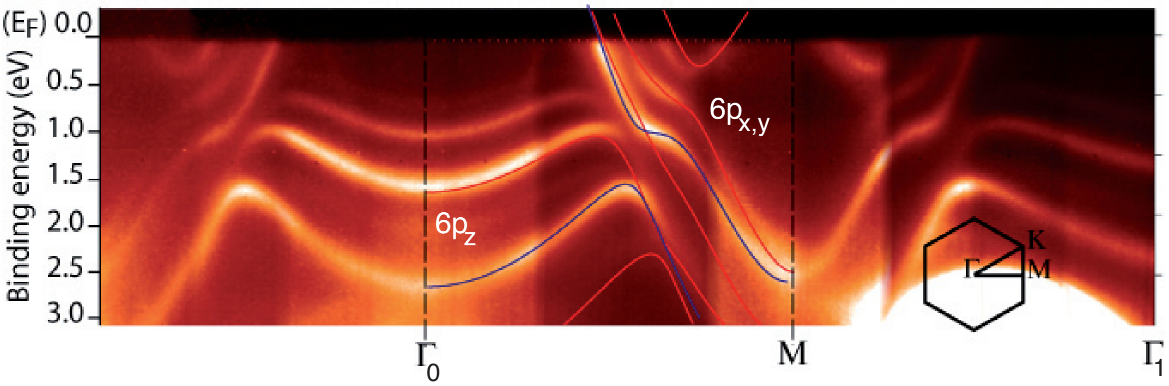

Figure 10: *Measured and calculated bandstructure of Pb QWS on crystalline graphite along the* $\overline{\Gamma}$-$\overline{M}$ *direction. Within the photon beam size two types of stable islands are present, which give rise to several electron-like subbands (red and black lines) around* $\overline{\Gamma}_0$. *The band structure of Pb QWS consists also of quantized* $6p_{x,y}$ *derived bands, which have band minima around the* $\overline{M}$*-point of the surface Brioullin zone (adapted from [51]).*

electron-like subbands, i.e. QWS, around normal emission ($\overline{\Gamma}$). These subbands arise from different k_z of the quantized p-like band as schematically shown in Fig. 8 and are derived from $6p_z$ orbitals. Another class of quantized bands is also visible for larger emission angles. These bands, derived from $6p_{x,y}$ orbitals, cross the Fermi level approximately half the way of $\overline{\Gamma}$-$\overline{\mathrm{M}}$ and feature a considerably larger dispersion.

A characteristic feature of the band structure is the avoided crossing hybridization between the $6p_z$ and $6p_{x,y}$ derived bands accompanied by an opening of energy gaps. These gaps are caused by interband spin-orbit coupling and further consequences will be discussed in more detail in Chap. 7.

Superimposed on the band structure are DFT calculations for a free-standing Pb slab with $d_1 = 2$ ML (blue curve) and $d_2 = 4$ ML (red curve), which perfectly match with the measured ARPES data. Therefore the deposition of nominal 2 ML Pb on the substrate forms two *magic islands* of even thickness, in line with the predictions by QSEs. This example also demonstrates how the microscopic composition of the film can be revealed from the energy spacings of the QWS together with DFT calculations.

In Chapter 4 we will discuss in more detail the dispersion of the $6p_z$ derived bands and show that the effective mass is sensitive to the interface formed between the Pb film and the Si substrate.

3.4 The Schottky barrier

The Schottky barrier (SB) is an important property of a metal-semiconductor (MS) contact as it is the rectifying energy barrier which determines current transport across the junction [54]. In the original model proposed by Walter Schottky the barrier height was solely determined by the difference between the work function of the metal (Φ_M) and the electron affinity of the semiconductor (χ_S) [55]:

$$\Phi_n^{SB} = \Phi_M - \chi_S \tag{31}$$

However this relationship could not be verified by experiments. The measured barriers were only weakly dependent on the metal's work function. The reason for the failure of this model is because it assumes no interaction to take place when the semiconductor is brought into contact with a metal. Or differently speaking, the charge is treated as a superposition of the isolated surfaces.

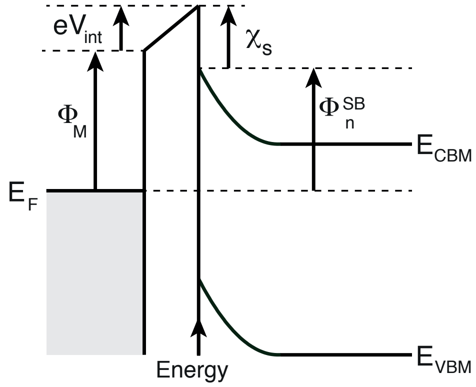

Figure 11: *Schematic band diagram (not to scale) of a metal-semiconductor (n-type) interface according to the interface dipole model (adapted from [54]).*

That this assumption must fail *per se* becomes evident when we consider the formation of a metal-semiconductor interface with a polar surface, such as the (7 × 7) reconstruction of Si(111). This surface contains dangling orbitals, which is an energetically unfavorable state. When foreign atoms are deposited on such a surface, chemical reactions with the Si atoms will break old bonds and create new bonds through charge rearrangement. This process, driven by energy minimization, will therefore establish an interface dipole, which directly contributes to the SB as schematically shown in Fig. 11. Within the *interface dipole model* (IDM) the correction to the Schottky model is written as [56]:

$$\begin{aligned}\Phi_n^{SB} &= \Phi_M - \chi_S + eV_{int} \qquad (32)\\ &= \gamma_B(\Phi_M - \chi_S) + (1-\gamma_B)\frac{E_g}{2} \qquad (33)\end{aligned}$$

where

$$\gamma_B = 1 - \frac{e^2 d_{MS} N_B}{\epsilon_{it}(E_g + \kappa)} \tag{34}$$

Here V_{int} is the voltage drop due to an interface dipole, d_{MS} is the distance between the metal and semiconductor atoms at the interface, ϵ_{it} is the dielectric constant of the interface region, N_B is the density of interface bonds, κ is the specific Coulomb interaction between the neighboring atoms at the interface, and E_g the band gap of the semiconductor. The Schottky limit is obtained for $\gamma_B \to 1$, that is the case of a vanishing dipole contribution. Several experiments performed in the past indicate the validity of the model, see Refs. [57–59]. For example, Tung reported a difference in the SB by 140 meV for two types of interfaces in Si(111)-NiSi$_2$, where in one of both the silicide is rotated by 180° [60, 61]. This difference cannot be explained by the bare Schottky model, because it does not account for interface chemistry. Also in Pb on Si(111) a correlation between the SB and the interface structure has been suggested to explain the difference in the measured barriers by Heslinga *et al.* [62]. For Pb films grown on the (7×7)-Si reconstruction a SB of 0.7 eV was measured, and 0.93 eV was measured when Pb films where grown on the $(\sqrt{3} \times \sqrt{3})R30^{\circ}$- Si reconstruction.

In Section 4.7 we will apply the interface dipole model to explain the modification in the SB by metallic interlayers placed between the Si substrate and the Pb film.

4 Controlling the electronic properties of Pb QWS through interface engineering

The goal of this chapter is to explore the influence of the transition region between the metallic Pb overlayer and the semiconducting Si substrate on the electronic properties of QWS. We focus on three different Si terminations using Bi, Pb, and Ag as interfactants, which form well-organized and abrupt interfaces. This chapter is organized as follows. First, an overview of experiments is given investigating the influence of the metal-substrate interface on the properties of Pb QWS. In the second part we will introduce the interfaces and investigate their surface symmetry and electronic structure. A special care is devoted to the change of the Si $2p$ core-level spectra upon formation of the interfaces. In the third part we focus mainly on Pb QWS grown on the Bi interface and demonstrate that this interface is abrupt and that high quality Pb layers can be grown on top. The main part of this chapter investigates the still debated origin of the unexpected anomalous effective mass found in Pb QWS on the Pb reconstructed Si substrate using several techniques as introduced in Chap. 2. In the last part we will determine the Schottky barriers of the systems and discuss possible correlations between the interface dipole and the effective mass.

4.1 Overview

In Chap. 3 the metal-substrate interface phase shift has been introduced which models the influence of the substrate on the electronic properties of QWS. The following example demonstrates how different interfactants can modify this boundary condition, thereby changing e.g. the thermal stability of the films. D. A. Ricci *et al.* studied the electronic and thermal properties of Pb films grown on Si(111) terminated by In, Au, and Pb as interfactants [63]. Figure 12 (a) shows the measured binding energy of the QWS as a function of film thickness, similar to Fig. 8 (b). Although In and Pb induce similar $\sqrt{3}$ reconstructions on Si(111), the binding energies of the QWS can vary up to ≈ 0.8 eV among the two interfaces for the same quantum number n and thickness $d_0 N$. This difference in E_b already indicates that the width of the effective confinement box (d_{eff}) is larger for the Pb reconstructed substrate, as $E \propto d_{eff}^{-2}$. The larger penetration depth of the envelope function in Pb/Pb/Si(111) can be approximated by inspecting the occupied energy levels closest to the Fermi level. The states in Pb/In/Si(111) nearly interlace the corresponding levels for Pb/Pb/Si(111) at $\Delta N = \pm 1$, i.e. the penetration depth differs by ≈ 2.85 Å. A simultaneous fit of the measured energies using the phase accumulation model together with the interface phase shift according to Eq. 28 allows to quantify the influence of the interfaces. The obtained phase shift difference of both interfaces $|\Phi_S^{Pb}(E) - \Phi_S^{In}(E)| \approx \pi$ suggests that both systems are nearly out of phase in regard to quantum well properties. This is nicely demonstrated in Fig. 12 (b), where the stability temperature (T_S) of the systems as a function of film thickness is shown. All three systems exhibit the typical bilayer oscillation of T_S due to the QSE. While in Pb/In/Si(111) the stable films are of odd thickness ($N = 5, 7, 9$), in Pb/Pb/Si(111) these are of even thickness, i.e. $N = 6, 8$. As discussed above the reason for the stability phase reversal is that the electronic structure of Pb/In/Si(111) is similar to that of Pb/Pb/Si(111) at thicknesses differing by $\Delta N = \pm 1$.

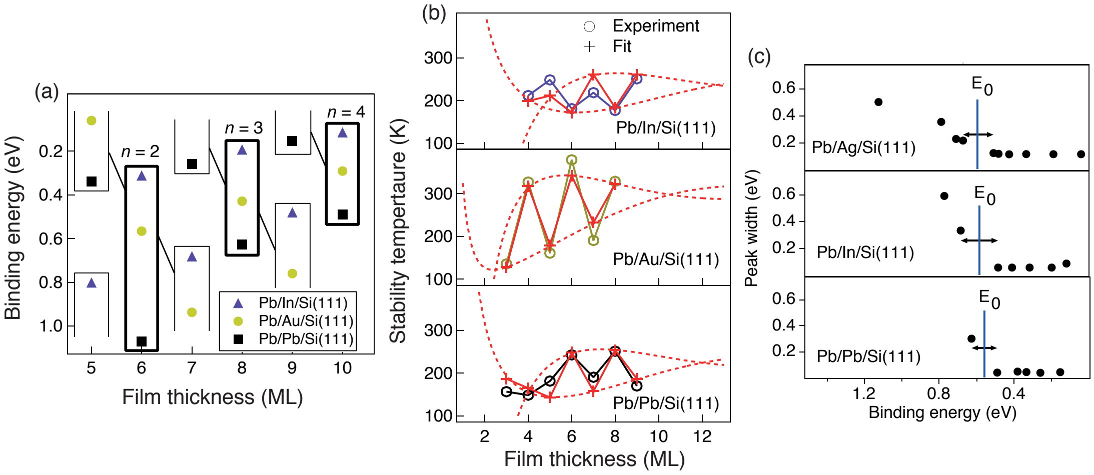

Figure 12: *(a) Measured binding energy of QWS in Pb films at normal emission grown on the In-, Au-, and Pb-terminated Si(111) surfaces as a function of film thickness* Nd_0. *(b) Temperature of the same systems at which the films become unstable (adapted from Ref. [63]). (c) Measured line width of QWS in Pb films at normal emission grown on the Ag-, In-, and Pb-terminated Si(111) surfaces as a function of film thickness* Nd_0. *The vertical line denotes the transition from QWS to QWR and hence the energetic position of the band edge of Si (adapted from Ref. [40]).*

Within the interface dipole model it is argued that the Schottky barrier is sensitive to the interface structure. Here we will present a work done by the same group that indicates the validity of this model. The authors investigated the SB of Pb films grown on n-type Si(111) substrates with different terminations made of Ag, In and Pb [40]. As explained in Sec. 3.1.2, QWS with energies within the band gap of the substrate cannot couple to any bulk states. As a consequence an electron that impinges on the interface will be perfectly reflected, resulting in an interface reflectivity, which is close to one. Such states give rise to narrow photoemission line shapes. On the other hand electronic states with energies outside the gap, commonly referred to as quantum well resonances, give rise to broad peaks due to the resonant coupling. By measuring the line width with ARPES as a function of QWS binding energy it is possible to determine the transition from QWS to QWR and derive the confinement edge (E_0) which is related to the SB. The results of applying this method are shown in Fig. 12 (c). For the Pb interface, electronic states with $E_b < 0.55$ eV are truly confined whereas for the In interface sharp peaks can be observed down to $E_b < 0.58$ eV. These findings are consistent with the determined Schottky barrier, which is 0.62 eV for the Pb and 0.55 eV for the In interface.

In the last part of the present Chap. we will apply the same method to determine the Schottky barriers of the Pb films containing interfactants. However in contrast to the study of Ref. [40] we will derive the resulting band energy diagram within the interface dipole model, and also relate the observed core-level-shifts of the Si $2p$ spectrum to charge transfer at the interface.

4.2 The (7×7) reconstruction of Si(111)

Silicon is an ideal substrate to study electron confinement in low-dimensional systems. This is because (i) it provides the necessary (global) band gap to confine electrons, (ii) high quality wafers are commercially available with variable doping concentrations of either p- or n-type, and most importantly (iii) Si(111) forms high quality interfaces with foreign atoms. The atomic structure of the (7×7) reconstruction of Si(111) has been studied for more than five decades. Nowadays the complicated surface superstructure is well described by the so-called dimer-adatom-stacking (DAS) fault model proposed by K. Takayanagi *et al.* based on data obtained using transmission electron diffraction [64].

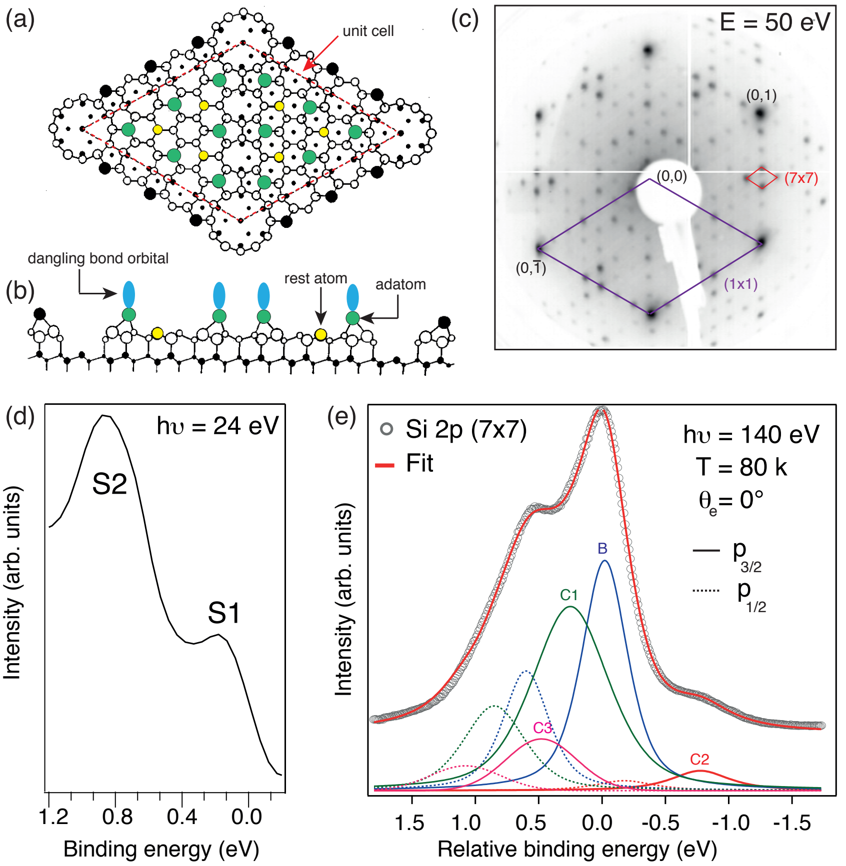

Figure 13: *(a) Top and side view (b) of the DAS model of the (7×7)-Si(111) surface (adapted from [65]). (c) LEED pattern of the surface indicating high surface quality. (d) Valence band spectrum at normal emission showing the characteristic surface states S1 and S2 corresponding to adatom and rest atom dangling bonds, respectively. (e) Si 2p core-level spectrum from the Si(111)-(7×7) surface obtained at 80 K. The spectrum was fitted assuming three surface C1, C2, C3 and one bulk B component, resulting in energy shifts of 250, -770, 490 meV, respectively. The spin-orbit splitting between the $p_{3/2}$ (solid curve) and $p_{1/2}$ (dashed curve) components was 602 meV and the branching ratio 0.5.*

The unit cell, as schematically shown in Fig. 13 (a), consists of 12 adatoms, 6 rest atoms and one corner hole atom. For example at each of the adatoms there is a partially filled dangling-bond orbital, which hosts a surface state responsible for the metallic character of the surface, in contrast to the semiconducting substrate [65–68]. This is seen in Fig. 13 (d), where the valence band spectrum exhibits strong surface state emission at binding energies $E_b = 0.20$ eV and 0.82 eV. Notice that the metallicity of this surface is still a subject of discussion in the literature. Emission from surface states can only be observed for clean surfaces without contaminations. To form a (7×7) surface reconstruction we degassed the wafer at 600 K for 24 h and flashed several times above 1300 K to remove adsorbates.

A complementary way of verifying a high surface quality is given by recording the Si $2p$ core-level spectrum. The rather broad and complicated shape of the Si $2p$ spectrum, shown in Fig. 13 (e), originates from Si atoms at the surface that are in different chemical environments due to the highly reconstructed surface. By using a standard curve-fitting procedure utilizing Voigt-profiles we can decompose the spectrum into three surface components and one bulk component following Ref. [69]. Due to spin-orbit interaction each component consists of a doublet characterized by the quantum number $j = l \pm s$. For $l = 1$ (p-orbital) it follows that the peaks are assigned as $j = 3/2$ and $j = 1/2$. In the fits we have constrained both, an energy splitting of $\Delta E = 602$ meV between the components of a doublet and the branching ratio which is related to the respective degeneracies $(2j + 1)$ and thus $2 : 1$. According to the authors of Ref. [69] the component $C2$ arise from rest atoms, the adatoms give rise to the component $C3$. The component $C1$ is due to atoms that bind to the adatoms. These assignments can be directly deduced from the fitting analysis. Recalling that the (7×7) unit cell consists of 12 adatoms and 6 rest atoms, we expect an intensity ratio between $C3$ and $C2$ of roughly 2. The intensity of $C1$ component is three times that of $C3$ because each adatom binds to three surface atoms [70].

The most important property of this surface reconstruction is its chemical reactivity due to the partially filled dangling bond orbitals pointing towards the vacuum, as schematically depicted in Fig. 13 (b). As will be shown in the next paragraph, the deposition of foreign atoms together with a mild annealing process will lead to severe restructuring at the surface and to the formation of a well-defined interface highly suitable for the growth of ultra-thin Pb films.

4.3 The $(\sqrt{3} \times \sqrt{3})R30^\circ$ reconstruction of Si(111)

The growth of high quality Pb films on Si(111) requires an atomically flat substrate. The Si(111)-(7×7) surface contains adatoms and corner holes, which make the surface rough [71], see Fig. 13 (b), with a surface corrugation of ≈ 2 Å [72]. Very similar to the formation of standing light waves within a resonator, e.g. a laser cavity, the mirrors have to be flat in order to avoid incoherent backscattering. Waves that are incoherently backscattered loose their phase information and do not contribute to the charge density of a QWS. In order to increase the quality of the interface (mirror), all Pb films in this work were grown on surface reconstructions with $(\sqrt{3} \times \sqrt{3})R30^\circ$ symmetry. The geometric and electronic structure of these interfaces will be briefly described in the following sections.

4.3.1 Si(111)-$(\sqrt{3} \times \sqrt{3})R30^\circ$-Bi($\beta$)

The deposition of approximately 3 ML of Bi onto the clean Si(111)-(7×7) at $T = 80$ K followed by subsequent annealing results in the formation of a Si(111)-$(\sqrt{3} \times \sqrt{3})R30^\circ$-Bi reconstruction (henceforth Bi-$\sqrt{3}$) [73–75]. From previous studies it is known that Bi has two $\sqrt{3}$ superlattice phases on Si(111) which form depending on the initial coverage and the annealing process [74]. The α-phase forms at T > 640 K with $\frac{1}{3}$ ML coverage in substrate units (1 ML = 7.83×10^{14} atoms/cm^2) whereas the denser β-phase forms for temperatures below 640 K and has a coverage of 1 ML. The corrugation of this structure is below the experimental resolution of a X-ray diffraction study performed in Ref. [76], suggesting only little or no surface relaxation. In our preparation method the annealing temperature was below 600 K, hence we conclude that the β-phase is formed. The top view of this phase is shown in Fig. 14 (a). The Bi atoms form trimers centered above Si atoms of the second layer[9]. The $(\sqrt{3} \times \sqrt{3})R30^\circ$ unit cell of the Bi trimer is rotated by 30° and expanded by a factor of $\sqrt{3}$ with respect to the (1×1) unit cell of the Si(111) substrate. The high quality of the interface is confirmed by LEED, as shown in Fig. 14 (b), where sharp spots are observed on a low background.

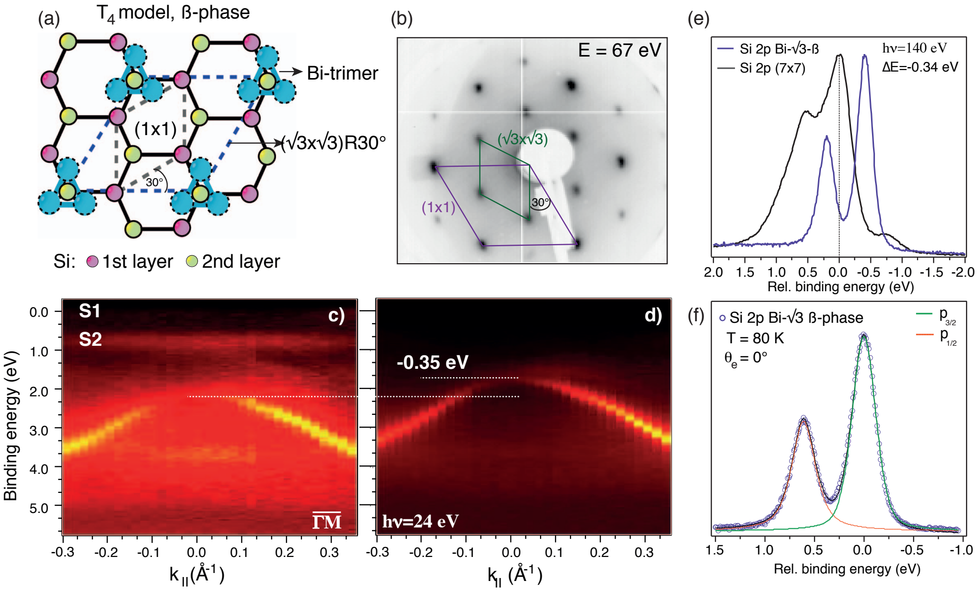

Figure 14: (a) Top view of the dense β-$\sqrt{3}$-Bi reconstruction on Si(111). (b) LEED pattern of the Bi reconstructed surface with electron energy of 67 eV demonstrating the $(\sqrt{3}\times\sqrt{3})R30^\circ$ symmetry of the surface. (c) Band structure of the clean Si(111)-(7×7) surface measured with ARPES. The surface states are labeled. (d) Band structure after preparation of the $\sqrt{3}$-Bi reconstruction. (e) Measured Si 2p spectra for the clean Si substrate and Bi-$\sqrt{3}$ indicating a strong modification of the Si surface. (f) Analysis of the background-corrected Si 2p spectrum on the Bi-$\sqrt{3}$ utilizing two Voigt-profiles spin-split by 602 meV and a branching ratio of 0.5.

---

[9] In the α-phase the trimer is replaced by one Bi atom that is centered at the Si atom of the 2nd layer.

After creation of the β-phase, the non-dispersing surface state bands $S1$ (adatom) and $S2$ (rest atom) disappear and the top of the valence band (VB) of Si is shifted by $\Delta E_{VB} = -0.35$ eV to lower binding energy from initially 2.1 eV to 1.75 eV, which is apparent from a comparison of Figs. 14 (c) and (d). This band shifting indicates that an electric dipole layer is created. The Schottky barrier of this interface will be discussed later.

Figure 14 (e) compares Si $2p$ spectra recorded from the clean (7×7) surface and from the Bi-$\sqrt{3}$ reconstruction. We observe not only a drastic change in the shape of the spectrum but also an energetic shift of $\Delta E_{CLS} = -340$ meV toward lower binding energies, which is in line with the shift of the VB. The spectrum has been fitted, after subtraction of a Shirley-type background, with two spin-orbit split Voigt profiles representing the bulk component. The width of the peaks was 226 meV, and hence close to the value, which we obtained for the width of the bulk component on the (7×7) surface, i.e. 220 meV. Surprisingly there is no need to add a surface component representing e.g. topmost Si atoms bound to the Bi trimers to improve the fit results. Similar findings were also observed in Bi/Si(110) [77], and in Sb/Si(111) [78].

4.3.2 Si(111)-$(\sqrt{3} \times \sqrt{3})R30°$-Pb$(\alpha)$

Pb/Si(111) is one of the prototype systems for studying the ordering of a two-dimensional overlayer on a semiconducting substrate. This is mainly because depending on the initial coverage, temperature and annealing history many phases can form. Any small changes in the temperature or/and in the coverage will lead to another phase. Such a behavior is known in the literature as the *devil's staircase* [79]. In this work the so-called α-phase with a corrugation of 0.23 Å and total coverage of $\frac{4}{3}$ ML has been used to improve the interface quality. A scheme of the reconstruction is shown in Fig. 15 (a). It consists of Pb trimers centered above Si atoms from the second layer with an additional Pb atom at the so-called T_4 site. The unit cell contains 4 Pb atoms and has $\sqrt{3} \times \sqrt{3}$ symmetry as confirmed with LEED shown in Fig. 15 (b). We point out that it is not possible to distinguish between the α- and the β-phase (coverage $\frac{1}{3}$ ML) from the LEED pattern alone, because of the identical unit cells. However, from our measured Si $2p$ spectrum (shown later) and the preparation procedure, i.e. annealing in front of the LEED optics just until $\sqrt{3}$ forms, we can safely exclude the formation of the β-phase, since this phase needs a higher activation energy for desorption of the excess Pb [80].

It should be noted that the nomenclature is inverted and that the Bi β-phase and the Pb α-phase are very similar in the sense that both form a trimer-type structure. To avoid confusion we will refer to both phases as the dense phase, based on the higher coverage compared to the competing phases.

Figure 15 (c) compares ARPES data of the clean Si(111)-(7×7) and of the Pb-$\sqrt{3}$, both taken at $T_s = 80$ K and a photon energy of 24 eV. We observe a rigid valence band shift toward lower binding energies and some weak emission from surface states having hole-like dispersion (marked as a green arrow). The band shift is larger by approximately 470 meV compared with the VB shift in Bi-$\sqrt{3}$. The larger upward band bending is also reflected in the Si $2p$ spectrum, that exhibits a similar shift by 780 meV, see Fig. 15 (d). Furthermore, in the Si $2p$ spectrum of Pb-$\sqrt{3}$ the

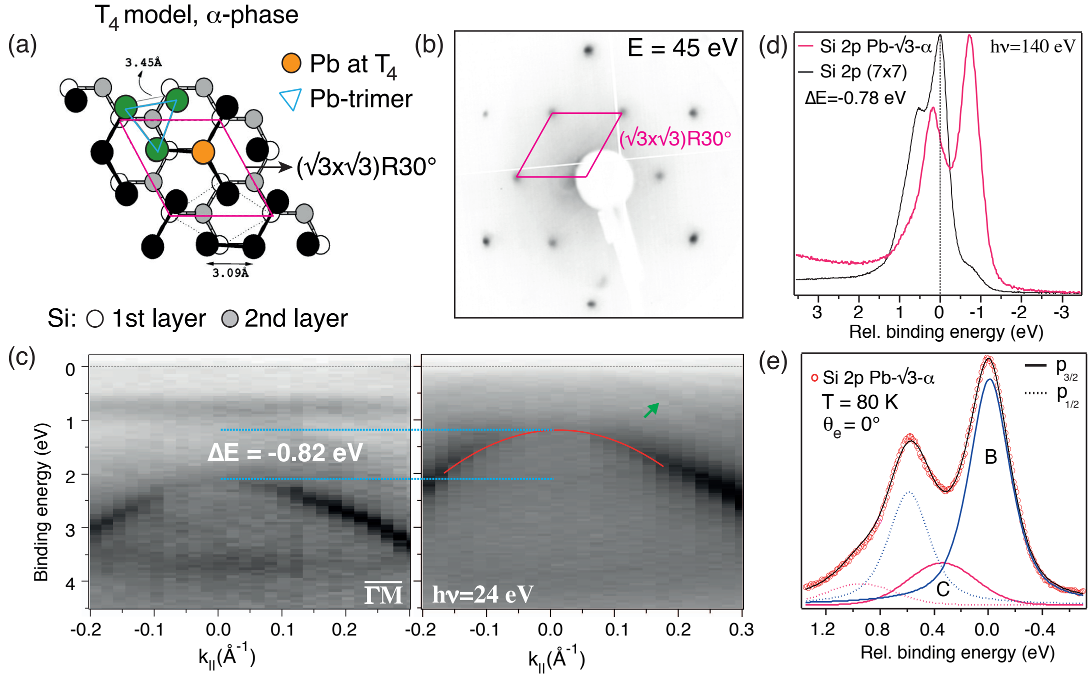

Figure 15: *(a) Structural model of the dense phase of Pb on Si(111) (adapted from [80]). (b) LEED pattern from the same phase obtained at an electron beam incident on the surface with an energy of 45 eV. (c) Comparison of valence band photoemission spectra from (left panel) the clean* (7×7) *reconstruction and (right panel) from the Pb reconstructed surface. (d) Si 2p spectra recorded from the clean and from the Pb reconstructed Si surface. (e) Decomposition of the Si 2p spectrum into a spin-orbit split bulk (B) and surface component (C). The fit was performed with the following constraints: branching ratio 0.5 and spin-orbit splitting 600 meV.*

filling of the minimum between the bulk doublet is larger and a shoulder at higher relative binding energies is seen, suggesting the presence of a surface component around this energy. We point out that the competing β-phase (0.33 ML) contains a pronounced surface component at lower binding energies which is absent in our spectrum [81,82]. According to Ref. [82] the C component is assigned to emission from Si atoms from the topmost layer.

4.3.3 Si(111)-$(\sqrt{3}\times\sqrt{3})R30^\circ$-Ag

The $\sqrt{3}$-Ag/Si(111) reconstruction is one of the most intensively studied systems by various techniques [83]. The geometrical structure with a lowest total energy is described within the inequivalent triangle (IET) model revealed by H. Aizawa *et al.* in 1999 [84] and experimentally confirmed in Refs. [85,86]. A schematic drawing of this model is shown in Fig. 16 (a). In contrast to the Bi- and Pb-induced reconstructions, Ag forms two trimers of different sizes in an unit cell with a coverage of 1 ML (in substrate units) that are centered on Si atoms of the second layer. The surface corrugation is 0.75 Å as determined with low energy ion spectroscopy [88]. The LEED

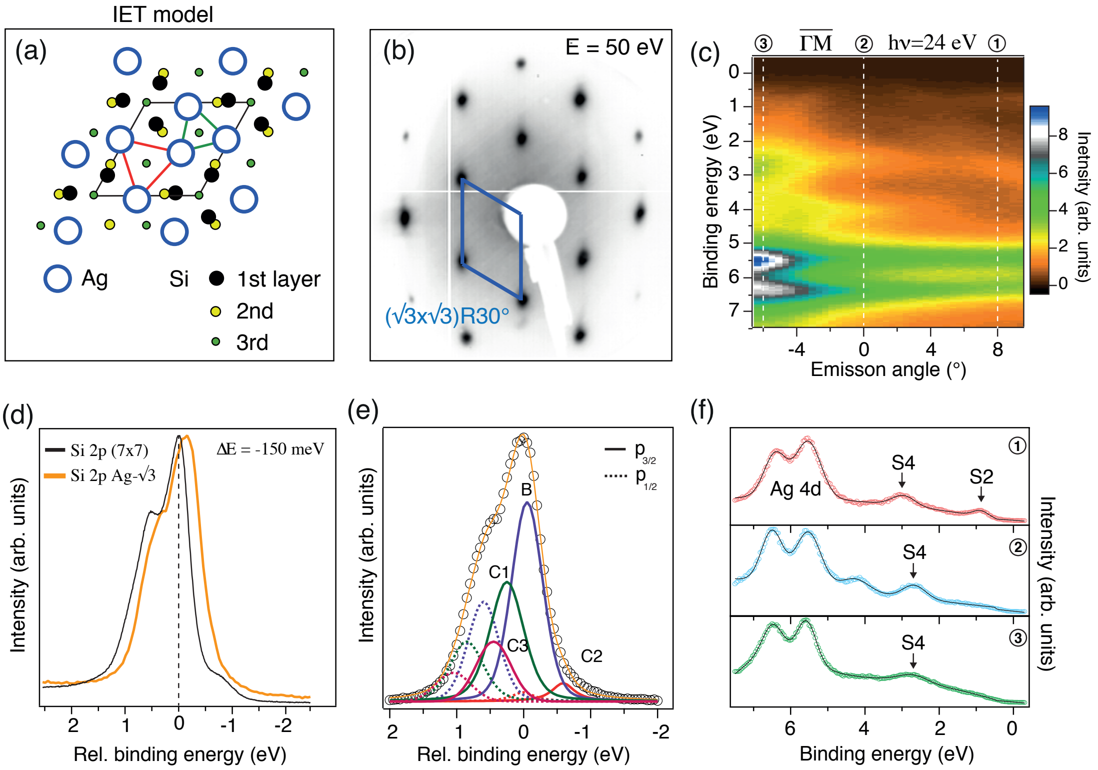

Figure 16: *(a) Top view of the Ag-$\sqrt{3}$/Si(111) surface according to the IET model (from Ref. [84]). (b) LEED pattern of the surface recorded with E_{kin} = 50 eV. (c) Band structure of the Ag reconstructed Si(111) indicating a high interface quality due to the observation of several surface state features (see text below). (d) Comparison of Si 2p spectra of the clean Si surface and of Ag-$\sqrt{3}$/Si(111). We measure a core-level shift of -150 meV. (e) Fit of the Si 2p spectrum according to Ref. [87]. The solid (dashed) lines represent the $p_{3/2}$ ($p_{1/2}$) components. The spin-orbit splitting was 602 meV and the branching ratio 0.5. (f) Cuts through the band structure of Ag/Si(111) (also indicated in (c)) at various emission angles.*

pattern of Ag-$\sqrt{3}$, shown in Fig. 16 (b), visualizes the $\sqrt{3} \times \sqrt{3})R30^\circ$ symmetry of this reconstruction. Figure 16 (c) shows the measured band structure of Ag-$\sqrt{3}$ along the $\overline{\Gamma}$-$\overline{\mathrm{M}}$ direction of the $\sqrt{3}$ surface Brillouin zone and in Fig. 16 (f) we show EDCs at various emission angles. Several features are observed. The intensive and non-dispersive bands at $E_b = 5{-}7.5$ eV arise from the $4d$ valence states of Ag. Following Refs. [89, 90] the surface state (labeled as $S2$) at ≈ 1 eV binding energy originates from the covalent interaction between Si and Ag. The state S4 at ≈ 3 eV is due to the backbonds of the topmost Si atoms forming Si triangles and the 5s component of the surface Ag atoms. Further, around $\overline{\Gamma}$ and $E_b = 1$ eV a third band with a hole-like dispersion becomes visible and its origin is the same as for $S3$ of Refs. [89, 90]. Compared to Bi/Si and Pb/Si, the Ag reconstruction produces the richest surface electronic structure and we do not observe emission from the Si VB. An estimation of shifts due to band bending is therefore not possible. However from our measurements of the Si $2p$ spectra, shown in Figs. 16 (d) and (e), we can deduce a shift toward lower binding energy by $\Delta E = $ -150 meV when the interface is formed. This is the smallest shift among the studied interfaces. Furthermore, the Si $2p$ spectrum of Ag/Si is rather broader indicating that several surface components are present. We have fitted the spectrum according to Ref. [87] with three surface components; the major component $C1$ originates from the top Si layer that bonds to the Ag trimers. The component $C2$ and $C3$ are attributed to subsurface layers.

4.4 Stability of the Bi interface and of the ultra-thin Pb film

Before we discuss the properties of the QWS in the Pb films on the Bi-$\sqrt{3}$ interface we will first show that this interface is stable against intermixing with the Pb overlayer and that the properties of the QWS do not change significantly on the time scale of days. Each Bi atom of the interface binds covalently with one Si atom of the substrate and with two neighboring Bi atoms forming the so-called trimer centered at the T_4 site [73]. The bonding to the Si atom is stronger than the bondings within the trimer, because with increasing substrate temperature the trimer-phase can be transferred into the α-phase, where only one Bi atom is bound to three Si surface atoms. To investigate possible intermixing we used X-ray photoelectron spectroscopy (XPS), see Fig. 17 (a), to map the $5d$ core-levels of Bi and Pb. The red spectrum corresponds to $\sqrt{3}$-Bi/Si(111) and the black spectrum to 9 ML of Pb on this substrate. The thin crystalline Pb film was grown by deposition at a rate of $\frac{1}{3}$ ML per minute onto the freshly prepared reconstruction after cooling down again to below 100 K. The $5d_{3/2}$ and $5d_{5/2}$ core-levels of Pb and Bi are easily identified and labeled accordingly in Fig. 17 (a). The intensities of the Bi core-levels are drastically reduced after Pb deposition, which is a first indication that no intermixing occurs at the interface. The remaining

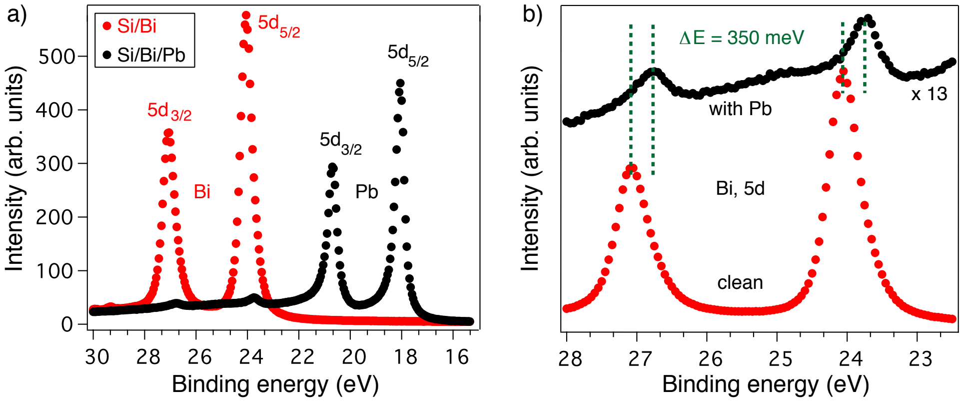

Figure 17: *(a) Photoemission of Pb and Bi 5d core-levels from Bi-$\sqrt{3}$/Si(111) (red/grey) and of 9 ML Pb/Bi/Si(111) (black). Both large-Z metals ($Z_{Pb} = 82$, $Z_{Bi} = 83$) show strong spin-orbit split d-states. (b) Core-levels of Bi before (red/grey dots) and after Pb deposition (black dots). The Pb overlayer induces a chemical shift by 350 meV towards lower binding energy. The curves are shifted on the vertical scale for clarity.*

Bi intensity is either due to the fact that the Pb layer is not fully closed and small regions with the bare substrate remain visible, or due to electrons emitted from Bi atoms at the interface. To quantify what Pb thickness one would require for the second scenario the spectrum after Pb deposition was further analysed according to Ref. [91] with the Bi interface taken as an 1 ML substrate and the Pb overlayer as a thin film:

$$\frac{I_{\mathrm{Pb}}\sigma_{\mathrm{Bi}}N^0_{\mathrm{Bi}}}{I_{\mathrm{Bi}}\sigma_{\mathrm{Pb}}N^0_{\mathrm{Pb}}} = \frac{1-\exp\frac{-d_{\mathrm{Pb}}}{\lambda_{\mathrm{Pb}}}}{\exp\frac{-d_{\mathrm{Pb}}}{\lambda_{\mathrm{Pb}}}-\exp\frac{-d_{\mathrm{Bi}}}{\lambda_{\mathrm{Pb}}}}. \tag{35}$$

Here I_{Pb} and I_{Bi} are the measured intensities, σ is the photoionization cross section [92], for Pb $\sigma_{\mathrm{Pb}} = 21.55$ Mbarn and for Bi $\sigma_{\mathrm{Bi}} = 28.03$ Mbarn, N is the surface atomic density with $N^0_{\mathrm{Pb}} = 9.43 \cdot 10^{14}$ atoms/cm^2 and $N^0_{\mathrm{Bi}} = 7.83 \cdot 10^{14}$ atoms/cm^2. d_{Pb} and d_{Bi} are the thicknesses of the Pb overlayers and of the Bi layer. $\lambda_{\mathrm{Pb}} = 5$ Å is the mean free path of the photoelectrons in the Pb layers. From Eq. 35 we obtain a thickness $d_{\mathrm{Pb}} = 18$ Å which corresponds to 6.1 ML of Pb. From the analysis of the binding energy of the QWS, which provides an intrinsic thickness calibration, we obtain a thickness of 9 ML. In case of intermixing, the ratio of the 5*d* core-level signals of Pb and Bi would be $I_{\mathrm{Pb}} : I_{\mathrm{Bi}} = 6 : 1$ for the same amount of Bi in a 9 ML Pb film, and thus significantly smaller than the measured ratio of 56 : 1. We therefore conclude that the Bi interface is stable against intermixing with Pb at the low temperatures under investigation. This result is not surprising since the bonding of the Bi to the Si substrate lowers the surface energy by filling dangling bonds. Although the Bi does not intermix with the Pb, its chemical environment is altered due to the Pb layer on top. As shown in Fig. 17 (b) this results in a shift of the Bi core-levels by about 350 meV to lower binding energies.

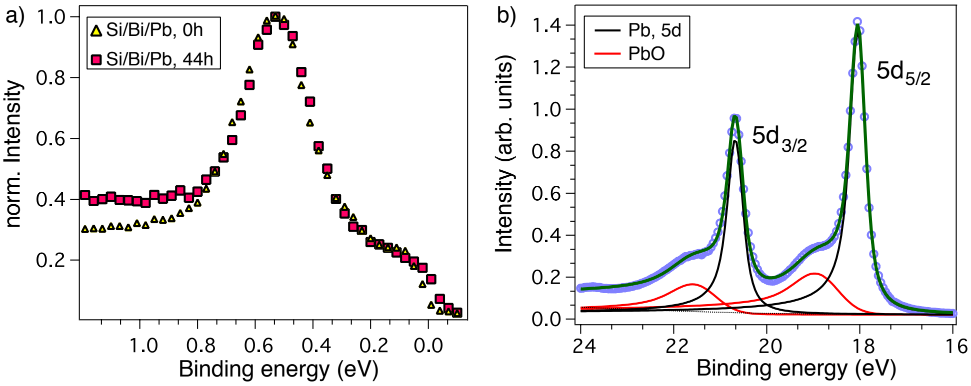

Figure 18: *(a) Spectrum of a QWS shortly after preparation (triangles) and after 44 h (squares). (b) 5d Core-levels of Pb 24 h after preparation fitted with the clean and oxidized Pb components.*

A further advantage of the investigated ultra-thin films is their stability over time. Figure 18 (a) shows energy distribution curves normalized to their maximum of a QWS shortly after preparation (triangles) and after 44 h (squares) exposure to the residual gas of the ultra-high vacuum chamber. The 5*d* core-levels of Pb (see Fig. 18 (b)) show an additional shoulder after 24 hours of measurement, which can be attributed to oxidation of the Pb top layer. However, the peak width and the binding energy of the QWS are not affected by this oxidation and remain constant over time. The only quantity that changes is the peak-to-background ratio, which decreases from $1 : 0.3$ to $1 : 0.4$ presumably due to an increased number of adsorbates on the surface. This temporal stability of the system is advantageous as it allows to perform long time measurements, but it also indicates that the QWS survive a significant contamination as long as the sample is kept at low temperature. One would expect a change of the metal-to-vacuum phase shift, when the topmost layer becomes oxidized which in turn should influence the binding energy of the QWS. However, Peng *et al.* have studied temperature dependent oxidation of the Pb(111) surface with STM [93] and found that at low temperature (≈ 80 K) and low coverage (< 6 L[10]) only small-size oxide clusters form. These clusters will serve as point defects resulting in an increase of the background without significant change in the confinement of the QWS. The oxidation processes may have an influence on Φ_V at higher coverages when a closed oxide layer forms [94].

4.5 Controlling the effective mass through interface engineering

Having shown that the Bi interface is stable against burial we will now turn to the main part of this chapter where we study the in-plane effective mass of quantum well states in thin Pb films on a Bi reconstructed Si(111) surface by angle-resolved photoemission spectroscopy. It is found that this effective mass is a factor of three lower than the unusually high values reported for Pb films grown on a Pb reconstructed Si(111) surface. Through a quantitative low energy electron diffraction (LEED) analysis the change in effective mass as a function of coverage and for the different interfaces is linked to a change of around 2% in the in-plane lattice constant. To corroborate this correlation, density functional theory calculations were performed on freestanding Pb slabs with different in-plane lattice constants. These calculations show an anomalous dependence of the effective mass on the lattice constant including a change of sign for values close to the lattice constant of Si(111). This unexpected relation is due to a combination of reduced orbital overlap of the $6p_z$ states and altered hybridization between the $6p_z$ and $6p_{xy}$ derived quantum well states. Furthermore we show that a similar effect can be also achieved with a Ag reconstructed Si substrate. In this system the effective mass is even further reduced compared to Pb/Bi/Si(111).

4.6 The in-plane dispersion of QWS

The unusual flat in-plane dispersion of Pb QWS on Pb-$\sqrt{3}$/Si(111) is still a subject of discussion. Before we present our results and discussion we will first review some previous measurements of band dispersions of Pb QWS on different types of interfaces.

ARPES is a suitable technique to investigate the in-plane dispersion $E(k_{\|})$ of QWS. The confinement of the states is present in the direction perpendicular to the surface whereas within the film plane the crystal can be regarded as infinite. Therefore the band structure around the surface

---

[10] 1 Langmuir (L) corresponds to an exposure of the surface to $\approx 1.3 \cdot 10^{-8}$ mbar during 100 sec.

Brillouin zone (SBZ) center $\bar{\Gamma}$ ($\mathbf{k}_{\parallel} = 0$) is well described by a free electron gas according to

$$E(k_{\parallel}) = E_{\Gamma} + \frac{\hbar^2}{2m^{\star}} k_{\parallel}^2 \tag{36}$$

with E_{Γ} as the binding energy of the state with $\mathbf{k}_{\parallel} = 0$, $m^{\star}$ as effective mass and $\mathbf{k}_{\parallel} = (k_x, k_y)$ as the parallel momentum.

It is known that the dispersion of a band is directly related to the degree of localization of the state; localized electronic states disperse less than delocalized states. The degree of localization is in simple systems inversely related to the degree of overlap between the orbitals of which the state is composed: a small orbital overlap results in a high degree of localization and vice versa. An example of a system with almost no interaction between the substrate and the overlayer is given by Pb on graphitized SiC as shown in Fig. 10 [51]. The dispersion of the QWS is free-electron-like with an effective mass of approximately m_e (free electron mass) around the SBZ center even for a low film thickness of 2 ML, where typically strain due to the lattice mismatch with the substrate is expected. Density functional theory slab calculations are able to reproduce the measured dispersion by assuming a free-standing Pb slab. In this system the inert graphene layer decouples the influence of the substrate. On the other hand Pb deposited on Pb-$\sqrt{3}$/Si(111) is an example of a strong influence of the substrate [95,96]. For coverages up to 25 ML the states around the SBZ center have unusually high effective masses of up to $m^{\star} \approx 10\ m_e$, which can not be modeled with a free-standing film assuming a bulk Pb in-plane lattice constant. Here we will show that the Bi interface acts similarly to the graphene layer to decouple the Pb overlayer from the substrate and that the dispersion increases. It will be argued that the strong in-plane localization observed in Pb layers on the Pb-$\sqrt{3}$/Si(111) substrate can be explained by an increased atomic spacing in the direction parallel to the surface induced by the substrate.

Figures 19 (a-c) show the in-plane dispersions of QWS for Pb film thicknesses of 10, 17 and 19 ML grown on the Bi interface measured along the high symmetry direction $\overline{\mathrm{M}}$-$\overline{\Gamma}$-$\overline{\mathrm{M}}$ of the (1×1) SBZ. In contrast to Pb films grown on the Pb-$\sqrt{3}$ interface, as shown in Fig. 19 (d), we do not observe states with an effective mass larger than 4 m_e. The effective mass was determined quantitatively by taking EDCs at momentum steps of 0.035 Å^{-1} for a total range of $\overline{\Gamma} \pm 0.3$Å^{-1} and fitting them with *Voigt* functions after subtracting a linear background contribution. From these fits one obtains the QWS energy versus in-plane momentum, which are finally fitted assuming a parabolic dispersion to determine $m^{\star}$.

It should be pointed out that all measured QWS bands presented in this work are derived from $6p$ orbitals, because the binding energies lie above the Pb sp symmetry band gap of the Γ-L direction, which expands from 4 to 8 eV binding energy [97]. Below this gap the QWS are $6sp_z$ derived. The electronic states described by a parabolic dispersion around the SBZ center have $6p_z$ orbital character and the downward dispersing bands at $k_{\parallel} > 0.4$ Å^{-1} have $6p_{xy}$ character [51].

It is remarkable that, independent of the Pb layer thickness, all measured QWS exhibit an enhanced in-plane dispersion compared to Pb/Pb/Si(111). The QWS displayed in Fig. 19 (a) which is found in a 10 ML thick film of Pb has an effective mass of 2.75 m_e and the QWS which arises in 19 ML Pb has an effective mass of 2.09 m_e. This trend indicates that the coupling to the

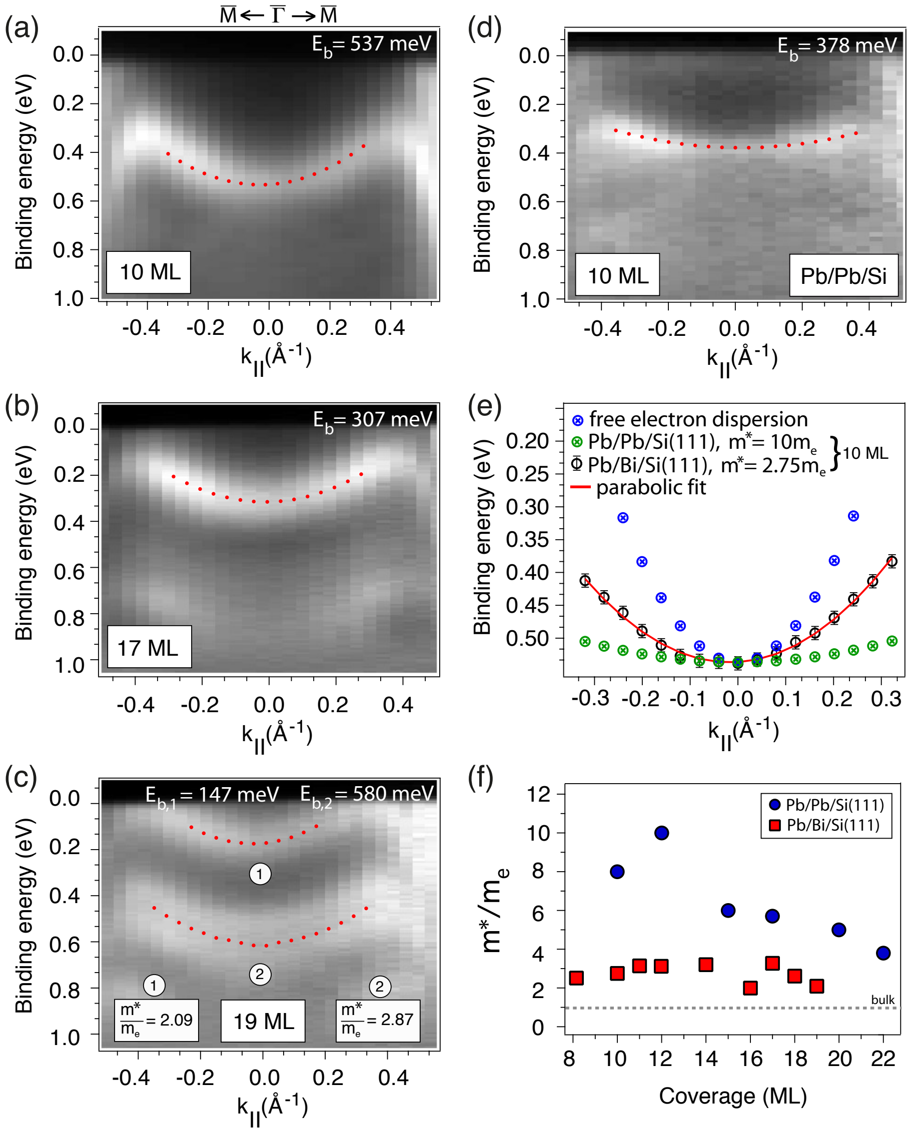

Figure 19: *(a-c) Band dispersion of QWS in 10, 17 and 19 ML Pb films on Bi/Si(111). (d) Band dispersion of Pb QWS on Pb/Si(111). (e) Extracted dispersion (red dots) from Fig. 19 (a) as described in the text. For comparison a free-electron-like dispersion and the dispersion of Pb/Pb/Si(111) are included. (f) Red squares: Effective masses of QWS for different thicknesses of Pb deposited on the Bi/Si(111) obtained from the fitting procedure as described in the text. Blue circles: effective masses of Pb on Pb/Si(111) taken from [96].*

substrate is reduced, even for the low coverage, where largest effective masses were reported for Pb/Pb/Si [96]. Figure 19 (f) shows the development of the effective mass of $6p_z$ derived states with increasing Pb layer thickness for the Pb and the investigated Bi interface. In Pb/Pb/Si(111) the effective mass decreases with thickness from $m^\star = 10\ m_e$ at low coverage towards $m^\star = 4\ m_e$ at 22 ML. With increasing film thickness the effective mass shows a trend towards the bulk limit

(N→ ∞, grey dashed line) of $m^\star = 1.14\ m_e$ [98]. Hence for low coverage the influence of the substrate and interface is most evident and with increasing thickness this influence becomes smaller. The substrate may force the atoms in the Pb overlayer into an in-plane lattice constant which coincides more with the lattice structure of the substrate. Thus the lattice constant of the overlayer appears for low coverage to be closer to that of Si than to that of Pb. As a consequence, and because the Pb films grow as close packed layers in *fcc* stacking along the [111] direction, an increase of the interatomic distance between nearest neighbor atoms will decrease the overlap of the $6p_z$ orbitals, as drawn schematically in Figs. 20 (a) and (b). This in turn will lead to more localized states with flat dispersion. The influence of the substrate becomes weaker for thicker films, therefore the lattice constant decreases with thickness.

4.6.1 Free-standing slab calculations using DFT

Our interpretation that the degree of orbital overlap influences the band dispersion of Pb QWS is also supported by our DFT calculations, which were performed using the *Wien2K* simulation package [31]. The generalized gradient approximation of Perdew *et al.* [99] was employed to a repeated slab geometry (8 ML Pb, 15 Å vacuum) with a muffin-tin radius set to 2.5 bohr, plane wave cut-off of 7.84 Ry and integration over the Brillouin zone with (16×16×1) k-points. Spin-orbit interaction was included in a second self-consistent cylce using pertubation theory with the scalar-relativistic orbitals as basis set. Figs. 20 (c) and (d) show two band dispersions along $\overline{\mathrm{M}}$-$\overline{\Gamma}$-$\overline{\mathrm{M}}$ for the in-plane lattice constants a = 3.5 and 4.0 Å as defined in Fig. 20 (e).

The increase of the in-plane lattice constant by 0.5 Å affects the entire band dispersion of the system. Both the $6p_z$ derived bands and the $6sp_z$ derived bands below the symmetry band gap of Pb become flatter throughout the whole energy range. However, the change of the dispersion of the $6p_z$ states is most significant, which can be assigned to an enhanced influence of the hybridization with the downward dispersing $6p_{xy}$ states. With the increasing in-plane lattice constant, the band width of these bands is reduced and in the energy range of interest they thus move down in energy and become flatter. The hybridization with the p_z bands, and the associated change from electron-like to hole-like dispersion in these bands, therefore starts at lower $|\mathbf{k}_{\|}|$.

In the following analysis we will focus on the first band below the Fermi level ($n = 4$), as this is the state we measured with ARPES. The effective mass of this band changes from initial 1.02 m_e to a hole-like dispersion with $m^\star$ of -4.10 m_e when the lattice constant is increased by 0.5 Å. Fig. 20 (f) shows calculated effective masses for lattice parameters between 3.5 and 4.0 Å, which are fitted for positive values with an exponential function according to:

$$m^\star_{n=4}(a[\text{Å}]) = 1.038 + 0.0585 \cdot \exp\left(\frac{a - 3.5}{0.1}\right) \tag{37}$$

in units of the free electron mass. Note that the influence of the lattice parameter on the effective mass is weak up to $a = 3.7$ Å and becomes stronger for higher values. This anomalous dependency of the effective mass on the in-plane lattice constant is thus not only a result of the reduced orbital overlap but also strongly enhanced by the hybridization of the $6p_z$ and $6p_{xy}$ derived bands.

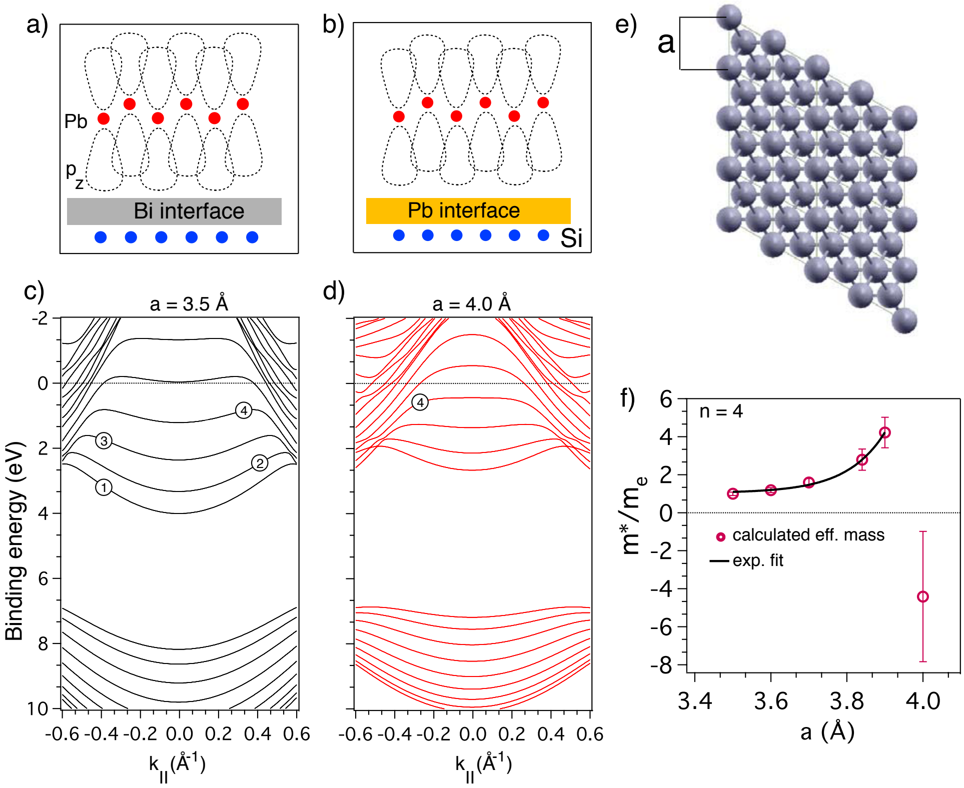

Figure 20: *(a) and (b) Simplified picture of p_z orbital overlap at both interfaces. (c) Calculated band dispersion along $\overline{M}$-$\overline{\Gamma}$-$\overline{M}$ with in-plane lattice constant a = 3.5 Å, and (d) a = 4.0 Å. The bands are labeled according to the number of anti-nodes in the envelope function (compare with Fig. 8). (e) Top view of the Pb(111) surface and (f) effective masses of the band with $n = 4$ for different in-plane lattice constants obtained from DFT calculations including an exponential fit as described in the text.*

4.6.2 Evolution of the in-plane lattice constant studied with LEED

Having confirmed with DFT the influence of the in-plane lattice constant on the band dispersion we now turn to the measurements of the surface in-plane lattice constants using LEED, which is sensitive to the surface atomic structure and thus allows the determination of relative changes in the in-plane lattice constant of the topmost layers, see also Fig. 5. We have recorded the (1×1) LEED pattern of the Pb surface for different coverages of Pb on Pb-$\sqrt{3}$/Si(111) and for a 10 ML thick Pb film on Bi-$\sqrt{3}$/Si(111). A comparison of the (1,0) spots for the 10 ML thick films grown on the different interfaces indicates that the spots are sharper on the Bi interface than on the Pb interface as shown in the raw data of Figs. 21 (a) and (b) and the profiles in Fig. 21 (c). Sharp LEED spots are either found for perfectly commensurate systems or when the interaction between the substrate and the overlayer is minimal [51]. For a more quantitative determination of the in-plane lattice constant the LEED data were analysed as follows: first, a $2D$ gaussian fit as shown in Figs. 21 (a) and (b) determines the position of each spot and the corresponding

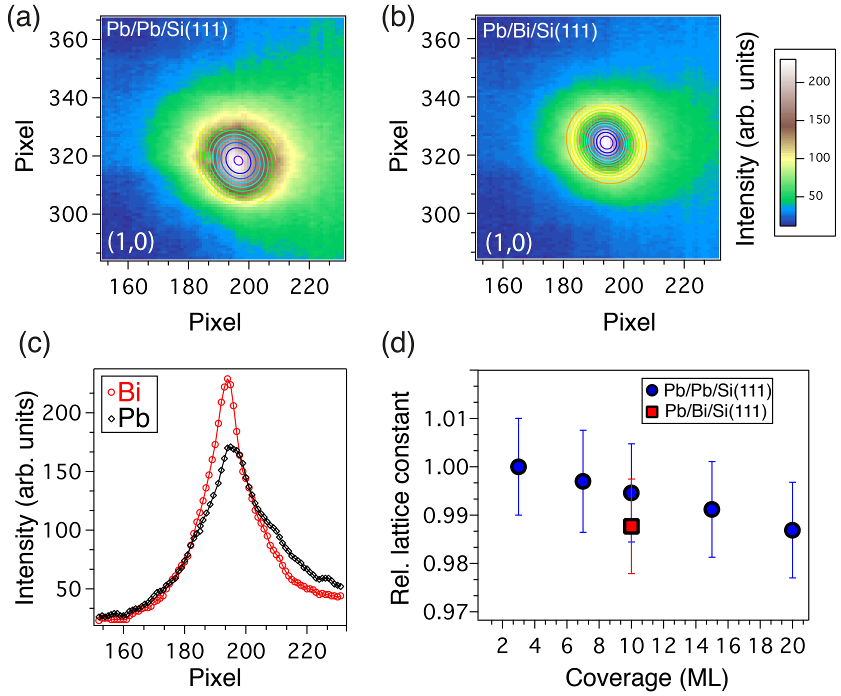

Figure 21: *(a) and (b) (1,0) LEED spot of the Pb/Pb/Si(111) and Pb/Bi/Si(111) surface. (c) Horizontal cut through the maximum of intensity of the (1,0) spot for Bi (red open circles) and Pb (black solid circles). (d) Relative lattice constant vs. coverage measured with LEED; blue circles represent Pb/Pb/Si(111) and the red square Pb/Bi/Si(111).*

(x,y) coordinates on the screen. Second, from these coordinates the distances between all three directions, e.g. $\overline{\Gamma}_{10}$-$\overline{\Gamma}_{00}$-$\overline{\Gamma}_{\overline{1}0}$, were determined, which are finally averaged. Although our LEED set-up is sensitive to relative changes of the lattice constant it is not calibrated for the precise determination of absolute values. In the following we therefore use values relative to the atomic spacing found for the lowest thickness of Pb on Pb-$\sqrt{3}$/Si(111). The findings are summarized in Fig. 21 (d) as a function of layer thickness. The thinnest Pb layer of 3 ML on the Pb interface has an almost 2% larger lattice constant than the 20 ML Pb film on the same substrate. Using the relation between lattice constant and effective mass obtained from DFT (Eq. 37) we can calculate the corresponding lattice constant for the 20 ML thick Pb film ($m^\star = 5\ m_e$) which is 3.92 Å and estimate the effective mass for this lattice constant expanded by 2% (3.99 Å). This gives us $m^\star = 9.689\ m_e$ which is in very good agreement with what is observed for low coverages. The lattice constant of the 10 ML Pb film grown on the Pb-$\sqrt{3}$/Si(111) differs by about 1% from the Pb film grown on the Bi interface. The comparison of these effective masses with our fit function leads to a lattice constant difference of almost 3%, which is consistent within our error margins.

These small changes in the in-plane lattice constant may in principle also be observed in surface X-ray diffraction (SXRD) studies, which has a higher resolution than LEED and probes the full layer and not only the topmost layers. In two SXRD studies on this system [100, 101] the exact in-plane lattice distance could unfortunately not be determined exactly and it was only found that the in-plane spacing is "bulk-like" with a relatively large distribution which is also reflected in the broad LEED spots shown in Fig. 21 (a) and (c). In STM measurements a mismatch between the substrate and overlayer in-plane lattice constants can be resolved through an analysis of the resulting Moiré pattern. From such measurements on Pb-$\sqrt{3}$/Si(111) combined with high resolution LEED data for low coverages [102] it could be determined that the Pb and Si lattice constants are not the same. Here again the exact in-plane lattice spacing of the Pb film can not be determined because the measured corrugation is a convolution of the Moiré pattern, the changes in the local density of states and the surface relaxation. Although the determination of the exact in-plane lattice constant has proven very difficult, the relative changes in the in-plane lattice constant obtained from our LEED analysis correlate well with the measured changes in effective mass, as supported by our DFT results.

4.6.3 Influence of the substrate on the dispersion

Upton *et al.* have attempted to explain the unusual high effective mass in Pb/Pb/Si(111) in terms of an avoided crossing of p_z derived states and valence states of Si(111) and the rapid oscillations of the phase shift in this energy region [103]. QWS with energies close to the confinement edge E_0 of the substrate will feel a repulsive force which tends to lower the binding energy and so to prevent a band crossing. Figure 22 (a) shows the band dispersion of a 8 ML Pb film grown on the Bi-$\sqrt{3}$ interface with a binding energy of $E_B = 690$ meV at the zone center and with an effective mass of $m^\star = 3.17\ m_e$.

The parabolic band dispersion of the Pb film intersects with the VB of Si around an in-plane momentum of $k_\| = (0 \pm 0.2)$ Å^{-1} and becomes less pronounced in this region. Electronic states further away from the VB are not affected. The interaction of film states with the VB of the substrate was also reported for Al/Si(111) [105], Ag/Ge(111) [106], and In/Si(111) [96] and explained in terms of hybridization of the film and valence states of the substrate. States within the specific momentum range around $\overline{\Gamma}$ are quantum resonances, because they are not confined within the absolute band gap of Si(111). The hybridization leads to a lower intensity and to a larger peak width because the reflectivity of the interface is no longer equal to one. Figure 22 (b) shows EDCs taken from $k_\| = -0.4...+0.4$ Å^{-1} and normalized to the maximum of intensity. Red (grey) EDCs represent truly confined states (QWS) with narrow line widths and blue (black) EDCs are quantum resonances. Also for the Bi reconstructed interface a clear hybridization between the QWS and the Si VB is thus observed. However, the effective mass is still significantly lower compared to QWS on Pb-$\sqrt{3}$/Si(111). Therefore the high effective mass for Pb/Pb/Si(111) can not be explained by the influence of the Si VB alone. The increase of the effective mass actually occurs in the energy and momentum space which is further away from the Si valence band and closer to the $6p_{xy}$ derived states. Thus the unusual effective mass in Pb/Pb/Si(111) arises from the structural and electronic properties of the Pb overlayer and can be reduced by replacing the Pb with a Bi interface.

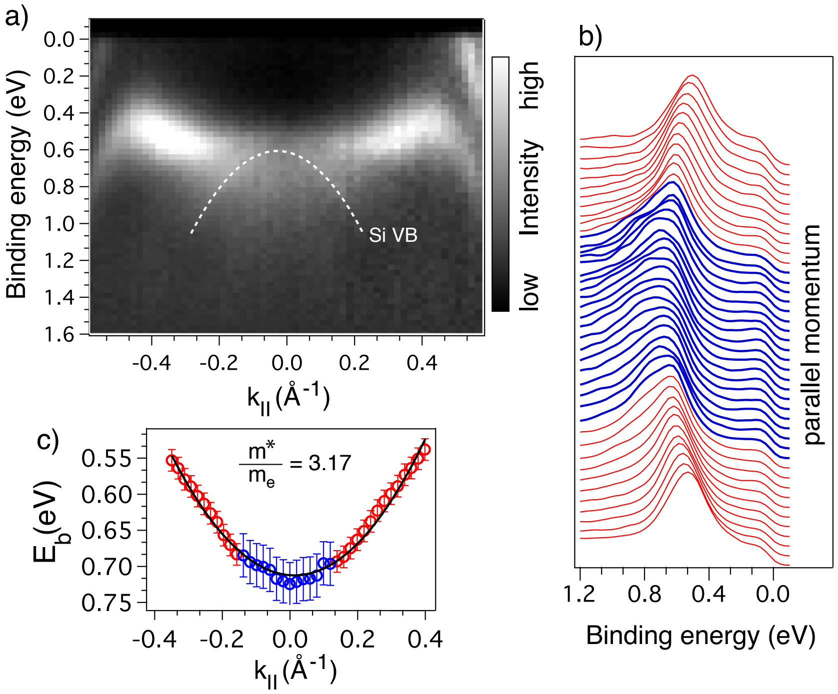

Figure 22: *(a) Band dispersion of 8 ML Pb deposited on top of Bi/Si(111). (b) Normalized energy distribution curves for in-plane momenta* $k_{||} = 0 \pm 0.4$ *Å*$^{-1}$*. Blue (black) spectra represent quantum resonances and red (grey) spectra fully confined QWS. (c) Parabolic fit including the quantum resonances.*

4.6.4 Influence of the Ag interface on the dispersion of QWS

The question arises, whether the reduction of the effective mass of Pb QWS can be also achieved with other types of interfactants. To investigate this question we have prepared Pb films on a Ag reconstructed Si(111) substrate. See Sec. 4.3.3 for details of this reconstruction.

Figure 23 (a) shows an exemplary band dispersion of 8 ML Pb on Ag/Si(111), which has been analysed as described before. The resulting parabolic fit, see Fig. 23 (b), nicely matches the extracted dispersion of the k-dependent intensity maxima. We obtain an effective mass of $m^\star = 2.4\ m_e$, which is slightly reduced compared to 8 ML Pb/Bi/Si(111), where $m^\star = 3.17\ m_e$ (see Fig. 22). The origin of the further reduced effective mass is likely the same as for Pb QWS on the Bi reconstructed substrate, i.e. a reduction of the interaction between the Pb film and the Si substrate. Using Eq. 37 we obtain an (average) in-plane lattice constant of $a_{Ag} = 3.81$ Å for the Pb film on the Ag reconstructed Si substrate, while for the same Pb coverage on the Bi interface the lattice constant is $a_{Bi} = 3.86$ Å and therefore expanded by 1.3 % with respect to a_{Ag}.

Obviously there is an influence of the interface on the structural properties, i.e. the in-plane lattice constant, of the Pb film. We again point out that small changes in the in-plane lattice constant and the resulting influence on the dispersion of the $6p_z$ derived QWS is strongly amplified by the hybridization with $6p_{x,y}$ bands. In the following Section we will seek for experimental evidence

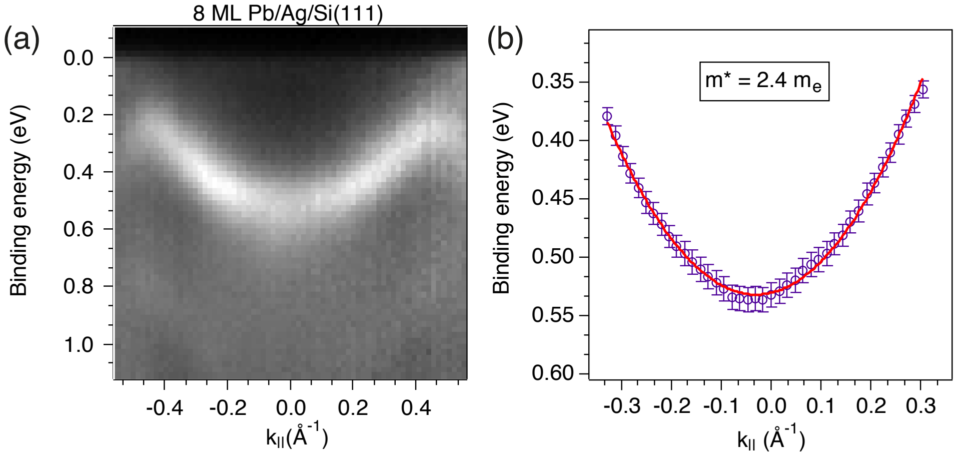

Figure 23: *(a) Band dispersion of QWS in 8 ML Pb/Ag/Si(111) measured with ARPES using a photon energy of 24 eV. (b) Extracted dispersion from (a) and parabolic fit.*

of what could mediate the interaction between the adsorbate and the substrate. By means of quantum well spectroscopy we will determine the Schottky barriers of the system and the size of the interface dipole.

4.7 Determination of the Schottky barrier

In Section 3.4 we have introduced the interface dipole model (IDM) for Schottky barrier (SB) formation of a metal-semiconductor (MS) junction. In contrast to the original (non-interacting) Schottky model, the IDM treats charge transfer between the constituents associated with the formation of an interface dipole. We will show that this model captures the physics of Schottky barrier formation in our systems, which contain interfactants.

Several techniques are commonly used to determine the Schottky barrier of a MS junction such as the measurement of the current-voltage characteristic [107] or by high-resolution core-level spectroscopy using synchrotron light. The latter has been intensively used in the last decades to study Schottky barrier formation in thin metallic overlayers on semiconducting substrates. Such an experiment is usually performed by measuring the Si $2p$ core spectrum of the clean (7×7) reconstruction and after preparation of the interface, as depicted in Figs. 24 (a) and (b). Because the Fermi level position in Si(111)-(7×7) is accurately known to be (0.63 ± 0.05) eV above the Si valence band edge [108] and the binding energy of the Si $2p$ core level relative to the valence band is constant throughout the band bending region, the measured Si $2p$ core-level shifts (ΔE_{CLS}) may be attributed to band bending in the depletion layer. However, the application of this method for determining the SB has been a subject of intense debate in the past [82, 109, 110]. For example, in a photoemission experiment the measured spectrum represents always an average of several atomic layers due to the finite probing depth, i.e. the inelastic mean free path of photoelectrons.

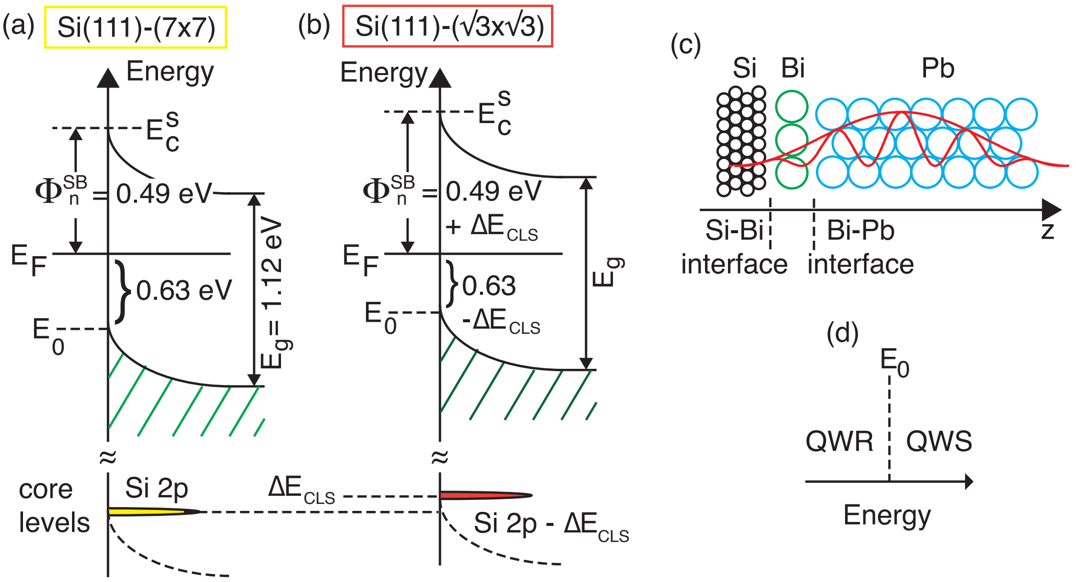

Figure 24: (a) Schematic energy vs. position diagram of the Si(111)-(7 × 7) reconstruction according to Ref. [108]. (b) Change of the energy diagram upon formation of an interface. The Schottky barrier can be directly deduced from the core-level shift of the Si 2p core-level. (c) Illustration of the property of a QWS which probes the properties of the deep lying interface, which are usually not accessible by PES due to the limited probing depth. (d) The transition between a QWS and QWR is well-defined by the energetic position of the valence band edge.

For our systems the situation becomes even more complex, because the deposition of Pb layers on top of the interface can alter the interface structure as argued by Le Lay and Hricovini [111]. Hence the SB of a MS junction at low coverages is not necessarily the same as for thick overlayers. Furthermore, one has to consider not only the interface between the substrate and the reconstruction, see Fig. 24 (c), but also the interface between the reconstruction and the Pb film. As shown in Fig. 17 (b) of Chap. 4.4 the deposition of Pb on the Bi reconstructed substrate leads to a CLS of the Bi 5d states to lower binding energy which is an indication that bonds between Pb and Bi are created. In the context of the IDM these bonds will then also contribute to the Schottky barrier. In conclusion, the determination of the SB from Si 2*p* CLSs of the reconstructed surface alone is for our junctions not applicable. However, from these measurement insights about the dipole formation at the interface can be drawn.

In this work we therefore employed an indirect method to determine the Schottky barrier by measuring peak widths of QWS and QWR using photoemission spectroscopy [40, 112]. We use the property that quantum well states arise from the coherent superposition of waves containing information about both, the metal-substrate and metal-vacuum interface. Keeping the metal-vacuum interface constant, while changing the interfactant, allows to isolate the influence of each interface.

As introduced in Sec. 4.1, electronic states which overlap energetically with valence states of

Si(111) can couple through the interface to the Si substrate states and therefore appear as broad features in the spectrum. States with energies that fall into the band gap give rise to sharp features in the measured spectra. In analogy of a Fabry-Pérot interferometer the peak width (W) of a state is related to the interface reflectivity (r) via [113]:

$$W \propto \frac{1-r}{\sqrt{r}} \tag{38}$$

We have collected sufficient data allowing us to determine the position of the valence band edge at which the transition between a QWR and QWS occurs, see Fig. 24 (d). The Schottky barrier is then calculated from:

$$\phi_n^{SB} = E_g - E_0 \tag{39}$$

with $E_g = 1.15$ eV as the global band gap of Si at T ≈ 80 K. Figure 25 shows the obtained results for the three investigated interfactants (Pb, Bi, Ag). From the band dispersions in Figs. 25 (a, d, g) normal emission spectra are extracted and fit assuming Voigt profiles with a linear background convoluted with the Fermi-function. The resulting fits are shown in Figs. 25 (b, c, f). While for the Bi and Ag interface the obtained peak widths of QWS are ≈ 200 meV, the peak widths on the Pb interface are considerably reduced down to 140 meV as a consequence of the reduced dispersion. As expected the peak widths of QWR are greatly enhanced compared to QWS. For example the peak width of a QWR in Pb/Bi/Si(111) shown in Fig. 25 (e) is roughly 600 meV - three times larger than the width of a truly confined state.

From these and further measured data sets we can deduce the energetic position of the Si band edge (E_0) as the arithmetic average of the binding energy of the QWS with the highest and the QWR with the lowest binding energy, see Figs. 25 (c, f, i). Our results are summarized in Tab. 1 and compared with experimental values from Ref. [40] and with those values based on the measured core-level shifts of the Si 2p spectrum in the reconstructed systems (Figs. 14, 15, 16).

	E_0 (eV)	$\phi_{n,exp}^{SB}$ (eV)	$\phi_{n,exp}^{SB}$ (eV) [40]	$\phi_{n,exp}^{CLS}$ (eV)
Pb	0.50 ± 0.07	0.65 ± 0.07	0.61 ± 0.05	1.27
Bi	0.57 ± 0.05	0.58 ± 0.05	–	0.83
Ag	0.62 ± 0.06	0.53 ± 0.06	0.55 ± 0.06	0.64

Table 1: *Energetic position of the band edge (E_0) of n-type Si(111) (measured from E_F). Measured SB of Pb films on different Si terminated surfaces. Comparison with values from Ref. [40]. Schottky barrier of the bare reconstruction obtained from Si 2p core-level shifts.*

We find in Pb/Pb/Si(111) experimentally the largest Schottky barrier of (0.65 ± 0.07) eV and the smallest for Pb/Ag/Si(111) with (0.53 ± 0.06) eV, both values in good agreement with those reported in [40]. For Pb/Bi/Si(111) we obtain an intermediate barrier of (0.58 ± 0.07) eV.

We now discuss the barriers of the reconstructed systems, i.e. without the ultra-thin Pb film on top, as determined from the Si 2p core-level shifts. Interestingly we observe for the bare reconstructions similar trends as for systems containing a Pb overlayer. Specifically we obtain for

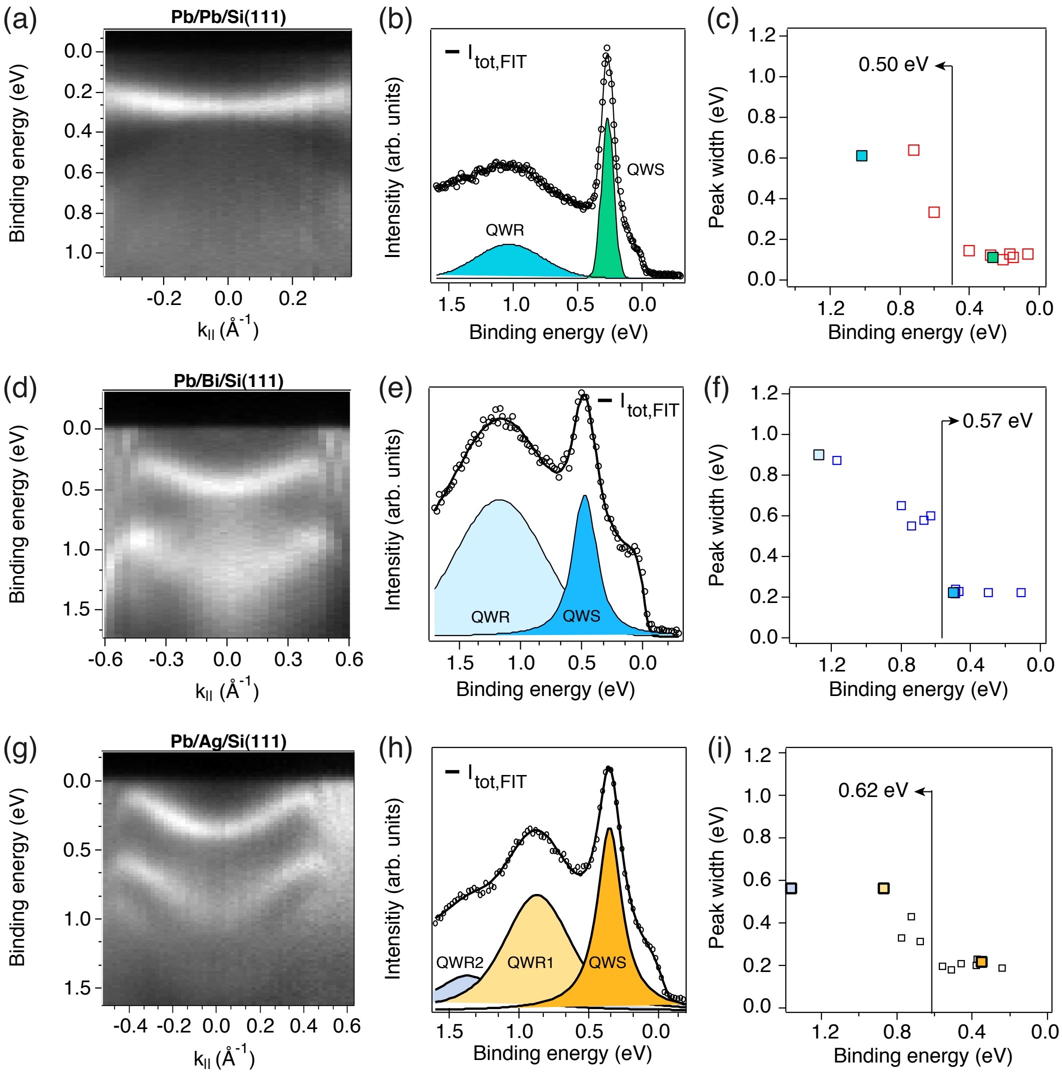

Figure 25: *(a) Band dispersion of 10 ML Pb deposited on top of Pb/Si(111). (b) Energy distribution curve at* $k_{\|} = 0$ *Å*$^{-1}$ *together with an intensity fit. (c) Peak widths of states as a function of binding energy. The position of the valence band edge is marked as a vertical line. (d) Band dispersion of 11 ML Pb on Bi/Si(111) and (e) the corresponding normal emission spectrum with a fit. (f) Peak widths of QWS and QWR for Pb/Bi/Si(111) as a function of* E_b*. (g) Band dispersion of 15 ML Pb on Ag/Si(111). (h) Intensity fit of the energy distribution curve at* $\overline{\Gamma}$*. (i) Peak widths of QWS and QWR on Ag/Si(111). Colored symbols in (c, f, i) represent the states in (b, e, h).*

Pb-$\sqrt{3}(\alpha)$ (4/3 ML) an exceptionally large barrier of 1.27 eV. Similar large values of 1.09 eV and 0.97 eV were reported by J. A. Carlisle *et al.* [82] and by Le Lay and co-workers [111], respectively. The discrepancy of 0.18 eV between our measured and the value reported in [82] may arise from the different sample fabrication procedures (deposition at elevated T_s) and measurement conditions (room temperature). Interestingly S. Ossicini and F. Bernardini published a theoretical work in 1992 [114] investigating the electronic structure of the Pb-Si interface. They computed a Schottky barrier of 0.6 eV assuming an unreconstructed interface, i.e. Pb-Si(111)-(1×1) with one Pb atom per unit cell. This value is very close to our experimental value, although their system was built up of only one monolayer of Pb on Si(111). We believe that this is an indication that the $\sqrt{3}$ reconstruction undergoes a structural transition upon deposition of Pb adlayers on top. Later, we will provide another indication based on the spin texture of this system. For the Bi-$\sqrt{3}$ reconstruction we find a barrier of 0.83 eV - a difference by 0.25 eV with respect to Pb/Bi/Si. Remarkably this difference is close to the measured core-level shift of 0.35 eV (to lower E_b) of the Bi 5d states upon deposition of Pb on the interface indicating a lowering of the SB. We find the smallest difference of 0.11 eV between Ag-$\sqrt{3}$/Si(111) and Pb/Ag/Si(111). In Ref. [115] the authors determined a Schottky barrier of 0.5 eV for the Ag-$\sqrt{3}$ reconstruction using scanning tunneling spectroscopy (STS). This implies that further deposition of Pb does not change the interface reconstruction significantly. In other words, the interaction between the Pb film and the Ag reconstructed Si surface is small.

From the barriers determined with quantum well spectroscopy we can draw the schematic energy vs. position diagram of each system using the work function of bulk Pb $\Phi_{Pb} = 4.25$ eV [116] and the electron affinity of Si, $\chi = 4.05$ eV [117], see Fig. 26.

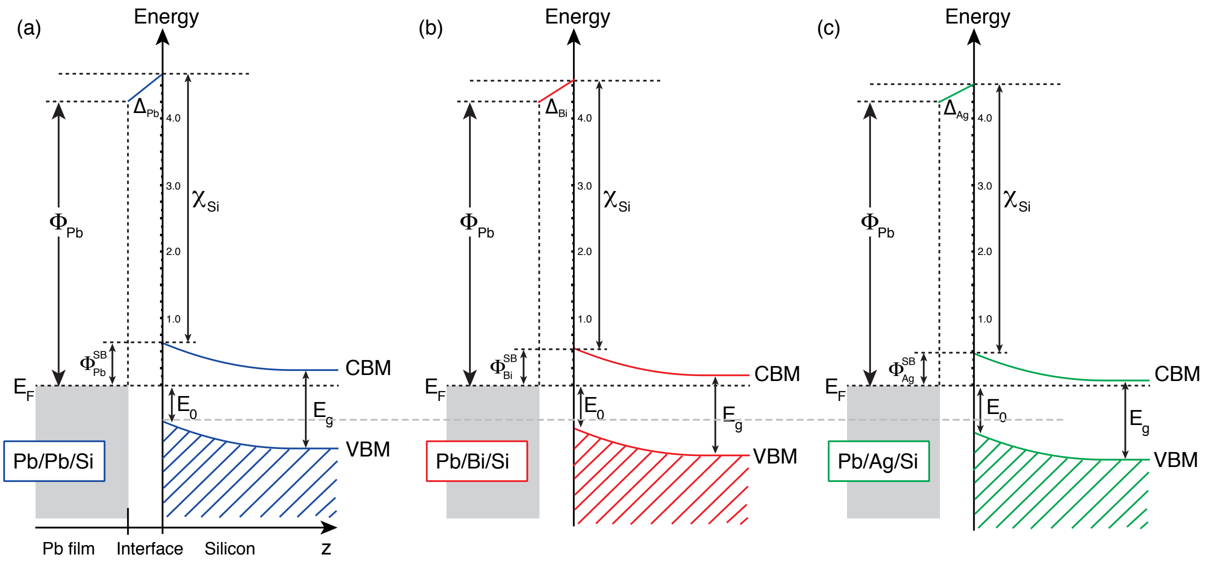

Figure 26: *Energy diagrams of the measured Pb films with different interfactants (a) Pb, (b) Bi, and (c) Ag. Notice that the z direction is not in scale.*

We obtain for Pb/Pb/Si(111) the largest dipole contribution to the SB of size $\Delta_{Pb} = 450$ meV. For Pb/Bi/Si(111) the dipole reduces to $\Delta_{Bi} = 380$ meV and for Pb/Ag/Si(111) we compute $\Delta_{Ag} = 330$ meV. To understand the size of the dipoles it is common to compare the electronegativitiy of the compounds using the *Miedema*[11] electronegativity [107, 118], see Fig. 27 (a).

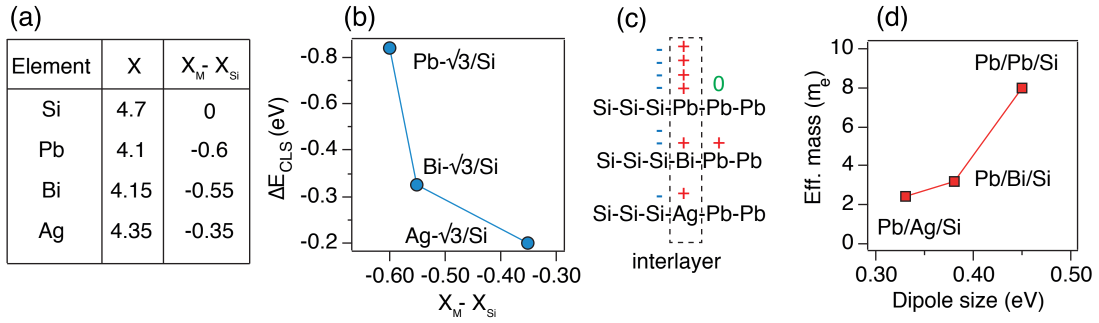

(a)

Element	X	$X_M - X_{Si}$
Si	4.7	0
Pb	4.1	-0.6
Bi	4.15	-0.55
Ag	4.35	-0.35

Figure 27: *(a) Miedema electronegativity and difference in electronegativity between the metal and the Si atom. (b) Si* 2*p core-level shifts determined from experiments as a function of difference in the electronegativity. (c) Schematic representation of charging states at the semiconductor-interlayer-metal interfaces. (d) Effective mass of* $6p_z$ *derived sub-bands in Pb films on various interfactants as a function of the size of the interface dipole.*

In general, the difference in electronegativity of two atoms describes the character of the bond; the larger the difference the more polar is the bond. If both atoms have similar electronegativity the bond is said to be covalent. We find the largest difference in Pb-Si and the smallest in Ag-Si. Interestingly, this tendency is also reflected in the measured Si $2p$ core-level shifts of the bare reconstructions as shown in Fig. 27 (b); the larger $(|X_M - X_{Si}|)$, the larger is ΔE_{CLS}. These findings nicely agree with the initial state model using Kopman‘s theorem [119]. That is, the binding energy of a core-level state is determined by the attractive Coulomb potential from the nuclear charge and a repulsive part from all other electrons. From this model one expects a shift toward lower binding energies ($\Delta E_{CLS} < 0$), when the atom accumulates negative charge. This is exactly what we observe. In Fig. 27 (c) we plot a schematic representation of atomic layers making up the semiconductor-interlayer-metal interface together with the charge states. Although the following statement remains speculative, but there is a correlation between the size of the interface dipole and the effective mass as shown in Fig. 27 (d). The nonlinear dependence of $m^\star$ as a function of the dipole size may reflect the discussed amplification effect through the hybridization with the $6p_{x,y}$ derived bands.

4.8 Conclusions

- **Bi interface**
  The influence of the Bi interface on the in-plane dispersion of $6p_z$ derived QWS has been studied with ARPES and LEED experiments and DFT calculations. In contrast to Pb/Pb/Si(111) we find: *i*) no effective masses larger than 4 m_e and *ii*) no significant dependence of the effective mass on the layer thickness. Compared to Pb/Pb/Si(111) the dispersion of $6p_z$ derived

---

[11] The Miedema electronegativity is derived for applications involving layers of material on semiconductors.

states in Pb/Bi/Si(111) is enhanced. With LEED we could confirm that in Pb/Pb/Si(111) the in-plane lattice constant of the ultra-thin film decreases with coverage in a similar manner as the effective mass. This is fully consistent with our DFT calculations and the corresponding picture of orbital overlap; the reduced overlap of the $6p_z$ orbitals reduces the dispersion, simultaneously the band width of the $6p_{xy}$ derived states is reduced. Together these effects alter the hybridization between the $6p_z$ and $6p_{xy}$ derived bands and cause the change from electron-like to hole-like dispersion to shift to lower $|\mathbf{k}_{\|}|$. Furthermore the in-plane lattice constant of a Pb film on the Bi reconstructed interface is smaller compared to a film of similar coverage on the Pb reconstructed interface, which is also reflected in the effective mass.

- **Ag interface**
  On the Ag interface the in-plane dispersion of $6p_z$ derived QWS is further enhanced compared with the Bi interface. For the same Pb thickness of 8 ML the effective mass reduces from 3.2 m_e to 2.4 m_e. Using the relation in Eq. 37 the smaller effective mass in Pb/Ag/Si is understood by a reduced in-plane lattice constant by 1.3% with respect to the in-plane lattice constant of the Pb film on $\sqrt{3}$-Bi/Si. The origin of this reduction is likely related to the size of the dipole at the interface, which is the smallest for Ag compared with the dipoles found at the Bi and Pb interface.

- **Schottky barrier and interface dipole**
  From our detailed analysis of the peak widths of QWSs and QWRs we have determined the Schottky barriers of the Pb films. We find the largest SB with (0.65 ± 0.07) eV for the Pb terminated Si(111) surface, and the smallest for the Ag interface with (0.53 ± 0.05) eV. Pb/Bi/Si(111) features an intermediate SB with (0.58 ± 0.06) eV being closer to the value found for Pb/Ag/Si. Based on the interface dipole model for Schottky barrier formation we could estimate the size of the dipoles. We find for the Pb interface the largest dipole. The dipole decreases in size when going from the Bi to the Ag interface, in line with the calculated electronegativity differences and measured core-level shifts.

5 Spin-orbit interaction in low dimensional systems

In this chapter we will derive the peculiar energy dispersion of a Rashba system and the corresponding spin texture. It will be shown that the Rashba Hamiltonian is derived from the relativistic Pauli equation with the canonical momentum $\mathbf{p}$ replaced by the crystal momentum $\mathbf{k}$, and the two-dimensional electron gas is subjected to an electric field normal to the plane of confinement while it moves field-free within the sample plane, i.e. $\mathrm{V}(\mathbf{r}) = \mathrm{V}(\mathrm{z})$. As a consequence the two-fold spin degeneracy of states is lifted and the free-electron-like dispersion of the 2DEG splits into two parabolas shifted in momentum apart from the $\overline{\Gamma}$ point. In the last part we will review important experiments in chronological order investigating spin-orbit coupling in low-dimensional systems. A particular emphasis is devoted to the Rashba effect in QWS.

5.1 Theoretical background

5.1.1 Atomistic spin-orbit coupling

The Schrödinger equation describes the motion of a *spinless* electron in an external potential. However, as a consequence of the Lorentz transformation, an electron moving with momentum $\mathbf{p} = \hbar\mathbf{k}$ experiences an electric field $\mathbf{E}$ of the nucleus as an effective magnetic field $\mathbf{B_{eff}}$ in the reference frame of the electron [121]:

$$\mathbf{B_{eff}} = \frac{1}{2m_e c}(\mathbf{p} \times \mathbf{E}) \tag{40}$$

Here m_e is the electron mass and c is the speed of light. The resulting interaction $(-\boldsymbol{\sigma} \cdot \mathbf{B_{eff}})$ of the spin with the generated field by the moving charge is correctly described within the frame of the Pauli equation, which is derived from the Dirac equation [120]. For a non-magnetic system, i.e. $\mathbf{B_{ext}} = 0$, only the spin-orbit coupling term survives as a correction to the Schrödinger equation [5]:

$$\left[-\frac{1}{2}\frac{\hbar^2}{m_e}\boldsymbol{\nabla}^2 + V(\mathbf{r}) - \frac{e\hbar}{(2m_e c)^2}\boldsymbol{\sigma} \cdot (\mathbf{E}(\mathbf{r}) \times \mathbf{p})\right]\psi_i = E_i\psi_i \tag{41}$$

where $\hbar$ is the reduced Planck constant, $\boldsymbol{\nabla}$ is the momentum operator in position basis, i.e. $\mathbf{p} = -i\hbar\boldsymbol{\nabla}$, $V(\mathbf{r})$ is an external potential, and $\boldsymbol{\sigma} = (\boldsymbol{\sigma}_x, \boldsymbol{\sigma}_y, \boldsymbol{\sigma}_z)$ denotes the spin operator with the Pauli matrices[12]:

$$\boldsymbol{\sigma}_x = \begin{pmatrix} 0 & 1 \\ 1 & 0 \end{pmatrix} \boldsymbol{\sigma}_y = \begin{pmatrix} 0 & -i \\ i & 0 \end{pmatrix} \boldsymbol{\sigma}_z = \begin{pmatrix} 1 & 0 \\ 0 & -1 \end{pmatrix} \tag{42}$$

The third term of Eq. 41, which describes the coupling between the spin-space $\boldsymbol{\sigma}$ and the crystal lattice via $\mathbf{E}(\mathbf{r})$ can be further rewritten assuming a spherically symmetric potential $V(r) = -Z/r$:

$$-\boldsymbol{\sigma} \cdot (\mathbf{E}(\mathbf{r}) \times \mathbf{p}) = \boldsymbol{\sigma} \cdot (\nabla V(\mathbf{r}) \times \mathbf{p}) = \frac{1}{r}\frac{dV(r)}{dr}\boldsymbol{\sigma} \cdot (\mathbf{r} \times \mathbf{p}) = \frac{1}{r}\frac{dV(r)}{dr}(\boldsymbol{\sigma} \cdot \mathbf{L}) = \xi\boldsymbol{\sigma} \cdot \mathbf{L}$$

---

[12] In this representation the quantization axis is along the z-direction.

where $\mathbf{L} = (\mathbf{r} \times \mathbf{p})$ is the orbital momentum operator and $\xi = \frac{1}{r}\frac{dV}{dr}$ is the spin-orbit coupling constant. A significant contribution is expected for electrons in high-Z elements because the Coulomb gradient is proportional to the atomic number Z, and for electrons that are close to the nucleus.

5.1.2 The Rashba-Bychkov effect

Solids are classified in terms of symmetry operations which leave the Hamiltonian describing a system invariant under application of a symmetry operation [122]. For non-magnetic systems the time-reversal operation reverses the wave vector $\mathbf{k}$ and spin $\mathbf{s}$ such that the energy of a right-moving electron with spin-up (↑) equals the energy of a left-moving electron with spin-down (↓):

$$\text{Time-reversal symmetry (TRS): } E(\mathbf{k},\uparrow) \;=\; E(-\mathbf{k},\downarrow) \tag{43}$$

Further in systems with inversion symmetry, i.e. $V(\mathbf{r}) = V(-\mathbf{r})$, the energy eigenvalue of a Bloch state should not depend, weather the state is moving to the left in a potential V or to the right:

$$\text{Inversion symmetry (IS): } E(\mathbf{k},\uparrow) \;=\; E(-\mathbf{k},\uparrow) \tag{44}$$

Notice that the spin is a pseudo vector and consequently a mirror operation: $\mathbf{r} \rightarrow -\mathbf{r}$, leaves the spin unchanged. Combining Eq. 43 with Eq. 44 leads to the so-called Kramers-degeneracy:

$$E(\mathbf{k},\uparrow) = E(\mathbf{k},\downarrow) \tag{45}$$

which states that (i) the band structure is symmetric with respect to the Brillouin-zone center, $\mathbf{k} = 0$, and (ii) all bands are doubly degenerate, i.e. each state is occupied by an spin-up and spin-down electron.

The spin degeneracy of bands may be lifted, either by breaking TRS or IS. Since the focus of this thesis is the study of systems without internal or external magnetic fields time-reversal symmetry holds. The lifting of spin degeneracy is then achieved whenever $V(\mathbf{r}) \neq V(-\mathbf{r})$ is fulfilled. In systems with a unit cell lacking an inversion center, e.g. zinc blende structures, the lifting of the degeneracy of bands is described by the so-called Dresselhaus effect [9]. For systems lacking of a structural inversion symmetry the lifting of the spin degeneracy is described by the Rashba-Bychkov model [8, 123]. Since both Pb and Si have inversion-symmetric unit cells (the unit cell of Pb is cubic and Si crystallizes in the diamond structure) breaking of IS is due to the presence of the metal-vacuum and the metal-substrate interface which naturally breaks the space inversion symmetry along the growth direction. In the following we will therefore only consider the Rashba effect.

The Hamiltonian of a two-dimensional electron gas (2DEG) confined within the (x, y)-plane and subjected to an electric field along the z-direction $\mathbf{E} \;=\; E\mathbf{e_z} = E(0,0,1)$ is:

$$\begin{aligned} H &= H_0 + H_{RB} \\ &= \frac{(\hbar \mathbf{k}_{\|})^2}{2m^\star} + \alpha_{RB}(\mathbf{e_z} \times \mathbf{k}_{\|}) \cdot \boldsymbol{\sigma} \end{aligned} \tag{46}$$

Here $m^\star$ is the effective mass, $\mathbf{k}_\parallel = (k_x, k_y)$ is the in-plane wave vector of a Bloch state and α_{RB} the Rashba constant, which is a measure for the size of spin-orbit coupling in the 2DEG. The Rashba Hamiltonian can be rewritten into:

$$H_{RB} = \alpha_{RB} \det \begin{pmatrix} 0 & 0 & 1 \\ k_x & k_y & 0 \\ \boldsymbol{\sigma}_x & \boldsymbol{\sigma}_y & \boldsymbol{\sigma}_z \end{pmatrix} = \alpha_{RB}(k_x \boldsymbol{\sigma}_y - \boldsymbol{\sigma}_x k_y) \tag{47}$$

Using $k_j = -i\frac{\partial}{\partial j}$, $j = x, y$ and the Pauli-matrices (Eq. 42) we obtain a (2×2) matrix representation of the Hamiltonian of a 2DEG including the kinetic and the Rashba term:

$$H = \begin{pmatrix} -\frac{\hbar^2}{2m^\star}(\frac{\partial^2}{\partial x^2} + \frac{\partial^2}{\partial y^2}) & -\alpha_{RB}\frac{\partial}{\partial x} + i\alpha_{RB}\frac{\partial}{\partial y} \\ +\alpha_{RB}\frac{\partial}{\partial x} + i\alpha_{RB}\frac{\partial}{\partial y} & -\frac{\hbar^2}{2m^\star}(\frac{\partial^2}{\partial x^2} + \frac{\partial^2}{\partial y^2}) \end{pmatrix} \tag{48}$$

The Eigenfunctions are written as a product of a plane wave $(\phi_{k_\parallel}(\mathbf{r}_\parallel))$ and a spin function $(\chi^\pm)$ where $\mathbf{k}_\parallel = k_\parallel(\cos\varphi, \sin\varphi, 0)$ (φ measures the angle between the x-axis and the momentum) and $\mathbf{r}_\parallel = (x, y)$ [5]:

$$\begin{aligned} \psi_{\pm k_\parallel}(\mathbf{r}_\parallel) &= \phi_{k_\parallel}(\mathbf{r}_\parallel)\chi^\pm \\ &= \exp i(k_x x + k_y y)\frac{1}{\sqrt{2}}\begin{pmatrix} ie^{i\varphi/2} \\ \pm e^{i\varphi/2} \end{pmatrix} \end{aligned}$$

For non-trivial solutions we find the energy dispersion from solving:

$$\begin{aligned} 0 &= \det(\mathbf{H}\psi - E\mathbf{I}) \\ 0 &= \det\begin{pmatrix} \frac{\hbar^2}{2m^\star}(k_x^2 + k_y^2) - E & -\alpha_{RB}\hbar(ik_x + k_y) \\ \alpha_{RB}(ik_x - k_y) & \frac{\hbar^2}{2m^\star}(k_x^2 + k_y^2) - E \end{pmatrix} \\ \rightarrow E^\pm(\mathbf{k}_\parallel) &= \frac{\hbar^2}{2m^\star}(k_x^2 + k_y^2) \pm \alpha_{RB}\sqrt{k_x^2 + k_y^2} \\ &= \frac{\hbar^2 {\mathbf{k}_\parallel}^2}{2m^\star} \pm \alpha_{RB}|\mathbf{k}_\parallel| = \frac{\hbar^2}{2m^\star}\left(\mathbf{k}_\parallel \pm \mathbf{k_0}\right)^2 \end{aligned} \tag{49}$$

where ± denotes the spin-up and -down state with respect to the quantization axis, $\mathbf{I}$ is the identity matrix, and k_0 is the characteristic momentum offset (see Fig. 28 (b)). The spin polarization $\mathbf{P}$ is a three-dimensional vector and defined as the expectation value of the spin operator $\mathbf{S} = \frac{\hbar}{2}\boldsymbol{\sigma}$ [124]:

$$\mathbf{P}^\pm(\mathbf{k}_\parallel) := \psi^\dagger_{\mathbf{k}\pm}\mathbf{S}\psi_{\mathbf{k}\pm} = \pm\frac{\hbar}{2}\begin{pmatrix} \sin\varphi \\ -\cos\varphi \\ 0 \end{pmatrix} \tag{50}$$

with the components

$$P_x^\pm = \mp\frac{k_y}{|\mathbf{k}|}, \quad P_y^\pm = \pm\frac{k_x}{|\mathbf{k}|}, \quad P_z^\pm = 0 \tag{51}$$

Several conclusion can be drawn from these results which are also visualized in Figure 28.

(a) The Rashba effect lifts the two-fold spin degeneracy of states with $\mathbf{k}_{\|} \neq 0$ by splitting the free-electron-like parabola into two branches that are oppositely shifted in momentum by the offset k_0 with respect to the high symmetry point $\overline{\Gamma}$. The state at $\overline{\Gamma}$, i.e. at $\mathbf{k}_{\|} = 0$, is doubly degenerate.

(b) The Rashba parameter $\alpha_{RB} = \hbar^2 k_0/m^\star$ is a measure of the size of SOI and is proportional to an average electric field or potential gradient, i.e. $\alpha_{RB} = \frac{e\hbar^2}{(2m^\star c)^2}\langle\, E_z \,\rangle \propto \langle \frac{\partial V}{\partial z} \rangle$.

(c) The spin or energy splitting $\Delta E := E_+(\mathbf{k}_{\|}) - E_-(\mathbf{k}_{\|}) = 2\alpha_{RB} k_{\|}$ is linear in $k_{\|}$.

(d) The momentum splitting between the spin-polarized bands is $\Delta k = 2k_0$.

(e) $\mathbf{P}_{\pm}(\mathbf{k}_{\|}) \cdot \mathbf{k}_{\|} = 0$, i.e. the polarization vector is perpendicular to the momentum.

(f) $\sum_{-\mathbf{k}_{\|}}^{+\mathbf{k}_{\|}} \mathbf{P}(\mathbf{k}_{\|}) = 0$, i.e. the net spin polarization is zero when averaged over all states.

(g) A Rashba system has no global quantization axis, such as magnetic systems. Moreover the quantization axis is a function of the momentum $\mathbf{k}_{\|}$ and the electric field E_z.

(h) The spin polarization vector lies fully in-plane for $\mathbf{E} = E(0, 0, 1)$.

(i) The helicity of the spin texture (lower panels of Figs. 28 (b, c)), i.e. the sense of rotation of the inner and outer circle, respectively, depends on the sign of the Rashba constant which in turn depends on the sign of the effective mass and on the sign of the momentum offset k_0.

The peculiar band splitting and the corresponding tangential alignment of the spins to the isotropic energy contour, as shown in Fig. 28 (a), is valid for an idealized 2DEG. Today, many systems show deviations from this model, which manifest themselves in non-isotropic Fermi surfaces and the appearance of an out-of-plane polarization P_z. The origin of this component can be an in-plane structural asymmetry resulting in additional in-plane electric field components E_x and E_y. The latter produce, in the rest frame of the electron, an effective B-field that is no longer purely in-plane, but also has a z-component to which the spin aligns.

Another origin of P_z has been discussed by L. Fu in Ref. [125] based on crystal symmetry arguments. Motivated by ARPES results from the 3D topological insulator Bi_2Te_3 [126], L. Fu proposed a Hamiltonian, which includes a term that is the counterpart of the cubic Dresselhaus spin-orbit coupling in rhombohedral structures:

$$H(k) = \frac{k^2}{2m^\star} + v_k(k_x\sigma_y - k_y\sigma_x) + \frac{\lambda}{2}(k_+^3 + k_-^3)\sigma_z \tag{52}$$

with v_k as the Dirac velocity and $k_\pm = k_x \pm ik_y$. The first two terms are the spinless part and the Rashba term, while the last part explains the hexagonal warping of the Dirac-like band and the appearance of a z-component in the spin polarization.

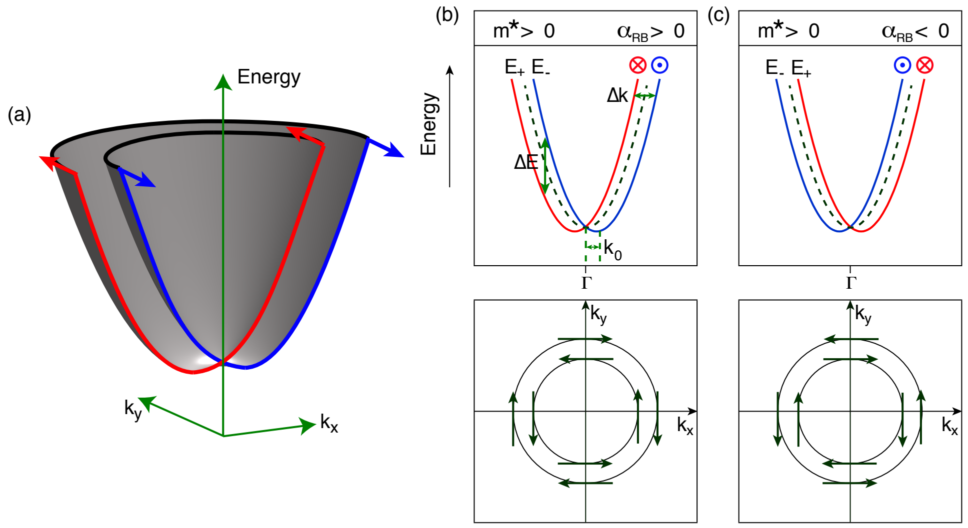

Figure 28: *(a) Schematic drawing of the two-dimensional energy dispersion of a 2DEG with electron-like dispersion, i.e.* $m^\star > 0$ *and Rashba-type spin-orbit splitting where* $\alpha_{RB} > 0$*. For each* $\mathbf{k}_{||}$ *the spins are tangentially aligned to the constant energy contour. (b, c) (upper panel) Dispersion of the 2DEG with (b)* $m^\star > 0$ *and* $\alpha_{RB} > 0$ *and (c)* $m^\star > 0$ *and* $\alpha_{RB} < 0$*. The lower panels show the corresponding spin texture at* E_F*.*

5.2 Review of spin-orbit interaction

The discovery of spin-split surface states on the non-magnetic high-Z metal surface Au(111) by La Shell *et al.* in 1996 [127], confirmed in 2001 by Nicolay *et al.* [128] by means of high-resolution photoemission spectroscopy, has triggered a research field in condensed matter physics investigating spin-orbit interaction (SOI) in surfaces. Both groups correctly interpreted the spin splitting as due to SOI of the surface state. In 2004 the spin splitting of the surface state was unambiguously verified by M. Hoesch *et al.* [129, 130] by means of spin- and angle-resolved spectroscopy using the COPHEE spectrometer. Nowadays Au(111) can be seen as the *drosophila* in this field where the spin splitting is described within the framework of the Rashba effect.

The size of the spin splitting found for Au(111), described by the Rashba parameter α_{RB}, was unexpectedly large. This is because one of the key-ingredients to induce the Rashba effect in a 2DEG is the presence of an electric field or potential gradient which directly contributes to the size of spin splitting, see conclusion (b) of section 5.1.2. At a crystal surface where the inversion symmetry along the surface normal is broken, a candidate for this field would be naturally the work function of the metal divided by the Fermi wavelength, i.e. $E_z = \Phi/\lambda_F$. For Au(111) this yields a Rashba parameter in the order of μeV and hence several orders of magnitude smaller than determined from the experiment. So what has been missed to correctly describe the strength of the Rashba effect?

The solution to the problem came from L. Petersen and P. Hedegård already in 2000 [131] and was expanded by G. Bihlmayer in his work published in 2006 [132]. Since surface states are derived from atomic levels the atomistic spin-orbit coupling (see Sec. 5.1.1) must play a significant role which scales with Z - the atomic number. Further, the size of the spin splitting is essentially determined by the asymmetry of the wave function near the nucleus. This asymmetry is caused by the lack of inversion symmetry and depends on the mixing ratio of the l and $l+1$ spherical components of which the wave function is composed, i.e. $\psi_{nk} = \psi_{nk,s} + \psi_{nk,p} + \psi_{nk,d}$ with s, p, and d as the orbital parts (n labels the band index and k is the momentum) [133].

5.2.1 Spin splitting in surface states due to SOI

To date, the lifting of spin degeneracy in surface states due to SOI has been found for many low-dimensional and non-magnetic systems [22]. Here we will review the most important achievements in this field in chronological order, as illustrated in Figure 29.

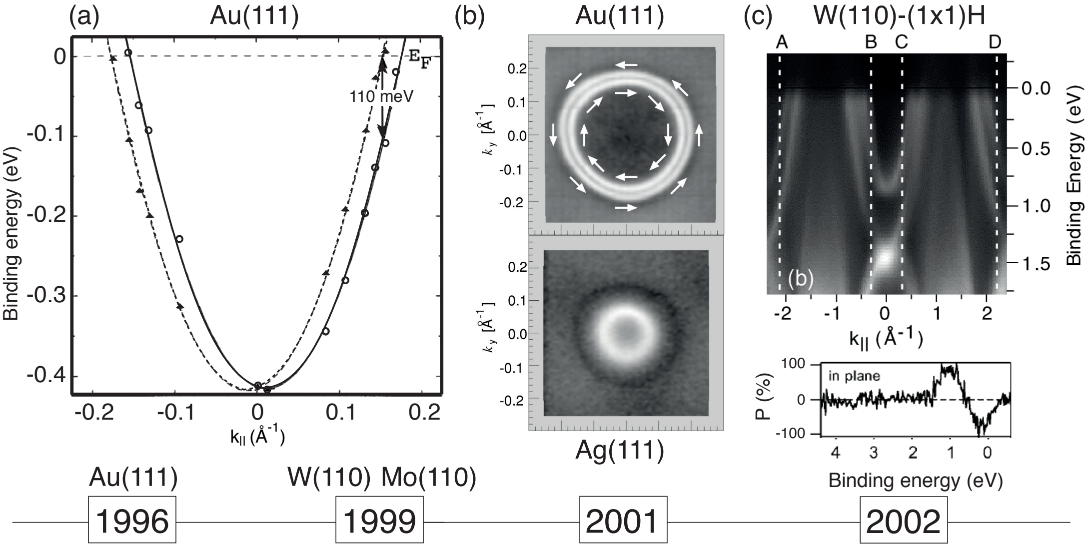

Figure 29: *(a) Proposed band splitting of the spin-orbit split surface state of Au(111) (from Ref. [127]). (b) Fermi surface contours of Au(111) and Ag(111). Due to the small atomic number ($Z_{Ag} = 47$) of Ag the two characteristic contours are not resolvable (from Ref. [128]). (c) (upper panel) band dispersion along $\overline{\Gamma}$-$\overline{S}$ in W(110)-(1×1)H and (lower panel) tangential polarization as a function of binding energy along the section in reciprocal space indicated by D (from Ref. [134]).*

The starting point was Au(111) in 1996 as mentioned before. In 1999 E. Rotenberg *et al.* interpret the d-derived surface state in the projected bulk band gap of W(110) being spin-split due to SOI and showed that the size of the spin splitting is greatly reduced for a surface state of the same symmetry on Mo(110) [135]. This finding indicates that the strength of SOI depends on Z, because for Tungsten $Z_W = 74$ and for Molybdenum $Z_{Mo} = 42$. The same argument applies for the study of surface states on Au(111) and Ag(111) done by G. Nicolay *et al.* [128] in 2001 as shown in Fig. 29 (b). While for Au(111) two concentric circles at the Fermi-energy can be clearly distinguished, for Ag(111) the momentum splitting ($\Delta k = 2k_0$) due to SOI is so small that it cannot be resolved with photoemission spectroscopy. One year later M. Hochstrasser *et al.* investigated for the first time surface states in W(110)-(1×1)H by means of SARPES (see Fig. 29 (c)) and demonstrated that the spin is oriented tangentially to the energy contour in the fashion of the Rashba effect [134].

In 2004 M. Hoesch *et al.* verified the spin texture of Au(111), as shown in the upper panel of Fig. 29 (b), using for the first time the COPHEE spectrometer for spin- and angle-resolved photoemission spectroscopy [129,130]. In the same year Y. M Koroteev *et al.* set a new benchmark in the size of spin-orbit interaction in surface states on low-index surfaces of Bi [136]. Although the dispersion of the states is far from being isotropic, in contrast to the surface state in Au(111), the Rashba parameter was almost doubled ($\alpha_{RB,Au} = 0.33$ eVÅ and $\alpha_{RB,Bi} = 0.56$ eVÅ). The enhanced SOI was understood by the three times larger atomic spin-orbit splitting of Bi. In 2006 K. Sugawara *et al.* [138] have shown that also in low-Z materials, such as Sb with $Z_{Sb} = 51$, a considerable band splitting of the surface state can exists. In 2009 this band splitting due to SOI has been confirmed with SARPES by D. Hsieh *et al.* [139] and the resulting size of the momentum splitting has been quantitatively estimated to be $\Delta k = 2k_0^{Sb} = 0.03$ Å^{-1}, and therefore slightly larger than the momentum splitting in the surface state on Au(111) with $\Delta k^{Au} = 0.026$ Å^{-1} [130]. These findings indicate the second requirement to observe large SOI, namely that the atomic structure of the surface and sub-surface layers is also relevant. For group V elements (Sb, Bi),

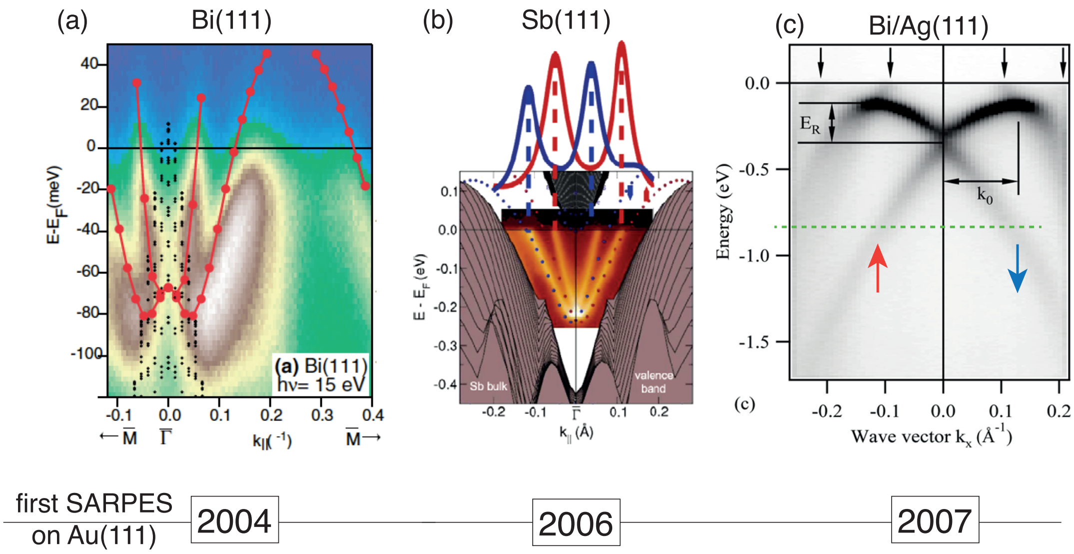

Figure 30: *(a) Band dispersion of surface states in Bi(111) together with DFT calculations including SOI (from Ref. [136]). (b) Band dispersion of surface states in Sb(111) together with spin-resolved intensities projected on a quantization axis perpendicular to the in-plane momentum. (from Ref. [22]). The spin splitting into alternating directions (up-down-up-down) is a clear indication of SOI. (c) Band dispersion of the surface alloy Bi/Ag(111) (from Ref. [137]).*

which crystallize in a rhombohedral structure the corrugation of the surface is larger than for fcc crystals such as Au(111). The resulting buckling of atoms in the surface layer, as experimentally verified with IV-LEED [140], enhances the l and $(l+1)$ ratio of the surface state wave function.

The discovery of a giant Rashba-type spin splitting in the long-range ordered $(\sqrt{3} \times \sqrt{3})R30^\circ$ - Bi/Ag(111) surface alloy by C. Ast *et al.* in 2007 [137] has stimulated both theory and experiment. One reason was that the size of the Rashba constant in Bi/Ag(111) ($\alpha_{\mathrm{RB}}^{\mathrm{Bi/Ag}} = 3.05$ eVÅ) is approximately six times larger than the one found for the surface state on Bi(111). At a first glance this is surprising since none of these materials, neither Ag nor Bi, have spin splittings of comparable sizes. However, the surface atomic structure of the alloy is highly corrugated with an outward relaxation of the Bi atoms as far as $\Delta z = 0.65$ Å [137]. Based on similar arguments the reduced spin splitting in the surface alloys Pb/Ag(111) ($\alpha_{\mathrm{RB}}^{\mathrm{Pb/Ag}} = 1.42$ eVÅ) and Sb/Ag(111) ($\alpha_{\mathrm{RB}}^{\mathrm{Sb/Ag}} = 0.36$ eVÅ) is understood by a smaller corrugation. While in Pb/Ag the Pb atoms are pushed outwards by $\Delta z_{Pb} = 0.46$ Å [141, 142], in Sb/Ag(111) the corrugation reduces to $\Delta z_{Sb} = 0.1$ Å [143, 144].

A further step towards the understanding of the Rashba effect in alloys have been achieved by F. Meier *et al.* by means of SARPES [145]. Figure 31 (a) shows a spin-resolved momentum distribution curve measured on Bi/Ag(111) along the dashed line displayed in Fig. 30 (c). The authors confirmed the large Rashba-type spin splitting for Bi/Ag(111) and for Pb/Ag(111) and found that some states show also large out-of-plane rotation of the spin polarization vector. As discussed in Sec. 5.1.2, the origin of the P_z component is a structural in-plane asymmetry due to the corrugated surface.

Later, it has been demonstrated that it is also possible to form mixed binary and ternary surface alloys with tunable physical properties. For instance, combining Bi and Pb to the binary alloy $\mathrm{Bi}_x\mathrm{Pb}_{x-1}$/Ag(111) results in a 2DEG with a tunable spin splitting and Fermi energy through the Bi concentration [148, 149]. In $\mathrm{Bi}_x\mathrm{Sb}_{x-1}$/Ag(111) it is possible to tune only the Rashba-type spin splitting [150] while the energetic position of the Fermi level is largely unaffected. Finally, in the ternary alloy $\mathrm{Bi}_x\mathrm{Pb}_y\mathrm{Sb}_{1-x-y}$/Ag(111) it is possible to tune both the spin splitting and the Fermi energy independently, which makes this system an interesting candidate to study transport properties because they are determined by the spin texture at the Fermi surface [150, 151].

In Section 5.1.2 the origin of a P_z component has been discussed within the model proposed by L. Fu [152] which includes the symmetry properties of the material. A nice experimental verification of this model has been performed by S. Y. Xu *et al.* in 2011 [146] and shown in Fig. 31 (b) by the example of the three-dimensional topological insulator BiTlSe_2. The energy contour of the 2DEG changes continuously its shape as a function of energy away from the Dirac point; from circular to hexagonal and to a snowflake-shaped Fermi surface. This change is accompanied by an evolution of an out-of-plane polarization that increases with increasing warping, i.e. is maximal at the Fermi surface.

Very recently, P. Höpfner *et al.* have discovered a complex spin texture at the surface of Au/Ge(111) [147], see Fig. 31 (c). Beside the helical Rashba-type alignment of the in-plane spins, this system features large out-of-plane polarizations being maximal along the $\overline{\Gamma}$-$\overline{\mathrm{M}}$ directions of the

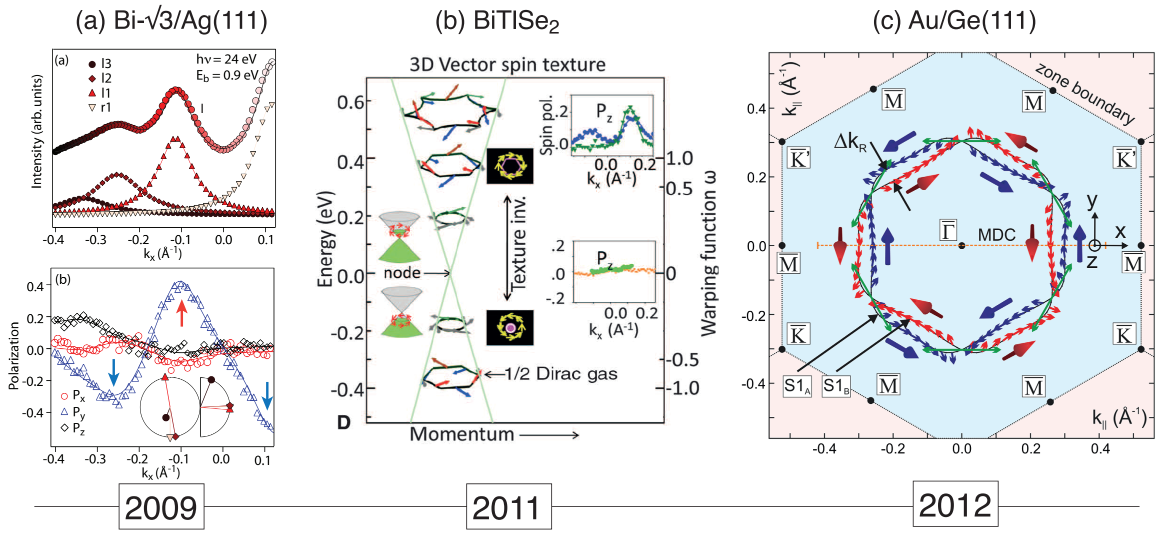

__Figure 31:__ (a) Spin-resolved momentum distribution curve measured on the alloy Bi/Ag(111). The measurement indicates that the state (labeled as l3) at large negative momenta possesses considerable out-of-plane spin polarization (adapted from Ref. [145]). (b) Spin texture of the 3D topological insulator BiTlSe$_2$ as a function of energy (from Ref. [146]). Spin texture of the surface reconstruction of Au/Ge(111) at the Fermi energy (from Ref. [147]).

$(\sqrt{3} \times \sqrt{3})$R30° surface reconstruction. Furthermore, for the first time also radial rotations of the in-plane spins at the corners of the hexagonal Fermi surface have been measured. The rich spin texture results from crystalline anisotropies that are described by a model Hamiltonian that includes not only a Rashba- and a Fu-term, but also sixth-order corrections in k in the spinless term and additional fifth-order term in k to describe the radial rotations of the in-plane polarization [153], see also supplementary online material of Ref. [147].

All here reviewed systems have in common that the spin splitting due to SOI is well described by the Rashba effect. Some refinements of the model, as shown for e.g. Au/Ge(111), need to be incorporated when the interaction in the 2DEG is strongly affected by the crystal potential.

5.2.2 Substrate-induced spin splitting

M. Shikin *et al.* investigated in 2008 [154] the question whether spin splitting of states due to spin-orbit interaction is induced by potential gradients e.g. at the metal-substrate interface and/or at the metal-vacuum interface or by atomic fields in the overlayer material or in the substrate material. For this purpose a systematic study of QWS in monolayers of a high-Z and low-Z material prepared on a high-Z and low-Z substrate has been performed of which the results are shown in Figs. 32 (a, b). First of all, neither the states in Au nor in Ag show sizable spin splittings when grown on the low-Z molybdenum substrate with $Z_{Mo} = 42$. Second, the energy splittings are independent on the nuclear charge of the deposited material. Both in Ag with $Z_{Ag} = 47$ as well as in Au with $Z_{Au} = 79$ similar splittings are measured on the high-Z substrate tungsten with $Z_W = 74$. Both findings indicate that the spin splitting of spin-polarized states due to SOI is induced by the high-Z substrate. However, in contrast to the Rashba model the investigated states show a decrease of spin splitting with increasing in-plane momentum, which is due to a strong hybridization of the Au and Ag monolayer states with those of the W substrate. In a follow-up experiment of the same group, A. Varykhalov *et al.* [155] measured QWS in ultra-thin films of Au and Ag on W(110) for larger film thicknesses. Also here spin-orbit interaction induced spin splittings are independent on the overlayer material, as shown in the upper panel of Fig. 32 (c) and almost none of the investigated states show Rashba-like dependence of the spin splittings as a function of the in-plane momentum, see Fig. 32 (d). It is concluded that spin-orbit splitting of the quantum well states is due to Bragg scattering at the W-metal interface, because QWS outside of the symmetry gap of W(110) are not spin-split at all.

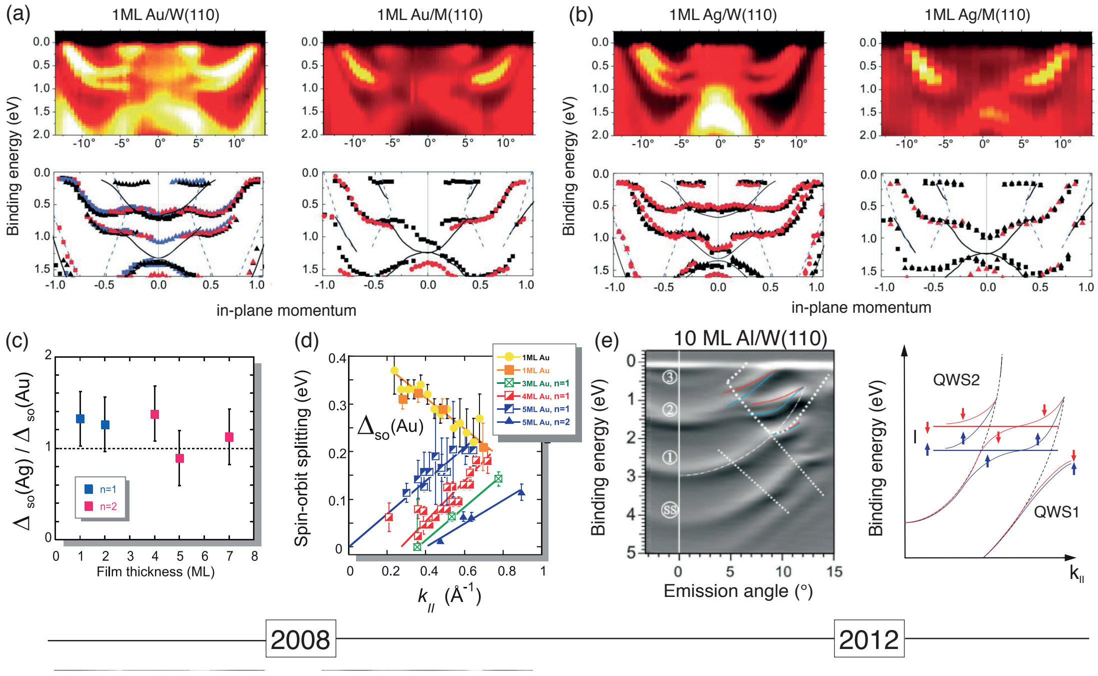

Figure 32: *(a) Experimental band structures of (left panel) 1ML Au on W(110) and (right panel) 1ML Au on Mo(110). (b) Measured band dispersion of (left panel) 1 ML Ag on W(110) and (right panel) 1 ML Ag on Mo(110) (from Ref. [154]). (c) Ratio of strength of SOI in QWS in Ag/W(110) and in Au/W(110). Although the ratio of the nuclear charge is $Z^{Au}/Z^{Ag} = 1.7$ both system experience almost the same spin splitting due to SOI. In the lower panel spin splittings as a function of parallel momentum are shown to prove whether a system behaves Rashba-like. Strictly speaking this is only fulfilled for the QWS with $n = 1$ in 5 ML of Au (from Ref. [155]). (c) Complex band splitting of subbands in Al on W(110) due to the spin-dependent avoided crossing with interface derived states (adapted from Ref. [156]).*

In 2012 A. G. Rybkin *et al.* [156] found that QWS in a low-Z material aluminum with $Z_{Al} = 13$ acquire large spin splittings through the interaction with spin-polarized interface states because of the avoided crossing hybridization. The left panel of Fig. 32 (e) shows band dispersion of 10 ML Al on W(110). A closer examination of the QWS with $n = 2$ shows that the free-electron-like dispersion suffers kinks at the border of the surface-projected band gap (dotted line) and within the gap a complicated band splitting evolves. The origin of the band splitting is a spin-dependent avoided crossing hybridization, which is sketched in the right panel of Fig. 32 (e) for the situation of two QWS that cross the only weakly dispersing interface states. Due to the Pauli exclusion states of the same symmetry and spin are not allowed to cross each other. As a result only bands with the same spin direction can hybridize in the vicinity of the crossing point. Because the spin-up (blue) band derived from the interface states is situated at lower energy, the spin-down band of the QWS continues its dispersion in the hybridization gap and hybridizes with the spin-down band of the interface states at higher energy. This leads to an enhanced spin splitting and the opening of hybridization gaps. A similar effect has been also found in the system of Ag films grown on Si(111) and covered with the $\sqrt{3}$-Bi alloy by K. He *et al.* [157] and by E. Frantzeskakis *et al.* [158]. Here the interaction of upward dispersing QWS and downward dispersing alloy derived states, both Rashba-type spin-split, leads also to a spin-dependent hybridization.

The band structure of Pb/Si contains also a momentum region where energy gaps are formed due to the avoided crossing hybridization between $6p_z$ and $6p_{x,y}$ derived states. In contrast to the mentioned studies, the hybridization is mediated by an interband spin-orbit coupling term that mixes states with opposite spin directions. For details see Chap. 7.

5.2.3 SOI in QWS induced by the high-Z film material

In 2008 Rashba-type spin-orbit interaction in the high-Z film material Pb ($Z_{Pb} = 82$) grown on the low-Z semiconductor Si ($Z_{Si} = 14$) has been discovered by H. Dil *et al.* [159]. In contrast to studies of Au/W(110) and Ag/W(110) the spin splitting in this system originates from the spin-orbit interaction in the ultra-thin film itself. Figure 33 (a) shows a band dispersion of a QWS formed in Pb/Pb/Si(111) measured in the spin-integrated mode of the COPHEE spectrometer. Apparently the spin splitting in this system is so small that the two characteristic Rashba parabolas, as schematically shown in Fig. 28 (b), cannot be resolved. The reason for the small α_{RB} will be discussed later. However, using the spin as an additional observable clearly resolves an energy splitting between the spin-up and spin-down state, as seen from Fig. 33 (d). Here we show spin-resolved intensities projected on the spin quantization axis along the x-direction which were calculated from the measured polarization curves (Figs. 33 (b-c)) using Eq. 13.

The Rashba model predicts a tangential alignment of the spins to the constant energy contour, as shown in Fig. 33 (g). This property is seen from the measured spin polarization curves that were taken in reciprocal space at $\mathbf{k}_{\parallel} = (k_x, k_y) = (0, -0.08)$ Å^{-1}, and displayed in Figs. 33 (b-c). Because for tangential spins the scalar product of the polarization and the momentum has to be zero, i.e. $\mathbf{P}_{\pm} \cdot \mathbf{k}_{\parallel} = 0$, only excursions in the x-direction are measured. The small measured polarization amplitude ($P < 10$ %, Fig. 33 (b)) results from the large overlap of bands with

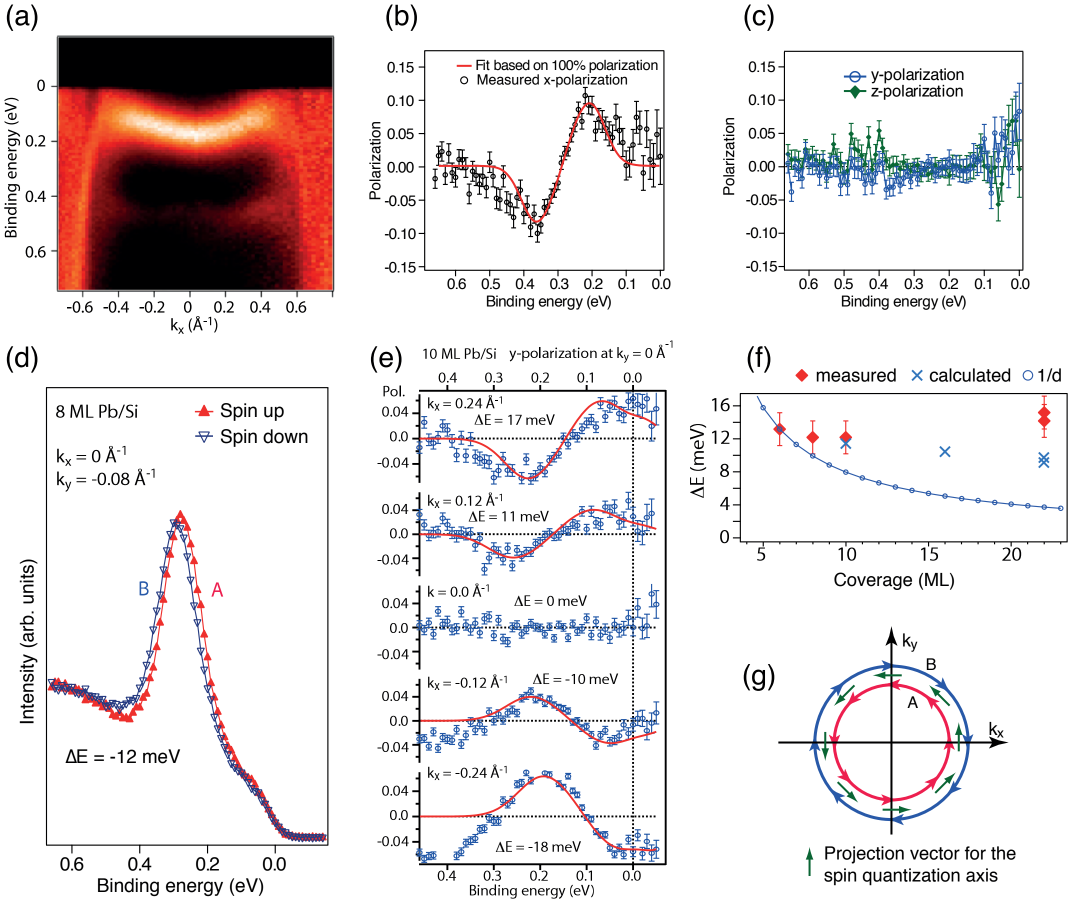

Figure 33: *(a) Band dispersion of QWS in 10 ML Pb on $\sqrt{3}$-Pb/Si(111). (b) and (c) show measured spin polarization curves for the three directions in the sample coordinate system at* $\mathbf{k}_{\|} = (k_x, k_y) = (0, -0.08)$ $Å^{-1}$. *The absence of excursions along y and z indicate Rashba-like behavior. (d) Spin-resolved energy distribution curve projected onto the quantization axis. (e) Spin polarization data taken at different in-plane momenta together with fits. (f) Energy splittings (ΔE) as a function of Pb thickness. (g) Spin texture of Pb QWS as revealed from the SARPES experiment (Figs. taken from Ref. [159])*

opposite spin direction and is a general property of Pb/Si due to the small spin splitting. Further indications of a Rashba effect are (i) the decrease of spin splitting with decreasing momenta, (ii) the spin splitting of states at the center of the (1 × 1) surface Brillouin zone, i.e. at $\mathbf{k}_{\|} = 0$, vanishes, and (iii) a reversal of the spin polarization curves when passing though $\overline{\Gamma}$. These properties are exactly fulfilled as seen from Fig. 33 (e) where a series of measured y-polarization curves at positive and negative in-plane momenta are shown together with fits. From these data the Rashba constant of Pb/Si(111) is deduced by plotting the energy splittings obtained from the two-step fit as a function of in-plane momentum and taking the half of the slope of the linear fit, see Fig. 34. Since the data presented in Fig. 33 (e) were measured with the COPHEE

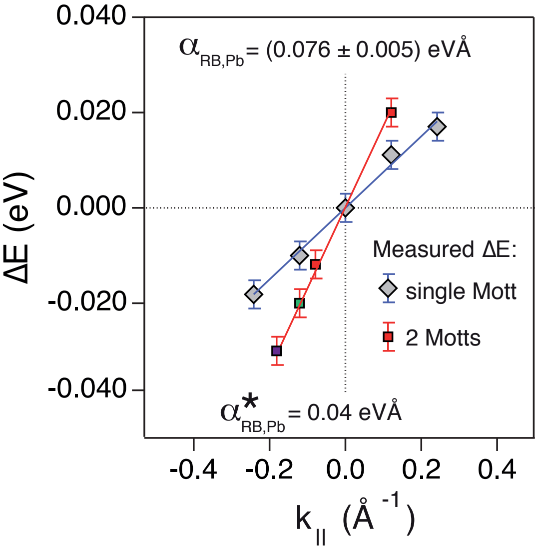

Figure 34: *Measured spin splittings (ΔE) as a function of in-plane momentum using the COPHEE spectrometer in single and two Mott mode, respectively. The single Mott measurement allows for a determination of the lower boundary of the Rashba constant ($\alpha^\star_{RB}$) (data points from Ref. [159]).*

spectrometer using one Mott detector (instead of two), only a lower boundary value for α_{RB} has been determined, i.e. $\alpha^\star_{RB,Pb} = 0.04$ eVÅ. In Fig. 34 we also included energy splittings obtained from SARPES measurements using two Mott detectors, which together are sensitive to all three polarization components. This way, we obtained a more precise value for the Rashba constant of $\alpha^\star_{RB,Pb} = (0.076 \pm 0.005)$ eVÅ [160]. Figure 35 clarifies the importance of using two Mott detectors to correctly determine spin splittings in a Rashba system showing a detailed analysis of spin-resolved EDCs for the two momenta $k_{\|} = -0.18$ Å^{-1} and $k_{\|} = -0.10$ Å^{-1} (also marked in Fig. 34)). As can be seen, at both momenta a Rashba-like polarization along the x- and y-direction is detected. The observed x-polarization is due to a constant sample tilt ($< 3°$), that (usually) cannot be corrected on our goniometer. Therefore the spin-resolved EDCs were taken at a fixed $k_y \neq 0$ Å^{-1} and for different values of k_x. The measured polarization along the x-direction is thus a direct consequence of $\mathbf{P}_\pm \cdot \mathbf{k}_{\|} = 0$. The vectorial fitting routine allows to determine the precise measurement position in the following way. From the fit we obtain the orientation of the spin polarization vector of each band that is defined by the spherical coordinates ϕ and θ. The measurement position in reciprocal space is then calculated according to:

$$\mathbf{k}_{\|} = \begin{pmatrix} k_x \\ k_y \end{pmatrix} = k_{\|} \begin{pmatrix} \sin\phi \\ \cos\phi \end{pmatrix} \tag{53}$$

For the polarization data shown in Figs. 35 (b, c) the fit gives $\phi_1 = 140°$ and $\phi_2 = 320°$ and for (e, f) $\phi_1 = 230°$ and $\phi_2 = 50°$. The polarization vectors are shown in Fig. 35 decomposed into the in-plane components (g) and into out-of-plane components (h) which are zero for all bands. In Figs. 35 (i, f) we show the precise measurement positions of the spin-resolved energy distribution curves that are $k_{\|} = -0.18$ Å$^{-1} = (-0.15, 0.1)$ Å^{-1} and at $k_{\|} = -0.10$ Å$^{-1} = (-0.08, 0.1)$ Å^{-1}, respectively[13].

---

[13] Notice that this procedure is only applicable for systems where the spin orientation is known to be tangentially to the constant energy contour.

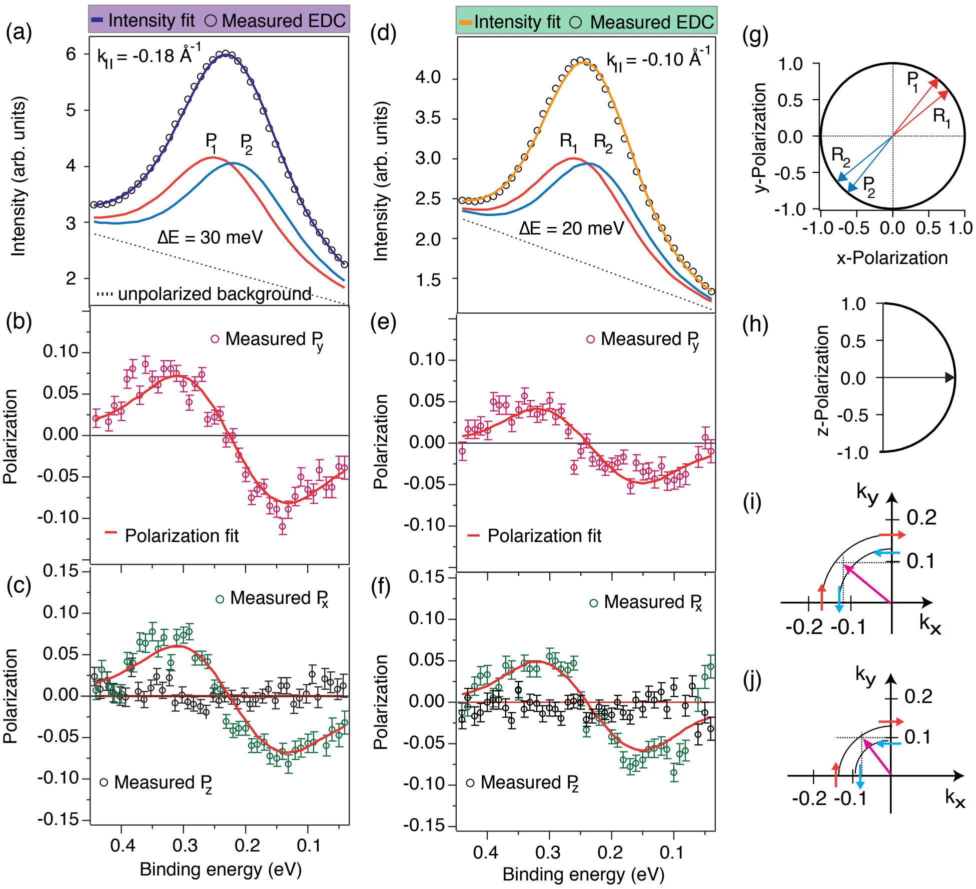

Figure 35: *SARPES data measured at* $k_{||}$ *= -0.18* Å^{-1} *(a-c) and at* $k_{||}$ *= -0.10* Å^{-1} *(d-f). (g) In-plane and (h) out-of-plane polarization vectors of the bands obtained from the two-step fitting routine. The absence of a z-polarization is a general property of Pb/Pb/Si(111). (i) and (j) show the precise measurement position of the spin-resolved EDCs in reciprocal space.*

Having shown that QWS in Pb/Si(111) are spin-split according to the Rashba model we now turn back to the results discussed in Ref. [159]. First, the sense of rotation of the inner and outer circle is reversed compared to the surface state of Au(111). Since both states have electron-like dispersions, i.e. $m_e > 0$, the reversal of the helicity originates from a sign change in the Rashba constant or more specifically from a sign reversal of k_0 (see conclusion (c) of Sec. 5.1.2). Figure 36 shows the results of an analysis of the spin texture of the surface state on Au(111). The band dispersion of the surface state is shown in Fig. 36 (a). We note that in contrast to the Fermi surface shown in the upper panel of Fig. 29 (b), the band splitting here is not resolvable in the spin-integrated mode due to the set resolution of the ARPES experiment. However, this is not relevant when discussing the spin texture. Figure 36 (b) displays a spin-resolved momentum distribution curve (SR-MDC) measured 40 meV below the Fermi level together with a fit that revealed a momentum splitting of $2k_0 = 0.03$ Å^{-1} and hence in good agreement with experimental values reported in Refs. [128,130,161]. Apart from the larger measured polarization amplitude (P ≈ 30%), which is due to the larger SOI. The bands split into an *up-down-up-down* spin configuration, which results in a spin texture (Fig. 36 (c)) that is inverted with respect to the spin texture of Pb/Si(111), compare with Fig. 35 (j). A comparison of the theoretical spin textures shown in Fig. 28 (b) and (c) with those revealed from the measurements yields a positive Rashba constant for Pb/Si(111) and a negative for the surface state of Au(111). This is in line with the sign of the slope of the linear fit to determine the Rashba constant of Pb/Si as shown in Fig. 34. Here the sign of the energy splitting at $k_{\|} > 0$ is defined via $\Delta E = E_{\uparrow}(k_{\|}) - E_{\downarrow}(k_{\|}) = 2\alpha_{RB} k_{\|}$, see conclusion (c) of Sec. 5.1.2. For Pb/Si at $k_{\|} > 0$ the spin-up state is at higher energy (lower E_b) than the spin-down state resulting in a $\Delta E > 0$, while for Au(111) this sign convention results in $\Delta E < 0$.

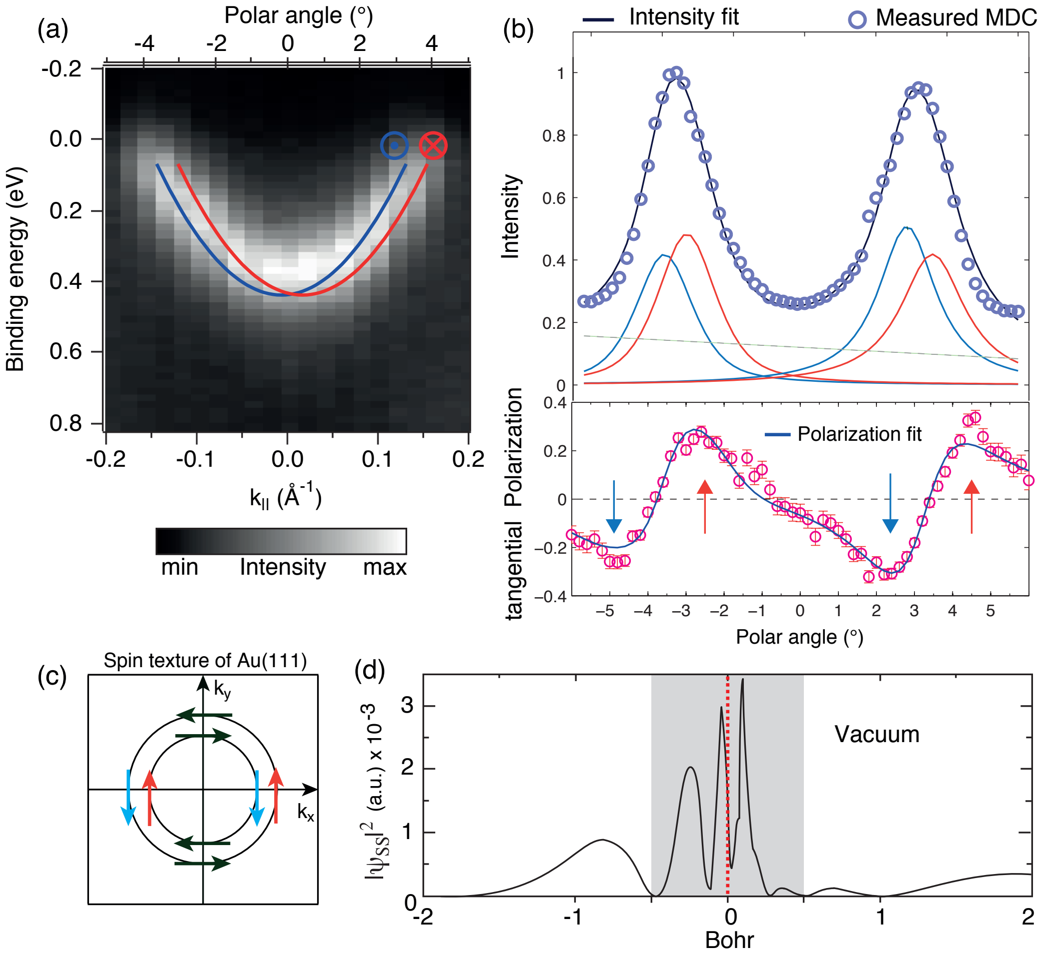

Figure 36: *(a) Electron-like band dispersion of the surface state on Au(111). (b) Measured momentum distribution curve close to the Fermi level (upper panel) and tangential polarization (lower panel) together with fits according to the two-step fitting routine. (c) Spin texture of Au(111) determined from the lower panel of (b). (d) Charge density plot of the surface state in Au(111) integrated around the surface atom* (0.2×0.2) *Bohr. The Au atom is at origin (calculated by G. Bihlmayer).*

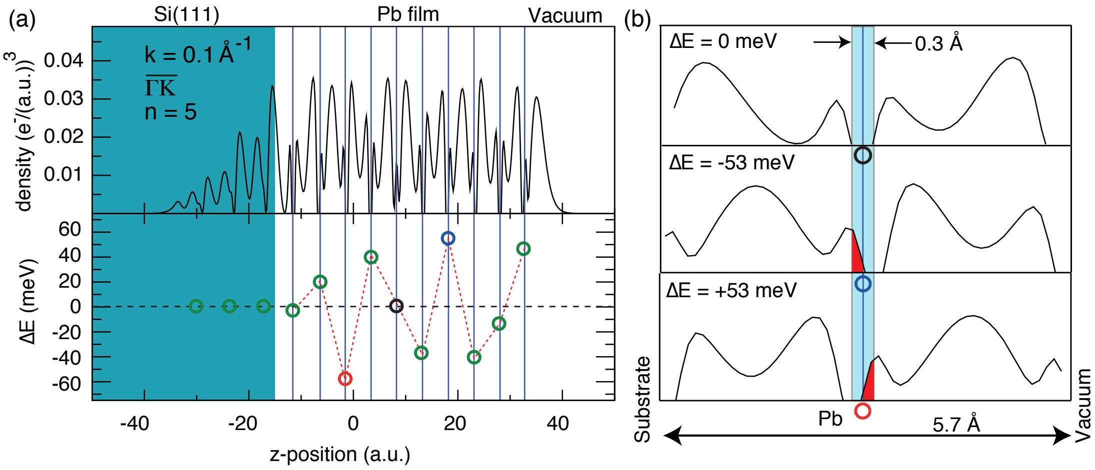

Figure 37: *(a) Charge density along the z-direction of a Pb QWS calculated with DFT (upper panel) and layer-resolved energy splittings (lower panel). (b) Magnifications into three specific regions of the slab as marked by the different colors of the circles.*

Second, the spin splitting in Pb/Si at the fixed momentum $|\mathbf{k}| \approx 0.1$ Å^{-1} is almost independent on the coverage, as seen from Fig. 33 (f). If SOI would solely arise from the potentials at the metal-substrate and metal-vacuum interfaces one would expect ΔE to decrease as a function of 1/thickness because the probability density ($|\psi|^2$) at the interface scales with 1/thickness, see Eq. 25. This is also in line with the explanation of the spin splitting in the surface state of Au(111) which cannot be explained as due to SOI originating from the surface potential gradient alone. As pointed out by G. Bihlmayer, L. Petersen and P. Hedegård, the atomic fields around the nuclei will have a larger influence, as will be demonstrated in the following using DFT calculations.

In the upper panel of Fig. 37 (a) we show a charge density plot ($|\psi(z)|^2$) of a QWS in 10 ML Pb at $k_{\|} = 0.1$ Å^{-1} calculated with density functional theory. The DFT calculations, performed by G. Bihlmayer, were employed in the local density approximation [162], using the full-potential linearized augmented plane-wave method in thin film geometry [163]. The simulation of Pb/Si(111) was performed with a Pb slab of variable thickness terminated with Si(111) assuming a commensurate interface where the lattice spacing of the Pb overlayer is expanded to match the Si lattice. As has been shown in Chap. 4, the expansion of the in-plane lattice constant toward the value of Si explains the high effective mass of the Pb QWS and therefore correctly describes Pb/Si.

The charge density distribution, averaged over the in-plane coordinates, shows a typical quantum beat structure due to the fast oscillating Bloch factor accounting for the slab periodicity and the standing wave solution (Eq. 25) with $n = 5$ as the number of antinodes in the envelope function. The Bloch factor forces the wave function to have minima at or close to the atomic positions which are marked by the vertical blue lines. This is better seen in Fig. 37 (b) where three specific regions of the slab are magnified. Another remarkable feature of QWS becomes evident by comparing the penetration depths of the QWS wave function at the metal-substrate and the metal-vacuum interface. While toward the vacuum the probability density is exponentially damped over a distance ≈ 4 Å, at the metal-substrate boundary the QWS penetrates almost 12 Å into the substrate. These different penetration lengths of the QWS wave function play an important role in determining the measured energy splitting ΔE in a SARPES experiment.

The lower panel shows spin splittings as a function of the position of the Pb nuclei in the slab, which were obtained by artificially turning off the SOI in the other layers. These local splittings oscillate in sign and magnitude throughout the entire layer and SARPES measures the sum, i.e. $\Delta E = \sum_i^N \Delta E_i$ where i indexes the layers and runs till N, the number of layers. Because these contributions alternate in the sign, the measured spin splitting is in general small and therefore not resolvable with spin-integrated ARPES.

To understand why these splittings oscillate we consider the expression to calculate ΔE_i suggested in Ref. [164]:

$$\Delta E_i = \langle \psi | H_{RB} | \psi \rangle \tag{54}$$

$$= |k_{\|}| \frac{2}{c^2} \int_{-z}^{z} \frac{dV}{dz} |\psi(z)|^2 \, \mathrm{d}z \tag{55}$$

where V is the spherical Coulomb potential of the nuclei and $\psi(z)$ the wave function of the QWS and the integration is taken within the interval of $\Delta z = -z ... +z$ with the nuclei at $z = 0$. It has been shown that 90% of the contribution arises within a sphere of only 0.13 Å ($\hat{=}$ 0.25 bohr) radius where the antisymmetric Coulomb gradient is most significant [132]. It is the local asymmetry of the charge density within Δz that determines the sign and magnitude of the local splitting as shown in Fig. 37 (b). Here we plot three characteristic shapes of $|\psi(z)|^2$, extracted from Fig. 37 (a), producing local spin splittings in the order $\Delta E = 0$, $\Delta E < 0$, and $\Delta E > 0$. If the charge distribution is symmetric with respect to the position of the Pb nuclei it follows from Eq. 55 that the energy splitting is zero. A negative contribution arises, when the integration of the charge density weighted with the Coulomb gradient is dominated from the substrate side (indicated by the red area). A positive energy splitting is obtained when the integration contains charge density facing the vacuum side. Consider a symmetric charge density distribution where all local contributions are equal to zero; an overall shift of the charge density distribution toward the substrate induces more positive contributions from the vacuum side than negative contributions from the substrate side resulting in $\Delta E > 0$. Because in our experiment we also measure positive spin splittings for positive momenta, this means that the wave function of Pb QWS has a larger extension toward the substrate. Recalling the particle-in-the-box model with finite potential barriers, the larger penetration of the wave function into the substrate region can be explained by an asymmetric quantum well with a larger barrier toward the vacuum.

It is instructive to compare our results for Pb QWS with the Rashba-split surface state of Au(111). Figure 36 (d) shows a calculated charge density distribution of the surface state. The asymmetric feature around the surface atom at origin is clearly larger than in Pb and its contribution dominates ΔE. This is in sharp contrast to the asymmetries around the Pb nuclei in the ultra-thin film. Furthermore the charge density distribution faces predominantly the vacuum side at the outermost

Au layer [164–166]. Consequently, the integration range of Eq. 55 contains more charge facing the substrate side. These differences are responsible for the larger size and the reversed sign of α_{RB} in Au(111) compared with Pb/Si. Thus the knowledge of the magnitude and sign of the Rashba parameter can reveal details about wave function localization [167].

5.3 Conclusions

Many insights into the origin of the size of the Rashba effect have been gained by studying surface states and surface alloys on noble metals. A necessary ingredient to observe large spin splittings is not only a high-Z material but also an asymmetric charge distribution around the core. For surface states, the orbital mixing ratio of the wave function determines the asymmetry, which in turn depends on structural properties such as the corrugation parameter Δz.

The Rashba effect in Pb QWS due to SOI in the high-Z material is also determined by the charge asymmetry around the Pb cores. However, several distinctions have to be considered. First, the charge density of a surface state is strongly localized within only a few atomic planes, while the charge density of a QWS expands over the entire film. Consequently, a surface state contains an asymmetric feature in the charge density which produces a spin splitting that dominates in magnitude and sign the contributions from other layers. In sharp contrast, the layer-resolved spin splittings of QWS are oscillating in magnitude and sign partly canceling each other. Second, the charge asymmetry of a surface state depends on the orbital mixing ratio, which is sensitive to structural properties of the surface such as the corrugation. In Pb QWS the charge asymmetry around the cores is also determined by the orbital mixing ratio with the addition that this asymmetry can be changed by the asymmetry of the quantum well which introduces different penetration lengths of the wave function into the substrate and into the vacuum region. From this it is clear that the Rashba effect in QWS is not only a function of the charge asymmetry, but also depends on the localization of the state in the film. The local charge asymmetry and the degree of localization are coupled to each other. Increasing the asymmetry lowers at the same time the localization of the state, which also enters the expression to calculate ΔE_i via $|\psi(z)|^2$ (Eq. 55).

It is especially the last property which makes Pb/Si(111) an ideal model system to study the Rashba-Bychkov effect of QWS because any change of the metal-substrate or metal-vacuum interface will influence both the local charge asymmetry and the localization of the states and thus the measured Rashba constant. In contrast to systems where the spin splittings of QWS are induced by the high-Z substrate, the Pb/Si system features several control knobs which are investigated in this thesis: the chemistry of the metal-substrate interface and the doping concentration of the substrate. Both parameters are the subject of the following chapter.

6 Manipulating the Rashba-type spin splitting in Pb QWS

In this chapter we study the influence of the metal-substrate interface on the spin splitting of Pb QWS. The first part is devoted to explore the influence of different Si(111) terminations using Bi and Ag. The obtained results are compared to our findings on the Pb reconstructed Si(111) substrate. For these systems the metal-vacuum boundary conditions are the same and all changes are thus related to the metal-substrate interface. The focus of the second part is to demonstrate that changes in the spin splittings in Pb QWS can also be achieved by varying the substrate charge density.

6.1 Influence of the interfactants

Figure 38 (a) shows the spin-integrated band dispersion of a QWS in a 10 ML (≈ 2.5 nm) thick Pb film deposited on Si(111)-($\sqrt{3} \times \sqrt{3})R30°$-Bi($\beta$). Details about the preparation method can be found in Chap. 4. The most important points are that Pb features layer-by-layer growth on both interfaces and that the effective mass of the $6p_z$ states around normal emission is reduced by a factor of three compared to Pb/Pb/Si(111) to $m^\star = 3.2\ m_e$ for the Bi interface and to $m^\star = 2.4\ m_e$ for the Ag interface [96,103]. This reduction is ascribed to the size of the interface dipole which lowers the adsorbate-substrate interaction and allows for a slightly smaller in-plane lattice constant in the film, for details see Sec. 4.7.

Figure 38 (b) shows the measured spin polarizations of Pb/Bi/Si in y-, x-, and z-directions (P_y, P_x, P_z) of the sample coordinate system of an energy distribution curve at the reciprocal point $\mathbf{k}_\| = (k_x, k_y) = (0.24, 0)$ Å^{-1} along $\overline{\Gamma}$-$\overline{\mathrm{K}}$ of the (1×1) surface Brillouin zone (SBZ). From the Rashba model one expects up-down polarizations in the y-direction being tangential to the constant energy contour, as sketched in Fig. 38 (e). The small P_y amplitude of only 8% results from the large overlap between peaks of opposite spin direction and the influence of the background. The data were analysed by the vectorial spin analysis, which has proven to be a very powerful tool to extract three-dimensional polarization vectors [145], see also Chap. 2. For short, the first step of this routine aims to fit the total spin-integrated intensity, as shown in Fig. 38 (c). We define two *Voigt* intensity peaks (labeled as *R1* and *R2*) and a linear background. The second step consists of the assignment of polarization vectors to *R1* and *R2*, which are defined by their polar angles θ_{Ri}, ϕ_{Ri} and length $c_{Ri} = 1$, with $i = 1, 2$. Peak widths, splittings and spin polarization vectors are then varied until a self-consistent best fit to the intensity and polarization data is reached. The result of the fit is shown in Fig. 38 (c) for the intensity and in Fig. 38 (b) for the polarization fit. In Fig. 38 (d) we show spin-resolved intensities calculated as: $I_y^\pm = \frac{I_{tot}}{2}(1 \pm P_y)$, where an energy splitting of 16 meV between the spin-up and -down state can be seen and an individual peak width of 240 meV. Furthermore, the polarization vector, as shown in Fig. 38 (f), is found to be rotated by $(32 \pm 2)°$ out of the sample plane, in sharp contrast to the purely in-plane polarizations found for Pb/Pb/Si(111) as discussed in the previous chapter.

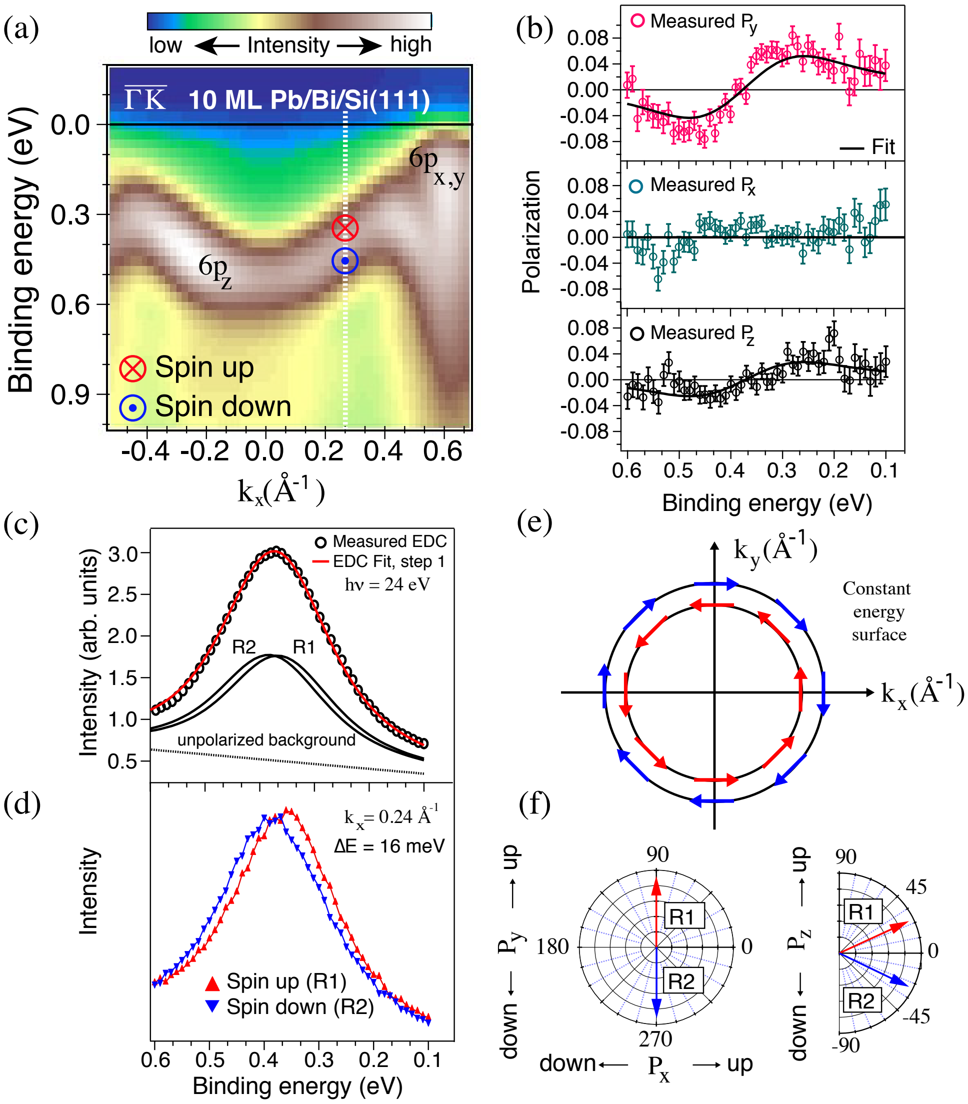

Figure 38: *(a) Band dispersion of the investigated QWS in a 10 ML thick Pb film grown on the Bi reconstructed substrate. (b) Measured and fitted polarizations along y-, x-, and z-directions. (c) Measured spin-integrated intensity and the resulting fit. (d) Spin-resolved energy distribution curve. (e) Schematic constant energy surface of Pb/Bi/Si(111). (f) In-plane and out-of-plane polarization components at* $k_x = 0.24$ *Å*$^{-1}$ *and* $k_y = 0$ *Å*$^{-1}$ *obtained from the two-step fit.*

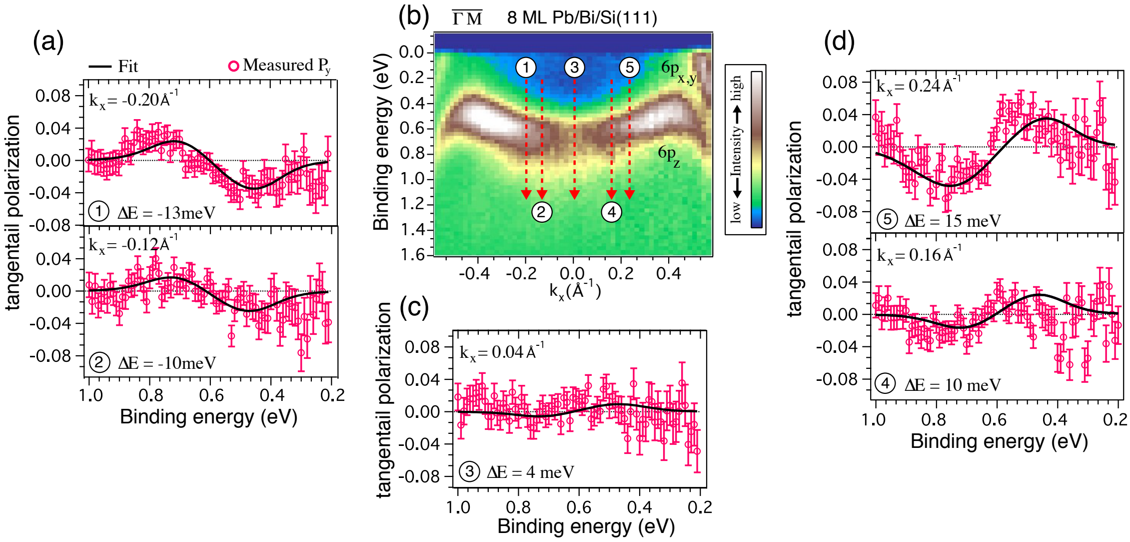

Figure 39: *(a, c, d) Measured and fitted P_y spectra at $k_y \approx 0$ Å^{-1} and for several values of k_x. (b) Band dispersion of the investigated 8 ML Pb film on the Bi interface.*

In the following we will determine the change of the Rashba constant $\alpha_{\mathrm{RB}} = \hbar^2 k_0/m^\star$ and the momentum splitting $2k_0$ induced by the Bi interface. To address this issue, we have measured P_y along $\overline{\Gamma}$-$\overline{\mathrm{M}}$, i.e. for $k_y = 0$ Å^{-1} and different values of k_x, because for these momenta the spin quantization axis lies along the y-direction. The band dispersion of the investigated QWS (8 ML) and the corresponding scans are shown in Figs. 39 (a-d). As expected for a Rashba system we observe a k-dependent energy splitting, i.e. the amplitude of the measured and fitted polarization curves decreases when approaching the Gamma point. At $\overline{\Gamma}$ the spin polarization has to vanish which is apparent from Fig. 39 (c) that shows polarization data taken close to normal emission. Further evidence of Rashba-like behavior is a sign change in the polarization when passing $\overline{\Gamma}$, compare e.g. Fig. 39 (d) and (a).

To confirm that the measured polarization curves represent the spin expectation value of the initial states we have performed a SR-EDC at the same Pb film and same high symmetry direction, but at a different photon energy of $h\nu = 26$ eV. The results together with our fit are shown in Fig. 40. As expected for a two-dimensional state, the binding energy does not change with photon energy, as seen from Fig. 40 (a), where the measured spin-integrated energy distribution curve is shown at $k_\parallel = 0.24$ Å^{-1}. Moreover, the polarization data are very similar to those obtained at $h\nu = 24$ eV. That is, we observe only up-down excursions in the tangential polarization (P_y), while $P_x = P_z = 0$. The fit reveals an energy splitting of same sign and magnitude, i.e. $\Delta E = 15$ meV, which suggests that intrinsic properties of the Rashba system are measured.

From the spin-polarized data in Figs. 39 (a, c, d) the Rashba constant can be deduced by plotting the energy splitting, determined via the fitting routine, versus in-plane momentum and taking the half of the slope of the linear fit. The result is shown in Fig. 41 (a). We obtain a Rashba constant

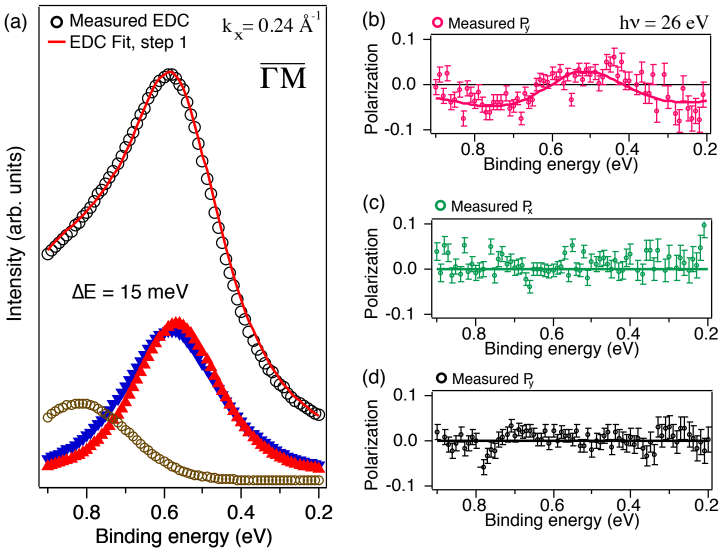

Figure 40: *(a) Measured spin-integrated energy distribution curve at $k_x = 0.24$ Å^{-1} and $h\nu = 26$ eV. Polarization data along (a) y-, (b) x-, and (c) z-direction together with fits.*

of $\alpha_{\mathrm{RB,Bi}} = (0.032 \pm 0.005)$ eVÅ, which is here reduced by 60% compared to Pb/Pb/Si(111), where we find $\alpha_{\mathrm{RB,Pb}} = (0.076 \pm 0.005)$ eVÅ, see Sec. 5.2.3. This decrease implies that the Bi interface induces more symmetric local charge distributions around the Pb nuclei in the overlayer, or equivalently an overall more symmetric wave function envelope. A smaller value of α_{RB} can be interpreted as a smaller penetration of the wave function at the metal-substrate interface, because the metal-vacuum interface is the same for both systems. This conjecture is fully consistent with our interpretation of the decreased $m^\star$ in the sense that the Bi interface reduces the coupling of the Pb overlayer to the Si substrate underneath. The Pb film becomes more free-standing-like, and it is expected that the Rashba effect of QWS in completely free-standing films vanishes due to the symmetric confinement [51,169]. Our experimental findings are also corroborated by DFT calculations as shown in Fig. 41 (b) where band structure calculations of 10 ML Pb on Si(111) are displayed. The influence of the Bi interface is here modeled indirectly via a decreased in-plane lattice constant of the Pb film toward the bulk value. The match between experiment and theory is remarkable not only for the enhanced dispersion but also for the reduced α_{RB}. The larger experimental value for $\alpha_{RB,Bi}$ is due to the fact that the in-plane lattice constant in Pb/Bi/Si is still slightly larger than the value for bulk Pb.

Figure 42 (b) shows the band dispersion of 8 ML Pb with $m^\star_{\mathrm{Ag}} = 2.4\ m_e$. As discussed in Chap. 4, the effective mass in this system is even further reduced compared to Pb/Bi/Si(111). The measured tangential polarizations are displayed in Fig. 42 (a) and (c) for off-normal emission angles. In contrast to data obtained from QWS on the Bi and Pb interface the Rashba-type spin splitting can not be resolved within the experimental resolution of our polarimeter. As discussed in the previous section, the spin splitting is determined by the local asymmetric charge distribution around the Pb cores. If the wave function penetrates to the same amount at the metal-substrate and the metal-vacuum interface this will generate symmetric charge distributions around the Pb nuclei and hence a vanishing spin splitting. We conjecture that Pb on a Ag reconstructed Si substrate is therefore a good approximation of an almost symmetric quantum well.

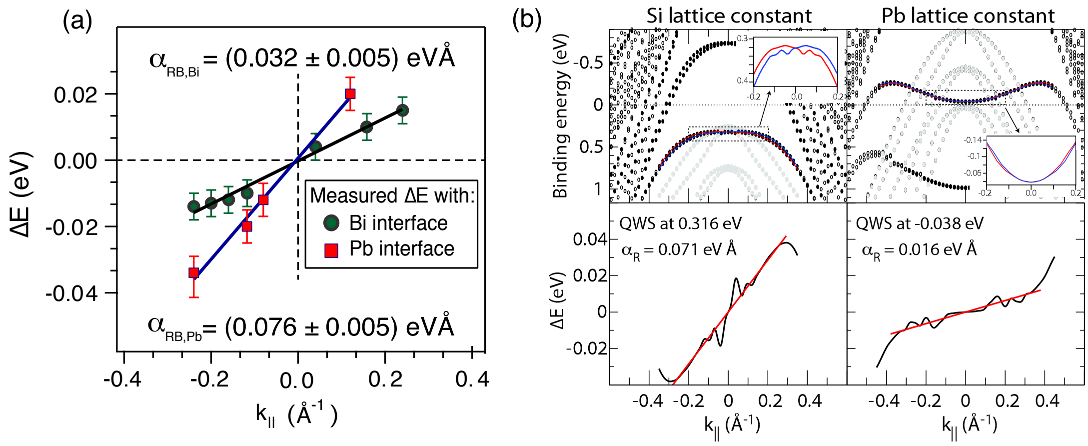

Figure 41: *Measured k-dependent energy splittings and linear fits (lines) to obtain α_{RB} for Pb/Pb/Si(111) and Pb/Bi/Si(111), respectively. (b) Simulated spin-resolved band dispersion of a 10 ML thick Pb film on Si(111)-*(1×1) *assuming a Si in-plane lattice constant (upper left panel) and a Pb lattice constant (upper right panel). The lower panels show the corresponding k-dependent energy splittings to evaluate the Rashba constant (adapted from [159]).*

Figure 43 compares spin-resolved band dispersions of QWS for all three interfaces, calculated from the experimentally determined α_{RB} and $m^\star$. The difference in the effective mass ($\mathrm{m}^\star_{\mathrm{Pb}}/\mathrm{m}^\star_{\mathrm{Bi}} \approx 3$) together with the reduced value of α_{RB} cause a reduction of the momentum splitting $k_0 = m^\star\alpha_{\mathrm{RB}}/\hbar^2$ by a factor of eight from $k_{0,\mathrm{Pb}} = (0.10 \pm 0.002)$ Å^{-1} to $k_{0,\mathrm{Bi}} = (0.0126 \pm 0.002)$ Å^{-1}.
The P_z curve shown in Fig. 38 (b) was measured in the high symmetry direction $\overline{\Gamma}$-$\overline{\mathrm{K}}$ of the hexagonal (1×1) surface Brillouin zone of Pb/Bi/Si(111). This polarization component has to fulfill time-reversal symmetry (TRS), i.e. $\mathbf{P}_z(\mathbf{k}_{||}) = -\mathbf{P}_z(-\mathbf{k}_{||})$ and since SOI couples the spin to the lattice it also has to reflect the C_{3v} symmetry of the surface. Figures 44 (a-c) display P_z data taken at different high symmetry directions and in-plane momenta of the SBZ. Fig. 44 (a)

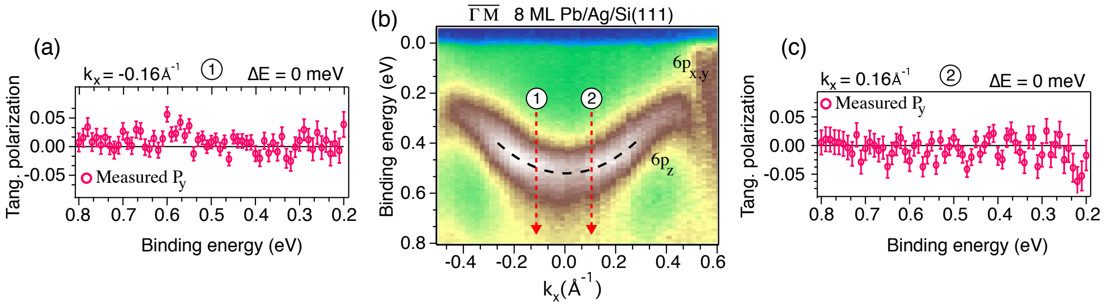

Figure 42: *(a) Measured tangential polarization at* k_x = *-0.16* Å^{-1}*. (b) Band dispersion of* $6p_z$ *states in 8 ML Pb on Ag/Si(111). (c) Tangential polarization as a function of binding energy probed at the reciprocal point* k_x = *0.16* Å^{-1}.

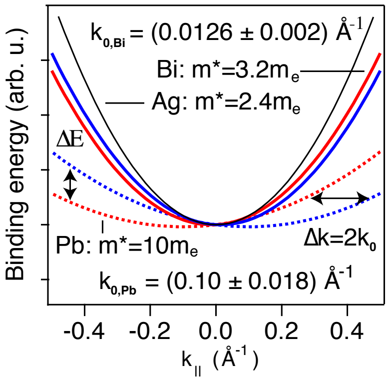

Figure 43: *Experimentally determined Rashba parabolae for the three investigated interfactants Pb, Bi and Ag.*

correspond to $\overline{\Gamma}$-$\overline{\mathrm{K}}$ and (c) to $\overline{\Gamma}$-$\overline{\mathrm{K}}'$ as sketched in Fig. 44 (d). In accordance with TRS we observe a sign change of P_z. The P_z curves shown in Fig. 44 (b) have been measured on the QWS in Pb/Bi/Si(111) displayed in Fig. 39 (b) (scans 2 & 3) along $\overline{\Gamma}$-$\overline{\mathrm{M}}$. Here, no significant P_z can be observed within the experimental resolution of the polarimeter. These high symmetry direction dependent P_z data are in line with the crystal symmetry of the fcc surface that is schematically shown in Fig. 44 (e). The three mirror planes perpendicular to the surface are labeled as $\delta_{1,2,3}$. Notice that the inclusion of a 2^{nd} layer reduces the symmetry actually from six-fold to three-fold, which is also reflected in the LEED pattern displayed in Fig. 44 (d). The intensities of the black spots labeled as $(1\bar{1})$, (01), and $(\bar{1}0)$ are stronger than those of the three other spots. The corresponding hexagonal SBZ is shown in Fig. 44 (f). The spin polarization vector, $\mathbf{P} = \langle\psi|\boldsymbol{\sigma}|\psi\rangle$ (Eq. 50), is a pseudovector and transforms differently than a normal vector under spatial symmetry operations. For instance, the application of a mirror plane symmetry to a pseudovector, as shown in Fig. 44 (f), leaves the $\perp$-component unchanged and reverses the $\|$-component. It follows immediately that the spin of an electronic state at a mirror plane must be orthogonal to this plane, i.e. fully in-plane. This is exactly what the SARPES experiment shows.

Currently three mechanisms have been discussed to explain an out-of-plane polarization of spin-orbit split states. For topological insulators the inclusion of third order correction in $\mathbf{k}$ to explain the warping of the surface states also induces an out-of-plane component of the spin expectation value [125, 146, 170], see Hamiltonian in Eq. 52 of Sec. 5.1.2. Further, spin frustration at the edge of the Brillouin zone can lead to an abrupt out-of-plane rotation of the Rashba spin [171]. Because in Pb/Bi/Si(111) the constant energy surfaces of the $6p_z$ derived states show no sign of warping and the measurements were taken far from the edge of the Brillouin zone [$k_{\max} \approx 0.25 < 0.64$ Å^{-1}], we propose that our observations are related to those for surface alloys [e.g. Bi/Ag(111)] where an out-of-plane spin component is induced by an in-plane potential gradient or an in-plane asymmetric charge distribution [137, 145]. Our previous photoemission measurements show that after deposition of Pb on the Bi reconstructed Si(111) the Bi 5d core-levels shift by 350 meV towards lower binding energy, which indicates a charge transfer between the Bi atoms and the Pb overlayer (see Fig. 17 (b)). Therefore the presence of the Bi interface influences the standing electron waves in the Pb layer and the in-plane charge density distribution around the Pb cores will be distorted.

It is interesting to note that the P_z data of Figs. 44 (a-c) resemble the symmetry of the (1×1) SBZ of the Pb film and not that of the $(\sqrt{3} \times \sqrt{3})R30°$ reconstruction.

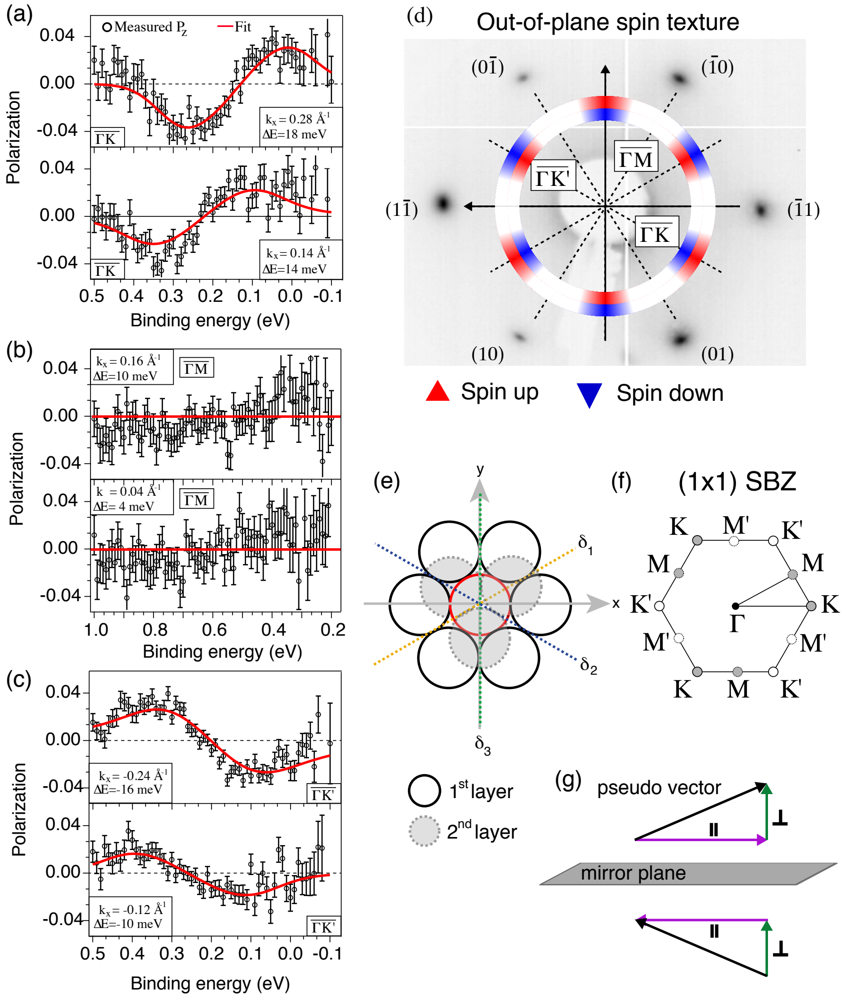

Figure 44: *(color online) (a-c) Measured and fitted P_z data for different high symmetry directions of the (1×1) SBZ of Pb/Bi/Si(111) along: (a) $\overline{\Gamma}$-$\overline{K}$. (b) $\overline{\Gamma}$-$\overline{M}$. (c) $\overline{\Gamma}$-$\overline{K}'$. (d) Spin texture of P_z overlayed with a LEED pattern of the 3-fold symmetric Pb(111) surface. (e) Pb(111) surface with the three mirror planes labeled as $\delta_{1,2,3}$. (f) Hexagonal surface Brillouin zone of Pb. (g) Transformation properties of a pseudovector under reflection at a mirror plane.*

Otherwise one would expect a vanishing P_z component along the $\overline{\Gamma}$-$\overline{\text{K}}$ direction [145]. The absence of any out-of-plane polarizations in Pb/Pb/Si(111) may result from the destruction of the Si(111)-$(\sqrt{3} \times \sqrt{3})$-Pb periodicity by burial as reported by P. B. Howes [172] and later by R. Feng [173], and also indicated by the close match between the theoretical and measured value for the Schottky barrier (see Sec. 4.7). Apparently the Bi interface maintains its symmetry upon deposition of Pb at low temperature. A X-ray scattering experiment could clarify this issue.

6.2 Influence of the substrate doping concentration

In the following section we demonstrate the possibility to tune the Rashba effect in Pb QWS through the doping dependence of the Schottky barrier, opening up the possibility of a terahertz spin-based field-effect transistor (spin-FET). As introduced in Section 5.1.2, in a Rashba system the inversion symmetry normal to the plane of a two-dimensional (2D) electron gas is broken which generates a Fermi surface spin texture reminiscent of spin vortices of different radii. This can be exploited in a spin-FET [7, 174], where the Rashba system forms a 2D channel between ferromagnetic (FM) source and drain electrodes. The electron spin precesses when propagating through the Rashba channel and spin orientations (anti)parallel to the drain give (low) high conductivity. Crucial is the possibility to tune the momentum splitting, and consequently the precession angle, through an external parameter.

6.2.1 Pb on n-type Si(111)

Figure 45 displays ARPES data from QWS formed in a N = 8 monolayers (ML) thick Pb film deposited on Si substrates with a high (a) and low (b) donor concentration. The films on both samples were prepared in the same way. The commercially available phosphorous doped Si wafers have the following room temperature resistances R and donor densities N_D[14]. For Pb on the highly n-doped substrate [henceforth Pb/h-Si(111)]: $R = 4\ \Omega\text{cm}$, $N_D = 1.14 \cdot 10^{15}\ \text{cm}^{-3}$. For Pb on the lightly n-doped substrate [henceforth Pb/l-Si(111)]: $R = 95\ \Omega\text{cm}$, $N_D = 4.65 \cdot 10^{13}\ \text{cm}^{-3}$. In our former studies on the sensitivity of the Rashba parameter on the interface (Sec. 5.2.3), we have grown Pb films on wafers with: $R = 53\ \Omega\text{cm}$, $N_D = 8.38 \cdot 10^{13}\ \text{cm}^{-3}$ [hereafter Pb/m-Si(111)].

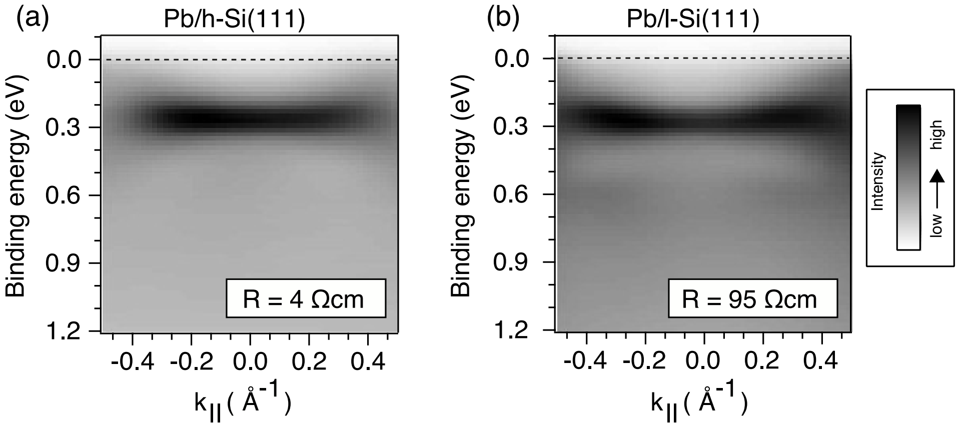

Figure 45: *Band dispersion of a QWS in 8 ML thick Pb film on (a) heavily n-doped and (b) lightly n-doped Si(111) substrate measured with ARPES using $h\nu = 24$ eV. The sample temperature was $T = 80$ K.*

---

[14] The resistance was taken from the companies data sheet and the donor concentration was calculated from www.cleanroom.byu.edu/ResistivityCal.phtml

Both band dispersions feature an anomalous high effective mass (>10 m_e), which is due to an increased in-plane lattice constant, and are very similar to those obtained for Pb films grown on a moderately doped Si(111) substrate, see Sec. 4.6. For the spin-resolved ARPES study we chose the QWS with $E_b \approx 0.3$ eV, because it has the largest signal-to-background ratio. The films on both samples were prepared by depositing the same amount of Pb with a rate of ≈ 0.3 ML/min. A change of the spin splitting can therefore be directly related to the influence of the donor concentration of the Si substrate, because the metal-vacuum boundaries are the same.

Figure 46 shows SARPES data from a Pb QWS grown on the lightly n-doped Si(111) measured for two energy distribution curves (EDCs) at (a) $\mathrm{k}_{\|} = -0.11$ Å^{-1} and (b) $\mathrm{k}_{\|} = -0.24$ Å^{-1}. For the measurements at both momenta displayed in Figs. 46 (c, d) the spin polarization data show typical up-down excursions in the tangential spin polarization components as expected for a Rashba system. A quantitative analysis of the spin-resolved data using a two-step fitting routine reveals a larger spin splitting between the spin-up (↑) and spin-down (↓) bands ($\Delta E := E^{\uparrow}(k_{\|}) - E^{\downarrow}(k_{\|})$) for the state with higher momentum. The corresponding fits are shown in Figs. 46 (a, c) for $\mathrm{k}_{\|} = -0.11$ Å^{-1} and in (b, d) for $\mathrm{k}_{\|} = -0.24$ Å^{-1}. We obtain a spin splitting of $\Delta E = -(22.2 \pm 1.4)$ meV and $-(33.8 \pm 1.4)$ meV, respectively, with fully polarized bands. The increased spin splitting with increasing momentum is in agreement with the Rashba model where $\Delta E \propto \mathrm{k}_{\|}$, and also seen in Figs. 46 (g) and (h), which display raw data as spin-resolved EDCs projected onto the quantization axis at both momenta, calculated as

$$I_{\mathrm{tan}}^{\uparrow,\downarrow} = \frac{1}{2} I_{\mathrm{tot}}(1 \pm P_{\mathrm{tan}}) \tag{56}$$

$$\text{with } P_{\mathrm{tan}} = \mathrm{sign}(P_y)\sqrt{P_x^2 + P_y^2} \tag{57}$$

Figures 46 (e) and (f) indicate the precise parallel momentum positions where the two EDCs were measured. For $k_{\|} = -0.11$ Å^{-1} the position was $(k_x, k_y) = (-0.086, 0.072)$ Å^{-1} (Fig. 46 (e)), for $k_{\|} = -0.24$ Å^{-1} it was $(k_x, k_y) = (-0.227, 0.072)$ Å^{-1} (Fig. 46 (f)). The strict Rashba-type spin-momentum locking requires the spins to be quantized in the direction perpendicular to the momenta, and the observed polarization along the x-direction is thus a consequence of the non-zero k_y component.

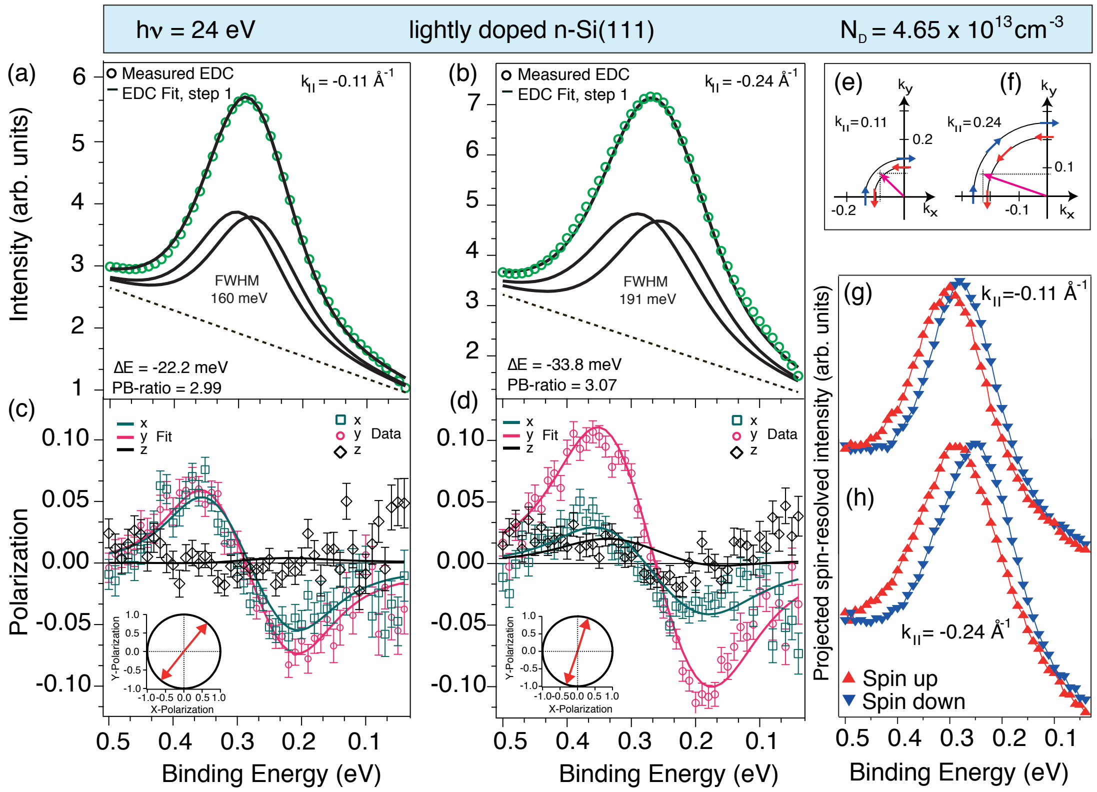

Figure 46: $\mathbf{Pb/l-Si(111)}$: *Measured spin-integrated energy distribution curve (a) at* $k_{\|} = -0.11$ $Å^{-1}$ *and at (b)* $k_{\|} = -0.24$ $Å^{-1}$ *with Voigt intensity profiles obtained from the self-consistent two-step fitting routine for the lightly n-doped Si(111). (c, d) Corresponding polarization data and fits in x-, y- and z-direction. (e, f) Part of a constant energy surface illustrating the measurement position of the EDC in reciprocal space obtained from the two-step fit. (g, h) Spin-resolved intensity profiles projected on the quantization axis for the two measured momenta.*

Figures 47 (a-b) show SARPES data at $k_{\|} = -0.24$ $Å^{-1}$ for a Pb film of the same thickness prepared on the heavily n-doped Si(111). The best self-consistent fit to the intensity and spin polarization data is here achieved with $\Delta E = -(48.0 \pm 1.8)$ meV. A direct comparison of both systems at $k_{\|} = -0.24$ $Å^{-1}$ reveals a larger energy splitting on the heavily n-doped substrate by almost 14 meV, which is well beyond the combined accuracy of 2 meV of the measurement and the fitting routine [28]. To illustrate that the larger ΔE of the QWS in Pb/h-Si(111) is not an artifact from our analysis procedure, we have performed a fit by keeping ΔE equal to the value found in Pb/l-Si(111) (dashed lines in Figs. 47 (b, d)). Although the total intensity fit is reasonably good, the fit to the polarization data obviously fails.

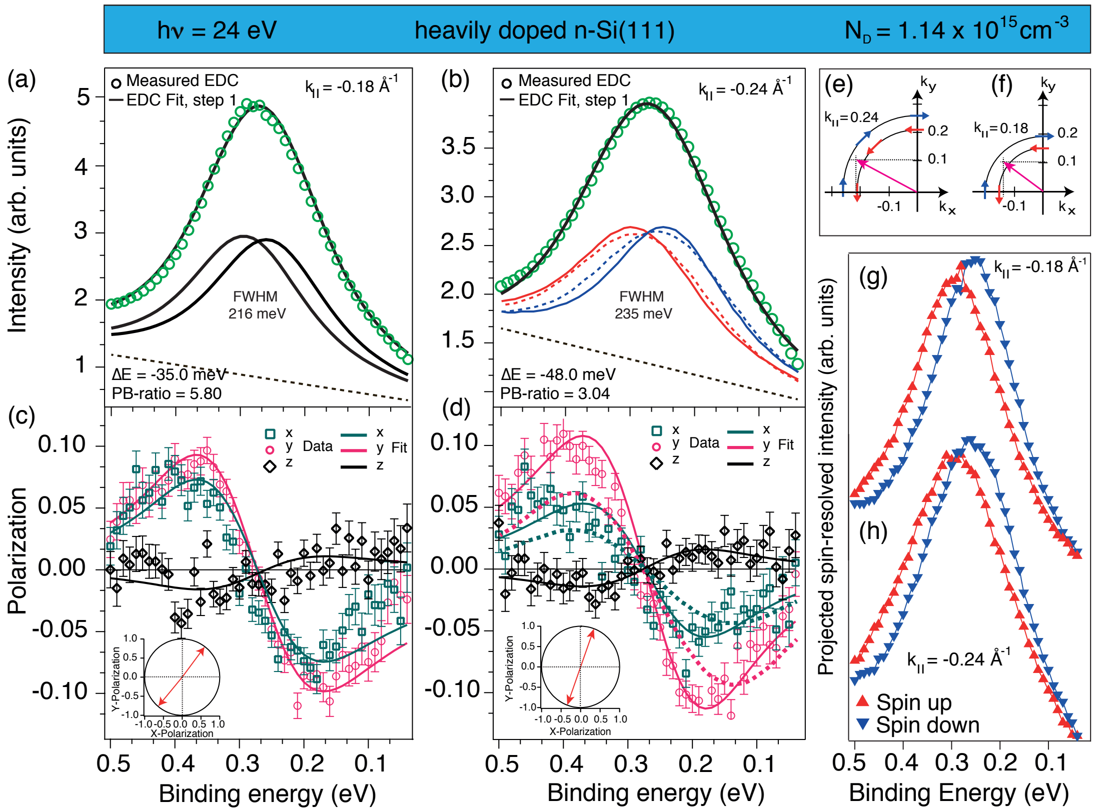

Figure 47: **Pb/h − Si(111)** : *Measured spin-integrated energy distribution curve at the in-plane momentum (a) $k_{||} = -0.18$ Å^{-1} and (b) at $k_{||} = -0.24$ Å^{-1} with Voigt intensity profiles obtained from the self-consistent two-step fitting routine. (c, d) Corresponding polarization data and fits in x-, y- and z-direction. The dashed lines in (d) are fits performed with $\Delta E = -33.8$ meV. (e, f) Part of a constant energy surface illustrating the measurement position of the EDC in reciprocal space obtained from the two-step fit. (g, h) Spin-resolved intensity profiles projected on the quantization axis for the two measured momenta.*

From these and further data sets measured at different parallel momenta we can deduce the Rashba constants α_{RB} for both doping levels by plotting the energy splittings, obtained from the fitting, versus the in-plane momenta (Fig. 48 (a)). Values for α_{RB} obtained by using

$$\alpha_{\mathrm{RB}} = \frac{\hbar^2 k_0}{m^\star} = \frac{1}{2}\frac{d(\Delta E)}{dk} \tag{58}$$

are $\alpha_{\mathrm{RB,h}} = (0.11 \pm 0.007)$ eVÅ for the heavily n-doped substrate, $\alpha_{\mathrm{RB,m}} = (0.076 \pm 0.005)$ eVÅ for the moderately n-doped Si(111) [160], and $\alpha_{\mathrm{RB,l}} = (0.070 \pm 0.011)$ eVÅ for the lightly n- doped Si(111).

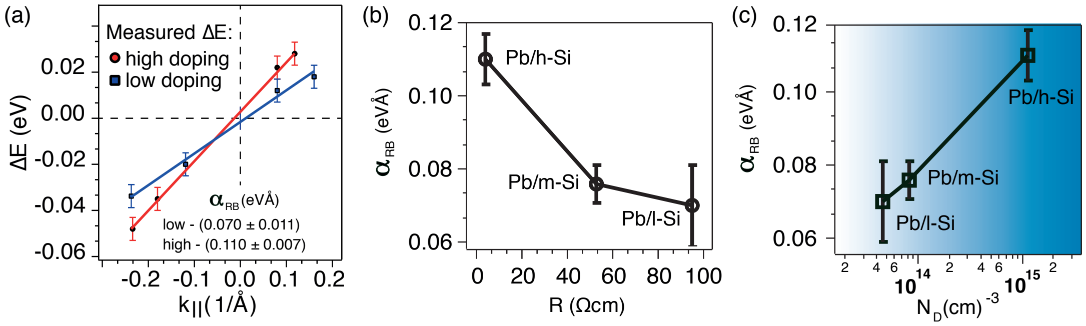

Figure 48: *(a) Measured k-dependent energy splittings and linear fits (lines) to obtain* α_{RB} *for the Pb/h-Si(111) and Pb/l-Si(111), respectively. Measured* α_{RB} *of the differently n-doped substrates vs resistance (b) and donor concentration (c).*

We now discuss the mechanism leading to the decrease of the Rashba constant in Pb QWS with increasing substrate resistance, as shown in Fig. 48 (b), or equivalently the increase of α_{RB} with donor concentration (Fig. 48 (c)). As demonstrated in Section 6.1 by the comparison of the Rashba effect in Pb QWS on a Pb and Bi terminated Si surface, a changed Rashba constant results from a modified charge density distribution in the Pb film which alters the local asymmetric features of the QWS wave function around the Pb cores. According to the phase accumulation model (see Sec. 3.1.1) the charge density distribution of a QWS is controlled by the phase shifts at the metal-substrate and metal-vacuum interfaces [37]. Because the phase shift at the vacuum side is the same for all three investigated systems, we focus in the following on the metal-substrate interface with its phase shift given by $\Phi_S \propto \sqrt{E - E_0}\Theta(E - E_0)$ [40] where E is the energy of a QWS and E_0 is the valence band edge of Si at $\overline{\Gamma}$ and Θ is the Heaviside function. States with energies inside the gap of a substrate are truly confined, while states outside the gap can couple to substrate states leading to quantum well resonances with a considerable fraction of charge spilling into the substrate. In between these two cases the confinement, i.e. the degree of localization, changes as a function of E_0. The goal of the following discussion is to show that the energetic distance between the QWS and E_0 is sensitive to the Schottky barrier (Φ^n_{SB}) and hence to the donor concentration because both quantities are related via: $\Phi^{SB}_n + E_0 = E_g$ where E_g is the energy gap of Si(111).

Our explanation is based on the interface dipole model for Schottky barrier formation, which was introduced in Sec. 3.4 and applied in Sec. 4.7 to explain the dependence of the Schottky barrier on the interfactant. In this model the formation of polar Pb–Si bonds at the interface results in a charge transfer and the establishment of an interface dipole that directly contributes to the SB [59]:

$$\Phi^{SB}_n = \Phi_M - \chi_S + eV_{int}. \tag{59}$$

Here Φ_M is the metal work function, χ_S is the electron affinity of the semiconductor, and V_{int} is the dipole induced voltage drop at the interface. We will argue that the size of V_{int} is not only determined by the interface chemistry, but also by the doping concentration and the type of dopant (donor or acceptor).

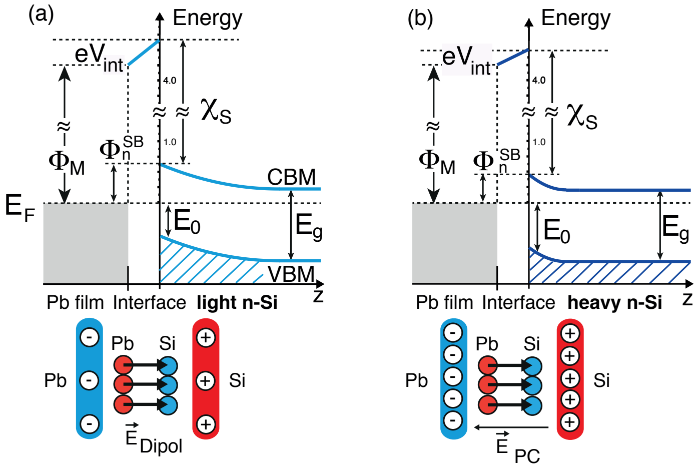

Figure 49: *(a, b) Energy diagrams of Pb/Si within the interface dipole model (not to scale) as a function of donor concentration (upper panels), and capacitor-dipole model (lower panels).*

The upper panel of Fig. 49 (a) shows the energy band diagram of Pb/Si deduced from measuring the peak widths of QWSs and QWRs as suggested in Ref. [40], and from core-level shifts of the Si 2p spectrum in the interface region that revealed an accumulation of negative charge at Si atoms when the Pb-Si interface is formed. For details see Sec. 4.7. This is in line with the predictions of the polarity of the Pb-Si bond using the Miedema electronegativity scale and with the study of Si 2p core-level shifts of Pb on n- and p-type Si that both revealed a shift toward lower binding energies [111]. According to Koopman's initial state model [119] this means that the electric field generated by the interface dipole ($\mathbf{E}_{\text{Pb-Si}}$) points from Pb to Si independent of the type of dopant. The lower panel of Fig. 49 (a) illustrates our model which explains the influence of the donor concentration on the band edge of Si(111). It consists of the aforementioned interface dipole placed in a parallel plate capacitor (PC) that generates an electric field of strength [175] $|\mathbf{E}_{\text{PC}}| = \sqrt{2eN_D(U_0 + U_G)/\epsilon\epsilon_0}$ at the interface due to the space charge in the depletion layer and hence depends on the density of ionized donors (N_D). U_0 is the built-in potential across the Schottky barrier, U_G is the gate voltage (for the moment $U_G = 0$ V) and $\epsilon = 11.9$ the dielectric constant of Si. For Pb in contact with n-type (p-type) Si the polarity of the capacitor is such that the positive (negative) space charge is on the semiconductor side, while the negative (positive) charge of equal size is balanced on the Pb side. Hence the direction of the electric field of the dipole and of the capacitor are *anti-parallel* (parallel) to each other for n-type (p-type) Si. Now, increasing the donor concentration increases the electric field in the capacitor and lowers V_{int} due to the screening of the interface dipole. Consequently, the SB decreases and the band edge of Si shifts to higher binding energies.

Our finding of a reduction of the SB with increasing N_D is consistent with previous results [176, 177]. As already pointed out the increased energetic distance between the QWS and E_0 influences the confinement of the QWS via the metal-substrate phase shift such that the QWS is more strongly localized in the Pb film, i.e. less charge spills into the substrate. This affects the local charge densities of the QWS wave function with respect to the Pb cores which determine the spin splitting, as discussed in Sec. 5.2.3.

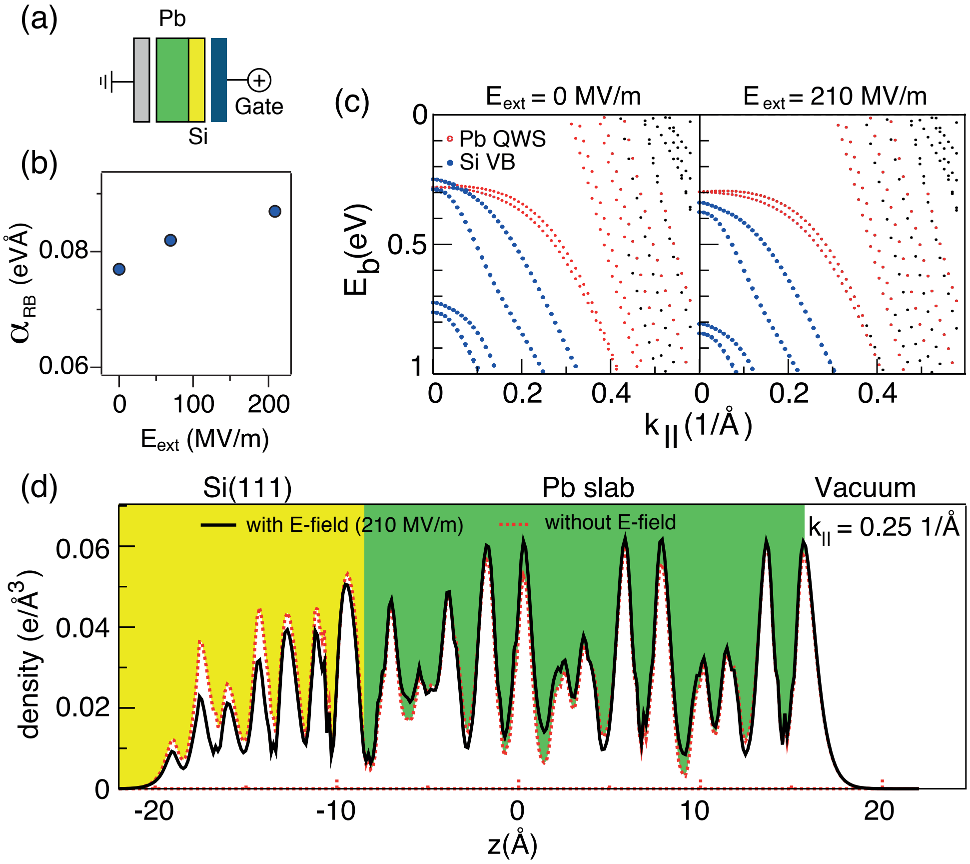

Figure 50: *(a) Pb/Si in a capacitor to illustrate how E_{ext} is applied to the system. (b) Calculated Rashba constant of Pb/Si as a function of applied external E-field. (c) Influence of E_{ext} on the energetic position of the Si valence band edge. (d) Charge density plots of QWS in Pb/Si with (solid line) and without (dashed line) E_{ext} at $k_{||} = 0.25$ $Å^{-1}$.*

We now show how the charge density distribution in the Pb film changes as a function of the energetic position of the valence band edge using DFT calculations. These calculations were performed on a 10 ML Pb film on Si(111) with the in-plane lattice constant of the Pb film commensurate with that of Si(111) and with Pb/Si placed into a parallel plate capacitor producing external electric fields (E_{ext}) of various strengths with the positive bias at the Si side, see Fig. 50 (a). The DFT calculations reveal that increasing E_{ext} from 0 to 210 MVm^{-1} shifts the Si valence band edge by $\approx$ 90 meV to higher binding energies, see Fig. 50 (c), and simultaneously the calculated Rashba constant increases by $\approx$ 12 % (Fig. 50 (b)) Notice that here E_0 shifts in the same direction as predicted by the interface dipole model when the donor concentration is increased. As already speculated the increased Rashba constant is a result of an increased localization of the state in the

Pb film, which is apparent from Fig. 50 (d) where we show charge density distributions producing a $\alpha_{RB} = 0.078$ eVÅ at $E_{\text{ext}} = 0$ MVm^{-1} and 0.087 eVÅ at 210 MVm^{-1}, respectively. As will be discussed below this interpretation is also consistent with our results obtained from Pb QWS on heavily p-doped Si(111) (acceptor concentration $N_A = 1.18 \cdot 10^{16}$ cm^{-3}) where we find the smallest Rashba constant among the studied systems of $\alpha_{RB}^{Pb/p-Si} = (0.061 \pm 0.004)$ eVÅ.
Having shown the sensitivity of the Rashba constant in Pb QWS to the donor concentration we now discuss the possibility to use Pb/Si as a candidate for future spintronic applications. Assuming ballistic spin transport through the Rashba channel we deduce the length (L) at which the injected spin - a coherent superposition of the two orthogonal Rashba spinors - precess by an angle of π while propagating along x, using $L = \pi/(2k_0)$ where $2k_0 = 2m^\star\alpha_{RB}/\hbar^2$ is the characteristic Rashba-type momentum splitting deduced from the experiment. For electrons in Pb/l-Si(111) we obtain $L_l = 1.71$ nm from $k_{0,l} = 0.092$ Å^{-1}, and in Pb/h-Si(111) $L_h = 1.08$ nm from $k_{0,h} = 0.146$ Å^{-1}, see lower panels of Fig. 51 (a). For a spin-FET made of Pb/l-Si(111) with a fixed channel length of 1.08 nm this means that changing the voltage drop at the interface by increasing the dipole screening via $|\mathbf{E}_{\text{PC}}| \propto \sqrt{U_0 + U_G}$ it is possible to go from a low ($\Delta\varphi \approx \pi/2$) to a high conducting state ($\Delta\varphi = \pi$) by ramping U_G from 0 to -12.8 V as simulated in Fig. 51 (b) which shows the interface electric field as a function of a gate voltage. In Pb/m-Si the conducting state is reached at $U_G \approx -6V$.

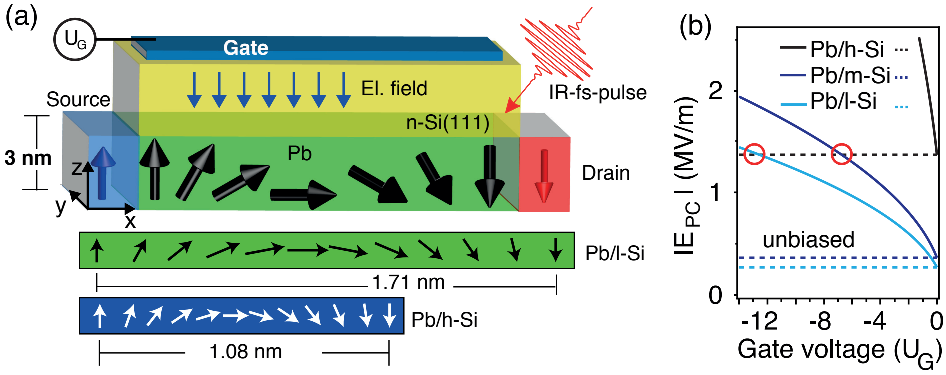

Figure 51: *(a) Sketch of a spin-FET device operated with a gate voltage (U_G) or by excitation with femto-second IR pulses (upper panel). Spin precession of π for electrons propagating along the x-direction in Pb films on l-Si(111) and h-Si(111) (lower panels). (b) Electric field in the parallel plate capacitor as a function of (reversed) gate voltage. The dashed lines mark the electric field at $U_G = 0$ V.*

An alternative way to operate a spin-FET device may also be achieved by optical means – thereby combining spin-based with electro-optical technologies. Recently it has been demonstrated that it is possible to change the SB and correspondingly E_0 in Pb/Si using ultra-short light pulses [178]. Now, consider a spin-FET in the non-conducting state which can be optically driven. Illuminating the device with fs-pulses leads to a modification of the charge balance at the interface and correspondingly to a shift of E_0 due to the changed interface dipole such that k_0 changes and the conducting state is reached. For high-speed applications, the FET should respond quickly to variations of the trigger pulse. In Pb/Si a complete built-up of the E_0 shift is reached within 100 fs and equilibrium is recovered after 600 fs [178] - the non-conducting state. This yields a switching frequency in the *terahertz* (THz) regime.

6.2.2 Pb on heavily p-doped Si(111)

In the following section we present data and analysis of the Rashba-type spin splitting in Pb QWS in an ultra-thin Pb film of 8 ML thickness prepared on heavily p-doped Si(111). We find that the Rashba parameter is the smallest among the here studied systems which is in line with the presented interface dipole model and the corresponding screening of the interface dipole. We will also show that the influence of the doping concentration on the spin splitting in Pb QWS can neither be explained by a semi-classical approach via the penetration depth of the QWS wave function into the barrier at the metal-substrate interface nor by the bare Rashba model.

In our study we have also measured spin splittings of QWS prepared on heavily p-doped Si(111) [hereafter Pb/p-Si]. Our results are summarized in Fig. 52. Figure 52 (a) displays the electronic structure of 8 ML Pb on p-type Si with a bulk resistivity of 1.25 Ωcm and an acceptor concentration of $N_A = 1.18 \cdot 10^{16}$ cm^{-3}. The band dispersion is similarly flat as found for Pb on n-type Si.

The upper panels of Figs. 52 (b) and (c) show the measured spin-integrated spectra and the lower panels spin polarization data together with fits that were taken at two different in-plane momenta, i.e. (a) at $k_\| = -0.16$ Å^{-1} and (b) at $k_\| = -0.24$ Å^{-1}, respectively. The measured spin polarization data reflect Rashba-type spin splitting which manifests itself in a tangential spin alignment to the energy contour and an increase of spin splitting with increasing momentum. The two-step fitting routine gives a spin splitting of $\Delta E = -21.0$ meV at $k_\| = -0.16$ Å^{-1} and $\Delta E = -32.0$ meV at $k_\| = -0.24$ Å^{-1}. A direct comparison of the measured spin splittings at $k_\| = -0.24$ Å^{-1} reveals the smallest spin splitting for Pb QWS on the heavily p-doped Si substrate [cf. Pb/l-Si: −33.8 meV and Pb/h-Si: −48.0 meV]. Correspondingly, when analyzing the spin splittings as a function of the in-plane momentum we find the smallest Rashba parameter in Pb/p-Si being $\alpha_{RB}^{Pb/p-Si} = (0.061 \pm 0.006)$ eVÅ, see Fig. 52 (d).

We now show that the reduction of the Rashba parameter is well explained by the interface dipole model although, at a first glance, this finding seems to be in conflict with the found dependence of α_{RB} in Pb QWS on n-type Si that increased with increasing donor concentration.

In Figs. 53 (a, b) we draw the schematic energy band diagram for Pb in contact with p-type Si for the case of (a) low and (b) high acceptor concentration. In the framework of the interface dipole model the Schottky barrier is calculated via [59]

$$\phi_p^{SB} = I_S - \Phi_M + eV_{int} \tag{60}$$

where I_S is the ionization energy of the semiconductor, Φ_M is the work function of the metal and V_{int} the dipole induced voltage drop.

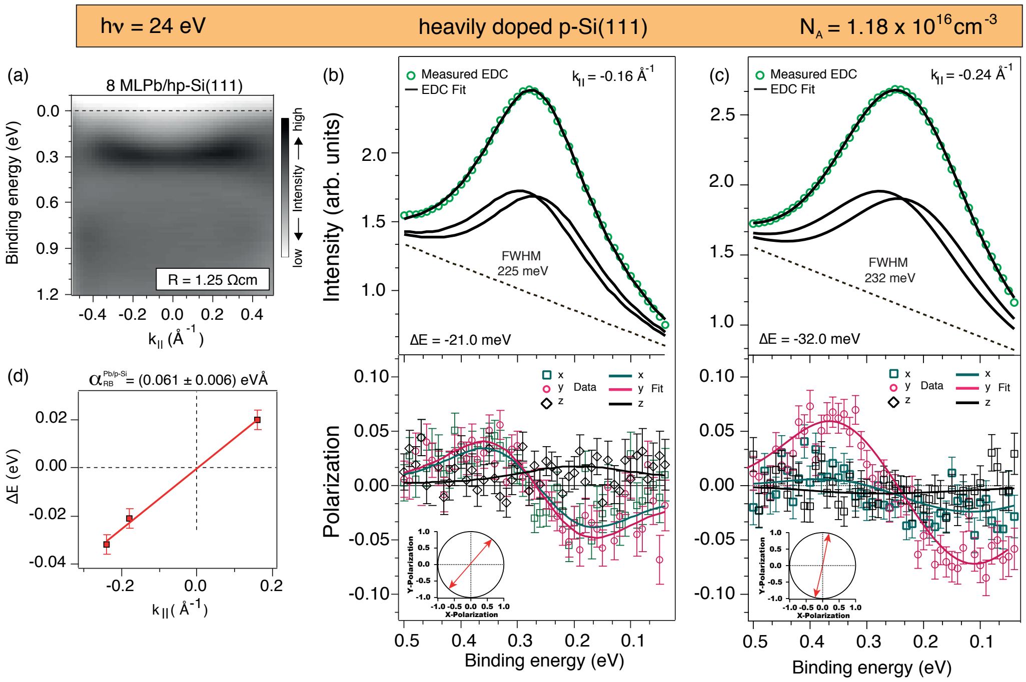

Figure 52: *(a) Band dispersion of a QWS in 8 ML thick Pb film on heavily p-doped Si. Measured spin-integrated EDCs for Pb/p-Si(111) (b) at* $k_{||} = -0.16$ *Å*$^{-1}$ *and at (c)* $k_{||} = -0.24$ *Å*$^{-1}$ *with Voigt profiles obtained from the self-consistent two-step fitting routine. The lower panels show the corresponding spin polarization data and fits in x-, y- and z-direction. Insets show the in-plane polarization vectors obtained from the two-step fit. (d) Measured k-dependent energy splittings and linear fit (line) to obtain* α_{RB} *for Pb/p-Si(111).*

According to Figs. 53 (a, b) the valence band edge of Si(111) equals the SB, i.e. $E_0 = \phi_p^{SB}$. As already mentioned in the previous section, the polarity of the parallel plate capacitor in Pb/p-Si is such that the electric field generated from the ionized (negative) acceptors points from the Pb toward the Si side and is therefore parallel to the electric field generated by the interface dipole. The parallel alignment of both electric fields results in an inverted dependence of the screening of the dipole upon increasing the acceptor concentration; increasing the acceptor concentration increases the electric field in the capacitor and due to the parallel alignment the voltage drop at the interface increases. Consequently the SB decreases (I_S and ϕ_M are constant) and so does the energetic distance between the band edge and the QWS. The decreased energetic distance alters the phase shift at the metal-substrate interface such that the QWS becomes more delocalized in the Pb film. This lowers the Rashba parameter because less charge density contributes to the local spin splittings at the Pb cores.

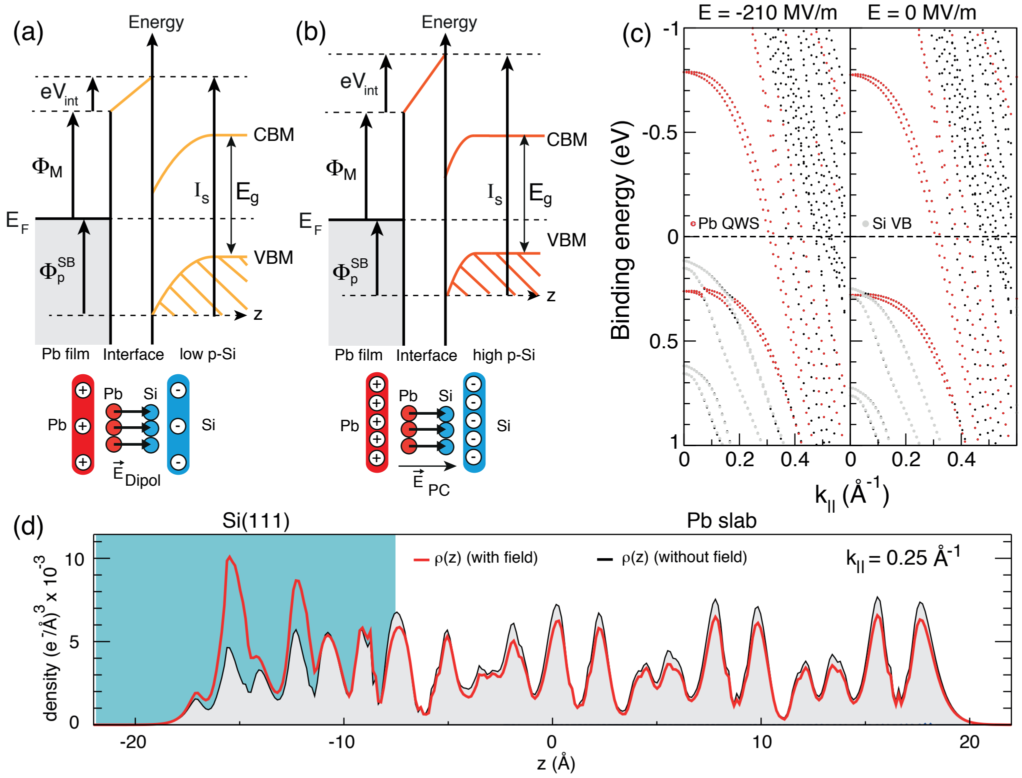

Figure 53: *(a,b) Energy diagram of Pb on p-type Si within the interface dipole model (not to scale) as a function of acceptor concentration (upper panels), and capacitor-dipole model (lower panels). Notice that the polarity of the capacitor is inverted with respect to Pb on n-type Si. (c) Calculated electronic structure of 10 ML Pb on Si with (left panel)* $E_{ext} = -210\ MVm^{-1}$ *and (right panel)* $E_{ext} = 0\ MVm^{-1}$. *(c) Corresponding charge density plots of the Pb QWS as a function of the electric field.*

Our explanation is well reproduced by DFT calculations. Figure 53 (c) shows the band structure of 10 ML Pb on Si(111) with an applied external electric field of -210 MVm^{-1} (left panel) and with $E_{ext} = 0$ MVm^{-1} (right panel). The electric field shifts the band edge of Si by roughly 120 meV toward lower binding energies, i.e. in the same direction when the acceptor concentration increases. The influence of this band shift on the charge density distribution of the QWS is displayed in Fig. 53 (d). The charge density in the case of $E_{ext} \neq 0$ MVm^{-1} spills to a larger amount into the Si substrate.

To summarize, while in Pb on n-type Si the Rashba parameter is found to increase with donor concentration, in Pb on p-type the opposite dependence is likely present, i.e. a decrease of α_{RB} with increasing acceptor concentration.

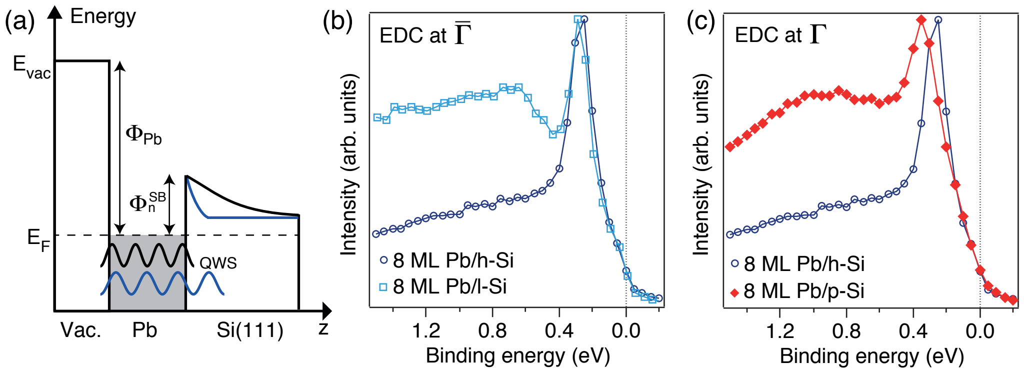

Figure 54: *(a) Schematic drawing of the confinement box of QWS in Pb/Si as a function of donor concentration. Comparison of normal emission spectra of a QWS in (b) Pb/h-Si and Pb/l-Si and in (c) Pb/h-Si and Pb/p-Si.*

6.2.3 Semiclassical penetration model

In the following we discuss the results of the study of Ref. [177] which investigated the influence of the barrier shape at the metal-substrate interface on the energetic positions of occupied and unoccupied QWS in Pb on n-Si(111) using scanning tunneling spectroscopy. The authors follow the idea that the Schottky barrier is independent on the doping concentration (corresponding to the Schottky limit) and that the confinement barrier for electrons approaching the substrate interface can be modeled via

$$eV(z) = \left[(E_{[111]} + \Phi_n^{SB}) - \frac{eN_D}{2\epsilon_0\epsilon_r}(z - z_D)^2\right]\Theta(z - z_D) \tag{61}$$

where $E_{[111]} = 9.685$ eV is the distance between the top of the s-like band of Pb in the $\overline{\Gamma}$-$\overline{\mathrm{L}}$ direction, z_D is the depletion layer width and Θ is the Heaviside function. Based on this model one would expect a larger penetration depth of the envelope function of the QWS into the substrate with a higher doping concentration, as schematically illustrated in Fig. 54 (a). According to the particle-in-the box model the eigenenergy $E_n \propto d_{eff}^{-2}$ of the state should then decrease because the effective width of the confinement box increases, see Eq. 25 of Sec. 3.1.1. However in their measurements the scientists observe exactly the opposite behavior; the occupied levels in Pb on the heavily n-doped Si substrate are at larger energies compared with states in Pb on the lightly n-doped Si (compare data presented in Fig. 2 of Ref. [177]). Because of the obvious conflict between the model and the experimental findings the authors concluded that the measured energetic positions of the QWS are an artifact of the measurement technique. However, in our ARPES experiment we find the same behavior of the energetics as a function of donor concentration which is exemplary shown in Fig. 54 (b). The state in Pb/h-Si is at lower binding energy compared to the state in Pb/l-Si(111), which strongly supports the interface dipole model for Schottky barrier formation. For clarity in Fig. 54 (c) we compare also normal emission spectra of QWS in Pb on the heavy p- and heavy n-type doped Si substrate. As already discussed the QWS in Pb/p-Si is more delocalized than in Pb/h-Si resulting in a larger binding energy at $k_{\|} = 0$ Å^{-1}.

6.3 Electric field contribution to the Rashba effect

Doping (n-type)	N_D [cm^{-3}]	$E_{\text{M-S}}$ [MVm^{-1}]	B_{eff} [T]	ΔE [eV]
low	$4.65 \cdot 10^{13}$	0.27	$8.4 \cdot 10^{-7}$	$4.8 \cdot 10^{-11}$
moderate	$8.38 \cdot 10^{13}$	0.36	$11.1 \cdot 10^{-7}$	$6.4 \cdot 10^{-11}$
high	$1.14 \cdot 10^{15}$	1.37	$4.24 \cdot 10^{-6}$	$2.4 \cdot 10^{-10}$

Table 2: *Donor density, interface electric field, effective B-field and energy splitting according to the Rashba model.*

In the originally derived Rashba model (Sec. 5.1.2) an electric field transforms via the Lorentz transformation into an effective magnetic field, which causes the energy splitting between spin-up and spin-down bands of size $\Delta E = -\mu_{\mathbf{s}}|\mathbf{B_{eff}}|$, with the spin magnetic moment $\mu_{\mathbf{s}} = -\frac{g_e \mu_B}{\hbar}|\mathbf{s}|$ and $\mathbf{B_{eff}} = -\frac{\hbar}{m_e c^2}(\mathbf{k}_{\|} \times \mathbf{E})$. From the donor density (N_D) and the built-in potential (U_0) we estimate the electric field at the metal-substrate interface via [175],

$$|\mathbf{E}_{\text{M-S}}| = \sqrt{\frac{2qN_D U_0}{\epsilon_0 \epsilon_r}} \tag{62}$$

and determine the corresponding energy splittings at $k_{\|} = 0.24$ Å^{-1}. For Pb/h-Si (high n-type doping) we obtain $E_{\text{M-S,h}} = 1.37$ MVm^{-1} and $\Delta E_h = 2.4 \cdot 10^{-10}$ eV, for moderate doping $E_{\text{M-S,m}} = 0.36$ MVm^{-1} and $\Delta E_m = 6.4 \cdot 10^{-11}$ eV, and for the low doping $E_{\text{M-S,l}} = 0.27$ MVm^{-1} and $\Delta E_l = 4.8 \cdot 10^{-11}$ eV. The trend in the energy splittings as a function of doping reflects our experimental findings, but the calculated absolute values are eight orders of magnitude too small and cannot explain the difference of 14 meV in the measured spin splittings of Pb/h-Si(111) and Pb/l-Si(111). The results are summarized in Tab. 2. Based on the bare Rashba model one would also expect the largest spin splitting in Pb QWS on p-type Si, because of the largest electric field due to the high acceptor concentration. However, this system features actually the smallest spin splittings which is a further indication that the simplified original Rashba model does not hold for Pb QWS.

6.4 Conclusions

Using spin- and angle-resolved photoemission spectroscopy we could show that the spin splitting and the spin texture of quantum well states in thin Pb films can be manipulated through changes in the interface and in the substrate charge density.

- **Influence of the interface on the Rashba-type spin splitting in Pb QWS**
  The Bi interface reduces the spin splitting of the Pb states by a factor of two and the spin polarization vector is rotated by 32° out of the sample plane compared to films grown on the Pb reconstructed Si(111) substrate. The rotation of the spin polarization out of the surface plane introduces an additional degree of freedom for the spin injection into a Rashba system. The spin splitting on a Ag reconstructed substrate reduces even further and is below the experimental resolution of the polarimeter.

- **Influence of the substrate charge density**
  The Rashba-type spin splitting of QWS in ultra-thin Pb films can be tuned effectively via the doping concentration of the Si(111) substrate. The Rashba constant of QWS on n-type doped Si(111) raises by a factor of two when the donor concentration is increased by a factor of ~ 20. On the other hand, QWS on heavily p-doped Si(111) feature the smallest Rashba constant among the systems containing a Pb interface. We conjecture that the energetic position of the Si valence band edge is the decisive factor for this effect. As has been shown by first-principles calculations this opens up the possibility to fine-tune the Rashba-type spin splitting in metallic QWS via a gate voltage or by excitation with ultra-short laser pulses.

We would like to emphasize that both presented studies seem to differ in their statements in what increases the size of the spin splitting in Pb QWS. In our first study on the influence of the interface on SOI in QWS the Rashba parameter increases because the valence band edge of Si shifts toward E_F, as summarized in Fig. 55 (a). The increase of α_{RB} is understood by the simple model, in which the resulting spin splitting is determined by the difference in the boundaries at the metal-vacuum and metal-substrate: increasing the penetration depth of the wave function into the substrate while fixing the vacuum boundary increases the local asymmetry and hence the net splitting.

In our second study on the influence of the substrate charge density on the Rashba splitting (Fig. 55 (b)), we obtain an increase of the Rashba parameter when the valence band edge moves away from E_F. At a first glance both findings seem to be contradicting. However, it is not only the asymmetry that defines the net splitting, but also the localization of the state in the film, as already pointed out in the conclusions of Chapter 5.

Having this in mind, Figs. 55 (a) and (b) are explained as follows. The Ag interface reduces the interaction between the film and the substrate, such that the QWS produces almost symmetric local asymmetries around the cores and hence a net spin splitting close to zero although the localization of the state is at maximum. On the Bi interface the QWS penetrates slightly deeper into the substrate than into the vacuum. The asymmetric confinement induces small local asymmetries in the wave function around the cores, and hence a finite Rashba splitting. In Pb/m-Si(111)

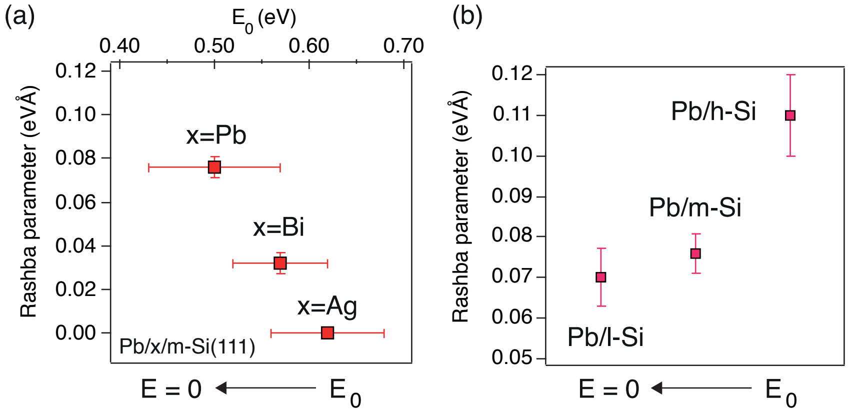

Figure 55: *(a) Rashba parameter α_{RB} of the investigated systems with the various interfactants Pb, Bi, and Ag, as a function of Si valence band edge $E_0 = E_g - \Phi_n^{SB}$. (b) Measured Rashba parameters of Pb films on the differently n-doped Si substrates (x-axis not in scale).*

the interaction is quite strong and the QWS penetrates considerably into the substrate. In this case, the asymmetry is at maximum, i.e. further increase of the penetration length of the QWS does not result in a larger splitting. On the contrary, the spin splitting decreases, as seen from the decreased α_{RB} comparing Pb/m-Si with Pb/l-Si. Here, the second ingredient for increasing the spin splitting becomes relevant - the localization of the state. It increases from Pb/l-Si to Pb/h-Si(111), as seen from Fig. 54 (c), while the asymmetry decreases.

7 Interband spin-orbit coupling in Pb QWS

In this chapter we investigate a momentum region in Pb/Bi/Si(111) where hybridization between bands of different orbital symmetries alters the band structure significantly. Starting from the Rashba regime where the energy-momentum dispersion of the quasi-free 2DEG is well described by the two spin-polarized parabolas, we find a breakdown of the Rashba behavior which manifests itself in a spin splitting that is no longer proportional to the in-plane momentum. Instead, we find that the spin splitting decreases with increasing momentum where the band dispersion of the QWS slows down. Using spin- and angle-resolved photoemission spectroscopy we identify the detailed interplay between the bands forming hybridized states. Our experimental findings are well explained by the inclusion of an interband spin-orbit coupling term that mixes Rashba-split states of the 2DEG with anti-parallel spins. In the last part of the Chapter we compare the results obtained from QWS in the system Pb/Bi/Si(111) with results from QWS in an ultra-thin Pb film deposited on Cu(111).

7.1 Introduction

Spin-orbit interaction (SOI) in non-magnetic low-dimensional systems is well known to lift the two-fold spin degeneracy of electronic bands in solids [22]. Depending on how the symmetry of a system is broken SOI, can take different functional forms resulting in effective Hamiltonians that lead to either the Rashba-Bychkov [123] or the Dresselhaus effect [9]. While in the latter case, the symmetry is broken by a unit cell which lacks an inversion center [termed as bulk inversion asymmetry], to induce the Rashba effect it is necessary to break the structural inversion symmetry. This is naturally the case at a surface or/and an interface parallel to the plane of confinement of a two-dimensional electron gas (2DEG).

It is found that most of the examined systems not only reflect the aforementioned predictions by the Rashba model, but also show deviations, manifested in the appearance of e.g. an out-of-plane rotation of the spin polarization vector [e.g. in the high-Z surface alloy Bi/Ag(111) [145]], or/and in-plane radial rotations as reported for the $\sqrt{3}$ reconstruction of Au on Ge(111) [147], see Sec. 5.2 for review. These deviations are not described by the simple Rashba model because they originate from the crystal potential, which is neglected in the derivation of the Rashba Hamiltonian. While surface states on high-Z noble metals are a good approximation of quasi-free 2DEGs and hence behave Rashba-like, the band structure of low-dimensional systems is usually more complex due to the presence of bands that eventually form energy gaps due to the avoided crossing hybridization as reported for QWS in Al/W(110) [156], or for electronic states in a Ag film covered with the high-Z surface alloy Bi/Ag [157, 158].

It is known that when bands belonging to the same group representation approach one another, SOI opens a hybridization gap resulting in an avoided crossing of bands [179, 180]. Close to this gap the orbital symmetry of the involved bands gets mixed and consequently the spins of the states get significantly altered due to SOI, i.e. $\mathbf{L} \cdot \mathbf{S}$. Here we provide direct evidence by using spin- and angle-resolved spectroscopy of an interband spin-orbit coupling between Rashba-type

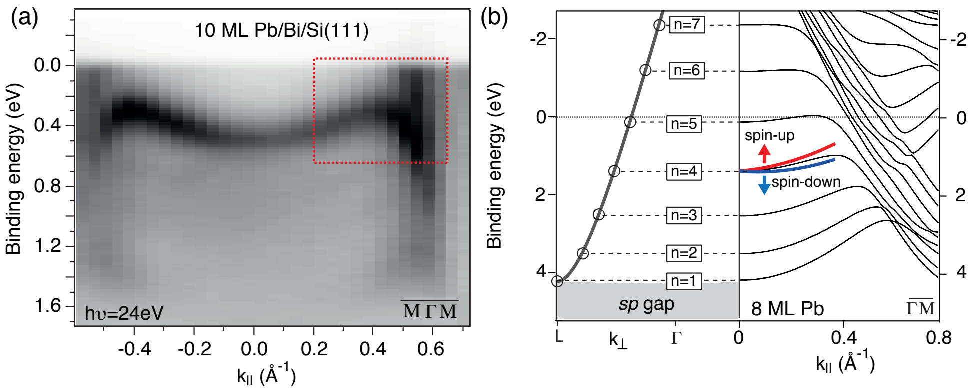

Figure 56: *(a) Electronic structure of 10 ML Pb on Bi-$\sqrt{3}$/Si(111) measured with angle-resolved photoemission spectroscopy. (b) (left panel) Quantization of the band structure along $k_{\perp}$ as a consequence of size reduction. (right panel) Calculated band structure of a 8 ML free-standing Pb film. The subband with the quantum number $n = 4$ is schematically split by the Rashba effect into two spin-polarized parabolas with opposite spin direction.*

spin split states of opposite spin directions. Our findings are distinctively different from the studies in Refs. [156,157] which reported a SOI-induced hybridization between states with parallel spins, and in line with studies on Bi/Cu(111) [179] and recently on the surface alloy BiAg$_2$ [181].

7.2 Results

Figure 56 (a) shows an electronic structure of an ultra-thin film formed by 10 monolayers of Pb grown on the dense $(\sqrt{3} \times \sqrt{3})$R30°-Bi($\beta$) reconstructed Si substrate. Details about this reconstruction and about the sample preparation are found in Sec. 4.3.1. The M-shaped QWS with a binding energy (E_b) $E_{\overline{\Gamma}} = 490$ meV at normal emission ($\overline{\Gamma}$) arises from the quantization of the band dispersion along the $\overline{\Gamma}$-$\overline{\text{L}}$ direction due to the size reduction. This is illustrated in the left panel of Fig. 56 (b) by the example of a 8 ML Pb film. The corresponding band structure, calculated with density functional theory, is shown in the right panel of Fig. 56 (b). The absence of sharp QWSs with binding energies larger than ≈ 0.5 eV in the ARPES data (Fig. 56 (a)) is due to the resonant coupling of the states in the Pb film with Si substrate states.

The main focus of this study is the outer region in the band structure marked by the dashed box in Fig. 56 (a) and enlarged in Fig. 57 (a). It consists of three bands labeled as α, β, γ, which are derived from Pb 6p ($l = 1$) orbitals, because the binding energies lie above the Pb *sp* symmetry band gap in the $\overline{\Gamma}$-$\overline{\text{L}}$ direction (cf. Fig. 56 (b)). More specifically, states that are described by an upward parabolic dispersion with band minimum at $\overline{\Gamma}$ are of 6p_z symmetry ($m_l = 0$), whereas states with downward dispersion and band maximum at $\overline{\Gamma}$ are of 6$p_{x,y}$ symmetry ($m_l \pm 1$).

Within a momentum range of $k_{\|} = \overline{\Gamma} \pm 0.3$ Å^{-1}, the dispersion of the α-band is well described by

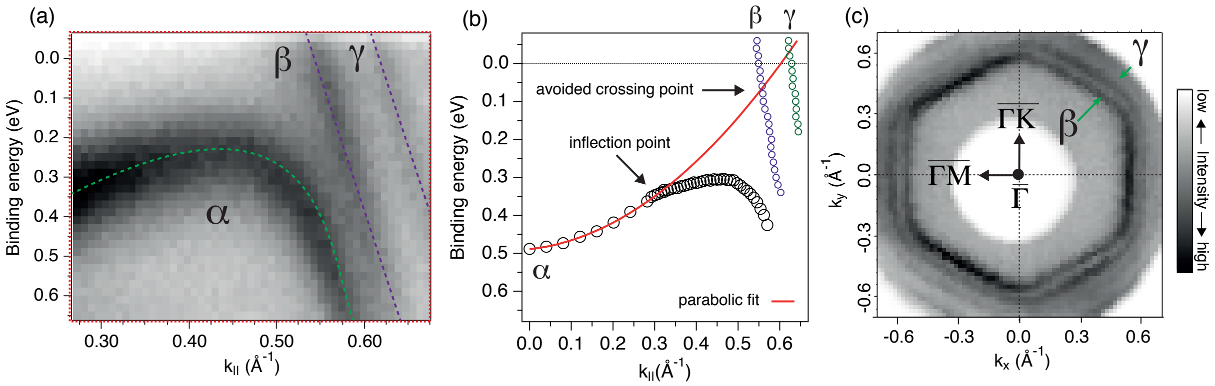

Figure 57: *(a) Magnification into the band structure region where the SOI-induced avoided crossing hybridization leads to the pronounced kink in the dispersion of the α-band. (b) Extracted dispersion of the α, β and γ band. The parabolic fit gives an effective mass of $m^\star = 3.2\ m_e$ and starts to deviate from the actual dispersion at $\approx$ 0.3 Å^{-1}. (c) Fermi surface of the ultra-thin Pb film (10 ML) with the high-symmetry direction $\overline{\Gamma}$-$\overline{M} \parallel k_x$ and $\overline{\Gamma}$-$\overline{K} \parallel k_y$.*

the relation of Rashba-type spin-split free electrons via

$$\alpha^{\pm}(\mathbf{k}_{\|}) = E_{\overline{\Gamma}} + \frac{\hbar^2}{2m^\star}\mathbf{k}_{\|}^2 \pm \alpha_{\mathrm{RB}}|\mathbf{k}_{\|}| \qquad (63)$$

where $m^\star = 3.2\ m_e$ [168] is the effective mass, $\mathbf{k}_{\|} = (k_x, k_y)$ is the parallel momentum, and $\alpha_{RB} = 0.033$ eVÅ [160] describes the strength of the Rashba effect.

Remarkably, the initially $6p_z$ derived α-band changes its curvature from being electron-like ($m^\star > 0$) to hole-like ($m^\star < 0$) for in-plane momenta $|k_{\|}| > 0.3$ Å^{-1} which is a first indication of avoided crossing hybridization. Such a pronounced change in the electronic dispersion has been also observed for monolayers of Pb on graphitized SiC and explained as due to SOI-induced hybridization and is therefore related to the particular band structure of the Pb film [51]. In Fig. 57 (b) we plot the dispersion of the α-band, which was obtained by fitting energy distribution curves as a function of momentum utilizing Voigt profiles. It is seen that the actual electron-like dispersion starts to deviate from the experimental data at $k_{\|} \approx 0.32$ Å^{-1} [hereafter termed the inflection point]. For clarity we have also included the dispersions of the hole-like β and γ bands, respectively. The parabolic fit of the α-band would intersect the β-band at $(E_b, k_{\|}) \approx$ (100 meV, 0.55 Å^{-1}) [hereafter termed the avoided crossing point] in the case of SOI-induced hybridization is turned off. The Fermi level crossing of the β- and γ-band is also resolved in Fig. 57 (c) which displays the Fermi surface (FS) of the ultra-thin Pb film. The hexagonal shape of the FS reflects the (111) crystal symmetry with corners pointing into the high symmetry direction $\overline{\Gamma}$-$\overline{\text{K}}$. Furthermore, by following e.g. the inner $6p_{x,y}$ band on the FS we observe an intensity modulation with a periodicity of $\frac{2}{3}\pi$, in line with the 3-fold rotational symmetry ($C_{3\nu}$) of the crystal structure and also apparent from the LEED pattern shown in Fig. 44 (d).

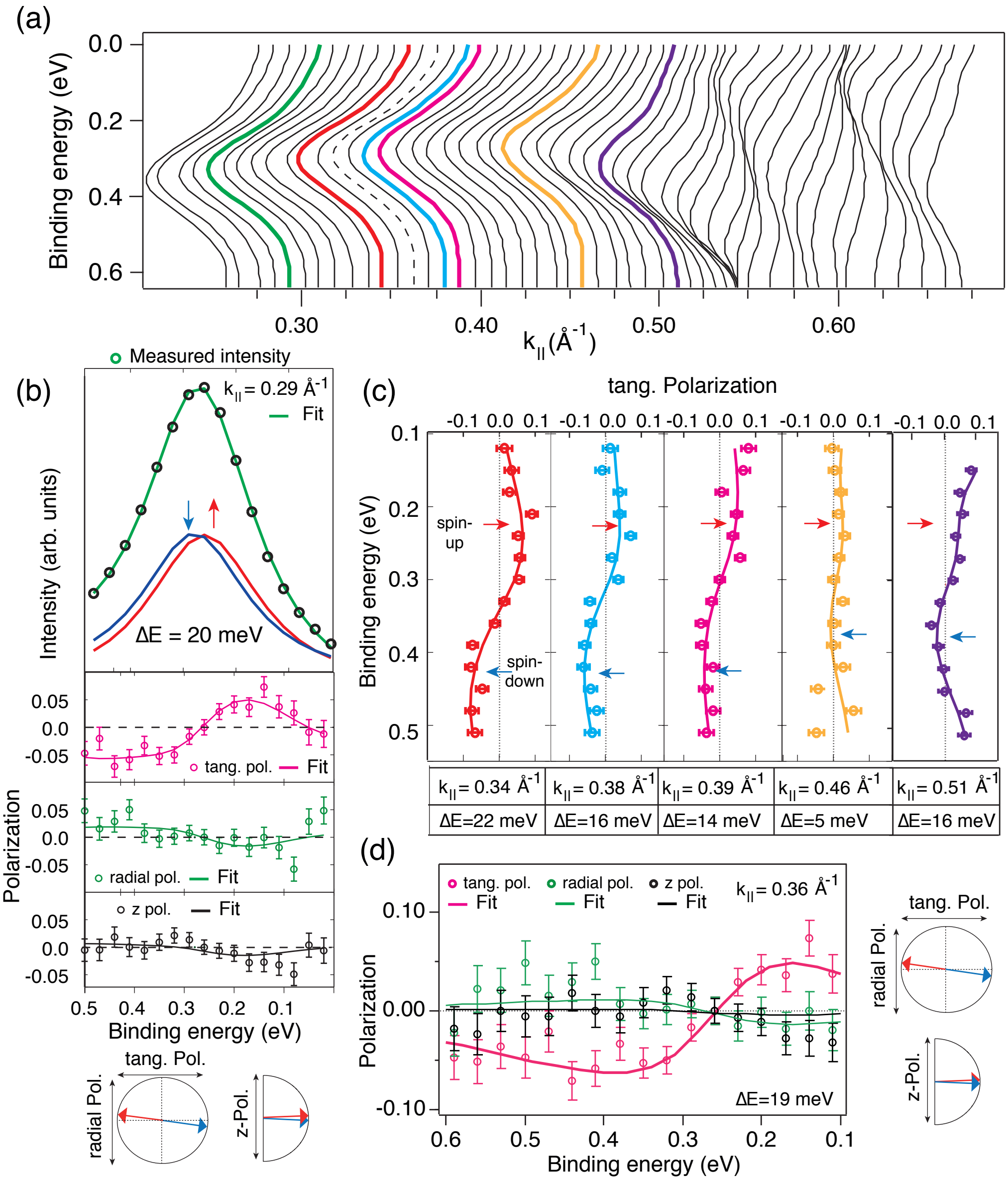

Figure 58: *(a) Energy distribution curves of the α-band as a function of $k_{\|}$. (b) (upper panel) Measured spin-integrated EDC at $k_{\|} = 0.29$ Å^{-1} with Voigt intensity profiles obtained from the two-step fitting routine. (middle panel) Corresponding spin polarization data and fits in the tangential, radial and z-direction. (lower panel) Spin polarization vectors revealed from the fit. (c) Tangential polarization data and fits at increasing in-plane momenta toward the inflection point. (d) Measured spin polarization data and fits (left panel) and polarization vectors (right panel) in the hybridization regime.*

Motivated by the peculiar dispersion of the α-band we first study the evolution of its spin splitting as a function of momentum, starting in the Rashba regime. In Fig. 58 (a) we show spectra recorded as a function of $k_{\|}$ extracted from Fig. 57 (a). We start with a spin-resolved energy distribution curve (SR-EDC) taken at $k_{\|} = 0.29$ Å^{-1} using the two-Mott detector scheme, which is sensitive to all three spin polarization components (P_x, P_y, P_z) [182]. At this momentum, far away from the region where the α-band bends downward [at ≈ 0.5 Å^{-1}], we expect a Rashba-like spin splitting and spin orientation. The data and the corresponding analysis using the self-consistent two-step fit [145] are shown in Fig. 58 (b). We observe up-down excursions in the tangential spin polarization ($P_{\tan}$) - the direction perpendicular to the momentum and a spin splitting of $\Delta E = 20$ meV between the spin-up (+) and spin-down (-) states. The polarization along the radial direction is below the detection limit of the polarimeter. An out-of-plane spin polarization (P_z), which has been reported in Sec. 6.1 for this system, is suppressed because we measured along the $\overline{\Gamma}$-$\overline{\mathrm{M}}$ direction, i.e. in the mirror plane of the (1×1) SBZ.

In the following we switch to the single Mott scheme and focus on the tangential spin polarization component. This way, we can decrease the Δk steps for similar overall acquisition time and precisely follow the evolution of the spin splitting along the dispersion. Figure 58 (c) shows exemplary $P_{\tan}$ data and fits obtained from SR-EDCs taken at increasing in-plane momenta. The color coding of the data corresponds to that in Fig. 58 (a). We observe first an increased polarization amplitude and spin splitting toward $k_{\|} = 0.34$ Å^{-1}, followed by a reduction toward $k_{\|} = 0.5$ Å^{-1}. In the region where the α-band bends downward the spin splitting seems to recover again with the same sign of the spin splitting, i.e. $\Delta E = 2\alpha_{RB} \cdot k_{\|} > 0$, which indicates a sign reversal in the momentum splitting $\Delta k = 2k_0$. As will be shown later, this sign change is better resolved in spin-resolved momentum distribution curves (MDC) rather than SR-EDCs. At this point we notice that in the region beyond the inflection point the tangential spin alignment persists and neither radial nor out-of-plane rotations of the spin polarization vector are observed. This is exemplified in Fig. 58 (d) which shows the 3D spin polarization data measured at $k_{\|} = 0.36$ Å^{-1}. The spin polarization vectors of the two Rashba-split states are very similar to those displayed in Fig. 58 (b).

Next, we focus on the spin texture of the α- and the β-band by analyzing SR-MDCs. Figure 59 (a) shows spin-integrated MDCs extracted from Fig. 56 (b). Starting from the high binding energy side, we observe maximum spectral weight on the downward dispersing α-band and a small shoulder at the high momentum tail from the β-band. With decreasing E_b the spectral weight shifts from the α- to the β-band. Closer to E_F both the β and γ bands can be clearly distinguished. Figure 59 (b) shows a series of spin polarization data from SR-MDCs. The polarization curve at $E_b \approx 0.6$ eV (scan 7) reveals a momentum splitting of the α-band, that is in line with data taken in the EDC mode (cf. Fig. 58 (c) and Fig. 61 (b)), i.e. $k^{\downarrow}_{\alpha,\|} < k^{\uparrow}_{\alpha,\|}$ translates into $\Delta E > 0$. This substantiates our finding that the sign of the momentum splitting of the α-band reverses upon passing the avoided crossing point. Because for this band both the sign of $m^{\star}$ and the sign of Δk changes, the Rashba constant maintains its sign since $\alpha_{RB} = \hbar^2 \Delta k / 2m^{\star}$.

For the adjacent β-band we find a similar behavior of a sign reversal of the Rashba constant. This

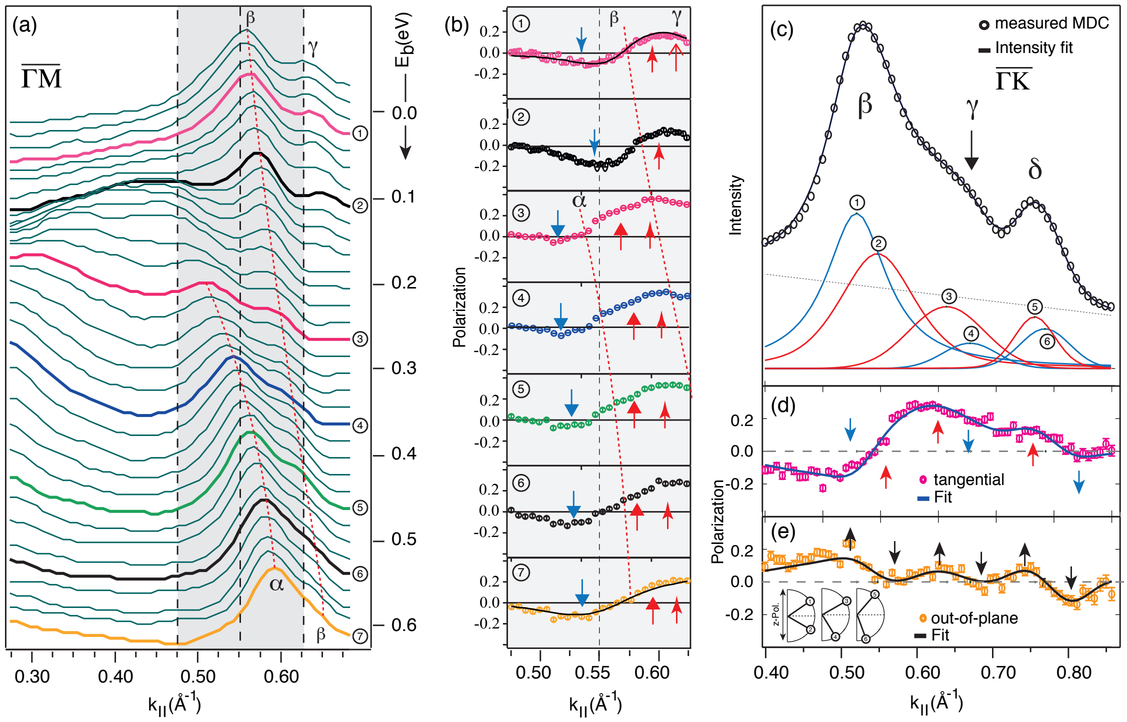

Figure 59: *(a) Spin-integrated momentum distribution curves as a function of binding energy. (b) Measured tangential spin polarization data at various values of E_b; the numbers correspond to those in (a). (c) Measured total intensity MDC at the Fermi level and corresponding spin polarization data and fits along the tangential direction (d) and the z-direction (e). The inset of (e) shows the out-of-plane rotation of the spin polarization vectors at increasing in-plane momentum obtained from the self-consistent two-step fit.*

is seen from a comparison between the measurements at $E_b \approx 0.6$ eV and E_F (Fig. 59 (b)). Scan 7 indicates that the spin-up peak (indicated by the second up-arrow at $k_{||} \approx 0.64$ Å^{-1}) is located at lower $k_{||}$ than the corresponding spin-down peak (not measured). In contrast, the analysis of scan 1 reveals that the spin-down peak is at lower momentum than the corresponding spin-up peak. This means, in between $E_b = 0.6$ eV and E_F the Rashba constant of the band changed its sign as it disperses toward E_F. Indeed, when we compare scan 3 (at ≈ 0.25 eV) with scan 2 (at ≈ 0.1 eV) we can localize this sign change, which is close to the avoided crossing point (cf. Fig. 57 (b)). This behavior is therefore different from the one of the α-band, where both the sign of the effective mass and the sign of the momentum splitting are changed.

To unravel how the spin textures of these bands interplay, we have performed a SR-MDC (single Mott) at the Fermi level in an extended momentum range and along the $\overline{\Gamma}$-$\overline{\mathrm{K}}$ high symmetry direction. The results are shown in Figs. 59 (c-e). First of all, the larger measured momentum range allows to investigate the spin texture of three $p_{x,y}$ bands (labeled as β, γ, δ) at the Fermi level. Figure 59 (c) shows the spin-integrated MDC, and in (d) and (e) we show tangential and out-of-plane polarization data together with our analysis, respectively. There is a clear difference between the P_z and P_{tan} data. While the z-polarization reveals a spin configuration of alternating up-down spin pairs, the tangential polarization shows down-up-up-down-up-down excursions. This means the Rashba constant changes sign between the β-band and the γ-band. Furthermore, it is found that the out-of-plane rotation of the spin polarization vector increases with the in-plane momentum, which is understood by the fact that states of $p_{x,y}$ orbital symmetry are more sensitive to the in-plane gradient of a potential. This finding is nicely in line with the observations for the high-Z metal surface alloys, e.g. Bi/Ag(111) [145].

7.3 Discussion

We start the discussion on the origin of the measured spin structure with Figure 60 (a) which displays the band dispersion of 8 ML Pb on Bi-$\sqrt{3}$/Si(111). Two different hybridization effects are common for this system. Around the $\overline{\Gamma}$ point the hybridization of the $6p_z$ derived QWS of the ultra-thin Pb film with the Si substrate states leads to quantum well resonances. This is seen by the sudden intensity drop in the measured photocurrent and by the larger peak widths as the electron-like dispersion enters the region of the heavy hole (HH) and the light hole (LH) bands. DFT calculations show that the HH band is of p_x orbital symmetry, while the LH band is mainly of p_z symmetry [104]. Although the valence band of Si is composed of p-like orbitals, an avoided crossing between the $6p_z$ QWS and the HH and the LH states is not observed. A similar hybridization scenario was also reported for Al/Si(111) [105]. This is understood by the fact that avoided crossing of bands occurs when the eigenfunctions belong to the same irreducible representation of a space group of the lattice; Pb crystallizes in the face-centered cubic structure (space group O_h^5) and Si in the diamond structure (space group O_h^7) [122].

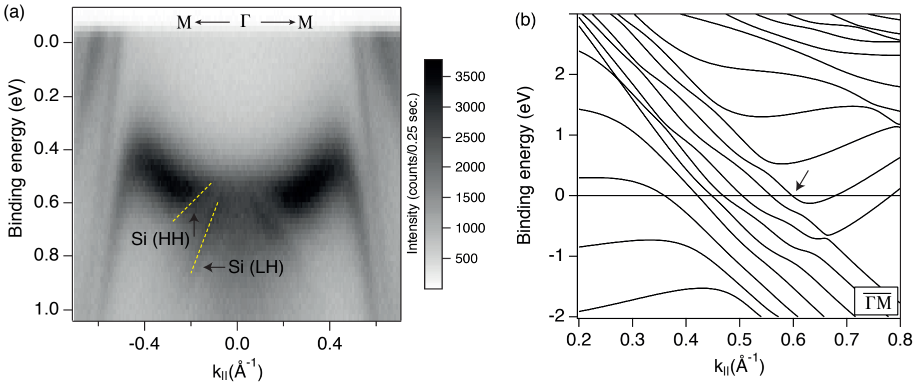

Figure 60: *(a) Electronic structure of a 8 ML Pb film on Bi/Si. Notice the hybridization between the $6p_z$ states of the Pb film with the heavy hole (HH) and light hole (LH) bands of the Si substrate. (b) Magnification of a calculated band structure into the avoided crossing region.*

Figure 60 (b) displays the band structure region of an ultra-thin Pb film (8 ML) where the second type of hybridization dominates. The avoided crossings of the bands are well reproduced by taking SOI into account. At larger momenta it is seen that the $p_{x,y}$ band that crosses E_F at $k_\parallel \approx 0.6$ Å^{-1} (the crossing is marked by an arrow), continues with an electron-like dispersion, adapted from an electron-like band, as long as no hybridization with a neighboring $p_{x,y}$ band occurs. As will be shown below this property has an important influence on the spin texture of the downward dispersing bands in between.

Figures 61 (a, b) summarize our main findings concerning the spin texture of the α-band. Figure 61 (a) displays our measured spin splittings of the α-band for the full investigated momentum range and in (b) we draw a schematic band dispersion based on our findings. In going away from the $\overline{\Gamma}$ point, the spin splitting increases with the in-plane momentum, in accordance with the Rashba model. In between $k_\parallel = 0.34$ and 0.5 Å^{-1}, the measured energy splittings are found to decrease with the in-plane momentum. Such a behavior is in sharp contrast to the Rashba model and was also observed in 1 ML Au on W(110) [183] (cf. Fig. 32 (d) of Sec. 5.2.2). We conjecture that hybridization starts to develop at the inflection point, i.e. as the interaction between the α- and the adjacent β-band increases the energy splittings decrease. Finally, beyond the avoided crossing point the spin splitting recovers with a larger slope as a consequence of the smaller effective mass, since $\Delta E \propto \alpha_{RB} \propto 1/m^\star$. Furthermore we find that the relative spin helicities of the spin-split components of the α-band are reversed upon passing the momentum region where the band bends downward. Figure 61 (b) displays schematically the spin texture along the dashed line.

Figures 61 (c, d) explain qualitatively the hybridization mechanism as revealed from the SARPES measurements. The SOI-induced avoided crossing hybridization between the α- and the β-band leads to a gap opening and a sign reversal in the effective mass of both bands. Close to the gap the states hybridize by mixing the orbital symmetry and the spin character of the corresponding wave functions. That way the α-band adapts the spin and orbital character of the β-band, which leads to a reversal of the sign of the momentum splitting and of the effective mass. On the other hand, beyond the hybridization gap the β-band continues to disperse with p_z character (i.e. $m^\star > 0$) adapted from the α-band and approaches the adjacent γ-band, as schematically drawn in Fig. 61 (c) for the case of no interaction between these bands. When we turn the avoided crossing hybridization on (Fig. 61 (d)), it is seen that the β-band adapts the $p_{x,y}$ orbital symmetry and the spin character of the γ-band. Consequently, it disperses again hole-like and with a relative order of momentum splitting given by the γ-band which leads to a hybridization-induced reversal of the Rashba constant. The same arguments apply for the next bands with $p_{x,y}$ symmetry, as long as other downward dispersing bands are present.

To gain a quantitative understanding of the SOI-induced hybridization we adapt an interband spin-orbit coupling model suggested in Ref. [181] which was successively used to explain the gap opening in the band dispersion of a strongly Rashba-type spin-split system formed in the surface alloy $BiAg_2$. This model assumes a hybridization between two Rashba branches with opposite spin direction. In the case of Pb/Bi/Si which represents a 2DEG with weak SOI due to the Rashba

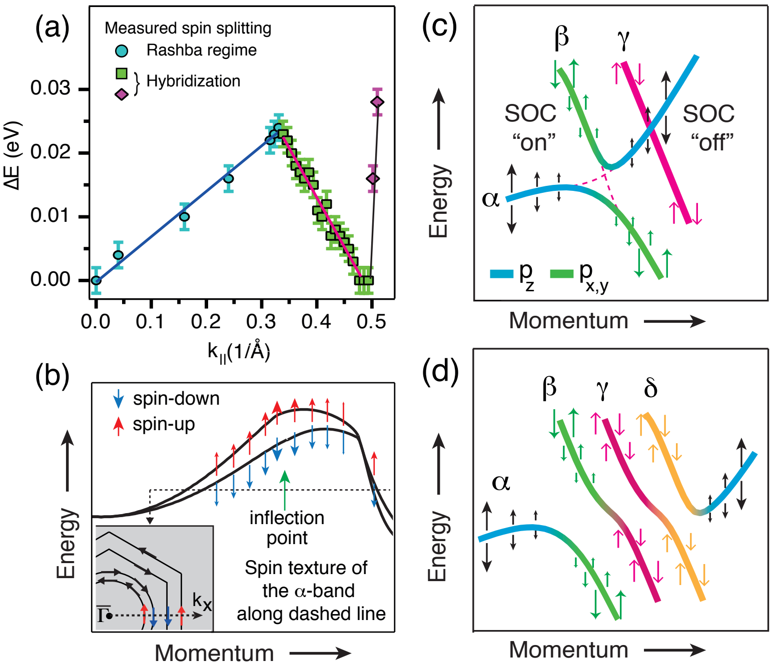

Figure 61: *(a) Measured k-dependent energy splittings of the α-band over the full investigated momentum range and linear fits. (b) Schematic drawing of the band splitting deduced from our fitting procedure to the experimental data. The inset shows the spin texture along the dashed line illustrating the sign reversal of the momentum splitting. (c) Schematic drawing of the resulting dispersion of the α- and the β-band when SOI-induced hybridization is taken into account. When the avoided hybridization is turned off, the β-band continues with an electron-like dispersion and crosses the γ-band. (d) Resulting schematic dispersion of the bands after the avoided crossing hybridization is turned on between the α- and the β-band, between the β- and the γ-band, and between the γ- and the δ-band.*

effect, we introduce the opening of two hybridization gaps, i.e.

$$\Delta_1 = \langle \alpha^+ | H_{\mathrm{SOC}} | \beta^- \rangle \qquad \Delta_2 = \langle \alpha^- | H_{\mathrm{SOC}} | \beta^+ \rangle \tag{64}$$

Here $|\alpha^\pm\rangle$ ($|\beta^\pm\rangle$) denotes the eigenstates of the Rashba Hamiltonian. The modified energy dispersion is calculated via [181]

$$H^\pm = \frac{1}{2}\left(\alpha^+ + \beta^-\right) \pm \sqrt{\left(\frac{\alpha^+ - \beta^-}{2}\right)^2 + \Delta_1^2} \tag{65}$$

$$G^\pm = \frac{1}{2}\left(\alpha^- + \beta^+\right) \pm \sqrt{\left(\frac{\alpha^- - \beta^+}{2}\right)^2 + \Delta_2^2} \tag{66}$$

where $\alpha^\pm$ and $\beta^\pm$ denote the spin-up (+) and spin-down (-) energy branches. Close to the avoided crossing point the interband SO coupling mixes the states $|\alpha^{\pm}\rangle$ and $|\beta^{\pm}\rangle$ in new eigenstates:

$$|H^{+}\rangle = h_k|\alpha^{+}\rangle + \sqrt{1-h_k^2}|\beta^{-}\rangle \tag{67}$$

$$|H^{-}\rangle = \sqrt{1-h_k^2}|\beta^{+}\rangle + h_k|\alpha^{-}\rangle \tag{68}$$

and

$$|G^{+}\rangle = g_k|\alpha^{-}\rangle + \sqrt{1-g_k^2}|\beta^{+}\rangle \tag{69}$$

$$|G^{-}\rangle = \sqrt{1-g_k^2}|\beta^{-}\rangle + g_k|\alpha^{+}\rangle \tag{70}$$

where h_k and g_k are k-dependent coefficients which determine the orbital and spin mixing ratio. Notice that the new eigenstates are formed by mixing of Rashba states with anti-parallel spins. Before we discuss the modification of the α-band dispersion induced by the interband spin-orbit coupling, we display in Fig. 62 (a) the eigenvalues of the α and β bands according to the Rashba model. For the β-band we use a momentum splitting of $2k_0 = 0.021$ Å^{-1} as obtained from the two-step fit presented in Figs. 59 (c-e) and an effective mass of $m^{\star} \approx -0.5\ m_e$. It is clear that this model alone can neither explain the sign reversal in the effective mass of the α-band nor the modified spin structure of the α- and the β-band across the avoided crossing point.

Figure 62 (b) shows the results of applying the interband SO coupling model, in addition to the Rashba-type SOI, on the energy dispersion of the α-band. We find a good agreement between the experimental data and the calculated dispersion by introducing a interband SO coupling strength of $\Delta_{1,2} = 120$ meV.

In contrast to the surface alloy BiAg$_2$ investigated in Ref. [181] where the Rashba-type SOC is larger than the interband SOC ($\Delta \approx 30$ meV, $E_{RB} = \alpha_{RB}^2 m^{\star}/(2\hbar^2) \approx 300$ meV), the relative energy scale of SOC induced by the Rashba effect and by the interband coupling is inverted for Pb/Bi/Si. We find the interband contribution to be three orders of magnitude stronger than the Rashba contribution, $E_{RB} = 0.23$ meV. The larger Δ in Pb/Bi/Si(111) by a factor of four compared to the one found in BiAg$_2$ is understood by the fact that in Pb/Bi/Si a Rashba-split electron-like band interacts with a Rashba-split hole-like band. In BiAg$_2$ the interband SO coupling mixes electronic states which all disperse with $m^{\star} < 0$. The sign change of the momentum splitting for the α-band is a direct spectroscopic evidence of the mixed and k-dependent (via h_k and g_k) spin character of the corresponding new wave functions.

In the following we demonstrate that in Pb/Bi/Si the interband SO coupling occurs between bands with anti-parallel spins, instead of a coupling of bands with parallel spins. Although the latter scenario can also explain the modification of the α-band dispersion (see dashed lines in Fig. 62 (b)), it fails to qualitatively reproduce the measured spin splittings as a function of momentum in the hybridization region, i.e. in the momentum region starting at the inflection point. A comparison between both models and the data is shown in Fig. 62 (c). The model of interband SO coupling of states with parallel spins neither predicts a decrease of the spin splitting, nor a vanishing spin splitting along the band dispersion. In contrast, the model of the coupling of states with anti-parallel spin matches qualitatively the experimental data. That the energy splitting between the

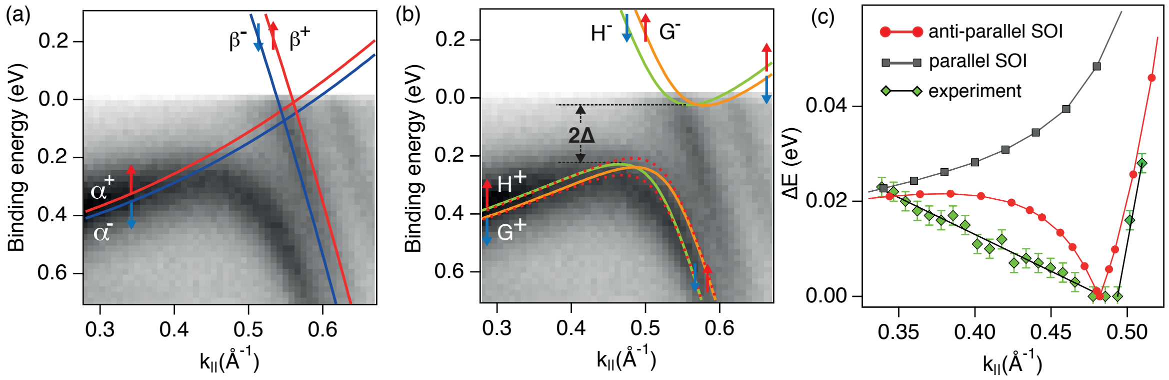

Figure 62: *(a) Comparison of the band structure in the avoided crossing region with the solution of the Rashba Hamiltonian. (b) The same region as in (a) overlaid by the new solutions of the model Hamiltonian incorporating SOI due to the Rashba effect and due the interband SO coupling for an interaction of strength* $\Delta_{1,2} = 120$ *meV. (c) Energy splitting as a function of* $k_{\|}$ *in the hybridization region that starts at the inflection point. The measured spin splittings are compared with an interband SO coupling model that mixes states with parallel (red diamonds) and anti-parallel (circles) spins. A closer match to the experimental findings is achieved with anti-parallel interband SO coupling.*

H^+ and the G^+ branch does not decrease linearly with momentum may serve as an indication that the degree of the spin polarization of the new eigenstates ($|H^+\rangle$, $|G^+\rangle$) which are formed by the superposition of the Rashba spinors with opposite spin directions, is no longer 100%. Indeed, theory predicts that toward the avoided crossing point the spin polarization of the states $|H^\pm\rangle$ and $|G^\pm\rangle$ reduces according to [184, 185]

$$P(k_{\|})^{H^\pm} = \frac{(\alpha^+_{k_{\|}} - \beta^-_{k_{\|}})}{\sqrt{(\alpha^+_{k_{\|}} - \beta^-_{k_{\|}})^2 + 4\Delta^2}} \tag{71}$$

$$P(k_{\|})^{G^\pm} = \frac{(\alpha^-_{k_{\|}} - \beta^+_{k_{\|}})}{\sqrt{(\alpha^-_{k_{\|}} - \beta^+_{k_{\|}})^2 + 4\Delta^2}} \tag{72}$$

Consequently the measured spin polarization of the α-band toward the crossing point is reduced (i) due to the crossing of branches H^+ and G^+ and (ii) because the spin polarization of each branch is reduced due to the mixed spin character. Another indication of the action of the spin-flip term is that both bands H^+ and G^+ change their spin direction when passing the crossing point. If the spin-conserving term would dominate the spin character would not change when going along these bands [186]. Whether the action of the spin-flip, or the spin-conserving term of the SOC operator is present in a system, depends on the details of the orbital symmetry of the interacting wave functions. For example, if the β-band were p_z derived then $\Delta^{\uparrow,\downarrow} = 0$ and $\Delta^{\uparrow(\downarrow),\uparrow(\downarrow)} \neq 0$, i.e. the spin-conserving part would dominate.

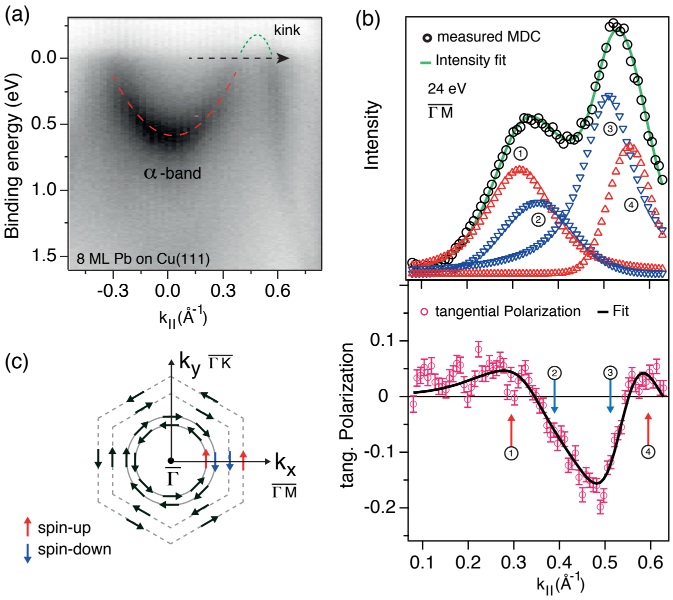

Figure 63: *(a) Band structure of a 8 ML thick Pb film on Cu(111). The dashed line is a fit of the k-dependent intensity maxima to quantify the effective mass. The dashed arrow indicates the location of the spin-resolved measurement. (b) (upper panel) Spin-integrated momentum distribution curve and decomposition into four peaks as revealed from the two-step fitting routine and (lower panel) tangential spin polarization data and fit. (c) Spin texture of the α-band in Pb/Cu(111) at E_F.*

7.4 Pb/Cu(111)

In the following we substantiate that the interband SO coupling, which explains (i) the modification of the dispersion of the α-band and (ii) the sign reversal in the momentum splitting, is independent of the supporting substrate by studying QWS in Pb/Cu(111)[15] [187–191].

Figure 63 (a) shows the electronic structure of 8 ML Pb on Cu(111). The Pb film was deposited from a water-cooled e-beam evaporator, at a pressure below 3×10^{-10} mbar, onto a Cu(111) sample held at 80 K, and cleaned before deposition by Ar ion bombardment and annealing. In contrast to the electronic structure of Pb/Bi/Si the effective mass of the α-band is significantly reduced from $m^{\star} = 3.2\ m_e$ to $0.86\ m_e$, and the pronounced change in the dispersion is situated above the Fermi level. The enhanced dispersion allows to perform a SR-MDC indicated by the dashed arrow in Fig. 63 (a). The results and our analysis are displayed in Figs. 60 (b, c) where we show the measured spin-integrated MDC close to E_F and the tangential spin polarization data, respectively. We find a sign change in the momentum splitting of the α-band which is consistent with previous results obtained from Pb QWS on the Bi reconstructed Si. This is further illustrated by comparing Fig. 63(c), which displays the spin alignment at E_F, with the inset of Fig. 61(b).

---

[15] Data from Pb QWS on Cu(111) was taken by J. H. Dil and F. Meier. Analysis of the data was performed by B. Slomski.

7.5 Conclusions

To summarize, we have identified a momentum region in Pb QWS where the description of the Rashba effect breaks down due to the interband spin-orbit coupling. Essential is that this coupling leads to a hybridization of Rashba states with *anti-parallel* spins thereby causing the pronounced change in the dispersion of the α-band, a sign change of the momentum splitting, and in particular a vanishing spin splitting toward the avoided crossing point. These modifications clearly reflect the SOC-induced hybridization mechanism because of the mixed spin and orbital character of the new wave functions. This finding is consistent with the results obtained from QWS in Pb on Cu(111). Furthermore, we have found that the interband contribution in Pb/Bi/Si is three orders of magnitude stronger then the SOI contribution by the Rashba effect. It is expected that this ratio is smaller in Pb/Pb/Si and larger in Pb/Ag/Si due to the different effective masses of the α-band.

8 Summary and outlook

The main goal of this thesis was to investigate possible mechanisms leading to a modification of the Rashba-Bychkov effect in Pb QWS. Our approach was to first explore the influence of the interface on the Rashba effect in the ultra-thin Pb film by studying the interfactants Pb, Bi and Ag, sandwiched between the metal Pb film and the semiconducting Si substrate. The following statements were known and served as a motivation of this thesis.

- The Rashba splitting in Pb QWS is generated at each Pb layer, where the asymmetric charge distribution around the nuclei determines the sign and the magnitude of the spin splitting. SARPES measures the sum of all layer specific contributions.
- The Rashba effect shows no significant dependence on the overlayer thickness.
- The spin helicity of the spin texture of Pb QWS is inverted with respect to the one found for the surface state on Au(111).

The main findings obtained in this thesis are summarized as follows:

- The spin splitting and the spin texture of Pb QWS on Si(111) can be manipulated by altering the interface:
  The Rashba parameter is reduced from $\alpha_{Pb} = 0.076$ eVÅ on the Pb interface by 60% down to $\alpha_{Bi} = 0.032$ eVÅ for Pb QWS on the Bi interface. The spin splitting of Pb QWS on the Ag reconstructed interface is below the experimental resolution of the COPHEE spectrometer.
- The spin polarization vector of QWS in Pb/Bi/Si is found to rotate by $\approx 32^\circ$ out of the sample plane along the crystallographic direction $\overline{\Gamma}$-$\overline{K}$, while being fully in-plane along $\overline{\Gamma}$-$\overline{M}$. The resulting 120° periodicity of the spin polarization reflects the $C_{3\nu}$ rotational symmetry of the (111) Pb surface

The vanishing Rashba splitting in Pb QWS on the Ag reconstructed Si can be interpreted by a QWS confined in an almost symmetric potential box in which the wave function has equal extensions into the metal-substrate and metal-vacuum barriers. Consequently the sum over all local spin splittings is zero. This system is therefore a promising candidate to study the reversal of the sign in the Rashba constant in Pb QWS upon the adsorption of e.g. alkali atoms to create an asymmetric confinement. Such a study is best performed with an ordered layer on the surface of the ultra-thin Pb film. LEED experiments and DFT calculations show that it is possible to form a $(\sqrt{3} \times \sqrt{3})R30^\circ$-K reconstruction on the surface of a Pb(111) single crystal that lowers the work function of the system by altering the surface dipole [192, 193].

From a technological point of view a study of the influence of oxidization of the ultra-thin Pb film on the QWS energies could provide further steps toward the realization of a device. In our experiments the exposure to the residual gas of the vacuum chamber has led only to a decreased signal-to-background ratio in the measured spectrum, while the QWS binding energy stayed constant, implying a non-sensitivity of the metal-vacuum phase shift on surface defects. It is expected that a fully oxidized PbO layer on top of the Pb(111) film alters this phase shift and correspondingly changes the confinement condition. A recent STM study demonstrated the ability to form smooth PbO islands on Pb(111) films and that the oxidation process can be enhanced by the presence of impurities formed by Cs atoms [194].

Especially noteworthy is that, by studying QWS in Pb films on the various interfaces, we have also encountered interesting phenomena in the more"traditional" fields of condensed matter physics such as band dispersions in low-dimensional systems or the Schottky barrier formation at the metal-semiconductor junction.

The ultra-thin Pb films on the $\sqrt{3}$-Pb interface feature an anomalous effective mass which was intensively debated in the literature. Based on our LEED study and DFT calculations we could unambiguously disentangle the origin of the flat dispersion as due to a decreased orbital overlap of the $6p_z$ states and hybridization between the $6p_z$ and $6p_{x,y}$ states. To further understand what mechanism influences the in-plane lattice constant of the ultra-thin film and correspondingly the orbital overlap, we have systematically studied the electronic properties of the interfaces. Using the methods of quantum well spectroscopy and high-resolution core-level spectroscopy we have identified a correlation between the size of the interface dipole, formed between the Si atoms and the interfactants, and the effective mass. Furthermore, by using the *interface dipole model* to explain the Schottky barrier formation at a metal-semiconductor interface we could also quantify the barriers for the various interfactants. Our main findings are:

1. Among the studied interfaces the QWS in Pb/Pb/Si feature the highest effective mass .
2. The effective mass of the states in a 8 ML thick Pb film reduced from $\approx 10\ m_e$ on the Pb interface down to 3.2 m_e on the Bi interface. On the Ag interface we find the smallest effective mass of 2.4 m_e.
3. The strength of the interface dipole reduced in a similar way. That is, it is maximal for Pb/Pb/Si(111) with $\Delta_{Pb} = 450$ meV, while in Pb/Bi/Si we find $\Delta_{Bi} = 380$ meV, and for Pb/Ag/Si we compute $\Delta_{Ag} = 330$ meV.
4. The Schottky barrier is found to increase with increasing interface dipole strength. For Pb/Pb/Si we find a barrier of 0.65 eV, for Pb/Bi/Si the barrier reduces to 0.58 eV and finally in Pb/Ag/Si it is the smallest with 0.53 eV.

Finally, it is concluded that the in-plane lattice constant of the ultra-thin Pb film is influenced by the substrate-adsorbate interaction whose strength depends on the size of the interface dipole. The variation of this size is simply explained on the basis of the polarity of the interface bonds. The Pb-Si bond has the largest difference in the Miedema electronegativity resulting in the largest dipole among the studied interfaces. In a future experiment, one could try to increase the anomalous high effective mass or even induce a sign change in the effective mass, i.e. induce a change from electron- to hole-like dispersion, using an interfactant with a larger dipole size than in Pb/Pb/Si. Promising candidates for this study are e.g. Mg (electronegativity $X = 3.45$) [195] and Tl ($X = 3.9$) [196], which form $\sqrt{3}$ reconstructions on Si. For interfactants such as Au

($X = 5.15$) [197] or B ($X = 5.3$) [198] the exact opposite behavior is expected, i.e. an increase of the band dispersion with respect to the one in Pb/Ag/Si.

In the last step of our approach we have investigated the influence of the carrier concentration (donors and acceptors) of Si on the Rashba-type spin splitting in Pb QWS. Our main findings are:

1. A change in the donor concentration by a factor of 20 raised the Rashba constant by almost a factor of two:
   For Pb QWS on the lightly n-doped Si with a donor concentration of $N_D = 4.65 \cdot 10^{13}$ cm^{-3} we have deduced a Rashba parameter of $\alpha_{RB} = 0.07$ eVÅ while for Pb QWS on the heavily n-doped Si substrate ($N_D = 1.14 \cdot 10^{15}$ cm^{-3}) the Rashba constant is found to increase to 0.11 eVÅ.
2. Pb QWS on a heavily p-doped Si(111) feature the smallest Rashba parameter with $\alpha_{RB} = 0.061$ eVÅ among the system Pb/Pb/Si.
3. The Schottky barrier and the energetic position of the valence band edge of Si(111) at the interface depends on the carrier (donor or acceptor) concentration.

Concerning finding (1), we found - to our surprise - a rather strong response of the size of the Rashba effect on the donor concentration. In contrast to what we expected, the increase of the Rashba splitting is mediated by an increased localization of the QWS in the Pb film as revealed from density functional theory calculations and also indicated by the measured binding energies of the QWS at $\overline{\Gamma}$. The change of the degree of localization of the state in the Pb film is discussed in terms of the phase shift at the metal-substrate interface which is sensitive to the energetic position of the valence band edge of Si(111) at the interface. Consequently, this variation can only be explained by a variable Schottky barrier. Since the measured range of donor concentrations was rather small, it would be of particular interest to investigate n-type substrates with larger donor concentrations, i.e. $N_D > 10^{15}$ cm^{-3}, for further SARPES measurements. Here, the remaining question is, how far can the Rashba parameter be tuned. Based on our model, we expect a transition, where the Rashba parameter decreases again as a function of donor concentration. Also an investigation of the Rashba effect on a lightly p-doped Si(111) could further corroborate our model, which predicts an increase of the Rashba splitting with decreasing acceptor concentration, i.e. the exact opposite behavior as found for Pb QWS on n-type Si.

As theoretically demonstrated a gate voltage of ≈ 12 V applied to an ultra-thin Pb film on the lightly n-doped Si is enough to reach the conditions found in Pb on the heavily n-doped Si, i.e. the increased interface dipole screening and the corresponding larger Rashba splitting. A SARPES experiment performed at Pb/Si as a function of an applied gate voltage could readily demonstrate the potential of Pb/Si for spin-FET application. One could also think of a gate voltage dependent scanning tunneling spectroscopy (STS) measurement performed at Pb/Si where the spin splitting manifests itself in a singularity in the local density of states [199]. That way, a change of the spin splitting as a function of a gate voltage could be also measured.

In the following we would like to motivate a spin-resolved ARPES experiment with time-resolution, such as frequently used in two-photon photoemission experiments (2PPE) [200]. Based on our findings on the tunability of the Rashba effect in Pb QWS via a variable Schottky barrier and on the results published in Ref. [178], we expect a dependence of the spin splitting as a function of the delay time between the pump and probe pulse. In fact, a change of the spin splitting should be also observed using a cw-laser, whose light modifies the charge density at the interface and correspondingly the Schottky barrier.

At last, we have identified a breakdown of the Rashba effect in Pb QWS by studying a momentum region, where avoided crossing hybridization induced by the interband spin-orbit coupling alters the band structure significantly. Our findings are summarized in the following points:

1. The interband spin-orbit coupling mixes Rashba states of opposite spin directions, thereby causing a sign reversal in the effective mass of the QWS band dispersion and a sign change in the characteristic momentum splitting.
2. Within the hybridization region specified by the in-plane momentum range of $k_{\|} \in [0.34, 0.5]$ Å^{-1} the measured spin splittings are found to decrease with $k_{\|}$, which is in sharp contrast to the Rashba model.
3. The decrease of the spin splitting as a function of momentum is qualitatively better described with an interband SOC model, which assumes a coupling between Rashba states with *anti-parallel*, rather than parallel spins.
4. Beyond the momentum region of the mass reversal the spin splitting of the QWS is found to recover again, however, with a reversed sign in the momentum splitting. This finding reflects the mixed orbital and spin character of the new eigenstates due to the SOI-induced hybridization.
5. This sign reversal of the momentum splitting of the QWS band dispersion is also observed in an ultra-thin Pb film on Cu(111) and is therefore related to the particular band structure of the ultra-thin Pb film.
6. The $6p_{x,y}$ derived bands, which cross the Fermi level, are found to be also spin-split. The avoided crossing hybridization induces, in contrast to the QWS band, a reversal of the sign of the Rashba parameter as the bands disperse toward E_F.

Especially finding (6), which shows that the states at the Fermi level are spin-polarized makes Pb/Si an ideal system for a spin-FET device. It is expected that the found mechanisms to manipulate the Rashba effect obtained for the $6p_z$ derived states are also applicable for these bands. We would like to emphasize that also in this system a spin-resolved 2PPE experiment, that probes the unoccupied states, could provide more insight into the subtle interplay of the hybridization above the Fermi level.

References

[1] W. Gerlach and O. Stern. *Das magnetische moment des Silberatoms.* Zeitschrift für Physik A Hadrons and Nuclei, **9**, 353–355 (1922)

[2] W. Demtröder. *Experimentalphysik 3: Atome, Moleküle und Festkörper. Springer-Lehrbuch* (2010)

[3] P. Grünberg, R. Schreiber, Y. Pang, M. B. Brodsky, and H. Sowers. *Layered magnetic structures: evidence for antiferromagnetic coupling of Fe layers across Cr interlayers. Phys. Rev. Lett.*, **57**, 2442–2445 (1986)

[4] M. N. Baibich *et al. Giant magnetoresistance of Fe(001)/Cr(001) magnetic superlattices.* Phys. Rev. Lett., **61**, 2472–2475 (1988)

[5] S. Blügel, D. Bürgler, M. Morgenstern, C. M. Schneider, and R. Waser. *Spintronics - From GMR to quantum information.* Forschungszentrum Jülich GmbH, Institut für Festkörperforschung (2009)

[6] G. A. Prinz. *Magnetoelectronics. Science*, **282**, 1660–1663 (1998)

[7] S. Datta and B. Das. *Electronic analog of the electro-optic modulator.* Applied Physics Letters, **56**, 665–667 (1990)

[8] Y. A. Bychkov and E. I. Rashba. *Oscillatory effects and the magnetic susceptibility of carriers in inversion layers.* Journal of Physics C: Solid State Physics, **17**, 6039–6045 (1984)

[9] G. Dresselhaus. *Spin-orbit coupling effects in zinc blende structures.* Phys. Rev. Lett., **100**, 580–586 (1955)

[10] Heinrich Hertz. *Über den Einfluss des ultravioletten Lichtes auf die elektrische Entladung.* Annalen der Physik, **31** (1987)

[11] A. Einstein. *Über einen die Erzeugung und Verwandlung des Lichtes betreffenden heuristischen Gesichtspunkt.* Annalen der Physik, **17**, 132 (1905)

[12] S. Huefner. *Photoelectron spectroscopy - principles and applications.* Springer (2010)

[13] S.D. Kevan. *Angle-resolved photoemission - theory and current applications.* Elsevier (1992)

[14] W. Schattke and M.A. Van Hove. *Solid-state photoemission and related methods.* WILEY-VCH (2003)

[15] A. Damascelli, Z. Hussain, and Z.-X. Shen. *Angle-resolved photoemission studies of the cuprate superconductors.* Rev. Mod. Phys., **75**, 473–541 (2003)

[16] J. Kessler. *Polarized electrons, 2nd edition.* Springer, Berlin Heidelberg (1985)

[17] U. Heinzmann and J. H. Dil. *Spin-orbit-induced photoelectron spin polarization in angle-resolved photoemission from both atomic and condensed matter targets.* Journal of Physics: Condensed Matter, **24**, 173001 (2012)

[18] J. Osterwalder. *Can spin-polarized photoemission measure spin properties in condensed matter?* Journal of Physics: Condensed Matter, **24**, 171001 (2012)

[19] U. Fano. *Spin orientation of photoelectrons ejected by circularly polarized light.* Phys. Rev., **178**, 131 – 136 (1969)

[20] J. Kirschner and R. Feder. *Spin polarization in double diffraction of low energy electrons from W(001): experiment and theory.* Phys. Rev. Lett., **42**, 1008 – 1011 (1979)

[21] N. F. Mott. *The scattering of fast electrons by atomic nuclei.* Proceedings of the Royal Society of London. Series A, **124**, 425 – 442 (1929)

[22] J. H. Dil. *Spin and angle resolved photoemission on non-magnetic low-dimensional systems.* Journal of Physics: Condensed Matter, **21**, 403001 (2009)

[23] P. D. Johnson. *Spin-polarized photoemission.* Reports on Progress in Physics, **60**, 1217 (1997)

[24] M. Hoesch. *Spin-resolved Fermi surface mapping.* PhD thesis, Universität Zürich (2002)

[25] V. N. Petrov, M. S. Galaktionov, and A. S. Kamochkin. *Comparative tests of conventional and retarding-potential Mott polarimeters.* Review of Scientific Instruments, **72**, 3728 – 3730 (2001)

[26] V. N. Petrov, V. V. Grebenshikov, B. D. Grachev, and A. S. Kamochkin. *New compact classical 40 kV Mott polarimeter.* Review of Scientific Instruments, **74**, 1278 – 1281 (2003)

[27] V. N. Petrov, V. V. Grebenshikov, A. N. Andronov, P. G. Gabdullin, and A. V. Maslevtcov. *Ultrafast compact classical Mott polarimeter.* Review of Scientific Instruments, **78**, 025102 (2007)

[28] F. Meier, J. H. Dil, and J. Osterwalder. *Measuring spin polarization vectors in angle-resolved photoemission spectroscopy.* New Journal of Physics, **11**, 125008 (2009)

[29] F. Meier. *Rashba-type spin-orbit coupling in the surface alloys on Ag(111) probed by spin- and angle-resolved photoemission spectroscopy.* PhD thesis, Universität Zürich (2011)

[30] W. Moench. *Oberflächenphysik des Festkörpers.* Teubner Studiennücher (1994)

[31] K. Schwarz and P. Blaha. *Solid state calculations using Wien2k.* Computational Materials Science, **28**, 259 – 273 (2003)

[32] W. Kohn and L. J. Sham. *Self-consistent equations including exchange and correlation effects.* Phys. Rev., **140**, A1133 – A1138 (1965)

[33] J. P. Perdew, K. Burke, and M. Ernzerhof. *Generalized gradient approximation made simple.* Phys. Rev. Lett., **77**, 3865 – 3868 (1996)

[34] P. Hohenberg and W. Kohn. *Inhomogeneous electron gas.* Phys. Rev., **136**, B864 – B871 (1964)

[35] P. M. Echenique and J. B. Pendry. *The existence and detection of Rydberg states at surfaces.* Journal of Physics C: Solid State Physics, **11**, 2065 – 2075 (1978)

[36] E. G. McRae. *Electronic surface resonances of crystals.* Rev. Mod. Phys., **51**, 541 – 568 (1979)

[37] T. C. Chiang. *Photoemission studies of quantum well states in thin films.* Surface Science Reports, **39**, 181 – 235 (2000)

[38] M. Milun, P. Pervan, and D. P. Woodruff. *Quantum well structures in thin metal films: simple model physics in reality?* Reports on Progress in Physics, **65**, 99 – 141 (2002)

[39] R. Otero, A. L. Vázquez de Parga, and R. Miranda. *Observation of preferred heights in Pb nanoislands: a quantum size effect.* Phys. Rev. B, **66**, 115401 (2002)

[40] D. A. Ricci, T. Miller, and T.-C. Chiang. *Chemical tuning of metal-semiconductor interfaces.* Phys. Rev. Lett., **93**, 136801 (2004)

[41] C. M. Wei and M. Y. Chou. *Theory of quantum size effects in thin Pb(111) films.* Phys. Rev. B, **66**, 233408 (2002)

[42] A. Mugarza, J. E. Ortega, A. Mascaraque, E. G. Michel, K. N. Altmann, and F. J. Himpsel. *Probing unoccupied bulk bands via the cross section of quantum well states in thin films.* Surface Science, **482 - 485**, 464 – 469 (2001)

[43] A. Mugarza *et al.* *Accurate band mapping via photoemission from thin films.* Phys. Rev. B, **69**, 115422 (2004)

[44] A. Mans, J. H. Dil, A. R. H. F. Ettema, and H. H. Weitering. *Quantum electronic stability and spectroscopy of ultrathin Pb films on Si(111)-*(7×7)*.* Phys. Rev. B, **66**, 195410 (2002)

[45] M. Jałochowski, M. Hoffman, and E. Bauer. *Quantized Hall effect in ultrathin metallic films.* Phys. Rev. Lett., **76**, 4227 – 4229 (1996)

[46] N. Miyata, K. Horikoshi, T. Hirahara, S. Hasegawa, C. M. Wei, and I. Matsuda. *Electronic transport properties of quantum-well states in ultrathin Pb(111) films.* Phys. Rev. B, **78**, 245405 (2008)

[47] X. Ma *et al.*. *Experimental observation of quantum oscillation of surface chemical reactivities.* Proceedings of the National Academy of Sciences, **104**, 9204 – 9208 (2007)

[48] M. Jałochowski and E. Bauer. *Quantum size and surface effects in the electrical resistivity and high-energy electron reflectivity of ultrathin lead films.* Phys. Rev. B, **38**, 5272 – 5280 (1988)

[49] D. Eom, S. Qin, M.-Y. Chou, and C. K. Shih. *Persistent superconductivity in ultrathin Pb films: A scanning tunneling spectroscopy study.* Phys. Rev. Lett., **96**, 027005 (2006)

[50] T.-L. Chan, C. Z. Wang, M. Hupalo, M. C. Tringides, and K. M. Ho. *Quantum size effect on the diffusion barriers and growth morphology of Pb/Si(111).* Phys. Rev. Lett., **96**, 226102 (2006)

[51] J. H. Dil, T. U. Kampen, B. Hülsen, T. Seyller, and K. Horn. *Quantum size effects in quasi-free-standing Pb layers.* Phys. Rev. B, **75**, 161401 (2007)

[52] L.-Y. Ma *et al.* *Quantum size effect on adatom surface diffusion.* Phys. Rev. Lett., **97**, 266102 (2006)

[53] K. L. Man, M. C. Tringides, M. M. T. Loy, and M. S. Altman. *Anomalous mass transport in the Pb wetting layer on the Si(111) surface.* Phys. Rev. Lett., **101**, 226102 (2008)

[54] R. T. Tung. *Recent advances in Schottky barrier concepts.* Materials Science and Engineering Reports, **35**, 1 – 138 (2001)

[55] W. Schottky. *Zur Halbleitertheorie der Sperrschicht- und Spitzengleichrichter.* Zeitschrift für Physik A Hadrons and Nuclei, **113**, 367 – 414 (1939)

[56] Raymond T. Tung. Formation of an electric dipole at metal-semiconductor interfaces. *Phys. Rev. B*, **64**, 205310 (2001)

[57] H. Fujitani and S. Asano. *Schottky barriers at* $\mathrm{NiSi_2}$*/Si(111) interfaces.* Phys. Rev. B, **42**, 1696 – 1704 (1990)

[58] R. G. Dandrea and C. B. Duke. *Interfacial atomic composition and Schottky barrier heights at the Al/GaAs(001) interface.* Proceedings of the 20th annual conference on the physics and chemistry of semiconductors interfaces, **11**, 1553 – 1558 (1993)

[59] Raymond T. Tung. *Chemical bonding and Fermi level pinning at metal-semiconductor interfaces.* Phys. Rev. Lett., **84**, 6078 – 6081 (2000)

[60] R. T. Tung, J. M. Gibson, and J. M. Poate. *Formation of ultrathin single-crystal silicide films on Si: Surface and interfacial stabilization of Si-Ni*$\mathrm{Si_2}$ *epitaxial structures.* Phys. Rev. Lett., **50**, 429 – 432 (1983)

[61] R. T. Tung. *Schottky-barrier formation at single-crystal metal-semiconductor interfaces.* Phys. Rev. Lett., **52**, 461 – 464 (1984)

[62] D. R. Heslinga, H. H. Weitering, D. P. van der Werf, T. M. Klapwijk, and T. Hibma. *Atomic-structure-dependent Schottky barrier at epitaxial Pb/Si(111) interfaces.* Phys. Rev. Lett., **64**, 1589 – 1592 (1990)

[63] D. A. Ricci, T. Miller, and T.-C. Chiang. *Controlling the thermal stability of thin films by interfacial engineering.* Phys. Rev. Lett., **95**, 266101 (2005)

[64] K. Takayanagi *et al. Structure analysis of Si(111)-(7×7) reconstructed surface by transmission electron diffraction.* Surface Science, **164**, 367 – 392 (1985)

[65] J. Ortega, F. Flores, and A. L. Yeyati. *Electron correlation effects in the Si(111)-(7×7) surface.* Phys. Rev. B, **58**, 4584 – 4588 (1998)

[66] R. Losio, K. N. Altmann, and F. J. Himpsel. *Fermi surface of Si(111)-(7×7).* Phys. Rev. B, **61**, 10845 – 10853 (2000)

[67] I. Barke, Fan Zheng, A. R. Konicek, R. C. Hatch, and F. J. Himpsel. *Electron-phonon interaction at the Si(111)-(7×7) surface.* Phys. Rev. Lett., **96**, 216801 (2006)

[68] M. D'angelo *et al. Conductivity of the Si(111)-(7×7) dangling-bond state.* Phys. Rev. B, **79**, 035318 (2009)

[69] R. I. G. Uhrberg, T. Kaurila, and Y.-C. Chao. *Low-temperature photoemission study of the surface electronic structure of Si(111)-(7×7).* Phys. Rev. B, **58**, R1730 – R1733 (1998)

[70] C. J. Karlsson, E. Landemark, Y.-C. Chao, and R. I. G. Uhrberg. *Atomic origins of the surface components in the Si 2p core-level spectra of the Si(111)-(7×7) surface.* Phys. Rev. B, **50**, 5767 – 5770 (1994)

[71] I. B. Altfeder, V. Narayanamurti, and D. M. Chen. *Imaging subsurface reflection phase with quantized electrons.* Phys. Rev. Lett., **88**, 206801 (2002)

[72] G. Binnig, H. Rohrer, Ch. Gerber, and E. Weibel. *(7×7) reconstruction on Si(111) resolved in real space.* Phys. Rev. Lett., **50**, 120 – 123 (1983)

[73] C. Cheng and K. Kunc. *Structure and stability of Bi layers on Si(111) and Ge(111) surfaces.* Phys. Rev. B, **56**, 10283 – 10288 (1997)

[74] K. J. Wan, T. Guo, W. K. Ford, and J. C. Hermanson. *Initial growth of Bi films on a Si(111) substrate: Two phases of* $(\sqrt{3} \times \sqrt{3})$ *low-energy-electron-diffraction pattern and their geometric structures.* Phys. Rev. B, **44**, 3471 – 3474 (1991)

[75] T. Takahashi, S. Nakatani, T. Shikawa, and S. Kikuta. *Surface structure analysis of Si(111)-*$(\sqrt{3} \times \sqrt{3})$*-Bi by X-ray diffraction - approach to the solution of the phase problem.* Surface Science, **191**, L825 – L834 (1987)

[76] J. C. Woicik *et al.* *Structural determination of the Si(111)-($\sqrt{3} \times \sqrt{3}$)-Bi surface by X-ray standing waves and scanning tunneling microscopy.* Phys. Rev. B, **50**, 12246 – 12249 (1994)

[77] K. Hricovini, G. Le Lay, A. Kahn, A. Taleb-Ibrahimi, and J. E. Bonnet. *Initial stages of Schottky-barrier formation of Bi/Si(111) and Bi/Si(100) interfaces.* Applied Surface Science, **5658**, 259 – 263 (1992)

[78] J. C. Woicik *et al.* *Local bonding structure of Sb on Si(111) by surface extended X-ray-absorption fine structure and photoemission.* Phys. Rev. B, **43**, 4331 – 4339 (1991)

[79] M. Hupalo, J. Schmalian, and M. C. Tringides. *ıDevil's staircaseȷ in Pb/Si(111) ordered phases.* Phys. Rev. Lett., **90**, 216106 (2003)

[80] T.-L. Chan, C. Z. Wang, M. Hupalo, M. C. Tringides, Z.-Y. Lu, and K. M. Ho. *First-principles studies of structures and stabilities of Pb/Si(111).* Phys. Rev. B, **68**, 045410 (2003)

[81] V. Dudr *et al.* *Evidence for valence-charge fluctuations in the Si(111)-$\sqrt{3} \times \sqrt{3}$-Pb system.* Phys. Rev. B, **70**, 155334 (2004)

[82] J. A. Carlisle, T. Miller, and T.-C. Chiang. *Photoemission study of the growth, desorption, Schottky-barrier formation, and atomic structure of Pb on Si(111).* Phys. Rev. B, **45**, 3400 – 3409 (1992)

[83] Ph. Hofmann and J. W. Wells. *Surface-sensitive conductance measurements.* Journal of Physics: Condensed Matter, **21**, 013003 (2009)

[84] H. Aizawa, M. Tsukada, N. Sato, and S. Hasegawa. *Asymmetric structure of the Si(111)-Ag surface.* Surface Science, **429**, L509 – L514 (1999)

[85] I. Matsuda *et al.* *Electronic evidence of asymmetry in the Si(111)-$\sqrt{3} \times \sqrt{3}$-Ag structure.* Phys. Rev. B, **68**, 085407 (2003)

[86] T. Toshio *et al.* *X-ray diffraction study of the phase transition of the Si(111)-($\sqrt{3} \times \sqrt{3}$)-Ag surface.* Surface Review and Letters, **10**, 519 – 524 (2003)

[87] G. Le Lay, M. Goethelid, A. Cricenti, C. Håkansson, and P. Perfetti. *Atomic origins of the Si 2 p surface core-level shifts of the prototypical Si(111)/Ag structure.* Europhysics Letters, **45**, 65 (1999)

[88] M. Katayama, R. S. Williams, M. Kato, E. Nomura, and M. Aono. *Structure analysis of Si(111)-($\sqrt{3} \times \sqrt{3}$)$R30°$-Ag surface.* Phys. Rev. Lett., **66**, 2762 – 2765 (1991)

[89] I. Matsuda *et al.* *Evolution of Fermi surface by electron filling into a free-electron-like surface state.* Phys. Rev. B, **71**, 235315 (2005)

[90] H. Jeong, H. W. Yeom, and S. Jeong. *Adatom-induced variations of the atomic and electronic structures of Si(111)-($\sqrt{3}\times\sqrt{3}$)-Ag: a first-principles study.* Phys. Rev. B, **77**, 235425 (2008)

[91] G. Ertl and J. Küppers. *Low Energy Electrons and Surface Chemistry.* VCH Weinheim, 2nd Edition (1985)

[92] J. J. Yeh and I. Lindau. *Atomic Calculation of Photoionization Cross-Sections and Asymmetry Parameters.* Gordon and Breach Science Publishers, Langhorne, PE (USA) (1993)

[93] J. Peng *et al. Two-step oxidation of Pb(111) surfaces.* Chinese Physics Letters, **26**, 016803 (2009)

[94] Z. Hu, Y. Yang, B. Sun, X. Shao, W. Wang, and P. Zhang. *Quantum oscillations in adsorption energetics of atomic oxygen on Pb(111) ultrathin films: a density-functional theory study.* The Journal of Chemical Physics, **132**, 024703 (2010)

[95] M. H. Upton, C. M. Wei, M. Y. Chou, T. Miller, and T.-C. Chiang. *Thermal stability and electronic structure of atomically uniform Pb films on Si(111).* Phys. Rev. Lett., **93**, 026802 (2004)

[96] J. H. Dil, J. W. Kim, Th. Kampen, K. Horn, and A. R. H. F. Ettema. *Electron localization in metallic quantum wells: Pb versus In on Si(111).* Phys. Rev. B, **73**, 161308 (2006)

[97] K. Horn, B. Reihl, A. Zartner, D. E. Eastman, K. Hermann, and J. Noffke. *Electronic energy bands of lead: angle-resolved photoemission and band-structure calculations.* Phys. Rev. B, **30**, 1711 – 1719 (1984)

[98] B. J. Hinch, C. Koziol, J. P. Toennies, and G. Zhang. *Evidence for quantum size effects observed by helium atom scattering during the growth of Pb on Cu(111).* Europhysics Letters, **10**, 341 (1989)

[99] J. P. Perdew, K. Burke, and M. Ernzerhof. *Generalized gradient approximation made simple.* Phys. Rev. Lett., **77**, 3865 – 3868 (1996)

[100] P. Czoschke, Hawoong Hong, L. Basile, and T. C. Chiang. *Surface X-ray-diffraction study and quantum well analysis of the growth and atomic-layer structure of ultrathin Pb/Si(111) films.* Phys. Rev. B, **72**, 035305 (2005)

[101] P. Czoschke, Hawoong Hong, L. Basile, and T. C. Chiang. *Quantum size effects in the surface energy of Pb/Si(111) film nanostructures studied by surface X-ray diffraction and model calculations.* Phys. Rev. B, **72**, 075402 (2005)

[102] M. Hupalo, V. Yeh, T. L. Chan, C. Z. Wang, K. M. Ho, and M. C. Tringides. *Interface relaxation and electronic corrugation in the Pb/Si(111)-Pb-α-$\sqrt{3}\times\sqrt{3}$* Phys. Rev. B, **71**, 193408 (2005)

[103] M. H. Upton, T. Miller, and T.-C. Chiang. *Unusual band dispersion in Pb films on Si(111).* Phys. Rev. B, **71**, 033403 (2005)

[104] C. S. Wang and B. M. Klein. *First-principles electronic structure of Si, Ge, GaP, GaAs, ZnS, and ZnSe. I. Self-consistent energy bands, charge densities, and effective masses.* Phys. Rev. B, **24**, 3393 – 3416 (1981)

[105] L. Aballe, C. Rogero, P. Kratzer, S. Gokhale and K. Horn. *Probing interface electronic structure with overlayer quantum-well resonances: Al/Si(111). Phys. Rev. Lett.*, **87**, 156801 (2001)

[106] P. Moras *et al. Influence of the substrate bands on the sp-levels topology of Ag films on Ge(111).* Phys. Rev. B, **80**, 205418 (2009)

[107] W. Moench. *Electronic properties of semiconductor interfaces.* Springer Series in Surface Sciences, March 5th (2004)

[108] F. J. Himpsel, G. Hollinger, and R. A. Pollak. *Determination of the Fermi-level pinning position at Si(111) surfaces.* Phys. Rev. B, **28**, 7014 – 7018 (1983)

[109] K. Karlsson, O. Nyqvist, and J. Kanski. *Final-state effects in photoemission from metal-semiconductor interfaces.* Phys. Rev. Lett., **67**, 236 – 239 (1991)

[110] T. C. Chiang. *Core-level photoemission-studies of surfaces, interfaces, and overlayer.* Critical reviews in solid state and materials sciences, **14**, 269 – 317 (1988)

[111] G. Le Lay and K. Hricovini. *Comment on atomic-structure-dependent Schottky barrier at epitaxial Pb/Si(111) interfaces.* Phys. Rev. Lett., **65**, 807 – 807 (1990)

[112] D. A. Ricci, Y. Liu, T. Miller, and T.-C. Chiang. *Analyticity of the phase shift and reflectivity of electrons at a metal-semiconductor interface.* Phys. Rev. B, **79**, 195433 (2009)

[113] J. J. Paggel, T. Miller, and T.-C. Chiang. *Quantum-well states as Fabry-Pérot modes in a thin-film electron interferometer.* Science, **283**, 1709 – 1711 (1999)

[114] S. Ossicini and F. Bernardini. *Fermi-level pinning and interface states at Pb-Si(111) interface.* Solid State Communications, **82**, 863 – 866 (1992)

[115] J. Schmeidel, H. Pfnür, and C. Tegenkamp. *Coulomb blockade effects in Ag/Si(111): the role of the wetting layer.* Phys. Rev. B, **80**, 115304 (2009)

[116] *Handbook of Chemistry and Physics, 60th edition.* CRC, Boca Raton, FL (1980)

[117] S. M. Sze. *Physics of Semiconductor Devices.* Wiley, New York (1981)

[118] R. T. Tung. *Schottky barrier height - do we really understand what we measure?* J. Vac. Sci. Technol., B: Microelectronics and Nanometer Structures, **11**, 1546 –1552 (1993)

[119] W. F. Egelhoff. *Core-level binding-energy shifts at surfaces and in solids.* Surf. Sci. Rep., **6**, 253 – 415 (1987)

[120] J.J Sakurai and S. F.Tuan. *Modern Quantum Mechanics.* Prentice Hall (1993)

[121] J. D. Jackson. *Classical Electrodynamics.* John Wiley & Sons, New York (1999)

[122] T. Inui, Y. Tanabe, and Y. Onodera. *Group Theory and Its Applications in Physics.* Springer-Verlag (1990)

[123] Y. A. Bychkov and E. I. Rashba. *Properties of a 2D electron gas with lifted spectral degeneracy. JETP Lett.*, **39**, 78 (1984)

[124] J. Henk, A. Ernst, and P. Bruno. *Spin polarization of the L-gap surface states on Au(111).* Phys. Rev. B, **68**, 165416 (2003)

[125] Liang Fu. *Hexagonal warping effects in the surface states of the topological insulator* Bi_2Te_3. Phys. Rev. Lett., **103**, 12 (2009)

[126] Y. L. Chen *et al.* *Experimental realization of a three-dimensional topological insulator,* Bi_2Te_3. Science, **325**, 178 – 181 (2009)

[127] S. LaShell, B. A. McDougall, and E. Jensen. *Spin splitting of an Au(111) surface state band observed with angle resolved photoelectron spectroscopy.* Phys. Rev. Lett., **77**, 3419 – 3422 (1996)

[128] G. Nicolay, F. Reinert, S. Hüfner, and P. Blaha. *Spin-orbit splitting of the L-gap surface state on Au(111) and Ag(111).* Phys. Rev. B, **65**, 033407 (2001)

[129] M. Muntwiler *et al.* *Spin- and angle-resolved photoemission spectroscopy study of the Au(111) Shockley surface state.* J. Electron. Spectrosc. Relat. Phenom., **137 – 140**, 119 – 123 (2004)

[130] M. Hoesch *et al.* *Spin structure of the Shockley surface state on Au(111).* Phys. Rev. B, **69**, 241401 (2004)

[131] L. Petersen and P. Hedegrd. *A simple tight-binding model of spin-orbit splitting of sp-derived surface states.* Surface Science, **459**, 49 – 56 (2000)

[132] G. Bihlmayer, Y.M. Koroteev, P.M. Echenique, E.V. Chulkov, and S. Blügel. *The Rashba-effect at metallic surfaces.* Surface Science, **600**, 3888 – 3891 (2006)

[133] L. Hyungjun and C. Hyoung Joon. *Role of d orbitals in the Rashba-type spin splitting for noble-metal surfaces.* Phys. Rev. B, **86**, 045437 (2012)

[134] M. Hochstrasser, J. G. Tobin, E. Rotenberg, and S. D. Kevan. *Spin-resolved photoemission of surface states of W(110)-(1 × 1)-H.* Phys. Rev. Lett., **89**, 216802 (2002)

[135] E. Rotenberg, J. W. Chung, and S. D. Kevan. *Spin-orbit coupling induced surface band splitting in Li/W(110) and Li/Mo(110).* Phys. Rev. Lett., **82**, 4066 – 4069 (1999)

[136] Y. M. Koroteev *et al. Strong spin-orbit splitting on Bi surfaces.* Phys. Rev. Lett., **93**, 046403 (2004)

[137] C. R. Ast *et al. Giant spin splitting through surface alloying.* Phys. Rev. Lett., **98**, 186807 (2007)

[138] K. Sugawara, T. Sato, S. Souma, T. Takahashi, M. Arai, and T. Sasaki. *Fermi surface and anisotropic spin-orbit coupling of Sb(111) studied by angle-resolved photoemission spectroscopy.* Phys. Rev. Lett., **96**, 046411 (2006)

[139] D. Hsieh *et al. Observation of unconventional quantum spin textures in topological insulators.* Science, **323**, 919 – 922 (2009)

[140] H. Mönig, J. Sun, Yu. M. Koroteev, G. Bihlmayer, J. Wells, E. V. Chulkov, K. Pohl, and Ph. Hofmann. *Structure of the (111) surface of bismuth: LEED analysis and first-principles calculations.* Phys. Rev. B, **72**, 085410 (2005)

[141] D. Pacilé, C. R. Ast, M. Papagno, C. Da Silva, L. Moreschini, M. Falub, Ari P. Seitsonen, and M. Grioni. *Electronic structure of an ordered Pb/Ag(111) surface alloy: theory and experiment.* Phys. Rev. B, **73**, 245429 (2006)

[142] G. Bihlmayer, S. Blügel, and E. V. Chulkov. *Enhanced Rashba spin-orbit splitting in Bi/Ag(111) and Pb/Ag(111) surface alloys from first principles.* Phys. Rev. B, **5**, 195414 (2007)

[143] L. Moreschini *et al. Assessing the atomic contribution to the Rashba spin-orbit splitting in surface alloys: Sb/Ag(111).* Phys. Rev. B, **79**, 075424 (2009)

[144] I. Gierz, B. Stadtmüller, J. Vuorinen, M. Lindroos, F. Meier, J. H. Dil, K. Kern, and C. R. Ast. *Structural influence on the Rashba-type spin splitting in surface alloys.* Phys. Rev. B, **81**, 245430 (2010)

[145] F. Meier, J. H. Dil, J. Lobo-Checa, L. Patthey, and J. Osterwalder. *Quantitative vectorial spin analysis in angle-resolved photoemission: Bi/Ag(111) and Pb/Ag(111).* Phys. Rev. B, **77**, 165431 (2008)

[146] S.-Y. Xu *et al. Topological phase transition and texture inversion in a tunable topological insulator.* Science, **332**, 560 (2011)

[147] P. Höpfner *et al. Three-dimensional spin rotations at the Fermi surface of a strongly spin-orbit coupled surface system.* Phys. Rev. Lett., **108**, 186801 (2012)

[148] C. R. Ast *et al. Spin-orbit split two-dimensional electron gas with tunable Rashba and Fermi energy.* Phys. Rev. B, **77**, 081407 (2008)

[149] F. Meier, V. Petrov, S. Guerrero, C. Mudry, L. Patthey, J. Osterwalder, and J. H. Dil. *Unconventional Fermi surface spin textures in the* Bi_xPb_{1-x}*/Ag(111) surface alloy.* Phys. Rev. B, **79**, 241408 (2009)

[150] I. Gierz, F. Meier, J. H. Dil, K. Kern, and C. R. Ast. *Tuning the spin texture in binary and ternary surface alloys on Ag(111).* Phys. Rev. B, **83**, 195122 (2011)

[151] H. Mirhosseini, A. Ernst, S. Ostanin, and J. Henk. *Tuning independently the Fermi energy and spin splitting in Rashba systems: ternary surface alloys on Ag(111).* Journal of Physics Condensed Matter, **22**, L5501 (2010)

[152] L. Fu and C. L. Kane. *Probing neutral Majorana fermion edge modes with charge transport.* Physical Review Letters, **102**, 216403 (2009)

[153] S. Basak, H. Lin, L. A. Wray, S.-Y. Xu, L. Fu, M. Z. Hasan, and A. Bansil. *Spin texture on the warped Dirac-cone surface states in topological insulators.* Phys. Rev. B, **84**, 121401 (2011)

[154] A. M. Shikin *et al. Origin of spin-orbit splitting for monolayers of Au and Ag on W(110) and Mo(110).* Phys. Rev. Lett., **100**, 057601 (2008)

[155] A. Varykhalov, J. Sánchez-Barriga, A. M. Shikin, C. Biswas, E. Vescovo, A. Rybkin, D. Marchenko, and O. Rader. *Electronic and magnetic properties of quasifreestanding graphene on Ni.* Phys. Rev. Lett., **101**, 157601 (2008)

[156] A. G. Rybkin, A. M. Shikin, D. Marchenko, A. Varykhalov, and O. Rader. *Spin-dependent avoided-crossing effect on quantum-well states in Al/W(110).* Phys. Rev. B, **85**, 045425 (2012)

[157] K. He *et al. Direct spectroscopic evidence of spin-dependent hybridization between Rashba-split surface states and quantum-well states.* Phys. Rev. Lett., **104**, 156805 (2010)

[158] E. Frantzeskakis, S. Pons, H. Mirhosseini, J. Henk, C. R. Ast, and M. Grioni. *Tunable spin gaps in a quantum-confined geometry.* Phys. Rev. Lett., **101**, 196805 (2008)

[159] J. H. Dil, F. Meier, J. Lobo-Checa, L. Patthey, G. Bihlmayer, and J. Osterwalder. *Rashba-type spin-orbit splitting of quantum well states in ultrathin Pb films.* Phys. Rev. Lett., **101**, 266802 (2008)

[160] B. Slomski, G. Landolt, F. Meier, L. Patthey, G. Bihlmayer, J. Osterwalder, and J. H. Dil. *Manipulating the Rashba-type spin splitting and spin texture of Pb quantum well states.* Phys. Rev. B, **84**, 193406 (2011)

[161] F. Reinert, G. Nicolay, S. Schmidt, D. Ehm, and S. Hüfner. *Direct measurements of the L-gap surface states on the (111) face of noble metals by photoelectron spectroscopy.* Phys. Rev. B, **63**, 115415 (2001)

[162] J. P. Perdew and A. Zunger. *Self-interaction correction to density-functional approximations for many-electron systems.* Phys. Rev. B, **23**, 5048–5079 (1981)

[163] H. Krakauer, M. Posternak, and A. J. Freeman. *Linearized augmented plane-wave method for the electronic band structure of thin films.* Phys. Rev. B, **19**, 1706–1719 (1979)

[164] M. Nagano *et al.* *A first-principles study on the Rashba effect in surface systems.* Journal of Physics: Condensed Matter, **21**, 064239 (2009)

[165] J. Henk, M. Hoesch, J. Osterwalder, A. Ernst, and P. Bruno. *Spin-orbit coupling in the L-gap surface states of Au(111): spin-resolved photoemission experiments and first-principles calculations.* Journal of Physics: Condensed Matter, **16**, 7581 – 7597 (2004)

[166] H. Lee and H. J. Choi. *Role of d orbitals in the Rashba-type spin splitting for noble-metal surfaces. Phys. Rev. B*, **86**, 045437 (2012)

[167] H. Bentmann, T. Kuzumaki, G. Bihlmayer, S. Blügel, E. V. Chulkov, F. Reinert, and K. Sakamoto. *Spin orientation and sign of the Rashba splitting in Bi/Cu(111).* Phys. Rev. B, **84**, 115426 (2011)

[168] B. Slomski, F. Meier, J. Osterwalder, and J. H. Dil. *Controlling the effective mass of quantum well states in Pb/Si(111) by interface engineering.* Phys. Rev. B, **83**, 035409 (2011)

[169] T Hirahara *et al.* *Origin of the surface-state band-splitting in ultrathin Bi films: from a Rashba effect to a parity effect.* New Journal of Physics, **10**, 083038 (2008)

[170] S. Souma *et al.* em Direct Measurement of the out-of-plane spin texture in the Dirac cone surface state of a topological insulator. *Phys. Rev. Lett.*, **106**, 216803 (2011)

[171] K. Sakamoto *et al.* *Abrupt rotation of the Rashba spin to the direction perpendicular to the surface. Phys. Rev. Lett.*, **102**, 096805 (2009)

[172] P. B. Howes *et al.* *Influence of interfacial atomic structure on the Schottky-barrier height of Si(111)-Pb.* Phys. Rev. B, **51**, 17740–17743 (1995)

[173] R. Feng, E. H. Conrad, M. C. Tringides, C. Kim, and P. F. Miceli. *Wetting-layer transformation for Pb nanocrystals grown on Si(111).* Appl. Phys. Lett., **85**, 3866–3868 (2004)

[174] S. A. Wolf *et al.* *Spintronics: A spin-based electronics vision for the future.* Science, **294**, 1488 – 1495 (2001)

[175] G. Ertl and J. Küppers. *Contacts to Semiconductors - Fundamentals and Technology.* Noyes Publications (1993)

[176] M.-S. Kang *et al.* *Metal work-function and doping-concentration dependent barrier height of Ni-contacts to 4H-SiC with metal-embedded nano-particles.* Material Science Forum, **857**, 717 – 720 (2012)

[177] X. Zhang *et al. Effect of substrate doping concentration on quantum well states of Pb island grown on Si(111).* Surface Science, **604**, 175 – 180 (2010)

[178] L. Rettig, P. S. Kirchmann, and U. Bovensiepen. *Ultrafast dynamics of occupied quantum well states in Pb/Si(111).* New Journal of Physics, **14**, 023047 (2012)

[179] H. Mirhosseini *et al. Unconventional spin topology in surface alloys with Rashba-type spin splitting.* Physical Review B, **79**, 245428 (2009)

[180] M. Endo, I. Sumio, and M. S. Dresselhaus. *Carbon Nanotubes.* Pergamon (1998)

[181] H. Bentmann, S. Abdelouahed, M. Mulazzi, J. Henk, and F. Reinert. *Direct observation of interband spin-orbit coupling in a two-dimensional electron system.* Phys. Rev. Lett., **108**, 196801 (2012)

[182] M. Hoesch *et al. Spin-polarized Fermi surface mapping.* Journal of Electron Spectroscopy and Related Phenomena, **124**, 263 – 279 (2002)

[183] A. Varykhalov, J. Sánchez-Barriga, A. M. Shikin, W. Gudat, W. Eberhardt, and O. Rader. *Quantum cavity for spin due to spin-orbit interaction at a metal boundary.* Phys. Rev. Lett., **101**, 256601 (2008)

[184] J. Fabian and S. D. Sarma. *Spin relaxation of conduction electrons in polyvalent metals: theory and a realistic calculation.* Phys. Rev. Lett., **81**, 5624 – 5627 (1998)

[185] M. Gradhand *et al. Spin polarization on Fermi surfaces of metals by the KKR method.* Phys. Rev. B, **80**, 224413 (2009)

[186] H. Ebert, H. Freyer, and M. Deng *Manipulation of the spin-orbit coupling using the Dirac equation for spin- dependent potentials.* Phys. Rev. B, **56**, 9454 (1997)

[187] J. H. Dil, J. W. Kim, S. Gokhale, M. Tallarida, and K. Horn. *Self-organization of Pb thin films on Cu(111) induced by quantum size effects.* Phys. Rev. B, **70**, 045405 (2004)

[188] S. Mathias, A. Ruffing, F. Deicke, M. Wiesenmayer, M. Aeschlimann, and M. Bauer. *Band structure dependence of hot-electron lifetimes in a Pb/Cu(111) quantum-well system.* Phys. Rev. B, **81**, 155429 (2010)

[189] J. Braun, P. Ruggerone, G. Zhang, J. P. Toennies, and G. Benedek. *Surface phonon dispersion curves of thin Pb films on Cu(111).* Phys. Rev. B, **79**, 205423 (2009)

[190] A. Zugarramurdi, N. Zabala, V. M. Silkin, A. G. Borisov, and E. V. Chulkov. *Lifetimes of quantum well states and resonances in Pb overlayers on Cu(111).* Phys. Rev. B, **80**, 115425 (2009)

[191] A. Zugarramurdi, N. Zabala, V. M. Silkin, E. V. Chulkov, and A. G. Borisov. *Quantum-well states with image state character for Pb overlayers on Cu(111).* Phys. Rev. B, **86**, 075434 (2012)

[192] F. M. Pan, M. Caragiu, N. Ferralis, and R. D. Diehl. *Substitutional adsorption geometry for Pb(111)-*$(\sqrt{3}\times\sqrt{3})R30^\circ$*-K.* Surface Science, **600**, 537 – 541 (2006)

[193] W. Lai, W. Huang, and D. Xie. *A first-principles study of K adsorption on Pb(111).* Physical Chemistry Chemical Physics, **10**, 1669–1674 (2008)

[194] J. Kim, A. A. Khajetoorians, W. Zhu, Z. Zhang, and C.-K. Shih. *Atomic scale control of catalytic process in oxidation of Pb thin films.* Surface Science, **606**, 450 – 455 (2012)

[195] D. Vandre, L. Incoccia, and G. Kaindl. *Structural studies of the Mg/Si(111) interface formation.* Surface Science, **225**, 233 – 241 (1990)

[196] K. Sakamoto, P. E. J. Eriksson, S. Mizuno, N. Ueno, H. Tochihara, and R. I. G. Uhrberg. *Core-level photoemission study of thallium adsorbed on a* Si(111)-(7×7) *surface: valence state of thallium and the charge state of surface Si atoms.* Phys. Rev. B, **74**, 075335 (2006)

[197] T. Nagao *et al. Structural phase transitions of* Si(111)-$(\sqrt{3}\times\sqrt{3})R30^\circ$-Au*: phase transitions in domain-wall configurations.* Phys. Rev. B, **57**, 10100 – 10109 (1998)

[198] A. B. McLean, L. J. Terminello, and F. J. Himpsel. *Electronic structure of* Si(111)-$(\sqrt{3}\times\sqrt{3})R30^\circ$-B *studied by Si 2p and B 1s core-level photoelectron spectroscopy.* Phys. Rev. B, **41**, 7694 – 7700 (1990)

[199] C. R. Ast *et al. Local detection of spin-orbit splitting by scanning tunneling spectroscopy.* Phys. Rev. B, **75**, 201401 (2007)

[200] M. Bauer. *Femtosecond ultraviolet photoelectron spectroscopy of ultra-fast surface processes.* Journal of Physics D: Applied Physics, **38**, R253 (2005)

Curriculum Vitae

Personal

Name	Bartosz Slomski
Date of Birth	02.08.1982
Place of Birth	Barlinek, Poland
Civil status	Married, 1 son
Nationality	Poland

University education

2009 – 2013	PhD student in the group of Prof. Jürg Osterwalder, Physic institute, University of Zurich PhD Thesis: *"A Spin- and Angle-Resolved Photoemission Study of the Rashba-Bychkov Effect in Lead Quantum Well States"*
2008 – 2009	Diploma work in the group of Prof. Michael Bauer, Institute of Experimental and Applied Physics, Christian-Albrechts University of Kiel. Topic: *"Frequency-Resolved Optical Gating and High Harmonic Generation"*
2002 – 2009	Study of physics at the Christian-Albrechts University of Kiel
2006 – 2007	Erasmus program at the Technical University Vienna

School education

1998 – 2002	Technical gymnasium, Kiel
1992 – 1998	Hans-Brüggemann-Realschule, Bordesholm
1990 – 1992	Elementary school, Wattenbek
1989 – 1990	Elementary school, Choszczno (Poland)

Teaching Experience

2004 – 2009	Teaching assistant in physics for medical, biology and physics students, Christian-Albrechts University of Kiel
2009 – 2013	Teaching assistant in physics for medical, biology and physics students, University of Zurich

List of publications

- B. Slomski, G. Landolt, G. Bihlmayer, J. Osterwalder and J. H. Dil. *"Tuning of the Rashba effect in Pb quantum well states via a variable Schottky barrier"*, Nature Scientific Reports, **3**, 1963 (2013)
- B. Slomski, F. Meier, J. Osterwalder and J. H. Dil. *"Controlling the effective mass of quantum well states in Pb/Si(111) by interface engineering"*, Phys. Rev. B, **83**, 072207 (2011)
- B. Slomski, G. Landolt, F. Meier, L. Patthey, G. Bihlmayer, J. Osterwalder and J. H. Dil. *"Manipulating the Rashba-type spin splitting and spin texture of Pb quantum well states"*, Phys. Rev. B, **84**, 193406 (2011)
- S. Y. Xu, M. Neupane, C. Liu, D. Zhang, A. Richardella, L. A. Wray, N. Alidoust, M. Leandersson, T. Balasubramanian, J. Sánchez-Barriga, O. Rader, G. Landolt, B. Slomski, J. H. Dil, J. Osterwalder, T.-R. Chang, H.-T. Jeng, H. Lin, A. Bansil, N. Samarth and M. Z. Hasan. *"Hedgehog spin texture and Berry's phase tuning in a magnetic topological insulator"*, Nature Physics, **8**, 616-622 (2012)
- P. Höpfner, J. Schäfer, A. Fleszar, J. H. Dil, B. Slomski, F. Meier, C. Loho, C. Blumenstein, L. Patthey, W. Hanke and R. Claessen. *"Three-Dimensional Spin Rotations at the Fermi Surface of a Strongly Spin-Orbit Coupled Surface System"*, Phys. Rev. Lett. **108**, 186801 (2012)
- S. V. Eremeev, G. Landolt, T. V. Menshchikova, B. Slomski, Y. M. Koroteev, Z. S. Aliev, M. B. Babanly, J. Henk, A. Ernst, L. Patthey, A. Eich, A. A. Khajetoorians, J. Hagemeister, O. Pietzsch, J. Wiebe, R. Wiesendanger, P. M. Echenique, S. S. Tsirkin, I. R. Amiraslanov, J. H. Dil and E. V. Chulkov. *"Atom-specific spin mapping and buried topological states in a homologous series of topological insulators"*, Nature Communications **3**, 635 (2012)
- S.-Y. Xu, Y. Xia, L. A. Wray, S. Jia, F. Meier, J. H. Dil, J. Osterwalder B. Slomski, A. Bansil, H. Lin, R. J. Cava and M. Z. Hasan. *"Topological Phase Transition and Texture Inversion in a Tunable Topological Insulator"*, Science, **560**, 332 (2011)
- P. D. C. King, R. C. Hatch, M. Bianchi, R. Ovsyannikov, C. Lupulescu, G. Landolt, B. Slomski, J. H. Dil, D. Guan, J. L. Mi, E. D. L. Rienks, J. Fink, A. Lindblad, S. Svensson, S. Bao, G. Balakrishnan, B. B. Iversen, J. Osterwalder, W. Eberhardt, F. Baumberger and Ph. Hofmann. *"Large Tunable Rashba Spin Splitting of a Two-Dimensional Electron Gas in* Bi_2Se_3*"*, Phys. Rev. Lett. **107**, 096802 (2011)

- T. Rohwer, S. Hellmann, M. Wiesenmayer, C. Sohrt, A. Stange, B. Slomski, A. Carr, Y. Liu, L. Miaja Avila, M. Kalläne, S. Mathias, L. Kipp, K. Rossnagel and M. Bauer. *"Collapse of long-range charge order tracked by time-resolved photoemission at high momenta"*, Nature **471**, 490-493 (2011)

- G. Landolt, S. V. Eremeev,Y. M. Koroteev, B. Slomski, S. Muff, T. Neupert, M. Kobayashi, V. N. Strocov, T. Schmitt, Z. S. Aliev, M. B. Babanly, I. R. Amiraslanov, E. V. Chulkov, J. Osterwalder and J. H. Dil. *"Disentanglement of Surface and Bulk Rashba Spin Splittings in Noncentrosymmetric BiTeI"*, Phys. Rev. Lett. **109**, 116403 (2012)

- C. Tegenkamp, D. Lükermann, H. Pfnür, B. Slomski, G. Landolt and J. H. Dil. *"Fermi Nesting between Atomic Wires with Strong Spin-Orbit Coupling"*,
Phys. Rev. Lett. **109**, 266401 (2012)

- S. Muff, F. von Rohr, G. Landolt, B. Slomski, A. Schilling, R. J. Cava, J. Osterwalder and J. H. Dil. *"Separating the bulk and surface n- to p-type transition in the topological insulator* $GeBi_{4-x}Sb_xTe_7$*"*, Phys. Rev. B. **88**, 035407 (2013)

Unpublished

- B. Slomski, G. Landolt, G. Bihlmayer, J. Osterwalder, J. H. Dil. *"Interband spin-orbit coupling between anti-parallel spin states in Pb quantum well states"*,
submitted to New Journal of Physics (May 2013)

Acknowledgements

Looking back at my project which ran for four years at the COPHEE end-station of the Swiss Light Source it is my pleasure to thank many people who have been very valuable during my studies:

I thank **Hugo Dil** for supervising my thesis. With Hugo I had the strongest academic interaction. He had the right ideas whenever I got stuck and he adsorbed the majority of my questions. Best wishes for your future academic career at the EPFL Lausanne. Furthermore many thanks to **Jürg Osterwalder** for giving me the opportunity to work as a Ph.D at the Physics Institute and the Swiss Light Source. I really enjoyed our meetings in your office for discussing the data and the manuscripts. Still, I am impressed by your way of perceptive and critical thinking. I thank **Fabian Meier**, **Gabriel Landolt**, **Dominik Leuenberger**, and **Stefan Muff** for being my office mates and fellow sufferers during beamtimes that did not work as wished. My special thank goes to Fabian who transferred his knowledge about handling the experimental setup at the very beginning of my thesis and Gabriel who tried to teach me Swiss German (with only little success). I really enjoyed our discussions about physics and other topics. Then, I would like to thank the present and past members of the group for the friendly working environment: **Matthias Hengsberger**, **Thomas Greber**, **Michael Greif**, **Silvan Roth**, **Martin Morscher**, **Thomas Brugger**, **Luca Castiglioni**, **Rasmus Westerstöm**, **Adrian Hemmi**, **Huanyao Cun**, **Roland Stania**, **Carlo Bernard**, **Adrian Schuler**, **Carmelina Genovese** and **Thomas Källin**.
Carrying out experiments at a large research facility such as the SLS is only possible when many brilliant people interact. Among many others, a special thank goes to **Matthias Muntwiler**, **Vladimir Petrov**, **Moritz Hoesch**, **Jorge Lobo-Checa**, and **Martin Klöckner** for the construction of the COPHEE setup. Also a special thank goes to the great technician trio **Christoph Hess**, **Fritz Dubi**, and **Markus Kropf** and to the rest of the present and past members of the SIS & Adress Beamline: **Luc Pathey**, **Thorsten Schmitt**, **Ming Shi**, **Vladimir Strockov**, **Milan Radovic**, **Elia Razolli**, **Claude Monney**, **Nick Plumb**, and **Juraj Krempasky**.
I also owe many thanks to **Gustav Bihlmayer**, from the Research Center in Jülich, for performing DFT calculations on Pb/Si, which helped me a lot to understand the spin-orbit interaction in quantum well states and to **Gian Salis**, from the IBM Research Lab in Rüschlikon, for being the second assessor of this thesis. I found it really helpful that you shed light on my project from a non-ARPES perspective.

Despite a distance of 1000 km between my parents and me I could always count on my mother **Marlena Siebels** and my stepfather **Jürgen Siebels**. Thank you so much for your support throughout my studies.
Finally, I thank my ravishing wife **Tine** and my son **Jakub**, who inspire me to no end!